Title
Probing Dark Energy with Theory and Observations

Author
de Putter, Roland

Publication Date
2010

Peer reviewed|Thesis/dissertation

Probing Dark Energy with Theory and Observations

by

Roland de Putter

A dissertation submitted in partial satisfaction of the

requirements for the degree of

Doctor of Philosophy

in

Physics

in the

Graduate Division

of the

University of California, Berkeley

Committee in charge:

Professor Eric V. Linder, Co-Chair

Professor Saul Perlmutter, Co-Chair

Professor Chung-Pei Ma

Professor Martin White

Fall 2010

Probing Dark Energy with Theory and Observations

Abstract

Probing Dark Energy with Theory and Observations

by

Roland de Putter

Doctor of Philosophy in Physics

University of California, Berkeley

Professor Eric V. Linder, Co-Chair

Professor Saul Perlmutter, Co-Chair

The discovery of cosmic acceleration twelve years ago implies that our universe is dominated by dark energy, which is either a tiny cosmological constant or a mysterious fluid with large negative pressure, or that Einstein's successful theory of gravity needs to be modified at large scales/low energies. Since then, independent evidence of a number of cosmological probes has firmly established the picture of a universe where dark energy (or the effective contribution from a modification of gravity) makes up about 72% of the total energy density. Whichever of the options mentioned above will turn out to be the right one, a satisfying explanation for cosmic acceleration will likely lead to important new insights in fundamental physics. The question of the physics behind cosmic acceleration is thus one of the most intriguing open questions in modern physics. In this thesis, we calculate current constraints on dark energy and study how to optimally use the cosmological tools at our disposal to learn about its nature.

We will first present constraints from a host of recent data on the dark energy sound speed and equation of state for different dark energy models including early dark energy. We then study the observational properties of purely kinetic k-essence models and show how they can in principle be straightforwardly distinguished from quintessence models by their equation of state behavior. We next consider a large, representative set of dark energy and modified gravity models and show that they can be divided into a small set of observationally distinct classes. We also find that all non-early dark energy models we consider can be modeled extremely well by a simple linear equation of state form. We will then go on to discuss a number of alternative, model independent parametrizations of dark energy properties. Among other things, we find that principal component analysis is not as model-independent as one would like it to be and that assuming a fixed value for the high redshift equation of state can lead to a dangerous bias in the determination of the equation of state at low redshift. Finally, we discuss using weak gravitational lensing of cosmic microwave background (CMB) anisotropies as a cosmological probe. We compare

different methods for extracting cosmological information from the lensed CMB and show that CMB lensing will in the future be a useful tool for constraining dark energy and neutrino mass. Whereas marginalizing over neutrino mass can degrade dark energy constraints, CMB lensing helps to break the degeneracy between the two and restores the dark energy constraints to the level of the fixed neutrino mass case.

In loving memory of my uncle Rienk (1952 - 2010)

Contents

List of Figures

List of Tables

Acknowledgments

I would like to thank a number of people who have in some way played an important role in the process leading to this thesis. First of all, I would like to thank Michelle for giving me so much joy throughout most of my time here in Berkeley and for helping me get my mind off physics every now and then. I would like to thank Anne Takizawa and Donna Sakima for their excellent and friendly help with all bureaucratic matters in the physics department. I would like to thank Martin White and Chung-Pei Ma for being so kind to be on my thesis and qualifying exam committees and for their useful advice throughout the years. I also want to thank two of my collaborators on the projects represented in this thesis: Dragan Huterer and Oliver Zahn. I am grateful to Saul Perlmutter for being willing to be my faculty advisor and for his active role on my thesis committee. By far the most important role during these four years was played by my advisor Eric Linder. He is truly a great advisor who was always available to help me and who supported me not just on the science side, but also with all other matters that are important for a beginning physicist to find his way in academia.

Chapter 1

Introduction

The mystery of cosmic acceleration is one of the biggest and most interesting questions in physics. About twelve years ago (in 1998) at the time of this writing, two independent teams [180, 187] studying Type Ia supernovae discovered that the expansion of the universe is accelerating. If gravity is described by general relativity, this means that the universe has to be filled by a component with negative pressure and (nearly) constant energy density. We do not know the nature of this substance, but we have a name for it: dark energy. One possibility is that dark energy is Einstein's cosmological constant, but this explanation has problems (for reasons explained later) so it is important to explore alternative explanations where the dark energy density is not constant. The main example of a dynamical dark energy model is quintessence, where the dark energy is described by a scalar field having a potential energy dominating over its kinetic energy. Yet another possibility is to take the radical step of giving up general relativity and ascribing the cause of cosmic acceleration to a modification in the theory of gravity, making it repulsive on cosmological scales. While there are many potential explanations around, the nature of dark energy is still very much an open question.

Currently, the evidence for dark energy[1] is overwhelming. Not only can we say at very high confidence level that dark energy exists, this conclusion comes from a combination of very different probes so that it cannot be due to the systematics of one individual probe. In the concordance model of the universe, about 72% of the total energy density is dark energy, about 23% dark matter and only the remaining 5% is made of the type of matter one finds in the standard model of particle physics: baryons (using the cosmologist's definition of baryons), radiation and neutrinos. This fact immediately gives one of the major motivations for studying dark energy: the vast majority of our universe is made of it! Furthermore, the fate of our universe, whether it will expand forever or come to an end in a big crunch or even a "big rip," depends

[1] If modified gravity explains cosmic acceleration, it can still be described in terms of an *effective* background dark energy density. Here we use a general meaning of the phrase "dark energy," not excluding modified gravity.

on the nature of dark energy. The second major motivation is that there is reason to believe that the solution to the problem will give us important new insights into the fundamental physics describing our universe. It is likely that a proper explanation for cosmic acceleration will require and/or lead to a deeper understanding of quantum gravity and thus what we hope will be a theory of everything.

Not only is the question of cosmic acceleration an exciting one, we also live in an exciting time to study this question. We are now exiting the time of discovery of its *existence* and entering the time where observations are getting sufficiently powerful to get strong constraints on the *nature* of dark energy. Some of the challenges for theorists therefore are the following. First of all, it is necessary to understand the observational properties of dark energy models very well and to find a way of modeling these properties such that, if dark energy indeed is more interesting than just a cosmological constant, we will be able to extract this information from the data, and not miss it, and then draw the right conclusions. Secondly, it is important to study the constraining power of different observational probes in order to design surveys that maximally constrain dark energy and other physics of interest and to develop the mathematical tools to use these probes optimally once the data are in.

In this thesis, we address a number of these issues. In chapter 2, we will discuss the current constraints on dark energy properties, where we go beyond just modeling the background properties, but include the dark energy perturbations. In chapters 3 and 4, we will first discuss a number of specific scalar field models and their observational properties. This work shows that despite the large class of available models, there are some simple, distinct observational properties that distinguish classes of models from each other. Since there is such a large class of possible models (a lot of which have not been invented yet), it makes sense to parametrize the properties of dark energy in a model independent way. We critically discuss such parametrizations in chapter 5. Finally, we study the use of weak gravitational lensing of the cosmic microwave background as a tool to learn about dark energy and neutrinos in the future.

In this chapter, we will give a brief introduction to dark energy. We will discuss the current observational evidence, candidate theories for dark energy and the most promising observational probes. Even though we will review a little bit of basic cosmology, for a proper introduction into the field, we refer the reader to one of the standard textbooks [136, 177, 175, 71]. For a more complete review of dark energy and cosmic acceleration, we recommend one of the recent review articles [91, 43], where the first focuses more on the observational side and the second more on the theory.

1.1 Observational Effects of Dark Energy

The main effect of dark energy is on the background evolution. A homogeneous, isotropic universe is described by the Friedmann-Robertson-Walker (FRW) metric

$$ds^2 = -dt^2 + a^2(t)\left(\frac{dr^2}{1-kr^2} + d\theta^2 + \sin^2\theta d\phi^2\right), \tag{1.1}$$

where $a(t)$ is the cosmic scale factor and k is the spatial curvature. We normalize $a(t_0) = 1$, where t_0 is the present age of the universe. The evolution of the scale factor is determined by the Friedmann equations

$$\left(\frac{\dot{a}}{a}\right)^2 \equiv H^2 = \frac{8\pi G}{3}\sum_i \rho_i - \frac{k}{a^2} \tag{1.2}$$

$$\frac{\ddot{a}}{a} = -\frac{4\pi G}{3}\sum_i (\rho_i + 3p_i), \tag{1.3}$$

where overdots represent derivatives with respect to time, $\dot{} = d/dt$, H is the Hubble parameter, ρ_i and p_i are the energy density and pressure of each component, G is Newton's constant and we work in units where the speed of light $c = 1$. We define the critical energy density as

$$\rho_c \equiv \frac{3H^2}{8\pi G}, \tag{1.4}$$

which is the total energy density needed to make the universe flat, $k = 0$. Its value today is $\rho_{c,0} \approx 1.9 \cdot 10^{-29} h^2 g/cm^{-3} \approx 8.1 \cdot 10^{-11}\mathrm{eV}^4$, where $h = H_0/\left(100\,\mathrm{km}/s/\mathrm{Mpc}\right)$ and H_0 is the current value of the Hubble parameter. A positive spatial curvature gives a closed universe and a negative value results in an open universe. The energy density in a component relative to the critical density is $\Omega_i(a) \equiv \rho_i(a)/\rho_c(a)$. Our conventions are such that an Ω_i without an argument stands for its value today, i.e. $\Omega_i \equiv \Omega_i(a = 1)$. The energy density of each component has to satisfy the continuity equation

$$\dot{\rho}_i + 3H(\rho_i + p_i) = 0. \tag{1.5}$$

This equation holds for an individual component as long as it is not directly coupled to the other components, and it also holds for the sum of all components. Note that out of the two Friedmann equations and the continuity equation, only two are independent.

In the standard picture, the universe consisting of radiation, matter and dark energy, i.e. $\sum_i \rho_i = \rho_m + \rho_r + \rho_{\mathrm{DE}}$. However, when discussing the late universe, which is when dark energy becomes important, we will often ignore the radiation component, since the radiation energy density today is $\Omega_r \approx 4 \cdot 10^{-5} \ll 1$ (assuming no relativistic neutrinos). The evolution of each component can be characterized by its equation of state

$$w_i \equiv p_i/\rho_i, \tag{1.6}$$

which, through the continuity equation, determines

$$\rho_i \propto e^{-3\int^a \frac{da'}{a'}(1+w_i(a'))}. \tag{1.7}$$

Matter and radiation have $w_m = 0, w_r = 1/3$ and therefore $\rho_m \propto a^{-3}$, $\rho_r \propto a^{-4}$. Since we do not know the nature of dark energy, its equation of state $w_{\rm DE}(a)$ can in principle be a general function of the scale factor. The second equation shows that in the absence of dark energy $\ddot{a} < 0$ and the expansion of the universe decelerates. This is why historically, the expansion history of the universe was analyzed in terms of the *deceleration* parameter

$$q(a) \equiv -\frac{\ddot{a}}{aH^2} = -\frac{1}{2}\sum_i \Omega_i(a)\left(1+3w_i(a)\right). \tag{1.8}$$

It follows from the above expression that to get an accelerating universe, one needs the dark energy component to have a large, negative equation of state, $w_{\rm DE} < -1/3$, and one needs the dark energy to make a significant contribution to the energy budget ($\Omega_{\rm DE} \sim 1$). The cosmological constant is a special case of this, where $w_\Lambda = -1$ so that $\rho_\Lambda = -p_\Lambda = $ const. We will discuss this option and its motivation from theory in section 1.4.1.

It is clear from the above, that by measuring the expansion history directly, through quantities like the Hubble parameter and cosmic distances, one can learn a great deal about the properties of dark energy. This has been the most successful path thus far. However, one can also learn about dark energy from its effects on the growth of perturbations. The main way dark energy influences matter perturbations is by changing the Hubble parameter and therefore the friction term in the linear growth equation

$$\ddot{\delta}_m + 2H\dot{\delta}_m = 4\pi G\rho_m\delta_m, \tag{1.9}$$

where $\delta_m \equiv \delta\rho_m/\rho_m$. This equation is exact (for a pressureless fluid in the synchronous gauge) in the case of a cosmological constant. When dark energy is not a cosmological constant, it must have spatial clustering itself and the equation above is formally no longer valid. However, in most dark energy models, the dark energy perturbations are strongly suppressed and can be ignored so that Eq. (1.9) can be used to a very good approximation. Dark energy perturbations, and our observational constraints on them, will be the subject of chapter 2.

1.2 Discovery

Even before the publication of the supernova results in 1998, there had been hints for the existence of an extra component behaving like a cosmological constant (see for example [172, 140]). Observations of large scale structure (LSS) implied that the total matter density was significantly smaller than the critical density. This in combination

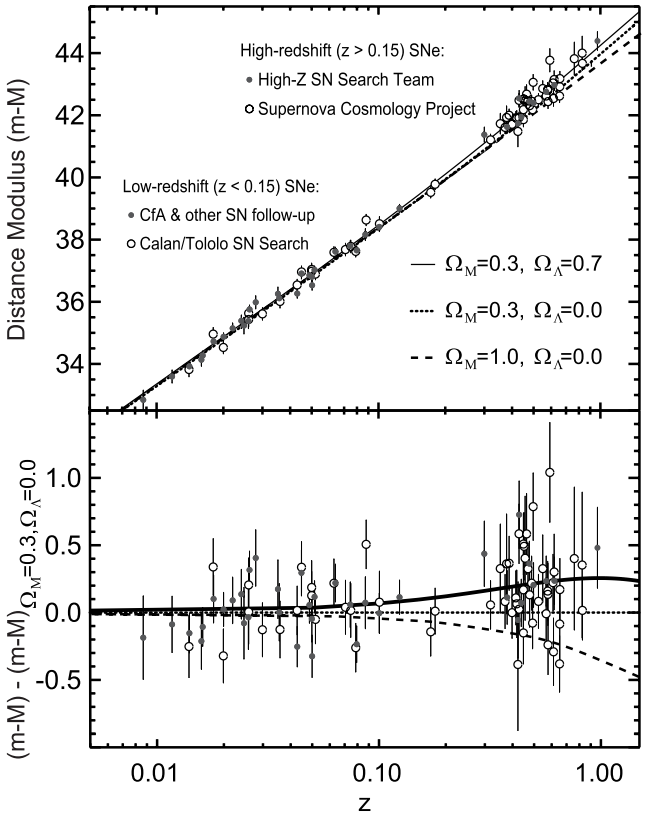

Figure 1.1: The supernova data used by the Supernova Cosmology Project and the High-z Supernova team to discover cosmic acceleration. Figure taken from [179].

with the theoretical prejudice from inflation that the universe is flat, suggested that there may be an extra component such that $\Omega_m + \Omega_\Lambda = 1$. In addition, for this component to not disturb structure formation too much, it must have only become important in recent times, which means it should decay more slowly than matter and thus have a negative equation of state. A cosmological constant fit this picture well. In addition, adding a cosmological constant helped to solve the age problem: observations of globular clusters told us that the age of the universe must be at least about 12 Gyr, which was higher than the age of the universe calculated in a matter-only universe. Adding a cosmological constant makes the universe older and resolves the disagreement.

However, even though there was clearly some evidence pointing towards a cosmological constant (or dark energy) before, what really changed everything was the discovery of cosmic acceleration using the Hubble diagram of Type Ia supernovae [180, 187]. Since supernovae have continued to play an important role and since they promise to do so in the future, let us take a look at this measurement in some more

detail. The reason that Type Ia supernovae can be used to reconstruct the expansion history is that they are *standardizable* candles. Up to a calibration factor obtained from the shape of the light curve (the luminosity as a function of time), all Type Ia SNe are believed to have the same intrinsic luminosity up to a scatter of about 15% of a magnitude. This allows one to infer information about the distance to these supernovae from measurements of their apparent brightness.

More quantitatively, the observed magnitude of a supernova is given by (modulo comparison with a standard star)

$$m = -2.5 \log_{10} \left[\frac{I}{4\pi d_L^2} \right] - m_\star, \tag{1.10}$$

where I is the intrinsic intensity, $m_\star$ is the magnitude of some astronomical object relative to which magnitudes are calibrated, and, assuming flatness,

$$d_L = (1+z)r = (1+z)\frac{c}{H_0} \int dz \frac{H_0}{H(z)} \tag{1.11}$$

is the luminosity distance (r is the coordinate distance appearing in the metric, Eq. (1.1)). In terms of the absolute magnitude $M_{10\mathrm{pc}}$ (the magnitude observed if the supernovae were at a distance of 10 pc), the magnitude becomes

$$m = M_{10pc} + 5 \log_{10}(d_L/10pc) \equiv \mathcal{M} + 5 \log_{10} \left((1+z) \int dz \frac{H_0}{H(z)} \right), \tag{1.12}$$

where

$$\mathcal{M} = M_{10pc} + 25 + 5 \log_{10} \left(H_0/c \times 1Mpc \right). \tag{1.13}$$

By analyzing the relation between redshift and magnitude of a large number of supernovae, it is thus possible to constrain the parameter $\mathcal{M}$, a combination of the Hubble parameter and the unknown absolute supernova magnitude, and more importantly, the redshift evolution of the distance modulus

$$\mu = 5 \log_{10} \left((1+z) \int dz \frac{H_0}{H(z)} \right), \tag{1.14}$$

which directly tells us about the expansion history.

By analyzing of order 50 SNe at redshifts $z < 1$, members of both the Supernova Cosmology Project and of the High-z SN Search found that distant supernovae looked fainter (larger magnitude) than expected based on a decelerating universe by typically about 0.25 magnitude, see Fig. 1.1. Heuristically, larger magnitude means a larger coordinate distance to the same redshift and therefore a longer conformal time between the time the universe had size $a = 1/(1+z)$ and now. In other words, the expansion must have been slower in the past. In fact the data showed that the expansion is accelerating, corresponding to a negative deceleration parameter $q < 0$. A

cosmological constant (or component with equation of state $w \approx -1$) would account for this behavior. In a model with only matter and a cosmological constant, these early data preferred $\Omega_\Lambda > 0$ at better than 99% confidence level [180], with a best-fit value of $\Omega_\Lambda = 0.72$.

1.3 Current Constraints

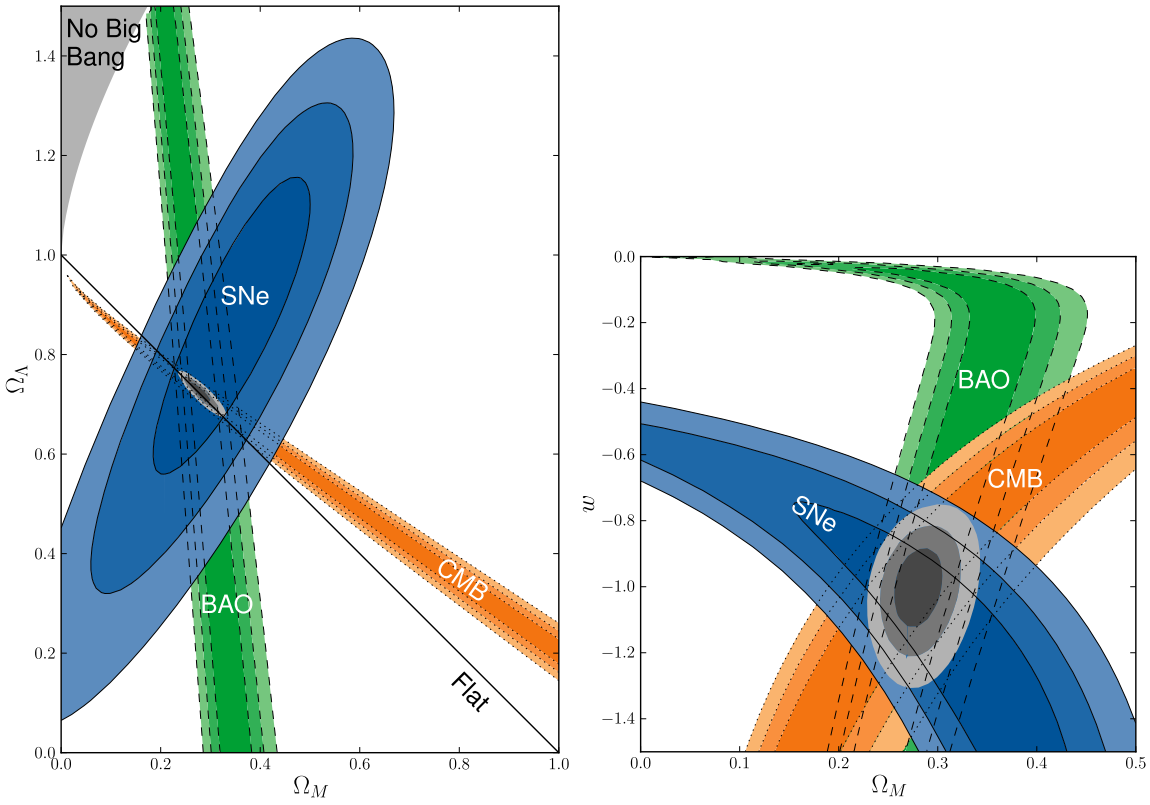

Figure 1.2: Left: Current constraints on Ω_m and Ω_Λ when the curvature is allowed to vary. Right: Constraints on a flat model with constant dark energy equation of state. Figures courtesy of [14]

.

Since the original discovery of cosmic acceleration, the evidence for a cosmological constant has become very strong. An important step was the measurement of the first acoustic peak in the spectrum of cosmic microwave background anisotropies, which gave observational support for the theoretical expectation that the universe is spatially flat [60, 125, 182], i.e. $\Omega_m + \Omega_{\rm DE} \approx 1$. Since then, CMB observations have become much stronger with the advent of the Wilkinson Microwave Anisotropy Probe (WMAP) so that even with CMB data alone, Ω_Λ is now constrained to be

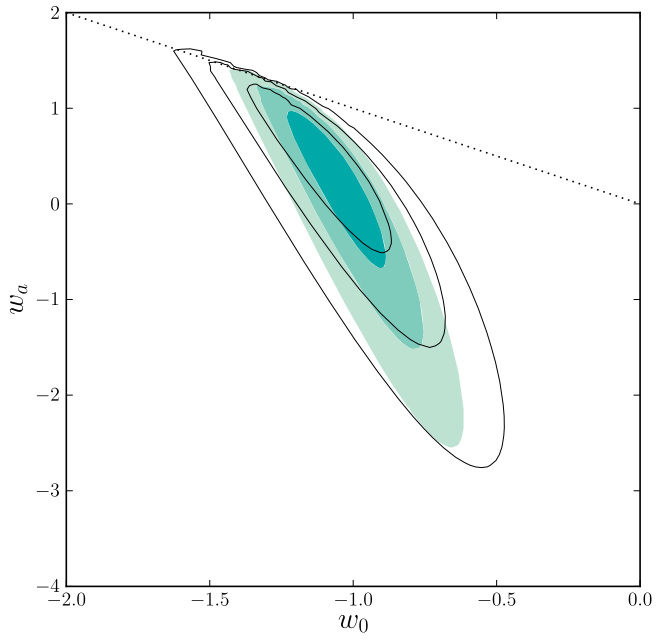

Figure 1.3: Current constraints from CMB, SNe and BAO on variation in the dark energy equation of state in the form of the linear parametrization $w(a) = w_0 + w_a(1 - a)$. A flat universe is assumed. Figure courtesy of [14].

$\Omega_\Lambda = 0.734 \pm 0.029$ (assuming flatness) [141]. The supernova data themselves have improved a great deal too. The latest compilation of supernova data [14] contains 557 supernovae in the range $z < 1.4$ as discovered by different groups, including SCP, SDSS, Essence and SNLS.

In addition, observations of the baryon acoustic peak scale shed light on dark energy by constraining the expansion history [178]. We will discuss this technique in the future data section. Finally, recent weak gravitational lensing measurements [106, 126, 164, 199], lower bounds on the age of the universe [139] and measurements of the ratio of baryonic to total mass in clusters [13] all help constrain dark energy. and help confirm the now standard ΛCDM picture. The most recent constraint is $\Omega_\Lambda = 0.722 \pm 0.015$ (assuming flatness) [138]. We show current constraints and complementarity of different probes for a model with Ω_k allowed to vary in the left panel of Fig. 1.2 and constraints in the $\Omega_m - w$ plane (here assuming flatness so that $\Omega_\Lambda = 1 - \Omega_m$) in the right panel. In Fig. 1.3 we show the current constraints from CMB, BAO and SNe on the dark energy equation of state for the parametrization $w(a) = w_0 + w_a(1 - a)$.

1.4 Explaining Cosmic Acceleration

1.4.1 The Cosmological Constant

The simplest explanation of cosmic acceleration involves a cosmological constant Λ. To date, this model fits all the observations perfectly. The history of the cosmological constant started when Einstein [80] added a cosmological constant to the equations of motion for the metric in general relativity (i.e. to the Einstein equations) in order to find a static universe solution.

$$R_{\mu\nu} - \frac{1}{2}g_{\mu\nu}R - \Lambda g_{\mu\nu} = -8\pi G T_{\mu\nu}, \tag{1.15}$$

where $R_{\mu\nu}$ is the Ricci tensor, $R \equiv R^{\mu}_{\mu}$ is the Ricci scalar, $g_{\mu\nu}$ is the metric tensor and $T_{\mu\nu}$ the total energy-momentum tensor.

Without going through the equations, the idea is simple. Ordinary matter has an attractive gravitational force and does not allow a static universe. A cosmological constant, because of its effective negative pressure has a repulsive effect and could counterbalance ordinary matter and Einstein's solution. Not much later, Hubble [118] found that the universe is not static at all and is in fact expanding, thus getting rid of the need for Einstein's cosmological constant. Later, Einstein would famously call this episode his biggest blunder, for he could have predicted an expanding (or non-static) universe.

Later however, it was realized in the context of quantum field theory that there must be a large energy associated with particles popping in and out of existence in the vacuum, which behaves exactly as a cosmological constant [240], i.e. $T^{\text{vac}}_{\mu\nu} = -\rho_{\text{vac}} g_{\mu\nu}$. A useful way of looking at this is to consider Λ a parameter of the model (just like for example the standard model couplings) that is renormalized by quantum effects. The problem is that the quantum corrections, or the vacuum energy, is many many orders of magnitude greater than the observed energy density of the universe. This can be seen by considering the contribution to the vacuum energy of a single particle. In quantum field theory, each Fourier mode with wave vector $\vec{k}$ essentially behaves like a harmonic oscillator with frequency $\omega = \sqrt{\vec{k}^2 + m^2}$ (we use natural units $c = \hbar = 1$) so that the contribution to the vacuum energy is a sum over all modes of the harmonic oscillator's vacuum state energy $E_0 = \frac{1}{2}\omega(\vec{k})$:

$$\rho_{\text{vac}} = \int_0^{E_c} \frac{4\pi k^2 dk}{(2\pi)^3} \frac{1}{2} \sqrt{k^2 + m^2}. \tag{1.16}$$

If we believed our model of particle physics up to infinitely high energies, the vacuum energy would come out infinite, but we believe that our current model of particle physics is only an effective theory valid up to a certain cutoff scale E_c, which cuts off the above integral. So what is the value of this cutoff? Since above the Planck scale gravity and quantum physics are in conflict, we know that the maximum value

of this cutoff is the Planck energy $E_c = E_{\rm Pl} \sim 10^{19}$ GeV. Assuming $m \ll E_c$, this gives $\rho_{\rm vac} \sim E_c^4 \sim 10^{76}$ GeV^4. However, observationally, the vacuum energy needs to satisfy $\rho_\Lambda \lesssim \rho_{c,0} \sim 10^{-10}{\rm eV}^4 = 10^{-36}{\rm GeV}^4$ leading to the famous and very worrying discrepancy of 122 orders of magnitude. This is called the *cosmological constant problem* (see [230] for a review). Another way of stating the problem is that the observed renormalized cosmological constant is at least 122 orders of magnitude smaller than the quantum corrections, thus requiring an enormous fine-tuning of the bare cosmological constant. The problem can be slightly ameliorated by assuming that the cutoff scale is lower than the Planck scale. For example, in supersymmetry (SUSY), the contributions to the vacuum energy of fermions and bosons exactly cancel each other out. If supersymmetry is indeed realized in nature, this means that we only have to integrate up to the scale of SUSY breaking $E_c = E_{\rm SUSY}$. Taking $E_{\rm SUSY} \sim 1$ TeV, as is commonly expected, this would give $\rho_{\rm vac} \sim 10^{12}\,{\rm GeV}^4$, which still gives a discrepancy of 58 orders of magnitude. In order for the fine-tuning problem to disappear, one would need a cutoff scale of order 10^{-2} eV, However, the standard model has been tested in accelerators up to energies not far below the TeV scale so we truly cannot get around this huge fine-tuning problem. Finally, in addition to the fine-tuning problem due to vacuum energy, phase transitions in particle physics (like the electroweak phase transition) also cause jumps in the cosmological constant that are much larger than the current observed value. This makes the fine-tuning problem even worse.

We would like to stress that the cosmological constant problem does not rely on the recent discovery of a non-zero cosmological constant (if it is a cosmological constant). Even without this measurement we would have an upper bound on the cosmological constant forcing fine tuning to at least one part in 10^{122}. Before the discovery of accelerated expansion, this was already considered a big, unsolved problem [230]. The one thing that has changed is that, before, some may have been content to assume that some theory will one day come along and set the the cosmological constant to zero in a natural way (perhaps by virtue of some symmetry), whereas now, if we have indeed measured the cosmological constant, the option of the cosmological constant being exactly zero is gone and we have to explain the specific observed, tiny value.

In summary, the cosmological constant so far fits all the data very well and is the simplest solution to the cosmic acceleration puzzle. The cosmological constant model has just one additional parameter that is naturally there in our theory of gravity and matter anyway. In fact, we expect it must be there because of the vacuum energy. The only problem is the cosmological constant problem, that an incredible fine-tuning is necessary in order for the cosmological constant to have the observed size. Although so far no better candidates exist, one hopes that eventually this fine-tuning problem will be resolved in an elegant way, perhaps within the ultimate theory of quantum gravity. Before we move on to explanations for cosmic acceleration where the dark energy is not a cosmological constant, but a dynamical component of our universe, $\rho_{\rm DE} \neq$ const, we first briefly discuss one specific approach to solving the cosmological constant problem, motivated by string theory.

1.4.2 The Multiverse and the "A Word"

One way of potentially explaining the small value of the cosmological constant without any fine-tuning is by using anthropic arguments. This approach was pioneered by Weinberg [229] and has recently experienced a revival after the emergence of the string theory landscape in the 1990's. We refer to [181, 33] for reviews. The general idea is simple. What if the cosmological constant is allowed to have different values in different parts of the universe, which for ease of language we will consider to be separate universes. The question is then which universe, i.e. with what value of Λ, will a typical observer live in? More specifically, one is interested in having a probability distribution that gives the probability for a certain value of Λ (and potentially of other parameters) to be *observed*. This distribution is a product of the actual probability distribution of Λ in this multiverse and the probability distribution of having observers in a universe, given a value of Λ. Even though the first distribution is typically completely unknown, the second one carries a lot of information. In particular, the requirement of structure formation (which seems to be a condition for observers to emerge) typically places an upper bound on the allowed values of ρ_Λ that is not more than a few orders of magnitude away from the observed value. This way, under mild assumptions on the distribution of Λ in the multiverse that do not involve fine-tuning, predictions for the value of Λ can be obtained that come close to the observed value.

The reason for much recent interest in this approach, besides the cosmological measurement of Λ, is that string theory predicts a "landscape" of different vacua with different vacuum energies. This results in a discrete set of at least 10^{500} different vacua so that one effectively ends up with a continuum of possible vacuum energies. Calculations of Λ using anthropic reasoning within the landscape scenario come very close to the observed value. However, there remain several issues with this approach. First of all, one needs to make some assumptions about the distribution of Λ within the string landscape (typically that it is flat in Λ) and until we have a better understanding of the landscape, we cannot be sure about these assumptions. Secondly, the calculations carried out so far are quite rudimentary, often varying only Λ. If Λ can vary between universes, it is likely that other parameters can too. This could potentially strongly change predictions for the most likely value of Λ [223]. Whereas a certain value of Λ may be too large to allow for observers if all other parameters are held fixed, this may well change when other parameters are allowed to vary in such a way as to help structure formation. Finally, string theory, or another theory allowing a multiverse would need to be more firmly established for the anthropic approach to be fully convincing. Having said this, the multiverse scenario in combination with anthropic reasoning is a very promising approach and is currently the only serious solution to the cosmological constant problem.

1.4.3 Dynamical Dark Energy

An alternative approach to the dark energy puzzle is to assume that somehow the cosmological constant problem is solved, setting $\Lambda = 0$, and that the present cosmic acceleration is caused by another component with a large negative equation of state and varying energy density. The most common set of dynamical dark energy models are quintessence models, in which dark energy is described by a scalar field rolling down its potential. The quintessence Lagrangian for an arbitrary potential $V(\phi)$ is

$$\mathcal{L} = \frac{1}{2}\partial_\mu\phi\partial^\mu\phi - V(\phi), \tag{1.17}$$

so that for a homogeneous field $\phi = \phi(t)$, the energy density and pressure are given by

$$\rho_\phi = \frac{1}{2}\dot{\phi}^2 + V(\phi) \tag{1.18}$$

$$p_\phi = \frac{1}{2}\dot{\phi}^2 - V(\phi). \tag{1.19}$$

Thus, one can get a large negative equation of state $w = p_\phi/\rho_\phi$ to explain cosmic acceleration if the kinetic energy term is much smaller than the potential energy: $\frac{1}{2}\dot{\phi}^2 \ll V(\phi)$.

The number of quintessence models is enormous and we will discuss a number of them in chapter 4. For quintessence models to deliver the goods observationally, the potential parameters typically have to be fine-tuned very strongly. This is not surprising since we want the potential energy density today to be of order $V \sim 10^{-10}$ eV^4. Moreover, we want the field to not have rolled down to its minimum yet (it would no longer be potential dominated and thus no longer cause acceleration in that case) so the typical mass has to be smaller than the present Hubble scale: $m \equiv \sqrt{d^2V/d\phi^2} \lesssim H_0 \sim 10^{-33}$ eV. One also usually ends up with scalar field values $\phi \sim M_P$. One of the few models in which at least the small potential parameters are *technically* natural (i.e. protected against quantum corrections by a symmetry), and therefore deserves special mention, is the pseudo-Nambu-Goldstone boson (PNGB) model [89], which we will come back to in chapter 4.

In addition to quintessence models, there are k-essence models [17] (see chapter 3), where the kinetic term of the scalar field Lagrangian density is modified to a non-canonical form, there are models based on more than one scalar field [34], models based on vector or tensor fields and there are more phenomenological models, where dark energy is not described by a fundamental Lagrangian, but by a relation between its pressure and energy density (for example the generalized Chaplygin gas [28]). People also consider models where the dark energy (for example described by a scalar field) is non-minimally coupled to some other component, like the dark matter or massive neutrinos. The latter possibility is particularly intriguing because the extremely low energy scale of the dark energy $E_{\rm DE} \sim 10^{-2}$ eV coincides roughly with the neutrino mass scale, suggesting a relation [84, 176, 98, 235].

1.4.4 Motivation

Since most of this thesis is devoted to current and future constraints on dynamical dark energy models, we would like to make some general comments about the justification for studying these models. On the down side, most if not all dynamical dark energy models are poorly motivated from a particle physics point of view. As mentioned above, they typically require a fine-tuning of parameters that is unprecedented in particle physics. Not only do all models require very small parameters compared to the natural ones in physics (i.e. the Planck scale and the electroweak scale, which suffers a hierarchy problem of its own), most of them moreover are technically unnatural (PNGB being one of the few exceptions, purely kinetic k-essence, described in chapter 3, being another one), meaning that as with the cosmological constant, the quantum corrections to the parameter in question are many orders of magnitude larger than the renormalized (observed) value. In terms of naturalness of parameters, these models are thus usually at least as problematic as the cosmological constant. Perhaps more importantly, the dynamical dark energy models that are in the literature do not solve, or even address, the cosmological constant problem. Hence, one is simply adding a problem. Not only do we now have to explain why the cosmological constant is zero, we also have to explain why we have a *dynamical* component with such unnatural parameters.

Appealing to Occam's razor, the cosmological constant solution is therefore preferable and dynamical dark energy models, rather than serious theories for cosmic acceleration, should be considered toy models. However, we will argue that it is still extremely important to study the possibility of dynamical dark energy and these toy models are very useful in this quest. First of all, the only previous period of cosmic acceleration we know of, inflation, was not caused by a cosmological constant, but in fact by a dynamical component to the universe, possibly a scalar field. We know this simply because inflation ended. Moreover, for inflation to explain the generation of cosmic perturbations, perhaps the greatest success of the inflationary paradigm, inflation must be described by some field or set of fields that can have perturbations. The simplest inflation models involve a single scalar field rolling down a potential just like the quintessence case. Secondly, we currently have very little guidance from the model building side as to what the solution to the cosmological constant problem might be and we should remain agnostic. It could be that the final solution to this problem does involve a dynamical degree of freedom relaxing to a zero energy density true vacuum, but not having quite reached it yet. This would look just like dynamical dark energy.

The observational status also inspires agnosticism. We have only just discovered dark energy and the constraints on its time evolution are still very weak. Using the fact that the current constraint on w is less than 10%, it is sometimes argued that we have already reached the point where deviations from Λ are strongly constrained and it is not worth the effort to look any further. However, this constraint only holds when

the equation of state is assumed to be constant, something that is rather contrived in the context of dark energy (toy) models. Even if we add just one parameter to include time variation of the equation of state, $w(a) = w_0 + w_a(1 - a)$, constraints become much weaker (see Fig. 1.3), leaving plenty of room for dynamical dark energy to be discovered or ruled out. Thus, from the observational point of view, it is too early to settle for the cosmological constant. The next decade will be a crucial period where our constraints will improve by an order of magnitude. It will be very exciting to see whether evidence for variation in the dark energy density will be found, or the simplest model will be confirmed. At least this way if we do end up settling for a cosmological constant, it will be firmly established by observations. In section 1.5, we will discuss the main cosmological probes by which we expect to make progress in this field, but first we will describe an alternative explanation for cosmic acceleration: modified gravity.

1.4.5 Modified Gravity

An alternative approach is to modify the laws of gravity itself to explain cosmic acceleration. In that case, there is no need for the addition of any new form of energy to our model of the universe. Examples of such models are $f(R)$ gravity [215, 61], where the Ricci scalar R in the Einstein-Hilbert action for gravity is replaced by a function of R, scalar-tensor theories [83], where gravity is non-minimally coupled to a scalar field (all viable $f(R)$ theories can in fact be recast as scalar-tensor models) and models with extra dimensions, like the Dvali-Gabadadze-Porrati (DGP) braneworld model [77]. Just like dynamical dark energy models, modified gravity theories often lack motivation from fundamental physics and require extreme fine-tuning to be compatible with observation. In general, it is much harder to come up with a working modified gravity model than dark energy model because it is difficult to modify gravity in the desired way without completely changing the way gravity works on smaller (for example solar system) scales, where we have very strong constraints. Currently, modified gravity models can be considered useful toy models. Even though they form another interesting set of possibilities, we will not discuss modified gravity much in this thesis.

1.5 Observational Techniques and Prospects

Even though there are many promising cosmological probes that can teach us about dark energy, there are four that are considered the most powerful [10]: Type Ia supernovae (SN), Baryon Acoustic Oscillations (BAO), Weak Lensing (WL) and galaxy clusters (CL). In addition, even though its direct sensitivity to dark energy is not as strong as the four preceding probes, the CMB will remain the most impressive precision cosmology tool for pinning down the other cosmological parameters. This

in turn allows the other probes to constrain dark energy. Below we will discuss each of these five probes in turn.

1.5.1 Supernovae

We have already discussed supernovae to some extent in section 1.2. As discussed there, supernovae purely measure the expansion history, which for $z < 2$ is very sensitive to dark energy. The next steps for supernova cosmology are to go to higher redshifts, to improve statistics by measuring a larger number of supernovae, and perhaps most importantly, to improve systematics by better understanding the nature of supernova explosions, dust extinction and the correlation of supernovae with host galaxy properties. One proposal for the Joint Dark Energy Mission (JDEM), now being planned by NASA/DOE, is to observe roughly 2000 SNe up to redshift $z = 1.7$ from space. This is based on the earlier proposal of the SNAP satellite, for which we calculate projected dark energy constraints (joint with other future probes) in chapters 5 and 6. An important advantage of going to space is that the relevant spectral features of high redshift ($z \geq 1$) supernovae are shifted to the infrared, which is obscured by the atmosphere, making a ground-based telescope less useful.

1.5.2 Baryon Acoustic Oscillations

Another direct expansion history probe is the measurement of the baryon acoustic scale in distribution of galaxies on large scales. The acoustic oscillations in the baryon-photon fluid before recombination imprint a fixed comoving length scale in the statistics of the distribution of galaxies, given by the comoving sound horizon at recombination,

$$s = \int_{z_{\rm rec}}^{\infty} \frac{c_s(z)dz}{H(z)}. \tag{1.20}$$

This scale determines the peak positions in the CMB anisotropy power spectrum and has been measured to be $s = 147 \pm 2$Mpc [141, 138]. After recombination, the baryons decouple from the photons and their perturbations evolve under the influence of only gravity, the effect of which is dominated by the dark matter since the dark matter density is about a factor of six larger than the baryon density. Eventually both the baryon and dark matter perturbations follow the same power spectrum, where the feature from the acoustic oscillations has been diluted with respect to the CMB, but is still present and observable, see Fig. 1.4.

Where supernovae are standardizable candles, the BAO scale can be used as a standard ruler. The angular size of this standard ruler at a given redshift is related to the angular diameter distance d_A by

$$\theta = \frac{s}{(1+z)d_A(z)} \tag{1.21}$$

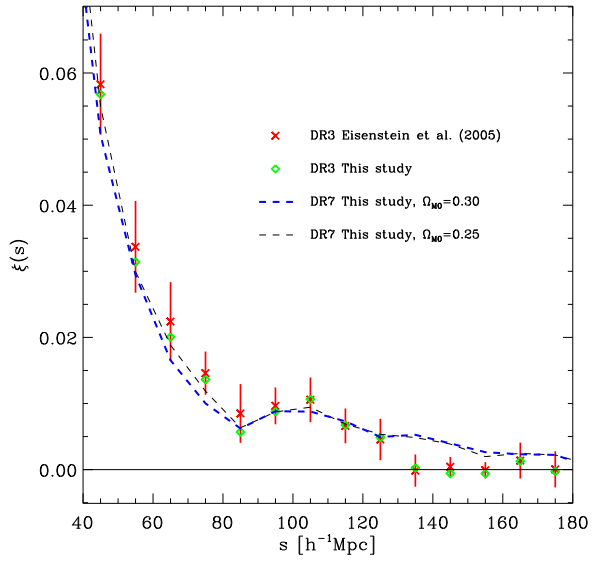

Figure 1.4: Detection of the BAO feature in the galaxy correlation function by [132].

and the size in redshift along the line of sight is related to the Hubble parameter by

$$\Delta z = H(z)s. \tag{1.22}$$

Since s is known from the CMB, one can use observations of the BAO scale at different redshifts to trace the expansion history. Alternatively, one can constrain the expansion history in a manner independent of the value of s, by taking ratios of the observed acoustic peak size at different redshifts.

Compared to other probes, the BAO systematics are quite clean, the main issues being the modeling of the effect of non-linear evolution and of galaxy bias on the peak position. A downside is that to get strong constraints, very large samples of galaxies need to be measured in large volumes of space. The BAO feature has been measured in galaxy catalogues from the Sloan Digital Sky Survey (SDSS) and the 2 degree Field (2dF) galaxy survey, giving a measurement of the ratio of the sound horizon to the distance to $z \approx 0.28$, accurate to 3% [178]. Currently, the BOSS survey [197] is taking spectra of 1.5 million luminous red galaxies (LRG's) and $150,000$ quasars in order to measure cosmic distance and the Hubble scale with 1% level accuracy at $z < 0.7$ and $z \sim 2.5$. A follow-up experiment to BOSS, BigBOSS [198], is already in the works.

1.5.3 Weak Lensing

The gravitational deflection of light by large scale structure along the line of sight distorts (or shears) images of galaxies (see [24, 119] for reviews). The correlations between perturbations in the matter distribution are thus mapped to correlations between the shear at different parts of the sky. The power spectrum or correlation function of cosmic shear thus carries useful information about cosmology. Weak lensing is sensitive to dark energy in two ways. Since the lensing signal depends on distances between observer, source and lens through the lensing kernel, it depends on the expansion history. However, unlike SNe and BAO, it also depends directly on the growth of perturbations since the lensing is done by perturbations in the metric. Since in general relativity these perturbations are directly related to the matter perturbations through the Poisson equation, weak lensing is a clean probe of the matter power spectrum, not involving issues like galaxy bias. By dividing source galaxies in different redshift bins, it is possible to see the evolution in the spectrum of matter perturbations with redshift. Using this tomographic information, it is possible to get very strong dark energy constraints [220, 29, 199].

A large number of source galaxies needs to be observed to distinguish the lensing induced average ellipticity of order $e \lesssim 10^{-2}$ from the much larger intrinsic ellipticity dispersion $e \sim 0.2$. The current state of the art in weak lensing are surveys like COSMOS [165, 199], with a sky coverage of a few square degrees and number density of galaxies $n \approx 65/\text{arcmin}^2$, and CFHTLS [92], covering of order 100 square degrees but with $n \approx 15/\text{arcmin}^2$. Future surveys like LSST (ground based) [4], JDEM [1] and EUCLID (space based) [3] are expected to have a source number density $n \approx 20-60$ arcmin^{-2} and would cover a much larger area than current surveys. The main challenges are the systematics, such as uncertainties in photometric redshifts, errors in the ellipticity due to the point spread function and intrinsic correlations between galaxy ellipticities that could be mistaken for a cosmic shear signal [101, 104, 163].

1.5.4 Clusters

Galaxy clusters are the largest virialized objects in the universe. The observed number density of galaxy clusters in a sample that selects clusters according to some observable O with selection function $f(O, z)$ is [91]

$$\frac{d^2N(z)}{dzd\Omega} = \frac{r^2(z)}{H(z)} \int_0^\infty f(O,z)dO \int_0^\infty p(O|M,z)\frac{dn(z)}{dM}dM, \tag{1.23}$$

where the halo mass function $dn(z)/dM$ is the number of clusters per comoving volume in the mass range $(M, M + dM)$ and $p(O|M, z)$ is the probability distribution for the observable O given a cluster mass M. It is sensitive to dark energy in two ways [167]. Firstly, the halo mass function $dn(z)/dM$ depends strongly on the evolution of the power spectrum of density perturbations and in particular its amplitude.

Secondly, what is observed directly is the number of clusters per steradian on the sky and per unit redshift, which is related to the number per (comoving) volume by the factor $dV/(dzd\Omega) = r^2(z)/H(z)$, telling us directly about the expansion history.

Since the halo mass function is a very steep function of halo mass, it is desirable to use observables O with a narrow, and well characterized distribution $f(O|M, z)$. In other words, one wants to be able to accurately estimate cluster mass. There are several techniques for this. One method is to use cluster optical richness, the number of galaxies observed in a cluster, as a mass estimator. A second method is to use x-ray luminosity and temperature, a third to use the Sunyaev-Zel'dovich effect (inverse Compton scattering of CMB photons by hot gas in the cluster) and finally one can estimate the mass using weak lensing of background galaxies. The availability of a number of methods allows for cross calibration.

1.5.5 The Cosmic Microwave Background

The CMB is currently the strongest probe of precision cosmology and it is expected to stay that way. Even by itself, it places $1-10\%$ level constraints on a large number of cosmological parameters, including the baryon and cold dark matter densities and the amplitude and tilt of the spectrum of primordial fluctuations. However, the CMB gives us a snapshot of the universe at $z \approx 1100$, when the dark energy density was negligible in the simplest models, i.e. $\Omega_\Lambda = 10^{-9}$ in ΛCDM (we will discuss early dark energy models, where dark energy *is* relevant at such early times, in chapters 2 and 6). Hence, as a probe of dark energy it is not as strong as the aforementioned probes. Still, it has two important functions in learning about dark energy.

First of all, for the other probes to constrain dark energy properties, the non-dark energy parameters need to be well constrained, which is exactly what the CMB does. For example, for BAO to be most effective, we need to know the size of the sound horizon at last scattering from the CMB. Moreover, even though the main sensitivity of the CMB is to early times, $z \gtrsim 1100$, it does have some dependance on late universe physics. First of all, the projection of the acoustic peaks onto the sky depends on the distance to the CMB last scattering surface. This is the reason the CMB alone can still constrain Ω_Λ to about 3%. In addition, the integrated Sachs-Wolfe (ISW) effect (CMB photons climbing in and out of time varying potential wells caused by large scale structure) adds anisotropy to the CMB sky and constrains the growth of perturbations, and thus dark energy, at late times. Finally, weak gravitational lensing of the CMB is a promising tool to learn about dark energy and other late universe physics such as massive neutrinos. Chapter 6 is devoted to the prospects for CMB lensing.

The state of the art for full-sky CMB data currently is the WMAP experiment, but the Planck satellite [5] is already taking data. This probe will significantly improve CMB power spectrum measurements. Observations of the temperature anisotropies will be cosmic variance limited up to wave number $l \sim 2000$. It will also strongly

improve our measurements of the polarization of the CMB.

1.6 Other Questions in Cosmology

Even though in this thesis the focus is mainly on dark energy, we wish to stress that there are many other extremely interesting open questions in cosmology and that dark energy science (and the work presented in this thesis) is not isolated from these questions. Experiments designed to study dark energy can be expected to yield other useful cosmology and astronomy results as well and the theoretical tools and models developed with dark energy in mind may be applicable to other topics too. To name just a few examples, another big mystery in cosmology and particle physics is the nature of dark matter. Cosmological observations useful for dark energy studies may also teach us about the nature of dark matter and perhaps advances in our theoretical understanding of dark matter will guide us to an explanation for cosmic acceleration. Another example are massive neutrinos. Massive neutrinos suppress the growth of structure on small scales at late times and can thus be studied with many of the same probes as dark energy. In chapter 6, we will discuss expected bounds on the neutrino mass from CMB lensing. Finally, cosmic inflation has a lot of theoretical properties in common with dark energy and advances in one field may help the other. Moreover, the way to probe inflation is by studying the primordial power spectrum from the CMB and large scale structure, an approach that has a lot of overlap with the observational quest for dark energy.

1.7 Outline

The rest of this thesis consists of five separate chapters on dark energy and probes of dark energy. The main goal of the work presented here is to advance the study of dark energy, by improving the way in which dark energy is modeled, by considering how current data constrain the dark energy properties, and by studying how best to learn about dark energy from future experiments. Although we believe the order in which they are presented is the most natural order to read them, the chapters stand on their own and can be read separately or in a different order.

In chapter 2, we calculate current dark energy constraints from CMB, SN and LSS data. We will focus on the sound speed of dark energy, which determines the behavior of perturbations in the dark energy fluid. We will find constraints on this and other dark energy parameters both in the context of dark energy with a constant equation of state and in the context of early dark energy, where the equation of state changes over time so that $\Omega_{\rm DE}(z)$ can be significant at $z \gtrsim z_{\rm dec}$.

The following three chapters are devoted to ways of modeling the equation of state behavior of dark energy in a general and complete way and to methods of distinguishing (classes of) dark energy models based on their equation of state evolution.

In chapter 3, we discuss the specific class of purely kinetic k-essence models. We find a simple relation between the Lagrangian $\mathcal{L}$ and the equation of state history $w(a)$ and point out how to distinguish these models from quintessence dark energy. In chapter 4, we study a large set of common dark energy models in terms of their equation of state and its derivative. We show that it is possible to divide models into a small set of classes with common, very specific properties. We also find that virtually all models can be described very well by a linear equation of state parametrization and present an explicit mapping between true equation of state and representative linear parametrization. In section 5, we discuss three model independent parametrizations of the dark energy equation of state: principal component analysis (PCA), uncorrelated bandpowers and binned equations of state. We analyze the pros and cons of each method in great detail and pay particular attention to the question of how to model the equation of state at high redshift and to the design of a figure of merit.

Finally, in chapter 6 we study constraints from current/future CMB missions like Planck/CMBpol on dark energy and neutrino properties, using CMB lensing. We compare two methods for extracting lensing information from the CMB and show among other things that these future data can put tight constraints on early dark energy models, ordinary dark energy models and on the sum of the neutrino masses.

Chapter 2

Measuring the Speed of Dark: Detecting Dark Energy Perturbations

A version of this chapter was previously published in *Physical Review D* [62].

2.1 Introduction

Although dark energy dominates the energy density of the universe and drives the accelerating cosmic expansion, we know remarkably little about it. Over the course of the past decade, cosmologists have devoted considerable effort to devising new and sharpening known methods for determining the equation of state of dark energy. The equation of state, defined as the pressure to energy density ratio, is generally a time dependent function and fully specifies the temporal evolution of dark energy density. The dark energy density in turn (along with the matter density) determines the expansion rate of the universe, as well as geometrical measures (distances and volumes).

The equation of state $w(z)$ does not, however, tell us about the microphysics of dark energy, nor does it describe all of the cosmological signatures. For example, even a perfectly measured $w(z)$ does not tell us whether dark energy arises from a canonical, minimally coupled scalar field, a more complicated fluid description, or modification of gravitational theory on large scales. The properties of the perturbations to the dark energy, which must exist unless it is simply a cosmological constant, do carry such extra information.

Perturbations to the energy density and pressure can be described through the sound speed, $c_s^2 = \delta p/\delta\rho$. The sound speed carries information about the internal degrees of freedom: for example, rolling scalar fields (quintessence) necessarily have sound speed equal to the speed of light, $c_s = 1$. Detection of a sound speed distinct

from the speed of light would indicate further degrees beyond a canonical, minimally coupled scalar field.

A low sound speed enhances the spatial variations of the dark energy, giving inhomogeneities or clustering. Heuristically, the sound speed determines the sound horizon of the fluid, $l_s = c_s/H$, where H is the Hubble scale. On scales below this sound horizon, the fluid is smooth; on scales above l_s, the fluid can cluster. Since for quintessence $c_s = 1$, the sound horizon equals the cosmic horizon size and there are essentially no observable inhomogeneities. However, if the sound speed is smaller, then dark energy perturbations may be detectable on correspondingly more observable (though typically still large) scales. These perturbations act in turn as a source for the gravitational potential, and affect the propagation of photons. For example, clustering dark energy influences the growth of density fluctuations in the matter, and large scale structure, and an evolving gravitational potential generates the Integrated Sachs-Wolfe (ISW) effect [189] in the cosmic microwave background. The observational signatures of these effects offer a way of probing the dark energy inhomogeneity and sound speed.

In this chapter we study the signatures of the sound speed of dark energy. We revisit and extend previous studies of dark energy clustering [117, 116, 81, 67, 232, 27, 7, 114, 100, 54, 135, 221, 236, 124, 169, 25, 225, 69, 21, 193], clarifying and quantifying the physical effects caused by the nonstandard values for the speed of sound. We then study models where the dark energy density was non-negligible at early times, which offer much better prospects for observable c_s signatures than the fiducial near-ΛCDM case. Finally, using current cosmological data, we constrain the speed of sound jointly with 7-8 other standard cosmological parameters.

This chapter is organized as follows. In Sec. 2.2 we describe dark energy perturbations and the physical influence of the sound speed and equation of state, deriving the dark energy density power spectrum. Section 2.3 describes the dark energy models we consider, and Sec. 2.4 treats the impact of dark energy inhomogeneity on the CMB, matter power spectrum, and their crosscorrelation. We consider models with both constant and time varying equation of state and sound speed in Sec. 2.5, and present constraints from current data.

2.2 Dark Energy Perturbations

We briefly review the growth of density perturbations, in both the matter and dark energy, focusing on the role of the sound speed. See [22, 134, 160] for more details. To derive the influence of the sound speed on dark energy inhomogeneity, and dark energy perturbations on the matter distribution, we assume adiabatic initial conditions for all components including dark energy and solve the perturbed Einstein equations for the density perturbations $\delta\rho_i$, pressure perturbations δp_i, and velocity (divergence) perturbations θ_i. We do not consider an anisotropic stress.

In the conformal Newtonian gauge, the perturbed Friedmann-Robertson-Walker metric takes the form

$$ds^2 = a(\tau)^2 \left[-(1+2\psi)d\tau^2 + (1-2\phi)d\vec{r}^{\,2}\right], \tag{2.1}$$

where a is the scale factor, τ is the conformal time, $\vec{r}$ represents the three spatial coordinates, and ψ and ϕ are the metric potentials. Conservation of the stress-energy tensor ($T^{\mu\nu}_{\ \ ;\nu} = 0$) of a perfect fluid gives the following equations in Fourier space (see, e.g., [160]) from the time-time and space-space parts:

$$\begin{aligned} \frac{\dot{\delta}}{1+w} &= -\theta + 3\dot{\phi} - 3\mathcal{H}\left(\frac{\delta p}{\delta\rho} - w\right)\frac{\delta}{1+w} \\ \dot{\theta} &= -\mathcal{H}(1-3w)\theta - \frac{\dot{w}}{1+w}\,\theta + \frac{\delta p}{\delta\rho}\,\vec{k}^2\frac{\delta}{1+w} + k^2\psi\,, \end{aligned} \tag{2.2}$$

where $\vec{k}$ is the wavevector, dots are derivatives with respect to conformal time, $\mathcal{H} = \dot{a}/a$ is the conformal Hubble parameter, $\delta \equiv \delta\rho/\rho$ is the density perturbation, $(\rho + p)\,\theta \equiv ik^j\delta T^0_j$ is the velocity perturbation, and $w = p/\rho$ is the equation of state. These equations hold for each individual component, i.e. matter or dark energy.

We define the effective (or rest frame) sound speed c_s through (see, e.g., [115])

$$\frac{\delta p}{\rho} = c_s^2\,\delta + 3\mathcal{H}(1+w)(c_s^2 - c_a^2)\frac{\theta}{k^2}\,, \tag{2.3}$$

where the adiabatic sound speed squared is

$$c_a^2 \equiv \frac{\dot{p}}{\dot{\rho}} = w - \frac{1}{3\mathcal{H}}\frac{\dot{w}}{1+w}\,. \tag{2.4}$$

In terms of c_s, Eqs. (2.2) and (2.3) read

$$\begin{aligned} \frac{\dot{\delta}}{1+w} &= 3\mathcal{H}(w - c_s^2)\frac{\delta}{1+w} \\ &\quad - \left[k^2 + 9\mathcal{H}^2(c_s^2 - c_a^2)\right]\frac{\theta}{k^2} + 3\dot{\phi} \end{aligned} \tag{2.5}$$

$$\frac{\dot{\theta}}{k^2} = (3c_s^2 - 1)\mathcal{H}\frac{\theta}{k^2} + c_s^2\frac{\delta}{1+w} + \psi\,. \tag{2.6}$$

One can readily see that the source term in a $\ddot{\delta}$ equation will have a negative term involving $c_s^2k^2$ from $\dot{\theta}$ (take the derivative of Eq. 2.5 and substitute in Eq. 2.6), indicating that growth is suppressed on small scales, $k > \mathcal{H}/c_s$. However, perturbations will exist in the dark energy density even for $c_s = 1$, albeit at a very low level within the Hubble scale $k > \mathcal{H}$. As c_s drops below unity, the suppression is itself suppressed and inhomogeneities in the dark energy can be sustained. All such perturbations

will vanish though as $1+w \to 0$, regardless of c_s^2. In the combination of Eqs. (2.5) and (2.6) into a single second order equation for δ, the terms involving the metric in this equation are all proportional to $1+w$ (or derivatives thereof) so that in the limit $1+w \to 0$ the perturbations decouple from the metric and do not experience a gravitational force leading to growth.

The dark energy perturbations affect the metric perturbations, and thus the perturbations in the matter, through the Poisson equation

$$k^2\phi = -4\pi G a^2 \sum_i \rho_i \left(\delta_i + 3\mathcal{H}(1+w_i)\frac{\theta_i}{k^2}\right), \tag{2.7}$$

where the sum runs over all components. For a perfect fluid, there is no anisotropic stress so $\psi = \phi$.

Therefore we expect the density power spectrum to be affected by the dark energy sound speed in distinct ways on different scales. On superhorizon scales, $k < \mathcal{H}$, the density power spectrum becomes independent of the dark energy sound speed. Here the perturbations are determined by the curvature fluctuation [22, 30]. Between the Hubble scale and the sound horizon, $\mathcal{H} \lesssim k \lesssim \mathcal{H}/c_s$, a sound speed $c_s < 1$ will enhance the density inhomogeneities (modulo gauge dependence around the Hubble scale). Finally, on smaller scales, $k \gtrsim \mathcal{H}/c_s$, inhomogeneity growth is always suppressed and the exact value of the sound speed becomes irrelevant. We illustrate these behaviors in Fig. 2.1. (All power spectra in this chapter are for linear theory and shown at $a = 1$, and are calculated using CAMB [146] and CMBeasy [73, 72].) Note that the strength of the deviation from the $c_s = 1$ behavior is a steep function of c_s for $c_s \lesssim 0.1$.

2.3 Dark Energy Models

We study three classes of dark energy models to elucidate the role of sound speed and $1+w$, from early to late times.

1) Constant w models. We begin with the simplest model of dark energy with sound speed different from the speed of light: a constant equation of state w and a constant sound speed c_s. This is mostly for historical comparison to [27], since the current constraint on constant equation of state is $w = -0.97 \pm 0.08$ [14] (using only geometric data independent of the sound speed) and so the effects of sound speed are suppressed due to $1+w \approx 0$.

2) Early dark energy with constant speed of sound (cEDE). In order to allow for a period where w is further from -1 and so the sound speed has more influence, we also consider a model with varying equation of state but constant sound speed. We choose the phenomenological early dark energy model of [74] but allow c_s to be a free (constant) parameter. At early times w approaches 0 in this model and so the value of c_s can have observational consequences. The model parameters are

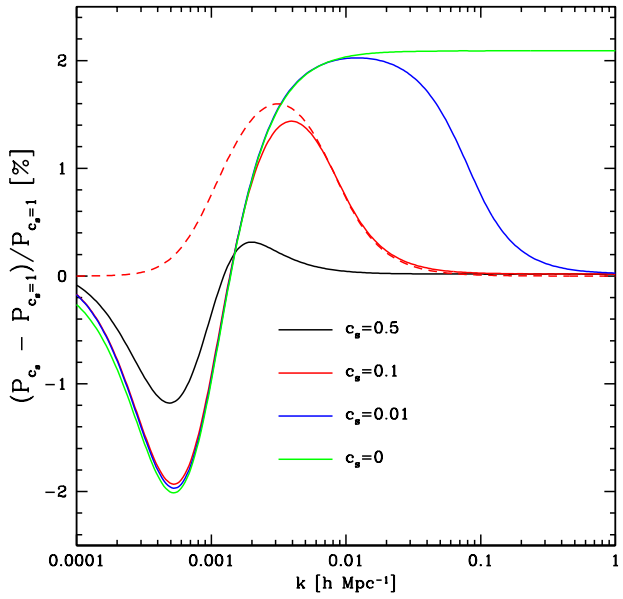

Figure 2.1: The deviation of the power spectrum of the matter density perturbations (Newtonian gauge) from the $c_s = 1$ case is plotted vs. wavenumber k. Three regions – above the Hubble scale (small k), below the sound horizon (large k), and the transition in between – can clearly be seen. The models have $w = -0.8$ (deviations will be smaller for w closer to -1) and constant sound speed as labeled. For the $c_s = 0.1$ case, we also show the result (dashed curve) in terms of the gauge invariant variable D_g as defined in [76] (in that work Φ is equal to minus our ϕ). This illustrates that the low k behavior is strongly gauge dependent.

the fraction of dark energy density at early times Ω_e (this approaches a constant), the equation of state today w_0, and c_s. We call this generalization the cEDE model. Here

$$\Omega_{\rm DE}(a) = \frac{\Omega_{\rm DE} - \Omega_e\,(1 - a^{-3w_0})}{\Omega_{\rm DE} + \Omega_m a^{3w_0}} + \Omega_e\,(1 - a^{-3w_0}) \tag{2.8}$$

$$w(a) = -\frac{1}{3[1 - \Omega_{\rm DE}(a)]}\frac{d\ln\Omega_{\rm DE}(a)}{d\ln a} + w_{\rm other}(a) \tag{2.9}$$

where the current dark energy density $\Omega_{\rm DE} = 1 - \Omega_m$ and $w_{\rm other}(a) \equiv p_{\rm other}(a)/\rho_{\rm other}(a) = \frac{1}{3}\rho_r(a)/\left(\rho_r(a) + \rho_m(a)\right)$ is the effective equation of state of the non-dark energy components, i.e. matter and radiation (including neutrinos). In this model, $c_s = $ const. We show an example of $w(a)$ in Fig. 2.2.

3) Barotropic ("aether") dark energy models. The third model we treat is a particular case of the barotropic class of dark energy, where there is an explicit

relation determining the pressure as a function of energy density. Several physical models for the origin of dark energy fall in this class, and have attractive properties as discussed below.

Ref. [158] showed that all such viable models could be written as a sum of an asymptotic constant energy density ρ_∞ (with $w_\infty = -1$) and a barotropic fluid, or aether, with positive equation of state $w_{AE} > 0$. The sound speed is equal to the adiabatic sound speed, $c_s = c_a$, and is thus completely determined by w_{AE}. In particular, it has the property that $c_s^2 \le w_{AE}$. Moreover, to admit an early matter dominated era, $w_{AE}(a \ll 1) \to 0$, and hence $c_s^2(a \ll 1) \to 0$. We adopt the form $w_{AE} = \beta a^s$ so

$$\rho_{\rm DE}(a) = \rho_\infty + \rho_{AE}(a) \tag{2.10}$$

$$\rho_{AE}(a) = \rho_{AE,0}\, a^{-3}\, e^{3\beta(1-a^s)/s} \tag{2.11}$$

$$w(a) = -\frac{\rho_\infty}{\rho_\infty + \rho_{AE}(a)} + w_{AE}(a)\,\frac{\rho_{AE}(a)}{\rho_\infty + \rho_{AE}(a)} \tag{2.12}$$

$$c_s^2(a) = w_{AE}(a) - \frac{s}{3}\frac{w_{AE}(a)}{1+w_{AE}(a)}\,, \tag{2.13}$$

where $\rho_\infty = \rho_{de,0} - \rho_{AE,0}$. There are two free parameters in addition to the dark energy density today: β and $\rho_{AE,0}$ – one less than in the cEDE case (we will fix $s = 3$ usually). Note that the effective early dark energy density $\Omega_e \approx (\rho_{AE,0}/\rho_{m,0})\, e^{3\beta/s}$ and the present equation of state is $w_0 = -1 + (\rho_{AE,0}/\rho_{de,0})\,(1+\beta)$. As discussed by [158], the barotropic model strongly ameliorates the coincidence problem, motivating why $w \approx -1$ today.

Our three models thus span constant w and constant c_s, varying w and constant c_s, and varying w and varying c_s (but with c_s determined by w). We illustrate their equation of state and sound speed behaviors in Fig. 2.2. We expect a cEDE early dark energy model with $c_s = 0$ to show the greatest effect of sound speed on the observables. Since cEDE can look so much like the barotropic model, in $w(a)$ and more approximately in c_s, we do not treat the barotropic model separately in the following sections, but rather consider it as a motivation for cEDE. The barotropic model possesses the advantage of having $c_s = 0$ at early times (and $w_0 \approx -1$ at late times) being determined by physics rather than being adopted as phenomenology.

2.4 Impact on Cosmological Observations

We now consider angular power spectra of cosmological observables that are sensitive to the speed of sound of dark energy, with the aim of comparing the predictions to current observations (so we do not here include higher order correlations, leaving for future work such signatures and their effect on constraining non-Gaussianity).

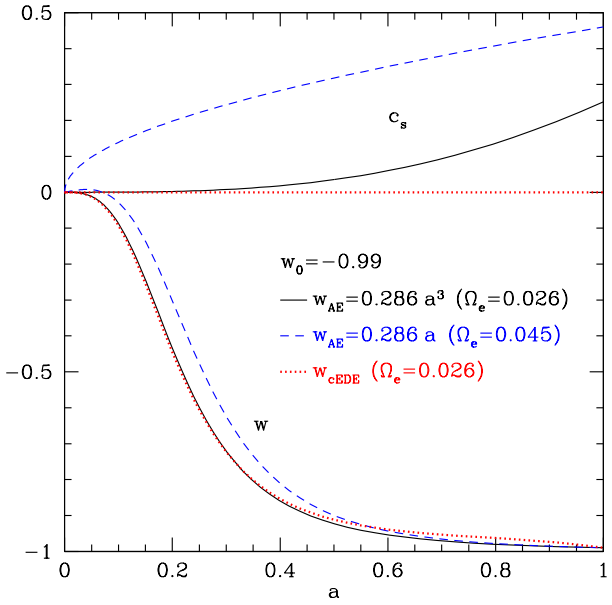

Figure 2.2: The equation of state (lower three curves) and sound speed (upper three curves) as a function of scale factor are illustrated for two models. The aether model takes $s = 3$ (solid curves) or $s = 1$ (dashed curves) and $w_0 = -0.99$; the early dark energy density Ω_e is determined from these parameters. Note that the cEDE model (dotted curves, also taking $w_0 = -0.99$, and here setting $c_s = 0$) is a close match to the aether model.

2.4.1 Angular Power Spectra

The matter density fluctuations, potential fluctuations, and the radiation field are influenced by the dark energy sound speed as discussed in Sec. 2.2. From these we can form, and measure, the angular auto- and cross-power spectra. We consider the CMB temperature anisotropy power spectrum, the power spectra of the galaxy (or other large scale structure tracer) overdensities in redshift bins (labeled by i), and the crosscorrelations between galaxy overdensity and CMB temperature, giving the power spectra C_l^{XY}, where $\{XY\} = \{TT, Tg_i, g_ig_j\}$. See the Appendix for a review of how the angular power spectra relate to the potential power spectrum.

Fig. 2.3 shows a typical temperature power spectrum. The signal from the sound speed dependence enters through the ISW effect, which is also plotted separately in the figure. The extra power from the ISW effect arises from the decay of the potential as the dark energy impacts matter domination at late times; in the concordance model the cosmological constant dark energy causes a decay in the potentials of about 25% between the matter dominated era and the present. While the decay arises from the

change in the expansion history due to the dark energy equation of state, it can be ameliorated by increased dark energy clustering if the dark energy sound speed is small. Figure 2.4 illustrates the influence of the sound speed.

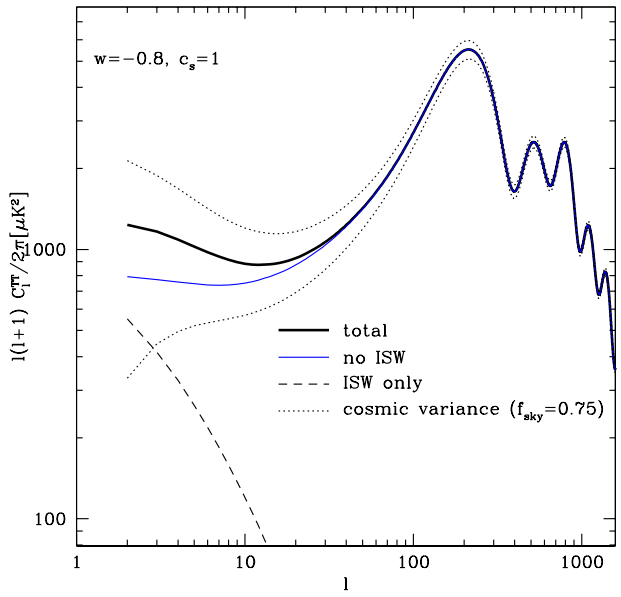

Figure 2.3: CMB temperature power spectrum for $w = -0.8$ and $c_s = 1$, explicitly showing the contribution of the late-time ($z < 10$) ISW effect.

The ISW effect can be measured [32, 170, 87, 200, 86, 174, 8, 38, 105, 93] and one might hope to constrain the sound speed in this way. However, since the effect occurs only on the largest angular scales, cosmic variance swamps the signal. This is demonstrated in the left panel of Fig. 2.4 for a cosmic variance limited experiment scanning 3/4 of the whole sky. The right panel explicitly displays the low signal-to-noise for each multipole, with the difference between $c_s = 0$ and $c_s = 1$ only amounting to $S/N = 1$ when summed over all multipoles.

For the galaxy or matter density fluctuations, the dark energy sound speed can have a larger effect. Note that the dark energy perturbations themselves remain small relative to the matter inhomogeneities, despite a low sound speed having a dramatic effect on the dark energy clustering. Fig. 2.5 shows that on superhorizon scales the level of dark energy power is $(1 + w)^2$ relative to the dark matter power (because at superhorizon scales the perturbations remain adiabatic and the ratio $\delta_{\rm DE}/\delta_{DM} = 1 + w$). On subhorizon scales, the ratio depends strongly on the dark energy sound speed. For $c_s = 0$, the ratio is scale independent in the subhorizon

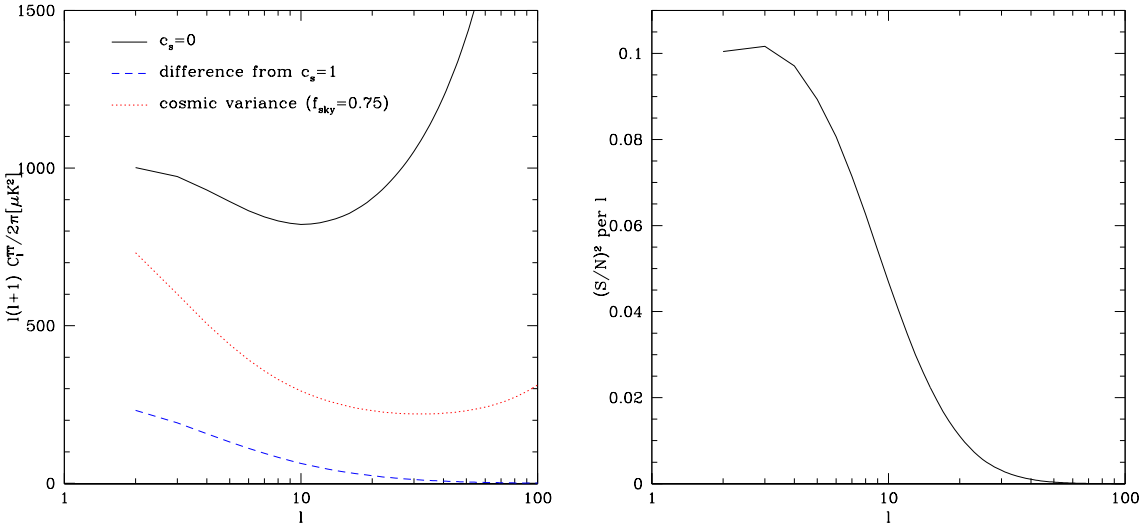

Figure 2.4: Left panel: CMB temperature power spectrum for $c_s = 0$, and its difference from the $c_s = 1$ case, are plotted for $w = -0.8$, along with the cosmic variance. Right panel: The signal relative to the noise (here just cosmic variance) is low, with the total summed over all multipoles $S/N \simeq 1.0$. Compensating the difference between the models by varying the other cosmological parameters would make the S/N even smaller.

regime: during matter domination, one can show analytically that then

$$\frac{P_{\rm DE}}{P_{DM}} = \left(\frac{1+w}{1-3w}\right)^2 \quad \text{(matter dominated)} \tag{2.14}$$

but this ratio becomes smaller by roughly a factor of two by today. For a canonical sound speed $c_s = 1$, the dark energy power is strongly suppressed relative to the dark matter power, with the ratio scaling as k^{-4}.

The matter power spectrum itself, however, is affected by the dark energy sound speed through the potential perturbations induced by the dark energy inhomogeneities. Fig. 2.6 shows in the left panel the *absolute* comparison of the dark matter and dark energy power (in contrast to the relative difference between the two in Fig. 2.5). For the constant w model, on this log scale, one cannot see the influence of the dark energy sound speed on the dark matter power, so the right panel plots the deviation with respect to the $c_s = 1$ case. We see that the deviation due to $c_s = 0$ is at the percent level in the matter density power and the tens of percent level in the potential perturbation power.

The density and potential are related through the Poisson equation. For example, for $w = -0.8$ and $c_s = 0$, the amplitude of the dark energy perturbations is about 4% of the dark matter perturbation (i.e. the power ratio is about 1.6×10^{-3} on subhorizon

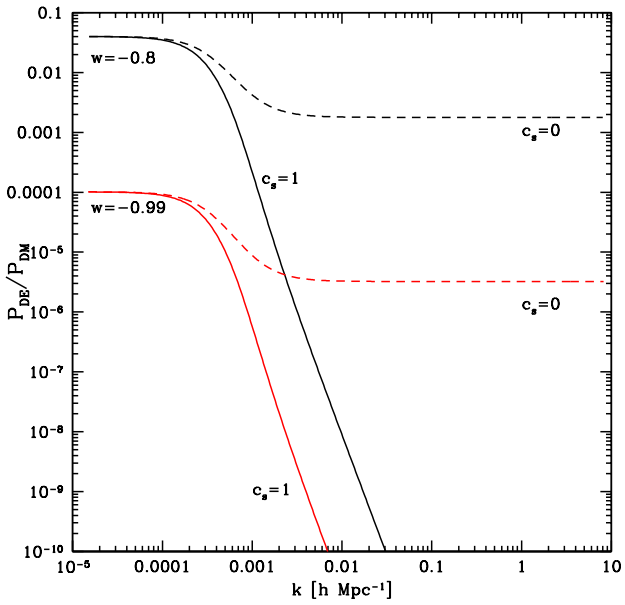

Figure 2.5: The ratio of the dark energy to dark matter density power spectra (Newtonian gauge) is plotted for various values of constant w and c_s. Although $c_s = 0$ gives dramatically more power on subhorizon scales than $c_s = 1$, the direct ratio of the dark energy power to the matter power is negligible.

scales as seen from Fig. 2.5). According to the Poisson equation, Eq. (2.7), this translates into about a 12% increase in ϕ going from $c_s = 1$ to $c_s = 0$, because today $\rho_{\rm DE} \approx 3\rho_m$ and because in the $c_s = 1$ case the dark energy contribution to the Poisson equation is negligible. Hence, as shown in the right panel of Fig 2.6, we get about a 25% increase in the power spectrum of ϕ.

Note that the (late) ISW effect is proportional to the *change* in potential $\Delta\phi$ between matter domination and today. In the standard case, this decay is about 1/4 of the potential during matter domination and thus about 1/3 of the potential today, i.e. $\Delta\phi \equiv \phi_0 - \phi_{MD} \approx -\frac{1}{4}\phi_{MD} \approx -\frac{1}{3}\phi_0$. Hence, the change in the potential at present of 12% due to enhanced dark energy clustering corresponds to a change in the ISW effect of approximately $3\times12\% = 36\%$ (i.e. in $[\Delta\phi(c_s = 0) - \Delta\phi(c_s = 1)]/\Delta\phi(c_s = 1)$). This enhancement gives the ISW effect extra sensitivity to dark energy clustering relative to other probes.

The matter density perturbation is of course also affected, but with only about a 1% increase in its amplitude. This effect on the potential today through the Poisson equation is therefore subdominant to the direct effect of the dark energy perturbation itself.

Now that we have seen the basic effects of the dark energy sound speed and

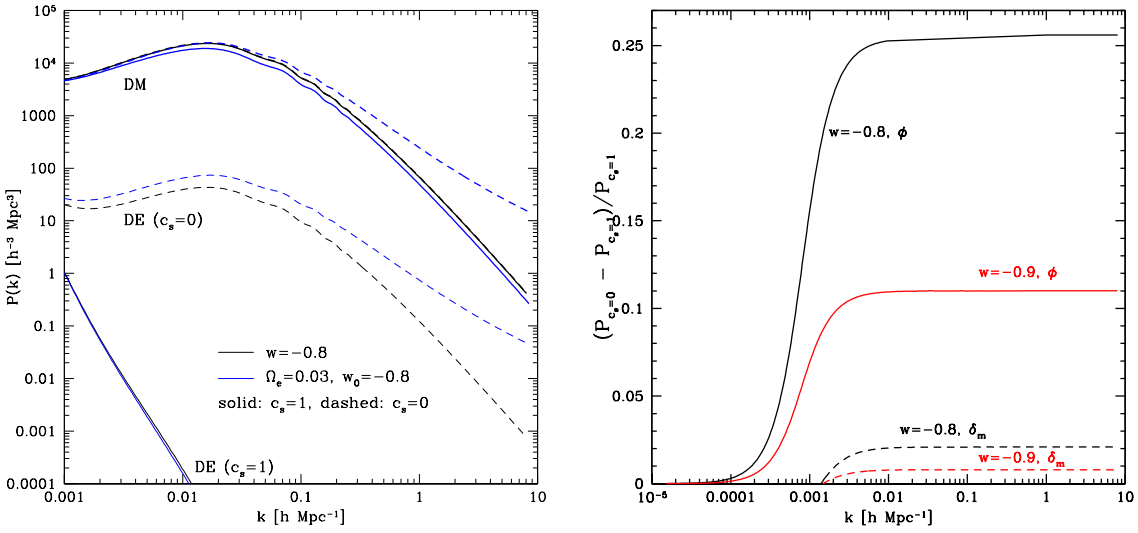

Figure 2.6: Left panel: dark energy (lower four, thin curves) and dark matter (upper, thick curves) density power spectra for different choices of the dark energy equation of state and sound speed. Right panel: relative differences in the potential (ϕ) and matter density (δ_m) power spectra between $c_s = 0$ and $c_s = 1$ (matter and dark energy perturbations in Newtonian gauge).

equation of state on the observables, we consider the specific instances of the constant w model and cEDE model. We can already guess that to obtain reasonable constraint on the sound speed we will want a model that has as large a $1 + w$ and as small a c_s as is consistent with the observations, for a substantial part of cosmic history.

2.4.2 Estimating Constraints in Constant w Model

We begin by estimating the chances of constraining the sound speed using the χ^2 between two extremes: $c_s = 0$ and $c_s = 1$. Since we consider angular power spectra and crosscorrelations of observables on the sky (labeled by capital letters below), χ^2 is in general given by

$$\chi^2 = \sum_{\ell} \sum_{\{XY\},\{ZW\}} \Delta C_\ell^{XY} \, (\mathbf{Cov}_\ell)^{-1}_{XY,ZW} \, \Delta C_\ell^{ZW}, \tag{2.15}$$

where $\Delta C_\ell^{XY} \equiv C_\ell^{XY}(c_s = 1) - C_\ell^{XY}(c_s = 0)$ is the difference in spectra between the two cases and the covariance is given by

$$(\mathbf{Cov}_\ell)_{XY,ZW} = \frac{1}{(2\ell+1) f_{\rm sky}} \left(\tilde{C}_\ell^{XZ} \tilde{C}_\ell^{YW} + \tilde{C}_\ell^{XW} \tilde{C}_\ell^{YZ} \right), \tag{2.16}$$

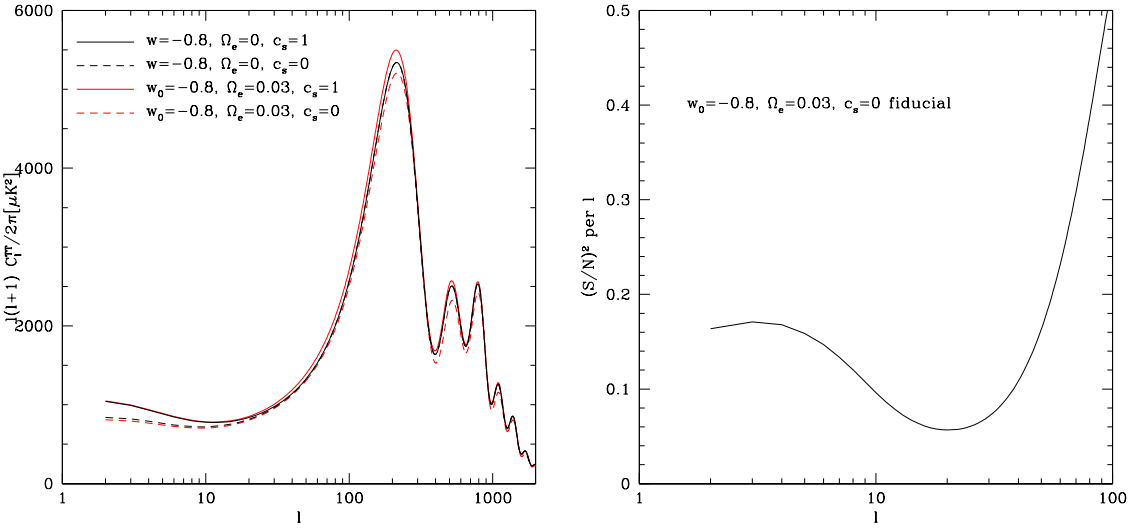

Figure 2.7: Left panel: CMB temperature spectra for the early dark energy cEDE model with $\Omega_e = 0.03$, $w_0 = -0.8$ is plotted for $c_s = 0$ and 1. The effect of changing the sound speed on the late ISW effect is a little stronger than in the case of ordinary $w = -0.8$ dark energy (also shown), but the major difference comes from higher ℓ, where the early dark energy exhibits significant differences between $c_s = 0$ and $c_s = 1$, while ordinary dark energy does not. Right panel: Signal to noise squared per mode for distinguishing $c_s = 1$ from the $c_s = 0$ fiducial is plotted vs. multipole. The late ISW (treated as $\ell < 21$) contributes only $(S/N)^2 = 1.8$; including higher ℓ, say all $\ell \leq 2000$, gives $(S/N)^2 = 8.8 \times 10^3$. However, the differences at high ℓ can at least partly be compensated by varying other cosmological parameters.

with

$$\tilde{C}_\ell^{XY} = C_\ell^{XY} + N_\ell^{XY} \,, \tag{2.17}$$

where $f_{\rm sky}$ is the fraction of the sky that is observed, C_ℓ^{XY} are the fiducial spectra and N_ℓ^{XY} are the noise power spectra so that $\tilde{C}_\ell$ are the observed power spectra that include the noise. (See the Appendix for further details.) For the χ^2 estimates of this section we only consider the CMB temperature power spectrum and we will consider the cosmic variance dominated limit where the noise power spectrum is much smaller than the fiducial power spectrum, $N_\ell^{TT} = 0$. Hence, Eq. (2.15) simplifies to

$$\chi^2 = \frac{1}{2} f_{\rm sky} \sum_\ell (2\ell + 1) \left(\frac{\Delta C_\ell^{TT}}{C_\ell^{TT}} \right)^2 . \tag{2.18}$$

Assuming Gaussian likelihood, the quantity χ^2 is equivalent to the signal to noise squared with which we can distinguish $c_s = 1$ from our fiducial $c_s = 0$ if all the other parameters were known exactly. Since in reality we should marginalize over

the other parameters as well, χ^2 is an *upper* bound on the signal to noise squared for distinguishing the two sound speeds. Therefore if we find a low χ^2 then there is little hope of constraining c_s with the assumed dataset. To amplify the chances of detection, we examine $w = -0.8$, since in the limit $w \to -1$ dark energy perturbations become irrelevant regardless of the value of the value of the sound speed; given that $w = -0.8$ is already an unlikely value given current data, the calculated signal to noise squared $(S/N)^2$ could be an overoptimistic estimate of the true value.

Fig. 2.4 confirms that the discrimination between sound speeds through the CMB temperature autocorrelation is poor, as discussed in the previous subsection. Cosmic variance swamps the difference between even the extremes, $c_s = 0$ and $c_s = 1$, and the total $(S/N)^2 \approx 1$. Note that this took cosmic variance to be calculated from the most optimistic case, $c_s = 0$, where the noise is significantly lower, so one truly cannot determine c_s with the CMB temperature anisotropy despite all the most optimistic assumptions.

The overall significance of the mere existence of the ISW effect (i.e. the χ^2 between the CMB power with the ISW effect artificially removed and the true CMB) is only $(S/N)^2_{ISW} = 3.7$. The potential decay in a model with dark energy sound speed $c_s = 0$ is a little less than half the contribution in the $c_s = 1$ case, thus explaining the $(S/N)^2_{\Delta c_s=1} \approx (1/4)\,(S/N)^2_{ISW} = 1.0$ quoted above. Thus the ISW signal in the CMB temperature spectrum is too blunt a tool to explore dark energy sound speed.

We must go beyond the CMB temperature spectrum to consider the galaxy-galaxy power and temperature-galaxy crosscorrelation data. Rather than proceeding further with halfway measures such as calculating the signal to noise to determine whether we would be able to place to constraints on c_s while fixing all other parameters, we instead carry out a full likelihood analysis in Sec. 2.5.

2.4.3 Estimating Constraints in cEDE Model

In the early dark energy case, we find that the ISW signal in both the CMB temperature autocorrelation and temperature-galaxy crosscorrelation is comparable to the signal in the case of ordinary dark energy (which typically has an energy density fraction relative to matter of $\sim 10^{-9}$ at CMB last scattering). However, there is another source of distinction. Dark energy in the cEDE model has $w \approx 0$ at CMB last scattering; if in addition $c_s = 0$, then cEDE behaves at early times just like dark matter, with significant clustering of the dark energy. This will affect not only the large scale, late time ISW contribution to the CMB but also the early Sachs-Wolfe effect and the acoustic peaks.

Therefore we expect a clearer observational signature of the sound speed than for ordinary dark energy. Fig. 2.7 shows the effect of changing the sound speed in the cEDE model. The CMB temperature autocorrelation alone delivers $(S/N)^2 \approx 9 \times 10^3$ (for $\ell_{\rm max} = 2000$). This seems more promising for constraining the sound speed, and again we proceed to a full likelihood analysis.

2.5 Measuring the Speed of Darkness

To obtain accurate constraints on the dark energy sound speed we perform a Markov Chain Monte Carlo (MCMC) likelihood analysis over the set of parameters $\{\log c_s, p_{\rm dark}, \omega_b, \omega_c, \Omega_{\rm DE}, \tau, A_s, n_s\}$, where $p_{\rm dark}$ is either w, in the constant w case, or $\{w_0, \Omega_e\}$, in the cEDE case (in both cases we do not allow the equation of state to go below -1), $\omega_b = \Omega_b h^2$ is the present physical baryonic energy density density, $\omega_c = \Omega_c h^2$ is the present physical cold dark matter energy density, $\Omega_{\rm DE}$ is the present relative energy density in the dark energy, τ is the reionization optical depth, A_s the amplitude of primordial scalar perturbations (defined relative to a pivot scale of $k = 0.05\,{\rm Mpc}^{-1}$) and n_s is the spectral index of the primordial scalar perturbations. Note that we choose $\log c_s$ as the sound speed parameter because most of the sensitivity is at small values of c_s.

For current data we include the CMB temperature power spectrum from WMAP5 [137], the crosscorrelation of these temperature anisotropies with mass density tracers including the 2MASS (2-Micron All Sky Survey), SDSS LRG (Sloan Digital Sky Survey Luminous Red Galaxies), SDSS quasars, and NVSS (NRAO VLA All Sky Survey) radio sources, following [105], and the SDSS LRG autocorrelation function from [224]. To break degeneracies with background cosmology parameters and constrain the expansion history, we use the supernova magnitude-redshift data from the Union2 compilation [14].

The MCMC package COSMOMC [144] is used to calculate the joint and marginalized likelihoods. The results for the marginalized 1D probability distributions are shown in Fig. 2.8 for the constant equation of state case and in Fig. 2.9 for the early dark energy, cEDE case. Dotted lines show the distributions when one fixes $c_s = 1$.

In the constant w case, no constraint can be placed on the sound speed, as expected from our earlier arguments. In addition, the other parameter distributions are essentially unaffected by the value of c_s. For the cEDE case, however, some preference appears for a low sound speed, $c_s \lesssim 0.1$, and this propagates through to the other parameters. The preference for a low sound speed does not depend strongly on the inclusion of the large scale structure data (i.e. the temperature-matter crosscorrelation and the galaxy power spectrum). If either or both of these observables are not included, the preference is still there, although slightly weakened. Since early dark energy with a low sound speed acts like additional dark matter at early times, this allows a lower true matter density.

It is intriguing to consider whether the apparent preference of current data for the ΛCDM model is merely a consequence of overly restricting the degrees of freedom of dark energy, and that instead a dark energy with dynamics ($w_0 \approx -0.95$), microphysics ($c_s \approx 0.04$), and long-time presence ($\Omega_e \approx 0.02$) could be the correct model.

Fig. 2.10 shows the 68.3%, 95.4% and 99.7% confidence level contours in the w-$\log c_s$ plane for the constant w model. We see that current data in this model

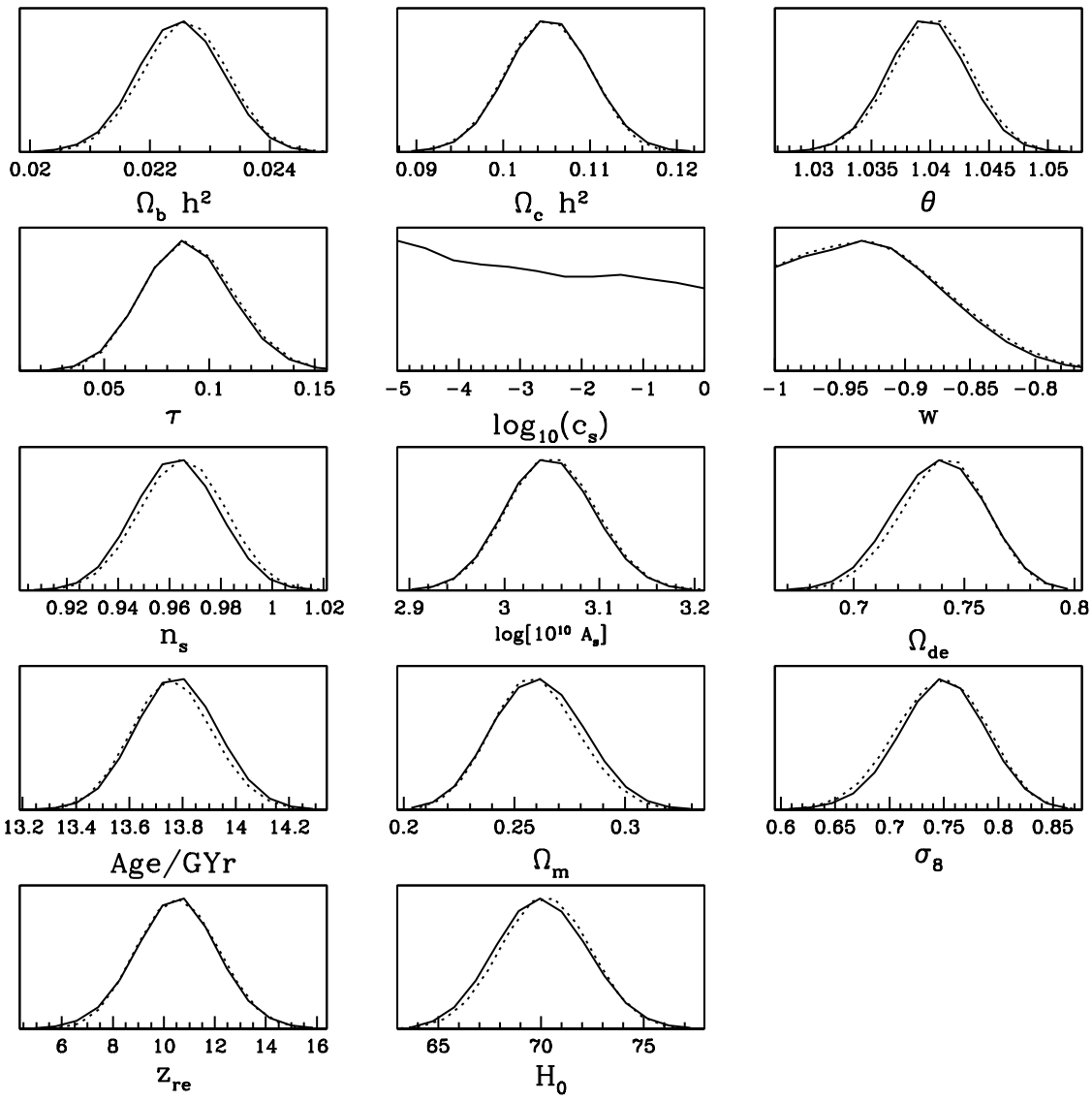

Figure 2.8: Constant equation of state case, plotting the marginalized one dimensional probability distributions using data from supernovae (Union2), CMB (WMAP5), galaxy autocorrelation (SDSS LRG), and the cross correlation between large scale structure tracers (see text) and CMB temperature anisotropies. Solid lines are for the model with $\log(c_s)$ a free parameter (with a flat prior), whereas the dotted lines correspond to fixed $c_s = 1$.

prefer $w \approx -1$ but are completely agnostic regarding c_s. For the cEDE model, Fig. 2.11 shows the joint probability contours among the dark energy parameters, in

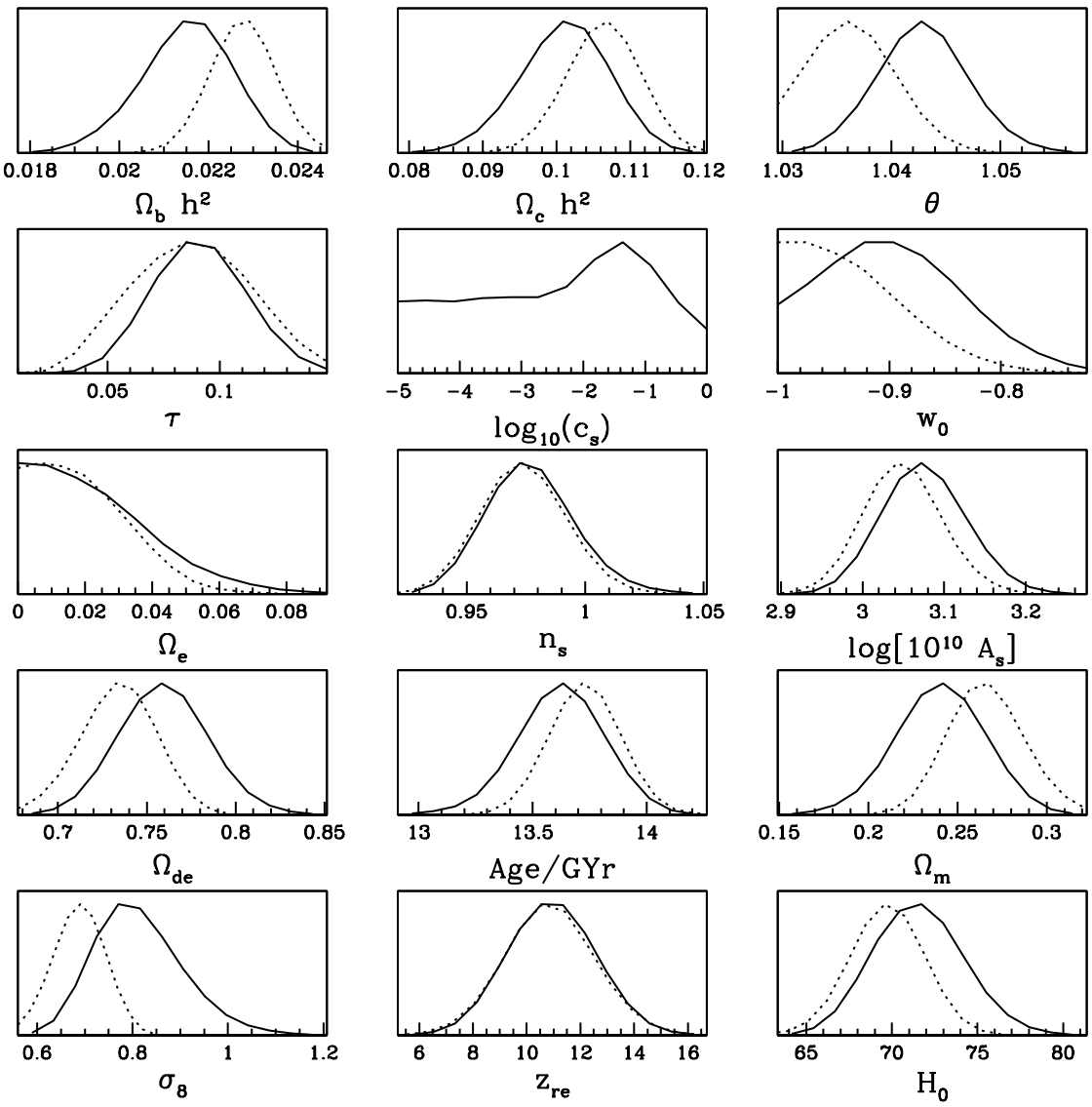

Figure 2.9: Early dark energy case, plotting the marginalized one dimensional probability distributions using data from supernovae (Union2), CMB (WMAP5), galaxy autocorrelation (SDSS LRG), and the cross correlation between large scale structure tracers (see text) and CMB temperature anisotropies. Solid lines are for the model with $\log(c_s)$ a free parameter (with a flat prior), whereas the dotted lines correspond to fixed $c_s = 1$.

the w_0-$\log c_s$, Ω_e-$\log c_s$, and Ω_e-w_0 planes, with all other parameters marginalized. Here we see that the model mentioned above, $(w_0, c_s, \Omega_e) = (-0.95, 0.04, 0.02)$, is

completely consistent with the data, as is the cosmological constant $(-1, 1, 0)$. It will be interesting to see how the best fit evolves with future data.

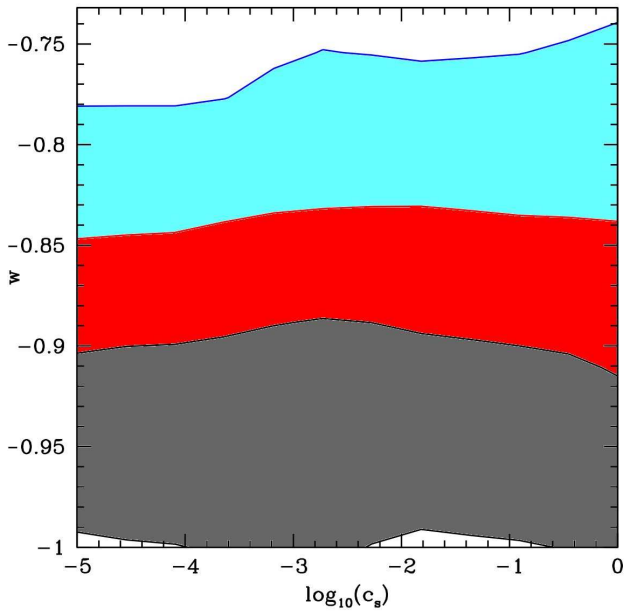

Figure 2.10: 68.3, 95.4 and 99.7% confidence level contours in the dark energy model with constant equation of state. The constraints are based on current data including CMB, supernovae, LRG power spectrum and crosscorrelation of CMB with matter tracers. The small likelihood variations at $w = -1$ are not physical (the sound speed has no observable effect when $w = -1$), but are due to finite chain length.

2.6 Conclusions

Current cosmological data are in excellent agreement with the standard ΛCDM universe, with equation of state $w = -1$. Nevertheless, the current data are also consistent with a wide variety of richer physics. It is not clear that it is wise to assume that the physical explanation for dark energy in the universe is indeed given by restriction to a spatially smooth, constant in time energy density: the cosmological constant. Even after allowing for dynamical dark energy, there could be further degrees of freedom – "hidden variables" or microphysics – in the dark energy sector, harbingers of deeper physics that have not yet shown clear signatures in the data. An explicit search for these signatures, and thus the physics behind dark energy, should be near the top of the list of current efforts in cosmology.

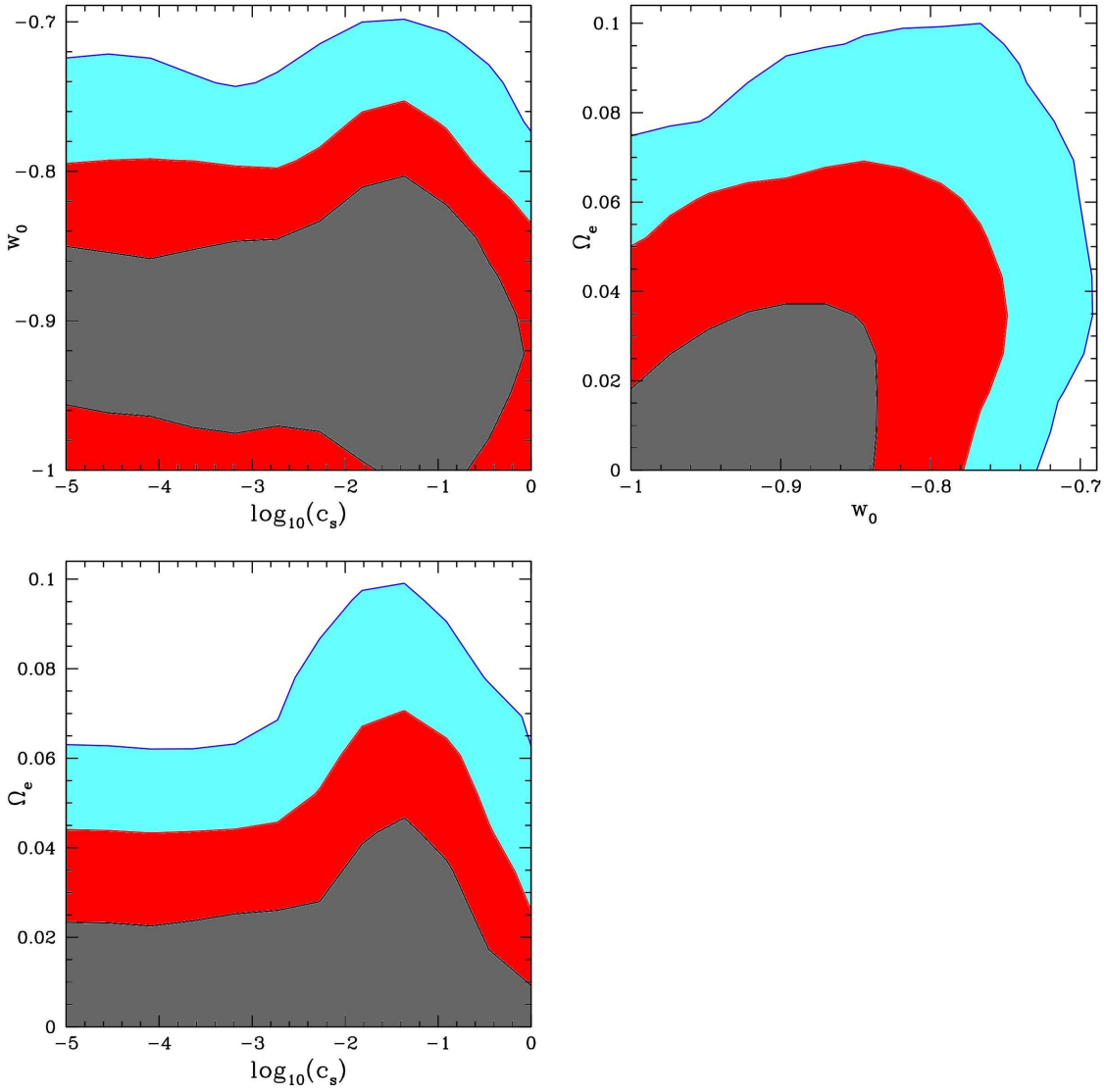

Figure 2.11: 68.3%, 95.4% and 99.7% confidence level contours in the cEDE early dark energy model in the w_0-$\log c_s$ (top left), Ω_e-w_0 (top right) and Ω_e-$\log c_s$ (bottom left) planes. The constraints are based on current data including CMB, supernovae, LRG power spectrum, and crosscorrelation of CMB with matter tracers.

In this chapter we search for degrees of freedom beyond quintessence by examining the influence of the sound speed of dark energy, and its resulting spatial clustering of dark energy, on key observables and in current data. This extends earlier analyses, quantifying the effects on the dark matter and dark energy density perturbation power spectra, the potential power spectrum, and their crosscorrelation. Where possible, we give simple scalings with $1 + w$ and c_s. We also explore models with time varying

equation of state and sound speed.

In the standard model with negligible dark energy at high redshift, the speed of sound is essentially not distinguishable with current data (see Fig. 2.8) because current data favor $w \simeq -1$, and the effects of clustering of dark energy vanish in this limit. As w gets further from -1, the influence of the sound speed increases; for models with $w \approx 0$ at high redshift there is also the possibility of non-negligible amounts of early dark energy density. Even just a couple percent of the total energy density in early dark energy dramatically improves the prospects for detecting dark energy clustering. One can view the early dark energy fraction Ω_e as another degree of freedom to explore. Indeed, carrying out a MCMC analysis we find in Figs. 2.9 and 2.11 that a model with dynamics, microphysics, and persistence: $(w_0, c_s, \Omega_e) = (-0.95, 0.04, 0.02)$ is completely consistent with the current data (although Λ remains consistent as well).

Discovery of the accelerating universe 12 years ago has propelled the physical interpretation of dark energy into one of the most important, exciting, and difficult problems in physics. Although current observations indicate that the equation of state, as a constant or broadly averaged over time, is close to -1, this leaves considerable room for further physics, as demonstrated here using recent data. To go further we should explore all three frontiers of the dynamics $w(a)$, the microphysics c_s and spatial inhomogeneities, and the persistence Ω_e.

Chapter 3

Kinetic K-Essence and Quintessence

A version of this chapter was previously published in *Astroparticle Physics* [63].

3.1 Introduction

In the quest for the physical origin of the cosmic acceleration, we have relatively little guidance from basic principles. For dynamical scalar field models, e.g. quintessence, one must posit a potential, ideally possessing naturalness, without fine tuning. However the potential receives quantum loop corrections from high energy physics, raising the problem of preservation of form, or technical naturalness. An alternative approach is adopting non-canonical kinetic terms in the scalar field Lagrangian, leading to k-essence models.

A subset of these – kinetic k-essence – offers the possibility of removing the potential altogether (or keeping it constant). With a shift symmetry in the field, $\phi(x) \to \phi(x) + \theta$, this provides technical naturalness, an important virtue for a physical theory, and so kinetic k-essence models are worth investigating. Furthermore, these are in a sense as simple as quintessence in that they also involve a single function, here $\mathcal{L} = F(X)$ where X is the kinetic energy.

In this chapter we study the interplay between equations of state $w(a)$, defined in terms of an effective pressure to energy density ratio $w = p/\rho$ or equivalently cosmic expansion dynamics, and kinetic k-essence Lagrangians possessing certain stability properties. This will enable us to establish to what extent cosmological expansion or distance data could encounter degeneracies in the interpretation of the physical origin of the cosmic acceleration. For example, what are the characteristics of a quintessence model appearing degenerate with a k-essence model, in the sense that they produce the same equation of state over some redshift range. We derive limits on this degeneracy by showing which regions of the w-w' phase space (where $w' =$

$dw/d\ln a$, with a the expansion scale factor) k-essence can lie in (see [44, 196, 155] for analyses of other DE models). We will also consider the converse issue by going from some specific equations of state to the corresponding k-essence Lagrangians.

In §3.2 we discuss some of the motivations for considering k-essence as a possible physical model for the origin of the cosmic acceleration. §3.3 presents a pedagogic overview and explanation of some of the main properties of (purely kinetic) k-essence. In §3.4, we analyze the stability of solutions and from this derive the condition the DE equation of state must satisfy for it to be degenerate with a stable kinetic k-essence model. In §3.5, we give the closed form solution for this degeneracy condition and present a simple prescription for predicting the behavior of any kinetic k-essence Lagrangian. In §3.6 we exhibit the results for several illustrative examples.

3.2 Motivation

Even though a cosmological constant is in good agreement with the current data, the problems above provide ample motivation to look for DE models beyond a cosmological constant. The most popular alternatives to Λ are scalar field models, in particular quintessence (see [53, 155] and references therein), which describes a single scalar field ϕ with a standard Lagrangian density $\mathcal{L} = X - V(\phi)$, with $X = \frac{1}{2}\partial_\mu\phi\partial^\mu\phi$. Quintessence models can describe a range of equations of state necessary for an accelerated expansion, but like Λ suffer from fine-tuning issues.

More recently, scalar field models with non-canonical kinetic energy have gained interest. These so called k-essence (the "k" standing for kinetic) models are described by Lagrangians of the general form [166] $\mathcal{L} = v(\phi)F(X) - V(\phi)$ (a canonical kinetic energy is given by $F(X) = X$ and $v(\phi) = 1$). K-essence was originally proposed as a model for inflation [16], and then as a model for dark energy [17], along with explorations of unifying dark energy and dark matter [31, 28]. It now appears increasingly likely from both theoretical stability issues and observational constraints (e.g. [192, 27, 15]) from matter clustering properties (dark matter is very clumpy while DE is quite smooth out to the Hubble scale) that dark matter and dark energy are not the same substance; we will treat k-essence purely as a dark energy candidate. One reason for the interest in k-essence is that it admits solutions that track the equation of state of the dominant type of matter (in the early universe this is radiation) until pressure-less matter becomes dominant, at which point the k-essence begins to evolve toward cosmological constant behavior [47, 17, 18]. Such behavior can to a certain degree solve the fine-tuning problems mentioned above.

A good way to look at k-essence is as a generalization of canonical scalar field models (i.e. quintessence). Let us consider the quintessence Lagrangian in a bit more detail. Where the fact that it must be a function only of X and ϕ comes from Lorentz invariance, the reason for the kinetic energy term being equal to X (i.e. canonical) is merely that we assume X to be small compared to some energy scale and higher

order terms to be irrelevant. Even though this is often a correct assumption because of the Hubble damping, there exist cases where it is not. In k-essence, we look at models where the higher order terms are not necessarily negligible. This can give rise to interesting new dynamics not possible in quintessence.

Another motivation for studying k-essence is the relation of scalar field theory to the quantum mechanics of a single particle (see also [20]). Heuristically, field theory can be viewed as the continuum limit of a grid of particles, with the field at a certain point describing the excitation of the particle at that point. The canonical scalar field theory Lagrangian density can in that picture be seen as the generalization of the Lagrangian of a non-relativistic point particle $L = \frac{1}{2}m\dot{q}^2$ (where q is the particle's position). The Lagrangian of a relativistic point particle $L = -m\sqrt{1-\dot{q}^2}$ on the other hand leads to a non-canonical field theory Lagrangian density $\mathcal{L} = -\sqrt{1-2X}$, i.e. a k-essence Lagrangian.

A third motivation for the study of k-essence is that non-canonical Lagrangians appear naturally in string theory. In particular, the tachyon effective Lagrangian ([204], also see [205], and specifically section 8, for a very readable review) has the Dirac-Born-Infeld-like form $\mathcal{L} = -V(\phi)\sqrt{1-X}$. Here, the field ϕ represents the tachyon condensate describing the evaporation of a D-brane.

As we discuss in a little more detail below, the Nambu-Goto action for a p-brane embedded in a $p+2$ dimensional space-time can be written in the same form [95], except that ϕ has the role of the coordinate transverse to the brane in this scenario. As an example, consider the simple case of a 3-brane embedded in a $4+1$ dimensional space-time with a fixed Minkowski metric η_{ij}, $i,j = 0,\ldots 4$. The brane can be parametrized by four world-sheet coordinates x^μ ($\mu = 0,\ldots 3$) so that the location of the brane in space-time (or target space) is given by $X^i = X^i(x^\mu)$ ($i = 0,\ldots 4$). In general, the Nambu-Goto action of a p-brane is given by the volume of its world-sheet

$$S_{\mathrm{NG}} = \int d^4x \sqrt{-\det(g_{\mu\nu})}, \tag{3.1}$$

where G_{ij} is the target space metric and $g_{\mu\nu} = \partial_\mu X^i \partial_\nu X^j G_{ij}$ is the induced metric on the brane. In our example, $G_{ij} = \eta_{ij}$.

In the static gauge, the world-sheet coordinates are chosen to coincide with the first four target space coordinates: $x^\mu = X^\mu$ for $\mu = 0,1,2,3$. We now call the fifth target space coordinate $X^4 = \phi$ to emphasize that it is a scalar from the world-sheet point of view. In this parametrization/gauge, $g_{\mu\nu} = \eta_{\mu\nu} - \partial_\mu\phi\partial_\nu\phi$. If we now assume that ϕ only depends on the time coordinate $t = x^0$, we get the Lagrangian

$$S = \int d^4x \sqrt{1-2X}. \tag{3.2}$$

This is equivalent to the Chaplygin gas Lagrangian (see also §3.6.4) if there we assume a fixed Minkowski background. We can reproduce Lagrangians of the more general

form $\mathcal{L} = -V(\phi)\sqrt{1-2X}$, with a variety of $3+1$ dimensional backgrounds, by having different $4+1$ dimensional backgrounds G_{ij}. The "potential" $V(\phi)$ then corresponds to a warp factor in the metric.

We wish to stress that this discussion is merely meant to show that there are physical ways to get k-essence Lagrangians. We do not claim that the above constitutes a realistic cosmological model.

A final piece of motivation is that, as mentioned in the Introduction, technical naturalness as from a shift symmetry gives an advantage for purely kinetic k-essence Lagrangians, and these involve only a single function, $\mathcal{L} = F(X)$, like quintessence.

3.3 The model

We study k-essence, dark energy described by a single, real scalar field ϕ, minimally coupled but with a non-canonical kinetic term. In general, the k-essence action is of the form

$$S = \int d^4x\sqrt{-g}\, F(\phi, X), \tag{3.3}$$

where $X := \frac{1}{2}\partial_\mu\phi\,\partial^\mu\phi$. We concentrate on the subclass of kinetic k-essence, with a ϕ-independent action

$$S = \int d^4x\sqrt{-g}\, F(X). \tag{3.4}$$

In this chapter, we assume a Friedmann-Robertson-Walker metric, with signature $(+---)$, given by $ds^2 = dt^2 - a^2(t)\, d\vec{x}^2$ (where $a(t)$ is the scale factor) and work in units $c = \hbar = 1$. Unless explicitly stated otherwise, we assume ϕ to be smooth on scales of interest so that $X = \frac{1}{2}\dot{\phi}^2$. Note that this implies $X \geq 0$.

Varying the action (3.4) with respect to the metric gives the energy momentum tensor of the k-essence

$$T^{\mu\nu} = F_X\partial^\mu\phi\,\partial^\nu\phi - g^{\mu\nu}F, \tag{3.5}$$

where a subscripted X denotes differentiation with respect to X. Using that for a comoving perfect fluid the energy momentum tensor is given by $T_{\mu\nu} = -pg_{\mu\nu} + (\rho + p)\delta^0_\mu\delta^0_\nu$, the k-essence energy density ρ and pressure p are

$$\rho = 2XF_X - F \tag{3.6}$$

and

$$p = F. \tag{3.7}$$

In this work, we will assume that the energy density is positive so that $2XF_X - F > 0$. The equation of state is

$$w = \frac{p}{\rho} = \frac{F}{2XF_X - F}. \tag{3.8}$$

The equation of motion for the field can be found either by applying the Euler-Lagrange equation for the field to the action (3.4), or by plugging the energy density and pressure given above into the continuity equation for a perfect fluid. Either way, the result is

$$F_X\ddot{\phi} + F_{XX}\dot{\phi}^2\ddot{\phi} + 3HF_X\dot{\phi} = 0, \tag{3.9}$$

or equivalently, in terms of X,

$$(F_X + 2F_{XX}X)\dot{X} + 6HF_XX = 0, \tag{3.10}$$

where a dot denotes differentiation with respect to t and $H = \dot{a}/a$ is the Hubble parameter. This equation can be integrated to give

$$XF_X^2 = ka^{-6}, \tag{3.11}$$

with $k \geq 0$ a constant [195].

Note that equation (3.11) tells us that the possible solutions $X(a)$, and therefore the behavior of all physical properties of the k-essence (like ρ, p and w) *as a function of the scale factor*, are completely determined by the function $F(X)$ and do not depend on the evolution of the other types of energy density. The only dependence of the k-essence component on other components enters through $a(t)$. One consequence of this is to preclude the possibility of tracking solutions [241] that automatically follow the equation of state of the dominant form of matter in the universe. Tracking behavior *is* possible in general k-essence models that do have ϕ-dependence in the action [47, 17, 18].

An interesting distinction when discussing dark energy models is between dark energies with $w > -1$ and those with $w < -1$. The latter are referred to as phantom dark energy [41] and can have rather exotic properties. For instance, their energy density is an increasing function of the scale factor, which can be seen from the Friedmann equation $d\ln\rho/d\ln a = -3(1+w)$ (see [6] for a discussion of problems arising in phantom k-essence theories). The boundary between the phantom and non-phantom regime is $w = -1$, e.g. a time independent cosmological constant. If a DE evolves from one regime to another, this is called phantom crossing, but [206], e.g., showed that this is impossible for a purely kinetic k-essence. We refer to [228, 42] for a discussion of phantom crossing in the context of other DE models.

For kinetic k-essence, one can use equation (3.8) to express the condition $w > -1$ ($w < -1$) as a condition on the function $F(X)$. We need to consider the two possibilities $F > 0$ and $F < 0$ separately. In the first case, demanding the energy density be positive immediately implies $w > 0$. For $F < 0$, a positive energy density means that $2XF_X/F < 1$ so

$$w = \frac{-1}{1 - 2XF_X/F} > -1 \tag{3.12}$$

when $F_X > 0$. All together, the conditions become (cf. [6])

$$F > 0 \implies w > 0, \tag{3.13}$$
$$F < 0 \quad \& \quad F_X > 0 \implies w > -1, \tag{3.14}$$
$$F < 0 \quad \& \quad F_X < 0 \implies w < -1. \tag{3.15}$$

(Recall the condition $\rho > 0$, or $F_X > F/(2X)$, is implicit).

We conclude this section by pointing out a useful scaling property of the kinetic k-essence Lagrangian, namely $F(X) \to CF(BX)$ with $B > 0$ and C arbitrary constants, leaves the physical properties, such as equation of state $w(a)$, unchanged. In other words, once we have found an $F(X)$ that reproduces an equation of state of interest, we are free to rescale both X and F without affecting $w(a)$. The freedom to rescale F by a factor C follows from the fact that both p and ρ are proportional to F; C could play the role of a constant potential (see §3.6.4). The freedom to rescale X comes from the fact that one can always redefine the field $\phi \to \phi/\sqrt{B}$ without changing the physics. The reason we mention this property is because in the following we will often use it to rescale $F(X)$ into a convenient form (for example with $X = 1$ and $F = -1$ at redshift zero) or to leave out multiplicative constants in expressions for X or F.

3.4 Restrictions on $w(a)$ from Stability

In this section we restrict possible equations of state by demanding that the k-essence be stable against spatial perturbations. Since the k-essence action only depends on X and not on ϕ, the relevant quantity for determining whether or not a solution of the equation of motion (3.11) is stable is the adiabatic sound speed squared

$$c_s^2 := \frac{p_X}{\rho_X} = \frac{F_X}{2XF_{XX} + F_X} = \frac{F_X^2}{(XF_X^2)_X}. \tag{3.16}$$

Perturbations can become unstable if the sound speed is imaginary, $c_s^2 < 0$, so we insist on $c_s^2 > 0$, or equivalently [6]

$$(XF_X^2)_X > 0. \tag{3.17}$$

Writing the condition $c_s^2 > 0$ in terms of $w(a)$, using $c_s^2 = (dp/da)/(d\rho/da)$ (which is valid as long as $dX/da \neq 0$), places a restriction on the equations of state $w(a)$ that can be described by stable k-essence solutions. Using

$$\frac{d\rho}{da} = -\frac{3(1+w)}{a}\rho \tag{3.18}$$

and

$$\frac{dp}{da} = \frac{dw}{da}\rho + w\frac{d\rho}{da} = \frac{a(dw/da) - 3w(1+w)}{a}\rho, \tag{3.19}$$

we get

$$c_s^2 = \frac{dp/da}{d\rho/da} = \frac{3w(1+w) - w'}{3(1+w)} > 0, \tag{3.20}$$

where $w' := dw/d\ln a$. This restricts the equation of state to lie within two regions of the $w - w'$ plane (see Figure 3.1), bounded by the lines $w = -1$ and $w' = 3w(1+w)$. The first line separates phantom k-essence ($w < -1$) from ordinary k-essence and the second is the constant pressure line, as can be seen from Eq. (3.19). As mentioned previously, it is not possible to cross between regions A and B [206]. As we will show later, the requirement that $w(a)$ lies in region A or B implies that a number of popular ansatzes for $w(a)$ cannot realistically describe (stable) k-essence.

Note that a combination of stable kinetic k-essence models stays in the stable region [155] (and a combination of unstable models stays unstable). However, Λ plus a matter component (or more generally a $w \geq 0$ component; also see [107]) can look like stable k-essence. Another potentially interesting requirement to consider is $c_s^2 \leq 1$, which says that the sound speed should not exceed the speed of light, which suggests violation of causality. This condition would add an extra line to Figure 3.1, given by

$$w' = -3(1 - w^2). \tag{3.21}$$

However, we will not impose this condition because even though $c_s^2 > 1$ means signals can travel faster than light, this does not appear to lead to causal paradoxes (see for example [37]).

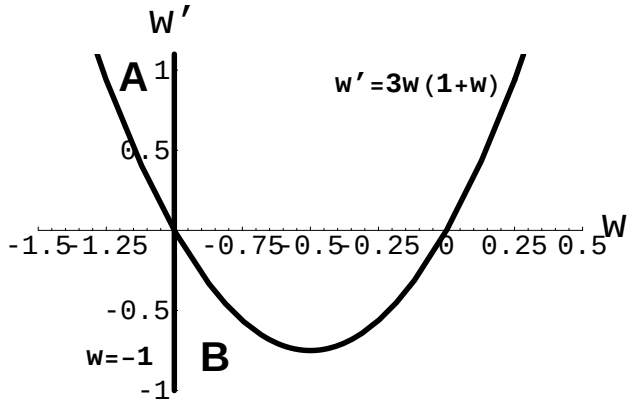

Figure 3.1: The requirement that $c_s^2 > 0$ restricts the equation of state to the two regions A and B, bounded by the lines $w = -1$ and $w' = 3w(1+w)$.

3.5 Distinguishing Kinetic K-Essence from Quintessence

If we know which equations of state can be reproduced by kinetic k-essence, we may be able to distinguish it observationally from other DE candidates. In the previous section, we derived a necessary condition on the DE equation of state for it to be described by a stable k-essence solution. In this section, we will answer a different question, namely what equations of state can be described by k-essence in the first place? We will find that condition (3.20) from the previous section is in fact a sufficient condition. Any equation of state that stays within region A or B of the $w - w'$ plane can in principle be described by a k-essence Lagrangian density $F(X)$. Moreover, we will show how to construct this function. Our method consists of finding F and X as a function of the scale factor by expressing them in terms of physical quantities that can in principle be measured. These functions can then be used to construct $F(X)$. The first part is well defined for any dark energy, i.e. we can always formally construct $X(a)$ and $F(a)$ once we know, say, $w(a)$. However, if the slope of $X(a)$ changes sign, one ends up with a double valued function $F(X)$. In those cases, the dark energy cannot be described by a well defined k-essence model. We will see that double valuedness is produced exactly when crossing one of the lines $w = -1$ or $w' = 3w(1 + w)$ in the $w - w'$ plane.

Now let us find $F(a)$ and $X(a)$. Equation (3.7) tells us that F is simply equal to the pressure

$$F(a) = p(a). \tag{3.22}$$

Inserting this into equation (3.8) and solving for XF_X gives

$$XF_X = \frac{1+w}{2w}p, \tag{3.23}$$

which squares to

$$X(XF_X^2) = \left(\frac{1+w}{2w}\right)^2 p^2. \tag{3.24}$$

Upon insertion of equation (3.11), this leads to

$$X(a) = Ca^6(\rho(a) + p(a))^2, \tag{3.25}$$

where $C > 0$ is a constant we can freely choose. Equations (3.22) and (3.25) define effective quantities for F and X even if there is no actual k-essence. If a well defined k-essence Lagrangian does exist, F and X have their standard meaning as the Lagrangian and as $\frac{1}{2}\partial_\mu\phi\partial^\mu\phi$ respectively.

It is useful to find an expression for $X(a)$ in terms of the equation of state $w(a)$. Unfortunately, since ρ and p are in general integrals of $w(a)$, it is not possible to find a closed expression. However, it is possible to construct a differential equation. Differentiating equation (3.25) with respect to a and using equation (3.18) gives

$$\frac{dX}{d\ln a} = -6\left(\frac{3w(1+w) - w'}{3(1+w)}\right)X = -6c_s^2X. \tag{3.26}$$

For $F(a)$, we have the equation

$$\frac{dF}{d\ln a} = -\frac{3w(1+w) - w'}{w} F. \tag{3.27}$$

Given some evolution of the equation of state, we can derive $X(a)$ using Eq. (3.26) and then use Eq. (3.27) to find $F(X)$. Alternatively, inverting the $X(a)$ from Eq. (3.26), one can use Eqs. (3.8) and (3.11) to get

$$F(X) \propto \frac{w(a(X))}{a^3(X)(1+w(a(X)))}\sqrt{X}. \tag{3.28}$$

From the dynamics in the w-w' plane, one can predict what sort of k-essence solution this corresponds to. If the dynamics crosses a boundary defining the four regions in Fig. 3.1, then c_s^2 changes sign, indicating a pathology within the k-essence picture. Note from Eq. (3.26) that c_s^2 changing sign corresponds precisely to the slope of $X(a)$ changing sign, and at the same time $F(X)$ becomes double valued. However, any equation of state that stays within one of the four regions can in principle be obtained from a k-essence Lagrangian. The stability argument from Section 3.4 selects regions A and B from those four regions. In conclusion, imposing stability, k-essence can generate precisely the equations of state that lie in regions A and B of the w-w' plane.

Conversely, one can look at a given $F(X)$ and determine whether it is a viable k-essence model and what a corresponding quintessence model would be like. (Note that [161] considered a similar question in terms of the effective quintessence potential.) First, from the slope of the function one can deduce by applying Eqs. (3.13)-(3.15) whether the model is phantom or not. Since the k-essence field cannot cross $w = -1$ then the function $F(X)$ cannot change the sign of its slope, and it cannot be double valued (requiring the slope to go infinite). From the curvature of the function (concave or convex), in combination with the slope, one can read off whether the adiabatic sound speed is real or imaginary, and hence look for stability:

$$w > -1 \quad : \qquad F_{XX} > -\frac{F_X}{2X}, \quad [\text{suff. } F_{XX} \geq 0] \tag{3.29}$$

$$w < -1 \quad : \qquad F_{XX} < -\frac{F_X}{2X}, \quad [\text{suff. } F_{XX} \leq 0]\,. \tag{3.30}$$

Here suff. indicates a sufficient (but not necessary) condition for stability; this also corresponds to $0 < c_s^2 \leq 1$.

Since by eye one can usually tell when the curvature is convex or concave, the sufficient condition can be a useful guide. However, if F_{XX} is near but on the wrong side of zero, then one must calculate the value to establish stability (although in any case the adiabatic sound speed would exceed the speed of light in these ambiguous cases). One can apply Eqs. (3.29)-(3.30) to the $F(X)$ plots in the examples of the

following section to verify their usefulness as a quick indicator of the stability of possible kinetic k-essence Lagrangians.

To clarify further possible degeneracies between k-essence and quintessence physics, we examine in the next section specific examples that illustrate the points made above.

3.6 Examples

We here consider a few particular ansatzes for the DE equation of state $w(a)$ and analyze their degree of degeneracy with a (stable) k-essence solution. To begin, we check whether the equation of state lies today ($z = 0$) in one of the allowed regions given by Eq. (3.20). If so, a function $F(X)$ can be constructed to reproduce this equation of state in a certain redshift range around $z = 0$. If $w(a)$ stays in the allowed region for all a, then we can find an $F(X)$ degenerate with this dynamics for all redshifts. (But it is important to note that it will not be equivalent to a quintessence field because the sound speed will not be unity; the two different physical models will be distinguishable to the extent that spatial inhomogeneities in the dark energy component are relevant.)

If $w(a)$ leaves the allowed regions after some time, then we can only match stable k-essence with quintessence over the redshift range where $w(a)$ does lie in one of the allowed regions. Since in practice we can only measure $w(a)$ in a limited redshift range anyway, the relevant question is whether we can reproduce a given equation of state in the redshift range constrained well by data, not necessarily for all redshifts. For each sample equation of state considered below, we establish the acceptable redshift range and evaluate the equivalent Lagrangian function $F(X)$ and sound speed c_s^2. The examples are designed to lie in different regions of the phase space with different stability properties, for illustration; see Fig. 3.2.

3.6.1 Constant w

A constant equation of state is simple and approximates some well known components. For example, radiation has $w = +1/3$, matter $w = 0$ and a cosmological constant $w = -1$. Moreover, a (canonical) free field theory, with zero self-interaction potential $V = 0$, where the Lagrangian is simply $F(\phi, X) = X$, has $w = +1$.

It is useful to discuss the cases $w = -1$ and $w \neq -1$ separately. From Eq. (3.8), there are two ways to obtain $w = -1$. The first is by having $X = \text{const}$. Since constant X implies constant ρ, such solutions can *only* give $w = -1$. From Eq. (3.11), $X = \text{const}$ is a solution if $F_X = 0$. These solutions are special because since $dX/da = 0$ we cannot use Eq. (3.20) for the sound speed; instead we have to go back to Eq. (3.16). We see that (under the assumption that $F_{XX} \neq 0$, otherwise we have a canonical scalar field) this case has $c_s^2 = 0$ and is thus marginally stable. If X is not constant, the only way to get $w \equiv -1$ is by having $F = \text{const}$. This is just a cosmological constant

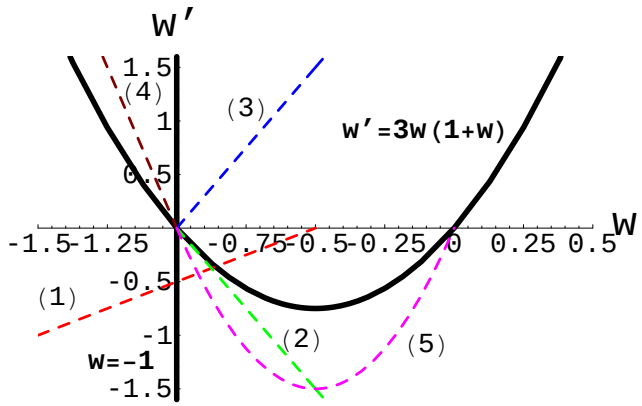

Figure 3.2: We investigate for a number of equations of state whether or not they can be described by kinetic k-essence model. The plot shows the trajectories in the $w - w'$ plane for some examples. It also shows the boundaries between stable and unstable k-essence regions (see Fig. 3.1): the lines $w = -1$ and $w' = 3w(1+w)$. The equations of state are: (1) $w = -0.9 + 0.4(1-a)$, see §3.6.2; (2) $1+w = (1-0.9)a^{-3}$, (3) $1+w = (1-0.9)a^{3}$, (4) $1+w = (1-1.1)a^{-6}$, all §3.6.3; (5) the Chaplygin gas, see §3.6.4. Note that $w =$ const equations of state (see §3.6.1) correspond to points on the horizontal axis.

and the adiabatic sound speed is not defined because there are no perturbations.

Next we look at $w \neq -1$. One can obtain constant $w \neq -1$ solutions if X is not constant and the functional form of $F(X)$ has the right form. Since constant equations of state are points on the horizontal axis in figure 3.1, we need $w \geq 0$ for the equation of state to be in the stable region. More quantitatively, from Eq. (3.20), we have

$$c_s^2 = w. \tag{3.31}$$

In other words, any solution leading to a constant negative equation of state ($\neq -1$) is unstable viewed as k-essence.

It is straightforward to explicitly construct k-essence Lagrangian densities corresponding to constant w without applying the machinery developed in the previous section (see also [48]). Instead, we can just use Eq. (3.8) to get

$$XF_X = \frac{1+w}{2w}F, \tag{3.32}$$

which integrates to

$$F(X) \propto X^{\frac{1+w}{2w}}. \tag{3.33}$$

Since the energy density should be positive, F must be positive for the $w > 0$ solutions and negative for the $w < 0$ ones. As discussed in §3.3, we are free to choose the magnitude of the proportionality factor.

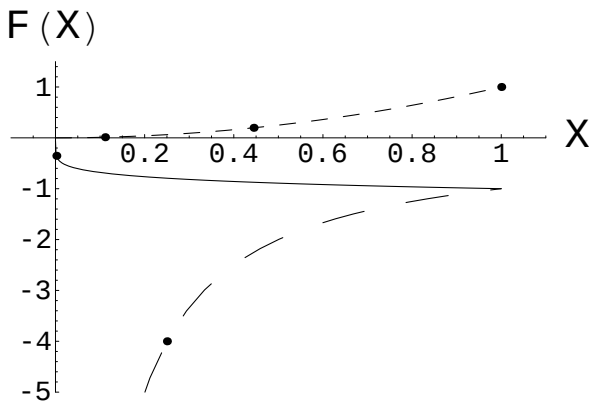

Figure 3.3: $F(X)$ for constant w (ansatz A) with $w = -1.5$ (solid), $w = -1/3$ (long dashed) and $w = +1/3$ (short dashed). For $w < 0$, we choose $X(z = 0) = 1$ to be at the end of the plotted domain; the field evolves with time from left to right and the marked points correspond to $z = 1$. For $w > 0$, the field moves toward $X = 0$ and the markers on the $w = +1/3$ curve indicate from left to right $z = 0, 1, 2$. The Lagrangians for negative constant w ($\neq -1$) correspond to unstable solutions. An equation of state $w \equiv -1$ can be obtained from any $F(X)$ with an extremum by letting X sit at that extremum (or from a cosmological constant $F = \text{const}$).

Let us now look at some specific cases. First of all, it is useful to note that we cannot reproduce matter-like behavior, as for $w = 0$ the k-essence Lagrangian (3.33) is not well defined. This result makes sense: $w = 0$ corresponds to a pressure-less material, whereas in the case of k-essence, the pressure is the same as the Lagrangian density. In other words, $w = 0$ would mean that the Lagrangian density is zero everywhere, which of course just means there is no DE model at all.

Equation (3.33) also confirms that $w = 1$ corresponds to a canonical free field (no potential) Lagrangian $F(X) = X$ (which is simultaneously a k-essence and a quintessence model). Note that skating models (see [155] and references therein), moving along a constant potential with $w' = -3(1 - w^2)$, stretch between true free fields $V = 0$, $w = 1$ and pure constant potentials $V = V_0$, $w = -1$, following $X \sim a^{-6}$. This leads by Eq. (3.11) to $F_X = \text{const}$, or $F \sim X + \text{const}$. In this sense one can think of kinetic k-essence models as skaters that "push off," altering their kinetic energy. Radiation-like behavior, $w = 1/3$, is generated by a function of the form $F(X) = X^2$. (Note this should not be interpreted as a perturbation around a minimum of a potential since the field motion does not correspond to rolling in $F(X)$.) Figure 3.3 illustrates several examples.

3.6.2 Time Variation: $w(a) = w_0 + w_a(1-a)$

A commonly used ansatz allowing for time variation is $w(a) = w_0 + w_a(1-a)$, which provides a good fit to many canonical scalar field and other model behaviors [149], at least over the past expansion history. Since $w' = -w_a a = w - (w_0 + w_a)$, in the w-w' plane the equation of state starts in the past somewhere on the w-axis (at $w(a \ll 1) = w_0 + w_a$). Thus from the previous subsection we know it cannot be wholly degenerate with a stable k-essence model. Its dynamics corresponds to a straight line with slope one that may cross through the stable region but again in the far future lie in an unstable region. Thus there is only a finite range of redshift when it may look like a stable kinetic k-essence model. The values of w and w' today are given by $w(a=1) = w_0$ and $w'(a=1) = -w_a$. For a model within the stable region today we consider $(w_0, w_a) = (-0.9, 0.4)$, in Fig. 3.4. This crosses the $w' = 3w(1+w)$ line at $a \approx 0.9$. This means that when calculating $F(X)$, starting at $a = 1$, it will become double valued at $a \approx 0.9$. In the future, the equation of state crosses the other boundary $w = -1$ at $a \approx 1.25$. Hence, this equation of state is only degenerate with a stable kinetic k-essence model in the very limited range $a \approx 0.9 - 1.25$.

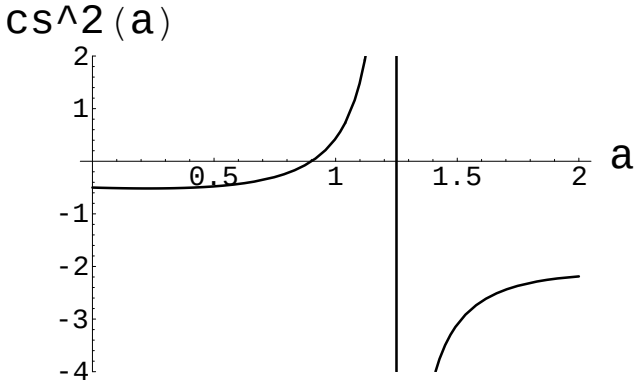

Figure 3.4: Ansatz B with $(w_0, w_a) = (-0.9, 0.4)$. The adiabatic sound speed squared c_s^2 is plotted vs. the scale factor a, clearly showing that $c_s^2 > 0$ today but becomes negative both at $a \approx 0.9$ and $a \approx 1.25$. Hence, this equation of state can only be described by a stable kinetic k-essence solution in the (rather limited) range between those times (also see Fig. 3.5).

To calculate the k-essence Lagrangian explicitly, we need to solve Eq. (3.26). This can be done analytically in the case at hand, giving

$$X(a) = C a^{-6(w_0+w_a)} [1 + w_0 + w_a(1-a)]^2 e^{6w_a a}\,, \tag{3.34}$$

where C is a positive constant. In the region between its extrema (the points where w crosses one of the boundaries in Fig. 3.1), $X(a)$ can be uniquely inverted and $F(X)$

can be computed after using Eq. (3.27) to find $F(a)$. The solution is shown in Fig. 3.5 for $(w_0, w_a) = (-0.9, 0.4)$. Note how $F(X)$ becomes double valued when going beyond the extrema.

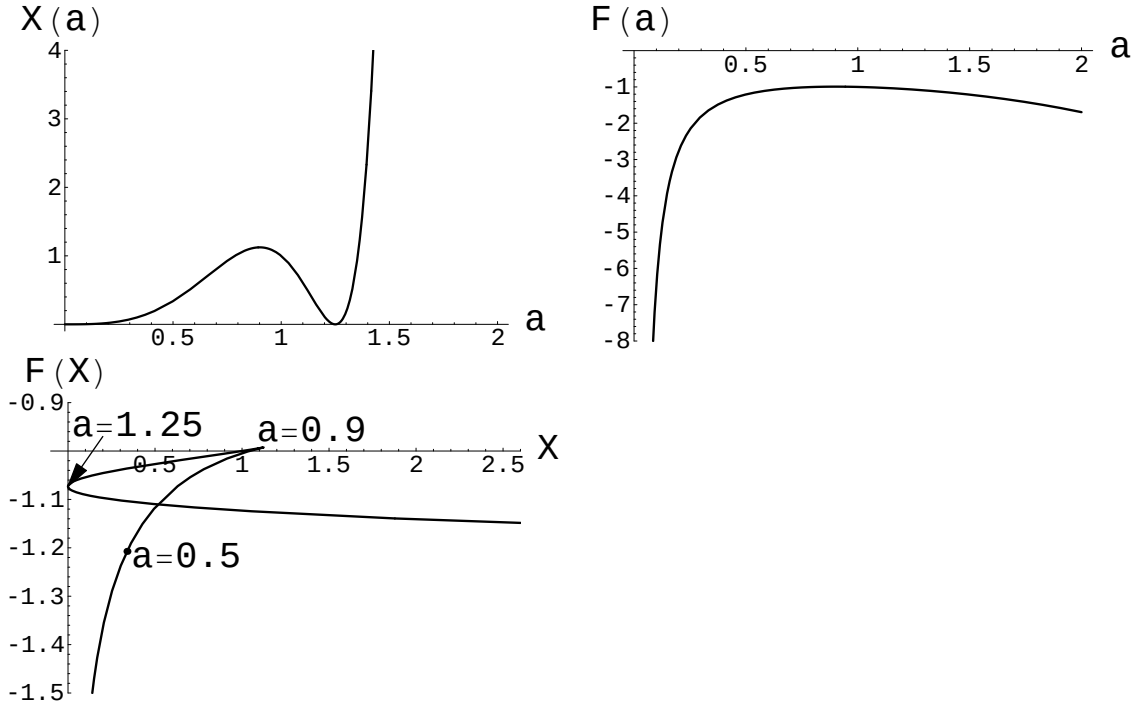

Figure 3.5: As Fig. 3.4, but plotting $X(a)$ and $F(a)$ (top left and top right, see text and Fig. 3.4 for details), normalized such that today $X = 1$ and $F = -1$. The bottom left panel shows the function $F(X)$ obtained from $X(a)$ and $F(a)$ over the range $a = 0.1 - 1.5$. $F(X)$ turns around at the points where $dX/da = 0$ (i.e. where c_s^2 becomes negative, at $a \approx 0.9$ and $a \approx 1.25$) and is therefore not single valued. Hence, this $(w_0, w_a) = (-0.9, 0.4)$ example model only corresponds to a well defined $F(X)$ in the region $a \approx 0.9 - 1.25$.

3.6.3 Thawing/Freezing Regions

The ansatz of $w' = x(1 + w)$ leads to an equation of state

$$1 + w(a) = (1 + w_0)a^x. \tag{3.35}$$

This describes a thawing model for $x > 0$, where the equation of state starts frozen at high redshift so $w = -1$, and then begins rolling away from it. This form describes well a number of renormalizable power law potentials and pseudo-Nambu-Goldstone boson (PNGB) models. For $x < 0$ it is simply a toy model of an equation of state approaching (freezing into) a cosmological constant state. See [44] for more on thawing and freezing models.

From Eq. (3.20), the adiabatic sound speed for these models is given by

$$c_s^2(a) = w(a) - \frac{x}{3}. \tag{3.36}$$

This shows that c_s^2 is positive today only if $x < 3w_0$. It is positive at all times if $w_0 > -1$ and $x < -3$ (for $w_0 < -1$, it can only lie in the stable region for a limited redshift range regardless of the value of x). Still, we see that the criterion that c_s^2 be positive already rules out all the thawing equations of state and part of the freezing ones.

To construct $F(X)$, we again solve Eq. (3.26), giving

$$X(a) = Ca^{2x+6}e^{-\frac{6(1+w_0)}{x}a^x}, \tag{3.37}$$

where C is a positive constant. Note that if $(x+3)/(1+w_0) > 0$ this function has an extremum at $a = \{(x+3)/[3(1+w_0)]\}^{1/x}$. After finding $F(a)$ from Eq. (3.27), we can again calculate $F(X)$.

We explore three different cases, corresponding to diverse physical situations. The example with $x = 3$ describes well a thawing equation of state, evolving away from cosmological constant behavior, but would be an unstable k-essence model. For $x = -3$, the dynamics is freezing, approaching a cosmological constant, and the corresponding k-essence model has positive sound speed squared for all redshifts. The model with $x = -6$ and $w_0 = -1.1$ gives a toy phantom model which approaches a cosmological constant, and lies in the stable region only at recent redshifts. These cases are illustrated in Figs. 3.6-3.9.

3.6.4 Generalized Chaplygin Gas

Dark energy that behaves like matter ($w = 0$) at early times and like a cosmological constant ($w = -1$) at late times can be described by an equation of state

$$1 + w(a) = \left[1 - \frac{w_0}{1+w_0}a^{3(n+1)}\right]^{-1}, \tag{3.38}$$

where we take $w_0 \in (-1, 0)$ and $n > 0$. A model that produces exactly this equation of state is the generalized Chaplygin gas (GCG, [28]), which can also be described by a perfect fluid/gas with equation of state $p = -A/\rho^n$, where A is a constant. The original model, the Chaplygin gas ([45, 130]), corresponds to the case $n = 1$. The GCG has been extensively studied in hope of providing a unified description of dark matter and dark energy, but in such an approach it has problematic issues with structure formation [192, 27, 15]. However, it is still interesting to study as a dark energy model. This equation of state can be reproduced by a k-essence model (see, e.g., [28]) and, of the dynamical equations of state we discuss here, this is the only one where an *explicit* expression can be found for the k-essence Lagrangian density

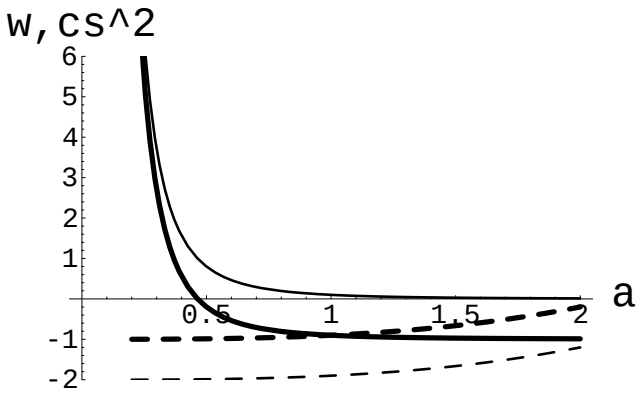

Figure 3.6: Ansatz C with $w_0 = -0.9$ and $x = -3$ (solid) or $x = 3$ (dashed). The equation of state (thick lines) and adiabatic sound speed squared (thin lines) are plotted vs. a. Note $x = 3$ lies in a forbidden region ($c_s^2 < 0$) for all a and therefore cannot correspond to a stable kinetic k-essence solution. For $x = -3$, the corresponding k-essence Lagrangian is exhibited in Fig. 3.7.

$F(X)$. The Lagrangian for $n = 1$ can be linked to the tachyon in string theory and to the dynamics of branes (as referred to in §3.2).

From the expression for $w(a)$ one finds that its dynamical trajectory is a parabola given by $w' = 3(n+1)w(1+w)$, with $w(a)$ evolving from 0 to -1 (also see the mocker model in [152]). For $n > 0$ this equation of state always lies completely in the allowed region B. It is therefore possible to reproduce it with a stable kinetic k-essence solution. Note that in the limit $n \to 0$ we approach the boundary of the allowed regions, the constant pressure line. (For $n > 1$ there will be epochs where the trajectory crosses the null line given by Eq. (3.21); see §3.4.) We consider two examples ($n = 0.5, 1$ with $w_0 = -0.9$) in Fig. 3.10.

To construct $F(X)$, we first solve equation (3.26) to find

$$X(a) = \left(1 - \frac{w_0}{1+w_0} a^{3(n+1)}\right)^{-\frac{2n}{n+1}}, \tag{3.39}$$

where we have chosen the normalization such that X goes from 1 at $a = 0$ to 0 at $a = \infty$. The expression can easily be inverted to give $a(X)$. Subsequently, Eq. (3.28) leads to

$$F(X) = -A^{\frac{1}{n+1}}(1 - X^{\frac{n+1}{2n}})^{\frac{n}{n+1}} \tag{3.40}$$

(cf. [28]), where A is the constant appearing in the GCG equation $p = -A/\rho^n$. We plot two examples in Fig. 3.11.

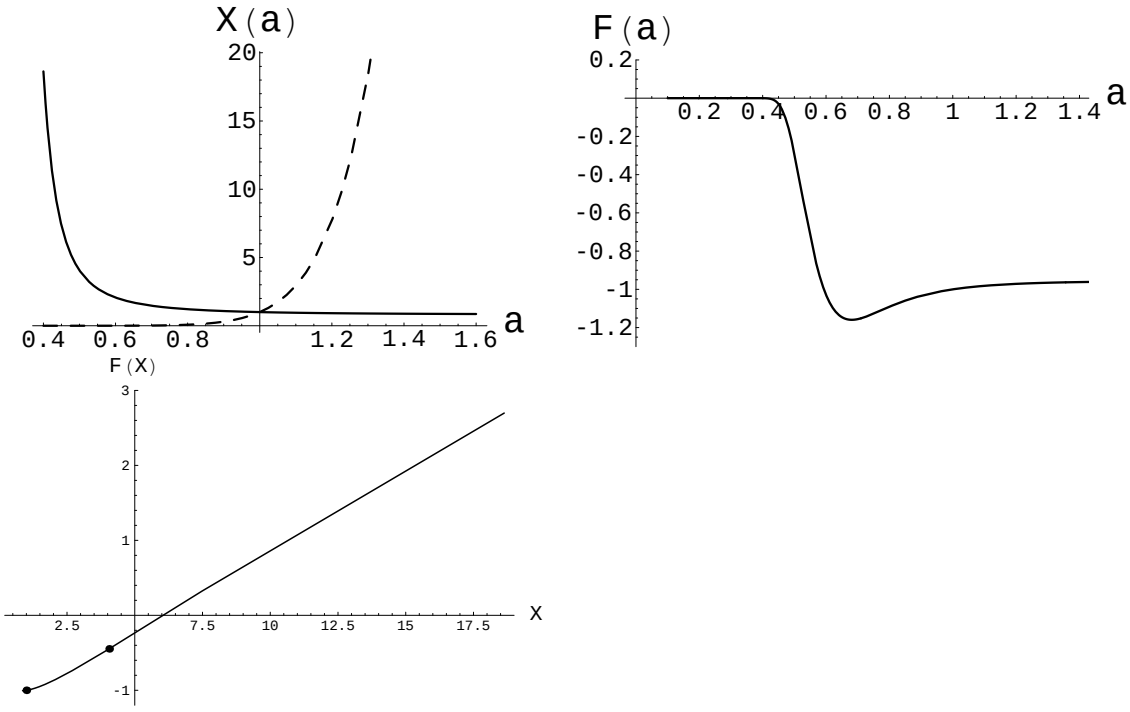

Figure 3.7: As Fig. 3.6 but showing the k-essence functions $X(a)$ (top left), $F(a)$ (top right), and $F(X)$ (bottom left). $F(X)$ is plotted for the stable $x = -3$ case over $a = 0.4 - 1.6$ (from top right to bottom left), with markers at $z = 1$ (right) and $z = 0$ (left).

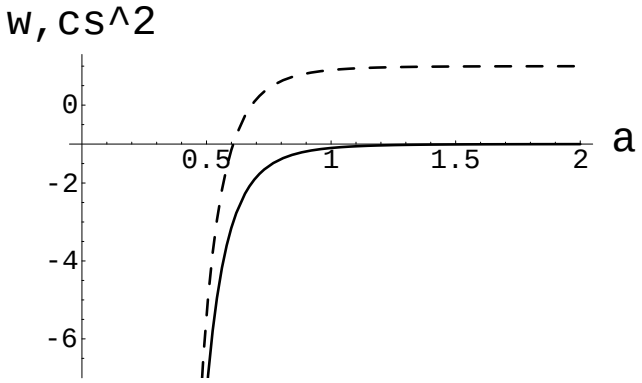

Figure 3.8: As Fig. 3.6, but for the phantom case $w_0 = -1.1$ and $x = -6$. Here the solid curve shows $w(a)$ and the dashed curve c_s^2.

3.7 Conclusions

Kinetic k-essence is in some sense an equally probable solution to the dark energy conundrum as quintessence, trading a single potential function $V(\phi)$ for a single

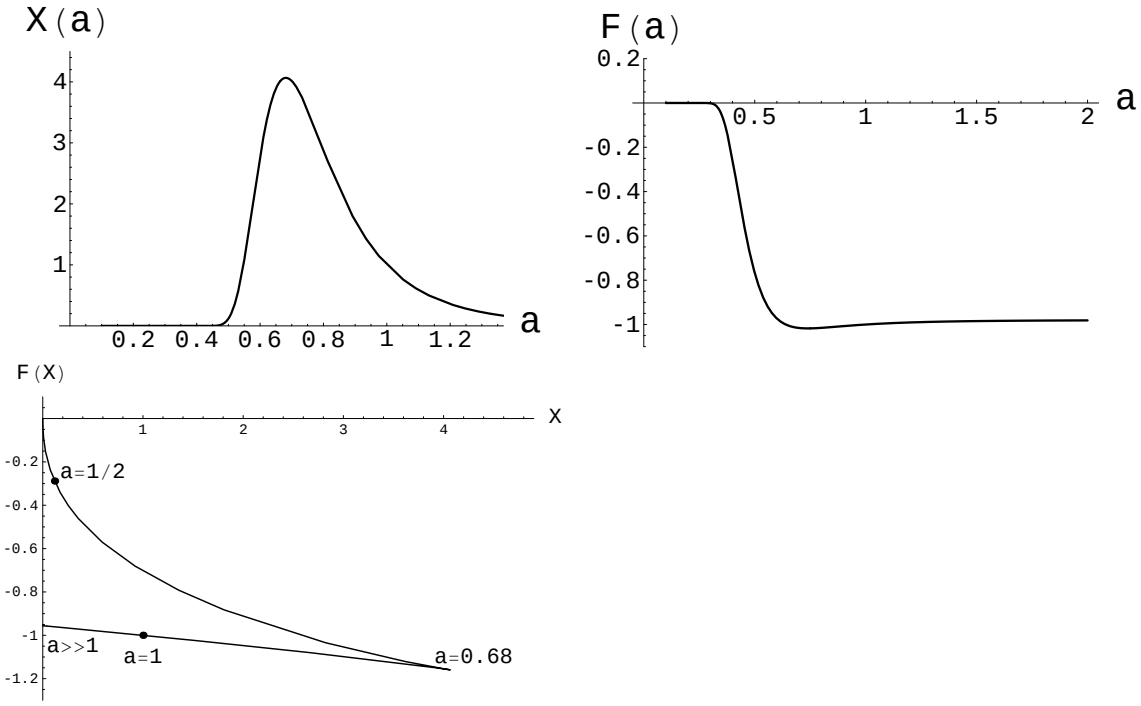

Figure 3.9: As Fig. 3.8, but showing the functions $X(a)$, $F(a)$, and $F(X)$.

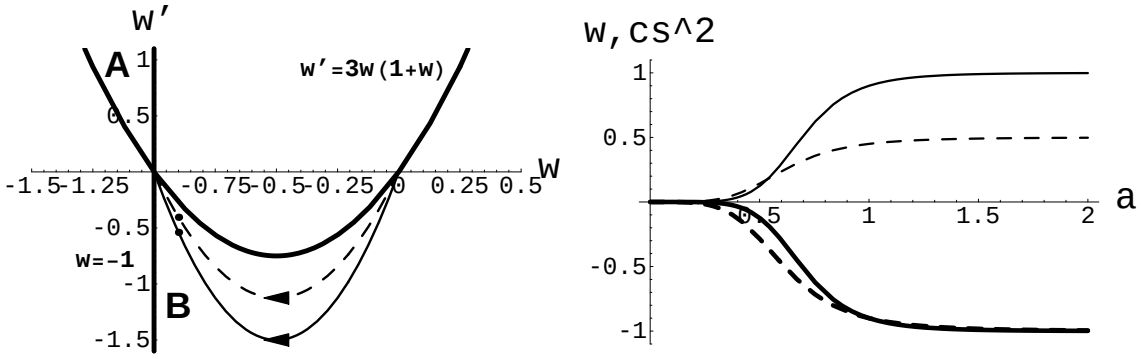

Figure 3.10: Ansatz D (the generalized Chaplygin gas) with $w_0 = -0.9$ and $n = 1$ (solid) or $n = 0.5$ (dashed). The left panel shows the trajectories in the w-w' plane. The direction of increasing scale factor is indicated by arrows and dots mark the values of w and w' today. Since the equations of state lie completely in region B, they can be obtained from purely kinetic k-essence Lagrangians (see Fig. 3.11). The right panel shows the equation of state w (thick lines) and the adiabatic sound speed squared c_s^2 (thin lines) as a function of scale factor a.

kinetic function $F(X)$. Similarly, one can find equivalent motivations for it from quantum field and extra dimension theories.

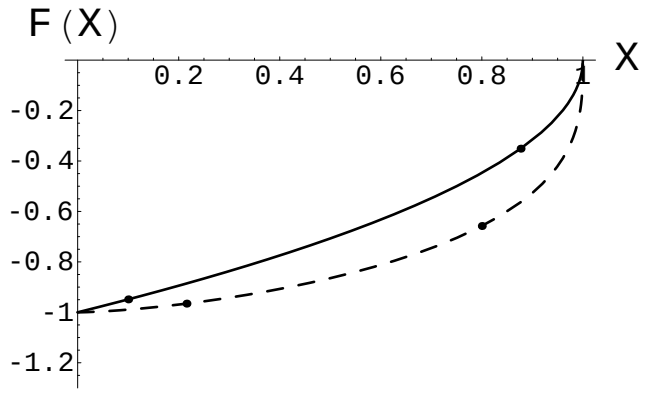

Figure 3.11: As Fig. 3.10, but plotting the corresponding k-essence Lagrangian density $F(X)$ (with F in units of $A^{1/(n+1)}$). X starts at one and then moves to zero as the scale factor increases. Markers indicate the points where $z = 1$ (right) and $z = 0$ (left).

We have established stability regions for such models within the equation of state phase space, based on the necessary condition of a non-imaginary sound speed. Conversely, we find closed form solutions, given some equation of state $w(a)$, for a dynamically corresponding kinetic k-essence Lagrangian $F(X)$. Eqs. (3.13-3.15) and (3.29-3.30) constitute a simple prescription – "by eye" – for characterizing kinetic k-essence theories.

Using these results, we investigated the limits to dynamical degeneracy between kinetic k-essence and quintessence. Analyzing four types of equations of state representing diverse dynamics, we found the limits in redshift defining the degeneracy region. For several equation of state models, both $w > -1$ and phantom, this implies that one could rule out all kinetic k-essence models with a sufficient redshift range of measurements. On the other hand, an equation of state similar in form to the generalized Chaplygin gas could be equally described by k-essence for all redshifts (as was already known). This clear definition of degeneracy regions offers increased hope that with future observational data on the dark energy dynamical and microphysical effects we can discern which approach describes the new physics behind our accelerating universe.

Chapter 4

Calibrating Dark Energy

A version of this chapter was previously published in the *Journal of Cosmology and Astroparticle Physics* [64].

4.1 Introduction

Guidance from theory is useful to predict observable signatures for cosmological probes such as distance and Hubble parameter measurements, in particular what level of accuracy is required to distinguish between models. From a model one can predict distance-redshift relations etc. but the number of models is vast; one would like to identify model independent or at least generic characteristics of the dark energy. Indeed, such properties exist, as discussed in detail recently by [39], for classes of behavior in the early time evolution of dark energy, valid for $z \gtrsim 2$ when the dark energy does not strongly affect the background expansion.

In this chapter we seek to extend characterization of the dark energy properties in terms of the equation of state to the entire observable history. This requires a different approach, calibrating the evolution through a "stretch" relation between the amplitude of the time variation and the time variable or scale factor of the expansion. The calibration then provides a physical basis for a compact and highly accurate parametrization of the dark energy influence on observables.

In §4.2 we examine several diverse models, looking for similarities and distinctions. We introduce the calibration in §4.3 and discuss its relation to a standard parametrization of the equation of state. §4.4 examines the utility of the description and shows that it achieves robustness and accuracy at the 10^{-3} level, sufficient for next generation data. We discuss some implications for figures of merit of dark energy science programs in §4.5. Those readers wanting to get right to the results could start in the middle of §4.3.

4.2 Dark Energy Dynamics

By examining the behavior of a diversity of dark energy models representing different physical origins, we can explore common and distinct elements within 1) a model as the parameters vary, 2) a family of models with some related property, and 3) different classes of models. Families of models might consist of those with similar functional forms, e.g. polynomial potentials, while classes might be those with similar early time behaviors, e.g. thawing models or freezing models [44].

We choose five representative families ranging over different physics and different evolutionary histories. These are the pseudo-Nambu-Goldstone boson (PNGB) model, or cosine potential, that thaws and moves away from an early cosmological constant state $w = -1$, the family of polynomial potentials, also thawing, the supergravity-inspired SUGRA model that has early tracking behavior and then moves toward the cosmological constant state (freezing behavior), the modified gravity model of DGP braneworld cosmology and its family of H^α modifications of the Friedmann equation, also with freezing behavior, and the Albrecht-Skordis or exponential times polynomial potential, whose history cannot be classified as purely thawing or freezing.

The dynamics is conveniently represented by the equation of state, or effective pressure to density ratio, w, and its variation $w' \equiv dw/d\ln a = \dot{w}/H$ where a is the expansion or scale factor. The Hubble parameter, or expansion rate, $H = \dot{a}/a$. We work in units where $8\pi G = 1$.

4.2.1 PNGB Model

Protected from radiative corrections by a shift symmetry, this model possesses technical naturalness and is characterized by a symmetry energy scale f [89]. The potential reads

$$V(\phi) = V_\star \left[1 + \cos(\phi/f)\right], \tag{4.1}$$

with $V_\star$ setting the overall magnitude, hence related to the present dark energy density. The equation of state, and the dynamics in general, is governed by f and the initial field position ϕ_i. (It is convenient, as seen from the form of Eq. (4.1), to use ϕ_i/f instead of ϕ_i.)

One can scan over the parameter space of these three variables and examine the evolutionary behavior and viability as a dark energy model. Figure 4.1 shows a selection of trajectories in the w-w' plane. The time coordinate runs along these tracks, and can be thought of as the scale factor a or the dark energy density fraction of the total energy density, $\Omega_w(a)$. As we change $V_\star$ or $\Omega_w = 1 - \Omega_m$, where Ω_m is the dimensionless present matter density, different points along a track for given f and ϕ_i/f correspond to the present. In fact, for some parameter values the dark energy never dominates and the density is restricted to $\Omega_w(a) < \Omega_{w,\max} < 1$. One can show that for fixed ϕ_i/f, then $\Omega_{w,\max} \propto f^2$, so models with symmetry energy scales much less than the Planck energy, $f \ll 1$, tend not to be viable.

Figure 4.1 shows a wide selection of trajectories that reach $\Omega_w = 0.72$ at the present. They fan out across the phase space, including ones that lie outside the conventional thawing region $3(1+w) > w' > 1+w$ (although these start along $w' = 3(1+w)$ at early times) [44]. The exceptions have $f \ll 1$, and are not generic in that for $f \ll 1$ we must fine tune ever more strictly the initial condition ϕ_i/f in order to achieve such a present density. Figure 4.2 plots the allowed values of ϕ_i/f, which decrease rapidly, roughly as $(\phi_i/f)_{\rm max} \sim e^{-1/f}$. For example, when $f = 0.1$, then the field must start exquisitely close to the top of the potential: rather than ϕ_i/f ranging freely over $[0, \pi]$, it is restricted to be less than 10^{-3}. For $f = 0.05$, this becomes $\phi_i/f < 10^{-7}$. Apart from unnaturalness, such values may run into physical problems such as a tachyonic instability [226, 55, 129].

In the future, the scalar field reaches the minimum of the potential and oscillates around it, giving an equation of state $w = 0$ (matter-like) when averaged over many oscillations. We discuss this further in comparison with the next model.

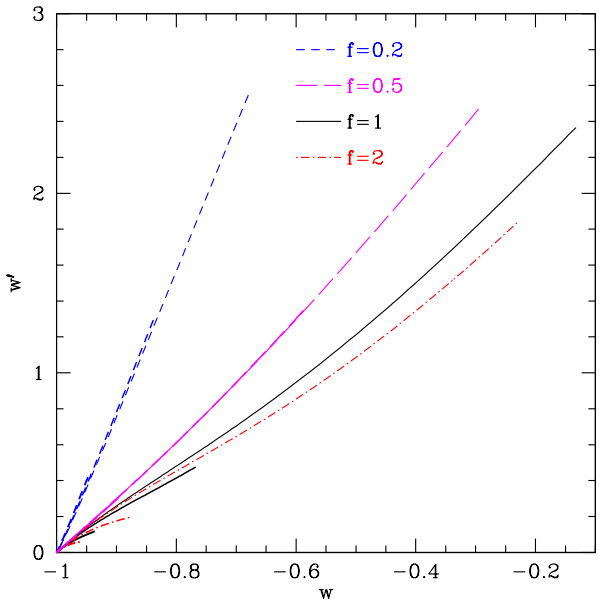

Figure 4.1: PNGB models fan out through phase space as their parameters vary (though still mostly within the thawing region). At early times the models all start frozen at $(w, w') = (-1, 0)$ and thaw, with the scale factor increasing along each curve, although at different rates in each case. Here we end the tracks when $\Omega_w = 0.72$.

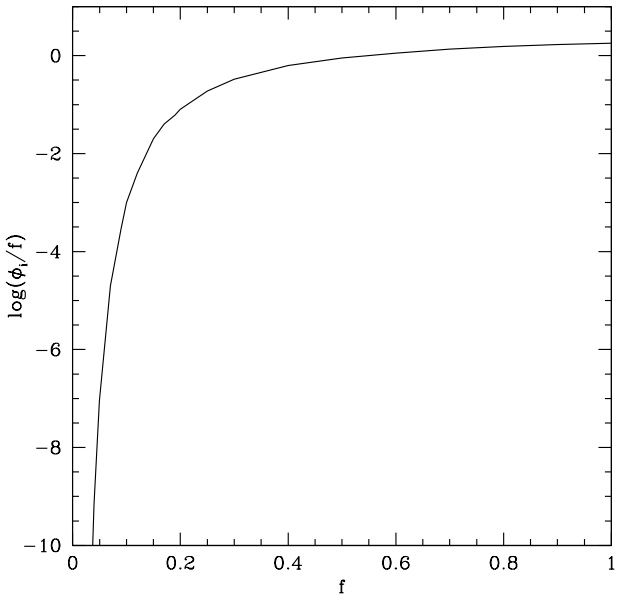

Figure 4.2: To achieve dark energy domination in the PNGB model before the field relaxes to its minimum, the initial field value ϕ_i must be small enough to give a long period of cosmological constant-like, or frozen, behavior. For very steep potentials, i.e. low symmetry energy breaking scales f, the field must initially be extremely finely balanced near the top of the potential, with the curve showing the maximum ϕ_i/f allowed to achieve $\Omega_w \geq 0.72$ at some point in the evolution.

4.2.2 Linear Potential

The linear potential tilts a flat potential, so the field rolls – although it is frozen by the large Hubble friction at early times. The potential is given by

$$V(\phi) = V_i + (\phi - \phi_i)\, V' \,, \tag{4.2}$$

where V' is the slope parameter, a constant [147, 231]. If the slope becomes too steep then the field never has time in its evolution to build up to appreciable energy density before the kinetic energy becomes substantial and $w > 0$, causing the fractional energy density relative to the matter density to decrease with scale factor. The evolutionary tracks for this model fan out in the phase space within the thawing region (some examples for this and other models appear in §4.2.6 in Fig. 4.7).

Figure 4.3 shows the long time evolution of the PNGB vs. linear potential models, showing the similarity of the tracks at first, then the dramatic difference in the fate of the universe as the PNGB field oscillates, acting like matter in a time averaged sense, and the linear potential field shoots away, leading to deceleration and a cosmic

doomsday collapse.

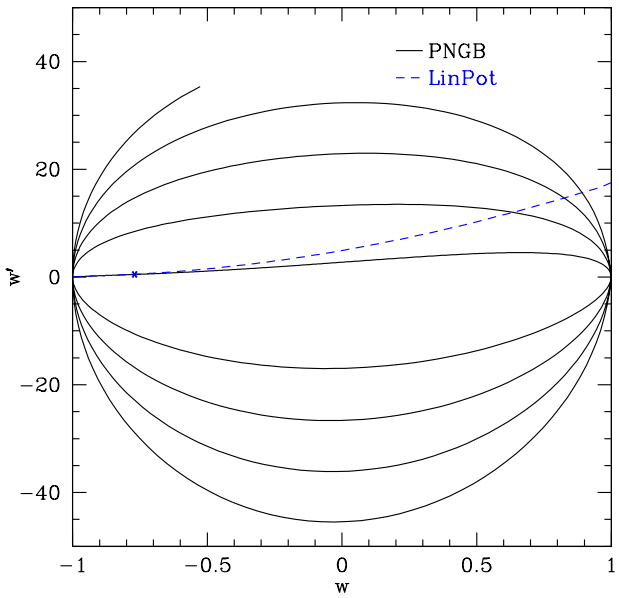

Figure 4.3: Long term evolutions of PNGB and linear potential models have distinct implications for the fate of the universe, both different from the cosmological constant case. The PNGB field oscillates while the linear potential rolls to negative infinity. Today the models shown have $w_0 = -0.77$, with $w_0' = 0.47,\ 0.52$ respectively. At $a = 2$, the PNGB model is still on the innermost track, with $w = 0.11$ (the curve end is at $a = 6.6$), while the linear potential is off the plot, on the way to collapse.

We also consider the related family of polynomial potentials, $V \sim \phi^n$ with $n = 2,\ 4$. These are also thawing models although their future behavior asymptotes to oscillation about a zero potential minimum. Hence they do not runaway to negative potential and a rapid, doomsday collapse. The equation of state during the oscillatory phase time averages to $w = (n-2)/(n+2)$ [227].

4.2.3 SUGRA Model

Tracking models have an early time attractor behavior that allows a large variety of initial conditions to give the same evolution in the matter dominated era, ameliorating fine tuning of initial conditions [241]. One example is the family of inverse power law potentials [183]. Including Planck scale corrections motivated by supergravity theory changes the potential to [36]

$$V(\phi) = V_\star\, \phi^{-n} e^{\phi^2/2}. \tag{4.3}$$

This has a local nonzero minimum, or cosmological constant. The equation of state behavior is governed by the power law index n.

Although the exponential factor has no effect on the attractor phase, it does permit a more rapid evolution after the field leaves that trajectory, moving the equation of state closer to $w = -1$. Since the dark energy has $w = -2/(2+n)$ while on the attractor trajectory, one requires $n \ll 1$ in the inverse power law model to accord with observations; this is somewhat eased for the SUGRA model. Today the field properties can cover a wide swath within the freezing region $0.2w(1+w) < w' < 3w(1+w)$.

4.2.4 Braneworld Gravity Model

Even dark energy theories that do not involve scalar fields can be viewed in terms of effective dynamics, where the equation of state is defined in terms of the Hubble parameter $H(a)$ and its modified Friedmann equation:

$$w_{\rm eff} = -1 - \frac{1}{3}\frac{d\ln \delta H^2}{d\ln a}, \tag{4.4}$$

where $\delta H^2 = H^2/H_0^2 - \Omega_m a^{-3}$. One example involving very different physics from scalar fields is the extension of gravity theory through extra dimensions. This can lead to a modified Friedmann equation and effective equation of state [78, 94]

$$H^2 = \rho_m(a)/3 + (1-\Omega_m)\, H_0^2\, (H/H_0)^\alpha, \tag{4.5}$$

$$w = -\left[1 + \frac{\alpha}{2-\alpha}\,\Omega_m(a)\right]^{-1}, \tag{4.6}$$

where ρ_m is the physical matter density and α is a parameter depending on boundary conditions between our four dimensional universe and the higher dimensional bulk volume. The best motivated model in this family is DGP braneworld gravity, corresponding to $\alpha = 1$ [77, 68]. At early times the effective potential looks like an inverse power law [39], with index $n = 2\alpha/(2-\alpha)$, and so has tracking behavior. At late times the field rolls asymptotically to a halt at a finite value of both the field and potential, acting as a cosmological constant. Indeed the trajectories lie within the freezing region.

4.2.5 Albrecht-Skordis Model

A scalar field potential with greater complexity is the Albrecht-Skordis [11], or exponential with polynomial prefactor, potential, motivated by string theory. This has the form

$$V(\psi) = V_0\,[\chi(\psi-\beta)^2 + \delta]\, e^{-\lambda\psi}, \tag{4.7}$$

in the notation of [35], with a more compact but equivalent notation being

$$V(\phi) = V_\star\,(1 + A\phi^2)\, e^{-\lambda\phi}, \tag{4.8}$$

where we shift to $\phi = \psi - \beta$, showing that only three parameters enter: $V_\star$, related to the dark energy density today, λ, and A. Away from $\phi \approx 0$ this behaves like an exponential potential, a classic tracker, so the initial conditions are not very important [233]. Near $\phi = 0$, the potential has a false minimum, so a field rolling through this region can have complicated dynamics, and indeed be trapped and oscillate about the nonzero potential minimum, eventually relaxing to a cosmological constant.

Figure 4.4 show trajectories for different parameter values, illustrating the wide variety of possible behaviors. In addition, Fig. 4.5 plots the equation of state $w(a)$ so one has another view of the damped, oscillatory evolution. Note that while the field sees an exponential potential, away from the false minimum, it exhibits not only tracking but tracing behavior – the dark energy equation of state is equal to the background, e.g. matter dominated, equation of state w_b. This means that the dark energy density is then a constant fraction of the background density, given by $\Omega_{w,\rm trace} = 3(1 + w_b)/\lambda^2$ [85, 52]. So as not to violate primordial nucleosynthesis or cosmic microwave background constraints, this requires the contribution to be no more than a few percent. We show the dynamics for two cases, the first using the parameter values in [35], corresponding to $\lambda = 3.4$ and $A = 106.7$, which has an early dark energy fraction $\Omega_e = 0.26$ during matter domination ($\Omega_e = 0.35$ during radiation domination), and the second using $\lambda = 10$, keeping A the same, giving $\Omega_e = 0.03$ (0.04) during matter (radiation) domination, close to the upper limit allowed [75, 26].

For values of λ allowed by nucleosynthesis and CMB limits, $\lambda \geq 10$, the oscillations are absent or negligible. One can show that the amplitude of the oscillations depends predominantly on the ratio λ^2/A (e.g. define $\varphi = \lambda\phi$ and the potential only explicitly contains the parameter combination λ^2/A). If this combination exceeds one, then there is no minimum but merely a slight local lessening of the exponential slope, and hence no oscillations. The amplitude increases as λ^2/A approaches zero. However, since $\lambda \geq 10$, small values of λ^2/A require $A \gtrsim 1000$, seemingly unnatural. Furthermore, the period of the oscillations is given by the effective mass and is inversely proportional to λ for fixed λ^2/A, and so for allowed λ the oscillations will be negligible for $z \lesssim 3$. These behaviors are illustrated in Fig. 4.6.

4.2.6 Cross Comparison

To compare the behaviors of different families, we plot selected representatives in Fig. 4.7. Varying the parameters within each model, as well as considering different models, spreads the evolution over regions of the w-w' phase space. Generally we see both similarities and distinctions between models and between families. One must also take into account the time coordinate along the curves, so that crossing of trajectories does not mean they have identical properties at any one moment. We plot the trajectories up to when the dark energy density is $\Omega_w = 0.72$.

We could extend the curves into the future, as was done in Figs. 4.3 and 4.4. The ϕ^4 potential will eventually settle at $w = 1/3$, acting as radiation, as discussed in

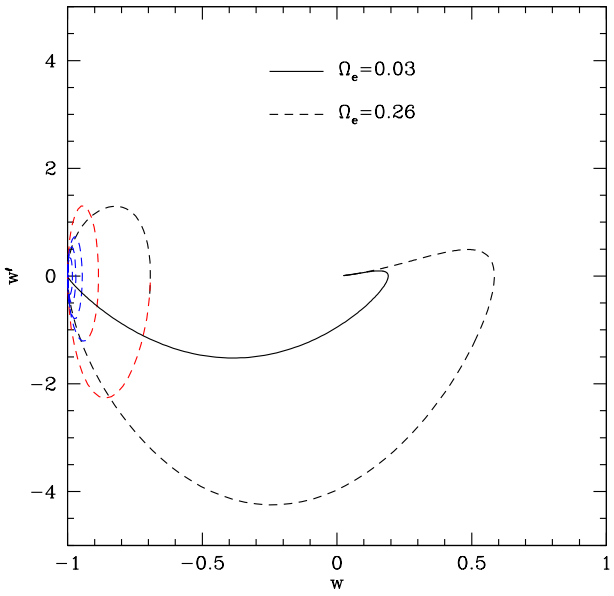

Figure 4.4: Albrecht-Skordis model acts like a tracer at early times, with a constant energy density fraction Ω_e and $w = 0$ in the matter dominated era, before oscillating around the nonzero minimum of the potential. We change the line thicknesses (and colors) at $z = 2$, 1, and 0. The oscillations are invisible for more viable $\Omega_e = 0.03$ case.

§4.2.2, after oscillating around the minimum. Note that the SUGRA, DGP/H^α, and Albrecht-Skordis models all have nonzero minima, i.e. hidden cosmological constants, so they settle to $w = -1$. The SUGRA field does not oscillate around the minimum because it approaches it with low kinetic energy, freezing to the cosmological constant state; the H^α family has only an asymptotic minimum, also approached by freezing.

As an alternative to showing the evolution of varied models at all times, we can take a slice at a particularly time, say when $\Omega_w = 0.72$, and construct phase space curves where the parameters of a potential vary along the curve. This can clear the illusion of overlap in behavior and provides an intermediate step toward the calibration in the next section.

Figure 4.8 gives an example of this for the PNGB model, where the parameter running along the curve is the initial field position ϕ_i/f. That is, every point along any curve has $\Omega_w = 0.72$ today, but corresponds to a different set of parameters for the potential and a different evolutionary behavior. This illustrates that different symmetry energy scales f define distinct paths to achieving a given dark energy density. (Of course not all of these are viable, with large values of ϕ_i/f along each curve corresponding to w far from -1, and small values of f suffering from the extreme

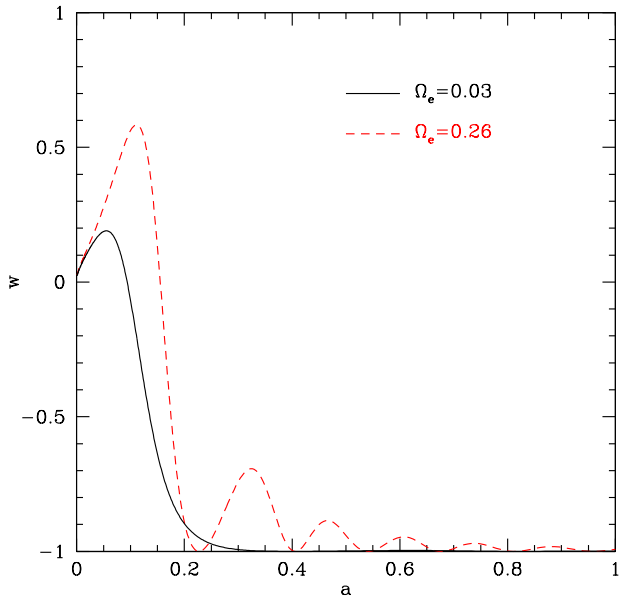

Figure 4.5: Equation of state $w(a)$ shows an alternate view of the evolution in Fig. 4.4. Note that for model parameters that do not violate early matter domination, the behavior relaxes swiftly to a cosmological constant, as shown by the solid, black curve.

fine tuning problem discussed in §4.2.1.) However, by evaluating the equation of state and its time variation at a single time, we lose all dynamical information. In the next section we combine the advantages of the parameter scan with those of the evolutionary trajectories.

4.3 Stretching Dark Energy

To keep the dynamics central, we want to preserve in some way the temporal information, i.e. the field evolving from its high redshift state along a trajectory describing the equation of state and its time variation. However, we are free to rescale the time coordinate and define a time variation other than $w' = dw/d\ln a$. In particular, we can ask whether there is a global transformation that in some way calibrates the dark energy characteristics. We call this the evolutionary stretch factor.

Stretching the time variation by different amounts at different times effectively introduces additional evolution beyond the scalar field behavior, so we consider a constant stretch factor, a simple renormalization. That is, we take $w'(a) \to w'(a)/a_\star$. Now, since realistic observations cannot map out the detail of the equation of state

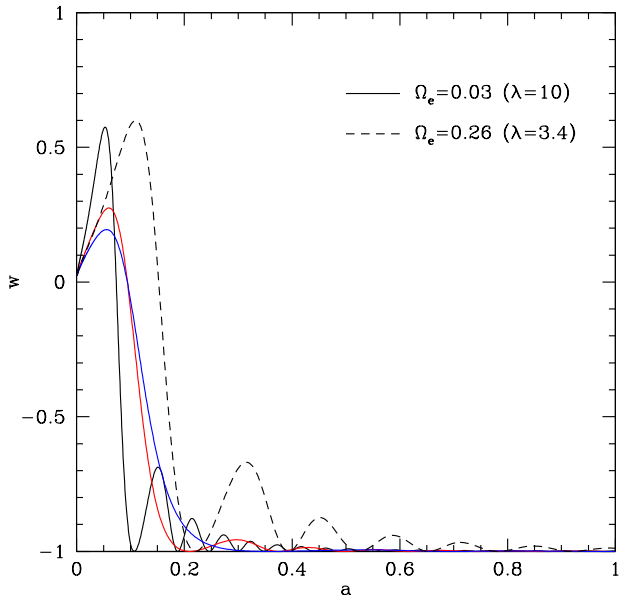

Figure 4.6: The amplitude of oscillations in the equation of state is governed by λ^2/A and the period goes as λ^{-1} (for fixed λ^2/A). The figure shows the equation of state history for $\lambda = 10$ ($\Omega_e = 0.03$ during matter domination) as solid curves, for $\lambda^2/A = 0.1$, 0.5, 0.9, from highest peak to lowest, and for $\lambda = 3.4$ ($\Omega_e = 0.26$), with $\lambda^2/A = 0.1$, as a dashed curve. For appreciable oscillations λ^2/A must approach zero, but for allowed (large) values of λ any oscillations damp away for $z \lesssim 3$.

function, we seek to condense the information on the evolution to a set that is robustly constrained by data. Overcompression loses important physical properties while undercompression leads to uninformatively large uncertainties. In the next section we will test the full stretch prescription to ensure that neither case occurs. To begin with, consider evaluating our new time variation quantity at a particular scale factor; furthermore, to keep the number of parameters in the stretch prescription to a minimum, we choose this scale factor to be the same as the stretch factor $a_\star$. That is, the procedure can be viewed illustratively as

$$w'(a) \to \frac{w'(a)}{a_\star} \to \frac{w'(a_\star)}{a_\star}\,. \tag{4.9}$$

For evaluating the value of the equation of state function itself, $w(a)$, we also avoid choosing an arbitrary scale factor. This leaves us with two choices: either $a_\star$ or the present epoch, $a = 1$. If we choose $a_\star$, then this procedure merely chooses a single point along the evolutionary trajectory, losing much of the global information. Thus we adopt $w_0 = w(a = 1)$ and examine the dark energy characteristics in the plane

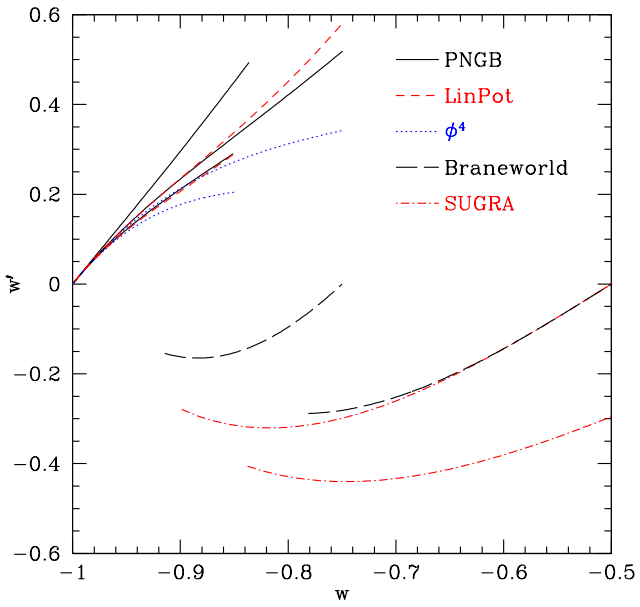

Figure 4.7: Representative models considered in this section are plotted for various parameter values in the w-w' phase space. Solid, black curves are PNGB, short-dashed, red curves are for the linear potential, dotted, blue curves are for ϕ^4, long-dashed, black curves for the braneworld model ($\alpha = 1$ DGP and $\alpha = 0.5$), and dot-dashed, red curves for SUGRA.

of the two parameters, w_0 and $w'(a_\star)/a_\star$ ($= dw/da(a_\star)$), to see if there is indeed a normalizing relation for the time evolution.

Figure 4.9 shows clearly that this prescription calibrates the evolution of the PNGB model. Instead of the fan of trajectories spreading through the w-w' phase space, as in Fig. 4.8, we now have a tightly calibrated, one parameter relation in the w_0 vs. $w'(a_\star)/a_\star$ plane. Despite scanning over the model space of f and ϕ_i/f, this stripe is narrow and well defined. Points within the stripe represent individual realizations of the PNGB model with choices of the symmetry energy scale ranging over the physically reasonable range $f \in [0.2, 5]$ and initial field position covering from 0 to the maximum value that allows $\Omega_w \approx 0.7$.

This tight calibration spreads little if we vary the present dark energy density as well as the potential parameters themselves. Allowing Ω_w today to range over 0.69-0.75 gives the slightly wider, lightly shaded region.

Calibration succeeds for the other dark energy models considered as well, covering a wide range of physical origins. Indeed, all the thawing models are closely related, nearly forming a single family under the calibration. The similarities extend to defining a single stretch parameter $a_\star = 0.8$ for the entire thawing class. Freezing

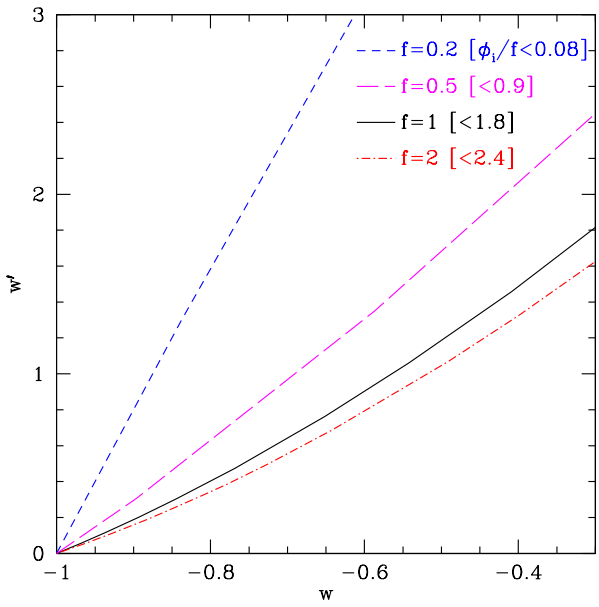

Figure 4.8: These curves for the PNGB model correspond to a scan over the potential parameter space to find those values where $\Omega_w = 0.72$. Each curve is for a different energy scale f, with the parameter ϕ_i/f running along each curve, from zero at $w = -1$ to a maximum possible value shown in brackets.

fields also can be calibrated, with a uniform stretch parameter $a_\star = 0.85$, though the families stay more distinct within the freezing class. Figure 4.10 shows the tight relations of the different dark energy models, in strong contrast with the "fan" nature of Fig. 4.7.

From the form of the stretch calibrated time variation, $w'(a_\star)/a_\star$, we can recognize this as nearly identical to w_a, the dark energy variable in standard use, defined by [149] as $w_a = -w'(a_\star = 0.5)/0.5$ to fit the equation of state function by $w(a) = w_0 + w_a^{(\mathrm{w})}(1-a)$. The superscript w indicates that the value of $a_\star$ was chosen to fit $w(a)$. Here, however, we defined the equivalent of w_a to calibrate dark energy families. This resulted in $a_\star = 0.8$ for the thawing class and $a_\star = 0.85$ for the freezing class. An interesting further implication is that the "new" form

$$w(a) = w_0 - \frac{w'(a_\star)}{a_\star}(1-a) = w_0 + w_a^{(\mathrm{d})}(1-a) \tag{4.10}$$

has excellent accuracy when fitting the observables of distance and Hubble parameter, as we discuss next.

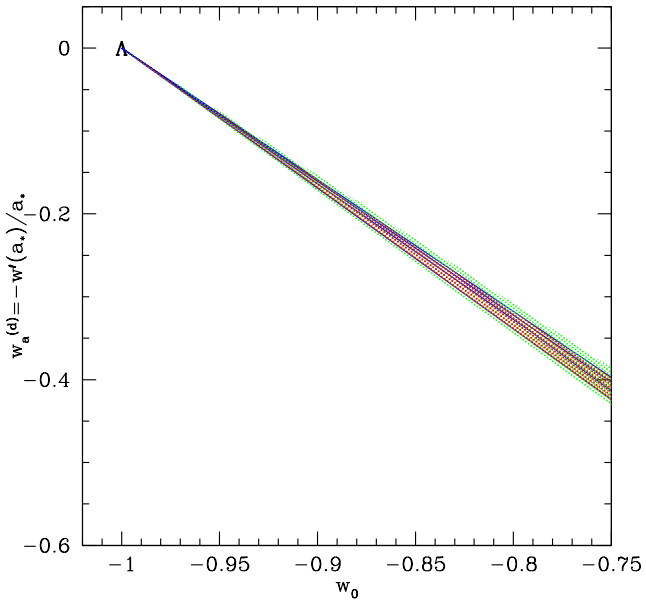

Figure 4.9: Defining a new time variation variable $w_a^{(\rm d)}$ from w' calibrates the PNGB model into a tight locus; compare the spread in Fig. 4.8. Solid lines are for fixed f parameter, the shading shows the range of behaviors for $f \in [0.2, 5]$. The lighter shading shows the effect of also scanning over $\Omega_m = 0.25$–0.31.

4.4 Observing Dark Energy

While the form (4.10) was just shown useful in interpretation of dark energy theory, we should also investigate its utility for interpreting dark energy observations. Three related, but slightly different, physical bases exist for using the form $w(a) = w_0 + w_a(1-a)$ to characterize dark energy: this can be interpreted as 1) a fitting formula to the equation of state, 2) a calibration relation for families of dynamics in the w-w' plane, or 3) a fitting formula for observables such as distances and the Hubble expansion rate. The last two in particular are closely related and give similar results; indeed, when models do not deviate greatly from cosmological constant behavior the two approaches are almost identical.

We now explore the accuracy of the form (4.10) in fitting the exact distance-redshift and Hubble parameter-redshift relations for the diverse dark energy models discussed in §4.2.

Table 4.1 summarizes the accuracies on d and H for a diverse range of models. These are generally good to the 10^{-3} level. Models closer to Λ would have better fits than shown here; models further from Λ are not favored by current data. For simplicity we henceforth denote the calibrated fit parameter simply as w_a.

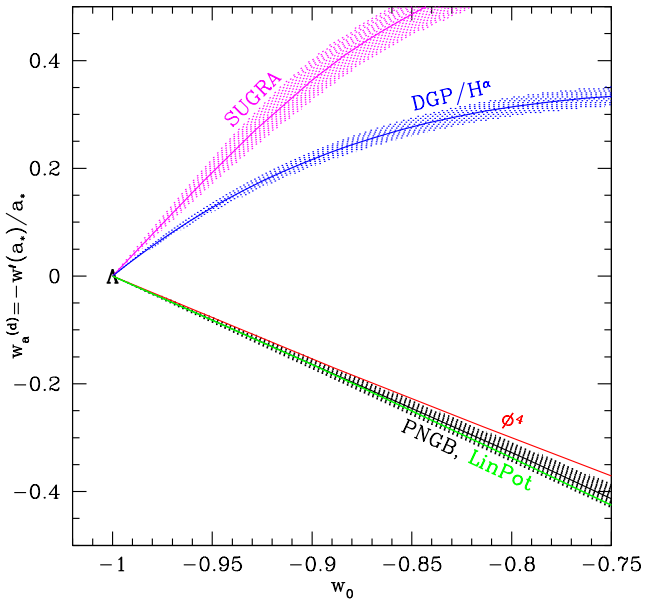

Figure 4.10: In terms of the calibrated dark energy parameters w_0 and $w_a^{(\rm d)}$, models and families lie in tightly homogeneous regions, in comparison to Fig. 4.7, showing the same models before calibration. We here vary over all parameters in the potentials. Shading shows the effect of scanning over ± 0.03 in Ω_m (we omit the shading for ϕ^4 and linear potential models to minimize confusion; the width would be about half that shown for PNGB). Thawing models, despite their differences in w-w', are nearly identical once calibrated. Distinctions from freezing models, and between freezing models, become highlighted with calibration.

We could push the accuracy even further by minimizing the deviation not globally, over the entire range $a \in [0, 1]$, but over a particular epoch, say $a \in [0.5, 1]$. However, we retain the global fit in general. Also, we have not taken advantage of the degree of freedom of w_0, which could improve the fits. We emphasize that the stretch factor is a function of the dark energy physics and not dependent on the experiment, priors, etc. (in distinction from a pivot redshift or pivot equation of state value).

Note that the results from this prescription also answer the important question of whether the calibration procedure preserves the information faithfully to the precision level of the data, or over- or under-compresses the model characteristics. A one parameter approach such as a constant value of w would have errors of order 1–2% in distance and up to 3% in Hubble parameter for the models we considered. This is insufficient for forthcoming observations. Conversely, since the two calibrated parameters of w_0 and w_a map the observables to better accuracy than expected from next generation data, these two parameters suffice and the data precision does not

Model	$\delta d/d$	$\delta H/H$
PNGB ($w_0 = -0.85$)	0.05%	0.1%
PNGB ($w_0 = -0.75$)	0.1%	0.2%
Linear Pot. ($w_0 = -0.85$)	0.05%	0.1%
Linear Pot. ($w_0 = -0.75$)	0.1%	0.3%
ϕ^4 ($w_0 = -0.85$)	0.01%	0.04%
ϕ^4 ($w_0 = -0.75$)	0.02%	0.06%
Braneworld ($w_0 = -0.78$)	0.03%	0.07%
SUGRA ($n = 2$)	0.1%	0.3%
SUGRA ($n = 11$)	0.1%	0.3%
Albrecht-Skordis ($\Omega_e = 0.03$)	0.01%	0.02%
Albrecht-Skordis ($\Omega_e = 0.26$)	0.1%	0.4%

Table 4.1: Accuracy of w_0-w_a in fitting the exact distances and Hubble parameters for various dark energy models. These numbers represent global fits over all redshifts (except for the last three cases, where the fit covers $z = 0$-3, due to early dark energy: see §4.5). Better fits can be found over finite redshift ranges.

call for further equation of state parameters.

This is not to say that some models could not exist where a third parameter carries information, but such models may not be generic or natural; the wide range of models considered here has no use for one. If we reach the stage of probing the cosmic expansion history below the 10^{-3} precision level, we should revisit the question of a further calibration parameter.

Finally, this prescription is meant to help us find our way through the dark forest [12] of models of cosmic acceleration, making accurate, more or less model independent assessments. Once precision data exist, they should be analyzed for every model of interest and within every applicable fit technique, parametric and nonparametric. We have seen that until we reach that point w_0-w_a serves as a robust indicator and guide for predicting and comparing cosmological probe information.

4.5 Figures of Merit

The accuracy of the w_0 and w_a form, defined in the manner discussed here, for characterization of observable properties of dark energy is at a level of order 10^{-3}, sufficient for next generation experiments. The calibration into tight families of equation of state properties, as seen in Fig. 4.7, suggests that not all combinations of w_0 and w_a are of equal insight. For example, one might distinguish models in the thawing class from the cosmological constant and from each other by constraining the combination varying exactly along the calibrated curve.

Since this curve is nearly straight, we can characterize it by slope m_t, and define a new variable

$$w_\parallel^t = w_0 + m_t w_a \,, \tag{4.11}$$

where the derivative with respect to this parameter runs parallel to the calibrated curve. Hence, determining $w_\parallel^t$ localizes the behavior and distinguishes the specific dark energy characteristics. The narrowness of the calibrated region means that it is not so useful within thawing models to constrain the direction perpendicular to the curve.

One can define a similar variable for the freezing class, although here the families are more spread out, so the slope is more of an average than a well defined value,

$$w_\parallel^f = w_0 + m_f w_a \,. \tag{4.12}$$

Values of $m_t = -1.75$ and $m_f = 3.5$ are reasonable choices. Note that the combinations $w_\parallel^f$ and $w_\parallel^t$ are not orthogonal, so the variable defined for each class does have utility in constraining the other class as well. For example, along the PNGB curve of Fig. 4.10 the parameter $w_\parallel^t$ runs from -1 to 0, while $w_\parallel^f$ goes from -1 to -2.2; along the SUGRA curve $w_\parallel^t = -1$ to -1.7 while $w_\parallel^f = -1$ to $+0.9$. This shows that each parameter, while optimized for a given physics question, does carry information on the other class.

Thus, knowledge of either parameter $w_\parallel^t$ or $w_\parallel^f$ answers the key questions of distinction from a cosmological constant, distinction between models, and to an extent distinction between classes. Constraining both parameters tightens the distinguishing ability, especially between classes, and provides a crucial crosscheck of the framework.

It does not seem natural or effective to combine the uncertainties in estimating these variables from observations into a single number, e.g. $\sigma(w_\parallel^t) \times \sigma(w_\parallel^f)$, since they represent very different physics. Moreover, further investigation is needed into the optimum values for m_f, m_t and other issues before defining ultimate figures of merit, if this is even possible. However, the tightness of the calibration does imply that some combinations of w_0 and w_a will provide insight into the nature of dark energy. Therefore, knowledge of the uncertainties $\sigma(w_0)$ and $\sigma(w_a)$ and their covariance are the main ingredients for a variety of future figures of merit that might be developed.

Finally, we note that the accuracy of the w_0-w_a form does start to degrade to the 10^{-2} level as dark energy becomes increasingly important in the early universe around $z \gtrsim 10^3$, upsetting standard matter domination. See, for example, the last three models in Table 4.1, where the dark energy equations of state at recombination are $w \approx -0.15$, 0, 0, respectively. It could be useful to treat such early dark energy models as a separate class, and include constraint on the dark energy density Ω_e at recombination (which can best be done through growth probes) as another desideratum for a dark energy science program.

4.6 Conclusions

Having investigated a diverse group of dark energy models to explain the acceleration of the cosmic expansion, we find a homogeneous "stretch" relation that calibrates the time variation behavior into tight families. This stretch factor is closely related to the standard time variation measure w_a, and we verify that the equation of state form $w(a) = w_0 + w_a(1-a)$, with w_a now treated as a fit parameter to observables, delivers fractional accuracy at the 10^{-3} level.

Such accuracy is sufficient for next generation data and the w_0-w_a form can be viewed as an appropriate compression of the expansion history information that can be extracted from such observations. That is, this form neither overcompresses (loses important information) nor undercompresses (lacks additional leverage). This indicates there is no need nor generic benefit for going to a third parameter. Note that [23] saw similar compression and tight relations within a principal component analysis relying on many modes.

To gain insight into the nature of dark energy, particular combinations of w_0-w_a may have enhanced leverage and hence merit, separating the cosmological constant from the thawing class, each from the freezing class, and possibly zeroing in on specific models within a class. The calibration, and its robustness and accuracy in accounting for the observable relations, offers a well-defined method for assessing the next generation dark energy science program. Interpretation of those observations should offer promising insights into the physics of the accelerating universe.

Chapter 5

To Bin or Not To Bin: Decorrelating the Cosmic Equation of State

A version of this chapter was previously published in *Astroparticle Physics* [65].

5.1 Introduction

Understanding the nature of the dark energy responsible for the acceleration relies on careful, robust measurements of the dark energy properties, in particular its equation of state (EOS), or pressure to energy density, ratio that directly enters the Friedmann equation for cosmic acceleration. As scientists design the next generation of dark energy experiments they seek to optimize the measurements for the clearest insight into this unknown physics.

Two critical pieces of information will be the value of the EOS at some epoch, such as the present, and a measure of its time variation, in much the way that early universe inflation theories are classified by the value of the spectral index and its running. The best parametrized EOS are physics based and model independent, i.e. able to describe dark energy dynamics globally, or at least over a wide range of behaviors. Such EOS are very successful at fitting to data and projecting the results of future experiments, and can be robust to bias against inexact parametrization.

Other approaches seek to remove one drawback of parametrized EOS by not assuming a functional form for the time variation, lest the true dark energy model lie outside the apparently wide range of validity of the form, i.e. they aim for form independence. Two major avenues for achieving this are decomposition into basis functions or principal components (e.g. [122], also see [58, 207, 209, 70, 216, 121]) and individual values of the EOS $w(z)$ over finite redshift bins, which become more general as the number of elements increases. However uncertainties in estimation of the

EOS properties also grow as the number of principal components or bins increases.

This chapter begins by examining general properties of the cosmological data and its dependence on the EOS in §5.2. Many of the later, detailed results will already be foreshadowed by this straightforward and general analysis. In §5.3 we examine principal component analysis of the EOS and in §5.4 uncorrelated bandpowers. Bins of EOS in redshift is investigated in §5.5, including figures of merit for quantifying the uncertainties. Further concentration on the crucial role of the high redshift EOS, and the risk of biasing parameter estimation, occurs in §5.6. We consider physical constraints on EOS properties in §5.7 and summarize our results and conclude in §5.8.

5.2 Cosmological Information and the Equation of State

Cosmological observations probe the EOS through its influence on the cosmic expansion history and the growth history of massive structures. The relation involves in general an integral (or double integral) over the EOS. This implies that the kernel, or response of the observables to the EOS, is broad in redshift, not tightly localized. For distances, the EOS at one redshift formally influences distances at all higher redshifts, while for growth variables that EOS value influences all lower redshifts; this implies a certain skewness. After setting up the simulated observations, we demonstrate that cosmological information is difficult to simultaneously localize and decorrelate, as well as highlighting some necessary cautions regarding treatment of data and priors.

5.2.1 Cosmological Variables

Information inherent in measurements of cosmological quantities regarding the EOS and other parameters can be estimated through the Fisher information matrix,

$$F_{ij} = \sum_{k,k'} \frac{\partial O_k}{\partial p_i}\, COV^{-1}[O_k, O_{k'}]\, \frac{\partial O_{k'}}{\partial p_j}, \tag{5.1}$$

where $\partial O_k/\partial p_i$ gives the sensitivity of observable O_k to parameter p_i, and COV gives the measurement covariance matrix. One often takes the measurement errors to be diagonal, $COV \to \sigma_k^2\,\delta_{kk'}$. Alternately one could use another likelihood estimator such as a Monte Carlo Markov Chain; the general results will not change. Each observable depends on the EOS and other parameters such as the present matter density relative to the critical density, Ω_m.

For the EOS, we begin by dividing the redshift interval $(0, z_{\rm max})$ into N bins of not necessarily equal widths Δz_i $(i = 1, \ldots N)$, where $\sum_i \Delta z_i = z_{\rm max}$. The index i is

taken to increase with z. The equation of state is written as

$$w(z) - w_b(z) = \alpha_i \, e_i(z) \tag{5.2}$$

(repeated indices are to be summed over), where $e_i(z) = 1$ inside the ith bin and zero outside. Such a binning is general, and serves as the first step for investigation of principal components (§5.3), decorrelated bandpowers (§5.4), or straight binning (§5.5).

The N coefficients α_i are the parameters describing the EOS in this model. Note that these coefficients measure the equation of state relative to some "baseline" equation of state $w_b(z)$. We can choose w_b to be some model, like the cosmological constant Λ ($w_b = -1$), to which we want to compare the data. We address issues of the baseline EOS and binning variable in §5.3. For convenience we sometimes write $e_i(z)$ as $\mathbf{e_i}$, and α_i, in the case where $\mathbf{e_i}$ is a unit box function, as w_i.

For cosmological observables, we focus here on various distances, including as measured by Type Ia supernovae (SN), by the cosmic microwave background (CMB) acoustic peaks, and by baryon acoustic oscillation (BAO) patterns in large scale structure. For all these the EOS enters through the Hubble parameter

$$H(z)/H_0 = \left[\Omega_m \, (1+z)^3 + \Omega_{\rm DE} \, f(z)\right]^{1/2}, \tag{5.3}$$

where the present dark energy density $\Omega_{\rm DE} = 1 - \Omega_m$ for a spatially flat universe as assumed here. The function $f(z)$ is the ratio of the dark energy density at redshift z to its current energy density. When z lies in the jth EOS bin,

$$f(z) = \left(\frac{1+z}{1+z_j}\right)^{3(1+w_j)} \prod_{i=1}^{j-1} \left(\frac{1+z_{i+1}}{1+z_i}\right)^{3(1+w_i)}, \tag{5.4}$$

where z_i is the lower redshift bound of the ith bin (note $z_1 = 0$) and w_i the fiducial value of the EOS in that bin.

The SN luminosity distance data set extends from redshift zero to $z_{\rm max} = 1.7$, with a distribution and systematic errors as given for the future SNAP mission in [133]. CMB data is treated as a 0.7% constraint on the reduced distance to last scattering, $d_{\rm lss} = (\Omega_m h^2)^{1/2} \int_0^{1089} dz/H(z)$, as should be available from the Planck mission. In addition to the N EOS bins between $z = 0 - z_{\rm max}$, we define a single bin for redshifts $z > z_{\rm max}$ having averaged, hence constant, EOS w_{N+1}. Note that freely marginalizing over w_{N+1} when only one data point depends on this parameter is equivalent to not including the parameter and the data point. We consider BAO in §5.6. Thus the Fisher matrix has dimensions $(N+3) \times (N+3)$, with Ω_m (or equivalently $\Omega_{\rm DE}$) and the parameter $\mathcal{M}$ giving the combination of SN absolute magnitude and Hubble constant in addition to the $N+1$ EOS values w_i. Unless otherwise stated, results shown marginalize over Ω_m and $\mathcal{M}$.

5.2.2 Information Localization

Ideally, binned EOS would reflect an invariant measure of the information (or conversely, uncertainty) at its particular redshift. Such a mapping between information and local variables, or bandpowers, works well for large scale structure (LSS), even into nonlinear scales, and we follow the approach of [99] but apply it to the EOS. To refine the localization of information one can attempt to use a large number of bins. We initially consider $N = 100$ EOS bins equally spaced in redshift.

Figure 5.1 plots five rows of the Fisher information matrix as a representation of the information as a function of redshift. An element $F(z, z')$ denotes the Fisher matrix entry F_{ij} with respect to parameters $p_i = w(z_i = z)$ and $p_j = w(z_j = z')$. Note that in contrast to the LSS case (see, e.g., Fig. 1 of [99]), the information is far from localized (the peaks are broad), is not "faithful" (the peaks do not generally peak at $z = z'$, especially for large z), and is skew (the matrix rows are not symmetric about the peaks). In the LSS case, the peaks were sharp and on the matrix diagonal, with amplitudes some two order of magnitude above the broader "continuum". For the EOS case the kernels are broad without well defined peaks, and the above properties indicate the matrix is far from diagonal.

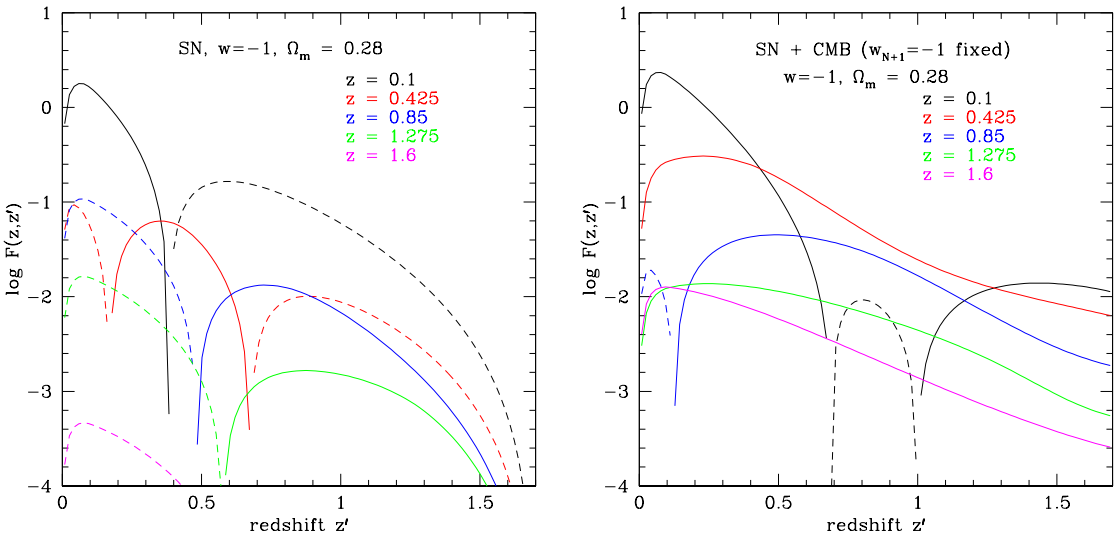

Figure 5.1: Five rows (or columns, **F** is symmetric) of the Fisher matrix calculated using a uniform binning in redshift z ($N = 100$ bins), showing the cosmological information as a function of redshift. Dashed lines show where F_{ij} is negative. The first panel uses only supernova data, the second panel includes the distance to CMB last scattering $d_{\rm lss}$, with the equation of state for $z = 1.7 - 1089$ fixed to the fiducial value $w_{N+1} = -1$. The curves of information are far from sharp spikes at $z = z'$, indicating the cosmological information is difficult to localize and decorrelate.

Further difficulties arise with respect to localization or characterization of information for the EOS case when considering priors or additional data, and changes in binning or variables. Suppose we add CMB data[1]. As shown in the second panel of Fig. 5.1, this has three effects: it increases the overall amplitude of the Fisher matrix $\mathbf{F}$, broadens the peaks of the rows, and shifts the peaks to lower z, decreasing their "faithfulness" (moving the peaks further away from where they would be in the diagonal case). The first effect is easy to understand. We add information so $\mathbf{F}$ becomes larger and uncertainties decrease. The second and third effects can be summarized by saying that $\mathbf{F}$ is made less diagonal. This is understandable too. The CMB information in $d_{\rm lss}$ has about the same dependence on all low z EOS parameters and thus adds to their correlation. To check this, Fig. 5.2 shows the resulting Fisher information when an extremely tight prior is put on CMB data, or the matter density Ω_m is fixed. Localization and faithfulness are almost completely lost (the EOS part of the Fisher matrix is far from diagonal).

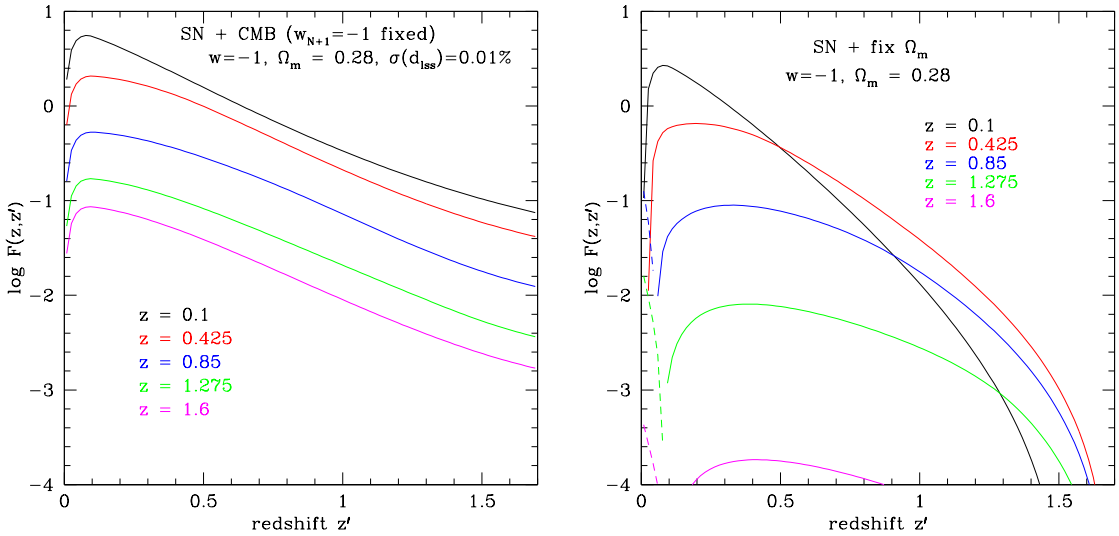

Figure 5.2: As Fig. 5.1, but with a very tight prior on the CMB information $d_{\rm lss}$ (first panel) or fixing the matter density Ω_m (second panel).

Information within a localized region is also not invariant when considering changes in the number of bins or binning variable. Note that changing the binning variable from redshift z to scale factor $a = (1+z)^{-1}$ or e-fold factor $\ln a$ is equivalent to changing the bins to non-uniform widths in z. Figure 5.3 demonstrates the variations that

[1]We here simultaneously fix the value of the EOS in the one bin beyond the SN data, w_{N+1}. As mentioned, adding one data point and marginalizing over the one new parameter is equivalent to not including the data and new parameter, i.e. it gives the same Fisher matrix as in the SN only case.

occur in the standard deviation of the EOS parameters when considering a binning uniform in z vs. one uniform in a, as well as when changing the number of bins N. A key point is that while the Fisher matrix behaves in a simple fashion when bin spacing is changed (as shown in §5.3), the uncertainties σ_i – which are square roots of the diagonal elements of the *inverse* of the Fisher matrix – behave in a complicated manner.

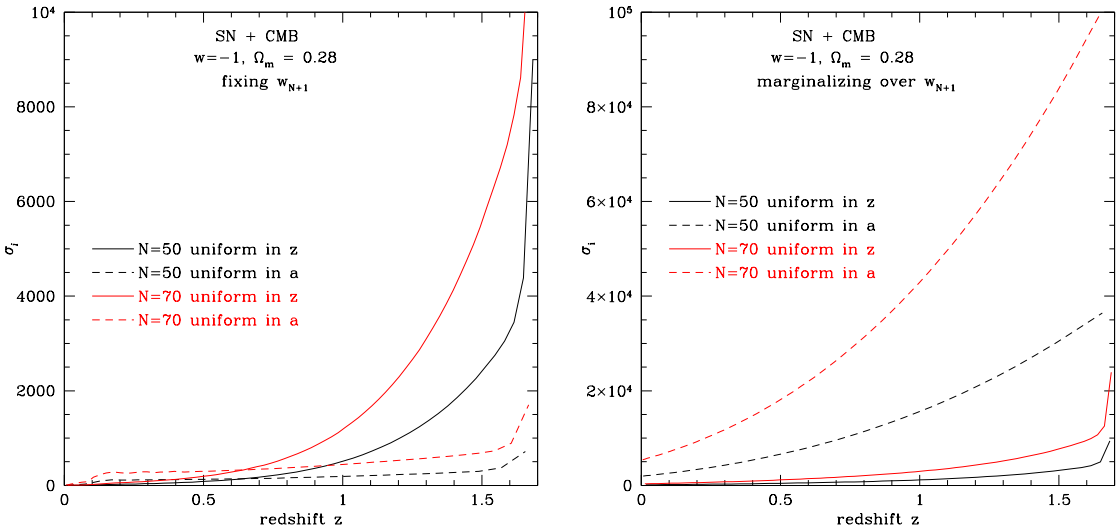

Figure 5.3: The standard deviation of the EOS in each bin for 50 and 70 bins uniformly spaced in redshift z or scale factor a. The first panel shows the case with fixed $w_{N+1} = -1$ and the second panel has w_{N+1} marginalized over. Note that the standard deviation depends on binning variable nontrivially and does not scale with number of bins N (i.e. the inverse of the bin width) as $N^{1/2}$.

First of all, when N is increased from 50 to 70, and so the bin width is correspondingly reduced for a given binning variable, the σ's do not simply scale by a factor $\sqrt{70/50}$ as one might have been tempted to think. Recall that N is the number of parameter bins not data bins. Thus a localized information quantity like $d\sigma^{-2}/dz$ does not have any real meaning, being dependent on the number of bins and the binning variable. Second, when considering a change in the binning variable, in the case where we marginalize over w_{N+1} (here equivalent to using only SN data), a binning uniform in a gives larger σ's across all redshifts when compared to the binning uniform in z, even if we use the same total number of bins in both cases. This is counterintuitive since at low redshift the bins uniform in a are smaller, and at high redshift they are larger than the uniform z bins so we would expect the EOS uncertainties to be relatively larger, then smaller, respectively. This indeed occurs when we fix w_{N+1}.

Exploring this behavior, we find that changes in the present dark energy density overwhelm the EOS parameters. For the higher redshift bins of EOS, the Fisher information is only contributed by the relatively few high redshift data points, and there the Fisher sensitivity to Ω_m can be more than an order of magnitude greater than to w_i. Computations show that only when Ω_m is fixed or restricted to a degeneracy surface by the CMB $d_{\rm lss}$ constraint does the natural behavior of the EOS bin parameters with changes in binning become manifest. We conclude that changes of binning variables, or equivalently non-uniform bin widths, affect EOS uncertainties in a nontrivial manner, and the treatment of the high redshift EOS needs care as well.

5.2.3 Extracting the Equation of State

The key lesson of this section has been that there is no well-defined measure for localized information on the EOS. Unlike for the LSS power spectrum, the cosmological EOS information has a very broad kernel and the Fisher matrix is far from diagonal. While one can always adopt a basis to transform the Fisher matrix to diagonal form, we will see that this does not help with localization and so the results cannot be interpreted as actual EOS values at a certain redshift. Another issue is the problem of defining a measure of uncertainty in the EOS estimation that does not depend on the specific binning chosen.

This general analysis foreshadows the problem of actually deciding how to quantify measurement of the EOS and any figure of merit to go along with that. In the following sections we investigate three concrete proposals for the meaning behind EOS measurement. One approach is principal component analysis (PCA; see, e.g. [122, 113, 142, 127, 168]), effectively making the number of bins very large, diagonalizing the Fisher matrix and using its eigenvectors as a basis $e_i(z)$ in Eq. (5.2). A second approach is uncorrelated bandpowers, using a small number of bins, diagonalizing and scaling the Fisher matrix in an attempt to localize the decorrelated EOS parameters (see, e.g., [120, 186, 217]). Finally, one can exactly localize the EOS parameters using a few bins, at the price of retaining correlations in their uncertainties. Advantages for a method will come from giving robust insight into the physical nature of dark energy.

5.3 Principal Components

It is important to recognize that PCA the way it is normally applied in astrophysics, e.g. to spectra, is very different from the qualities desired in measuring the EOS. In conventional PCA one wants to maximize the variance, essentially the signal, while for the application of PCA to cosmological parameter estimation ([122, 113, 142, 127, 168]) one wants to minimize the variance because it represents the observational uncertainty. In the former case, using a basis of eigenvectors (or

eigenmodes) is very useful because it extracts the specific linear combinations of parameters that have the most signal. In the latter case, at least when applied to the dark energy EOS where we want the small variations of data to be revelatory, i.e. arise from very different EOS and so point to the physics, we will see that it is less obvious what the quantitative advantages of PCA are beyond decorrelating the parameter uncertainties. (PCA is still useful in obtaining impressions of sensitivity, i.e. what qualities of the data are best constrained.) For example, for CMB analysis one still prefers to work with quantities having clear physical interpretations rather than principal components, despite the decorrelation [79].

To decorrelate the EOS characteristics, one diagonalizes the Fisher (or inverse covariance) matrix by applying a basis transformation to a basis of eigenmodes. In this new basis $\mathbf{e'_i}$,

$$w(z) - w_b(z) = \alpha'_i \, e'_i(z), \tag{5.5}$$

such that the uncertainties in the new parameters α'_i are uncorrelated. It is important to note that in general the basis vectors, or modes, tell us how to interpret the uncertainties in the parameters α'_i in terms of their effect on the equation of state function $w(z)$ through

$$e'_i(z) = \frac{\partial w(z)}{\partial \alpha'_i}. \tag{5.6}$$

We discuss various important mathematical properties regarding modes in Appendix B; here we summarize the most relevant characteristics and results.

- There are an infinite number of bases that decorrelate the coefficients α'_i
- Because the Fisher matrix transforms nontrivially under change of basis, the eigenvectors are not invariant. They are not equivalent between different binning variables or bin widths.
- Each eigenvector has arbitrary normalization and so the meaning of uncertainty in measuring a mode is not well defined.

5.3.1 Eigenmodes

Despite the first point in the list above, we can of course choose a particular basis and work from there. We proceed to do this and illustrate the second and third points. Starting with the unit box basis $\mathbf{e_i}$ introduced in §5.2 we calculate the eigenmodes (but remember that this set depends on this particular starting point). The fiducial model is ΛCDM: $w = -1$ with $\Omega_m = 0.28$ and we consider initial binnings uniform in z, a and $\ln(1+z)$.

Figure 5.4 illustrates the first four modes, after marginalization over Ω_m and $\mathcal{M}$. For convenience we suppress the primes indicating the new basis. The first panel has the EOS at $z > 1.7$ fixed to its fiducial value, $w_{N+1} = -1$; in the second panel, w_{N+1}

is treated as a free parameter and marginalized over. For each binning variable or coordinate $x = z$, a, or $\ln(1+z)$, we normalize the modes according to $\int dx\, e_i^2(x) = 1$. Although completely arbitrary, this choice is common.

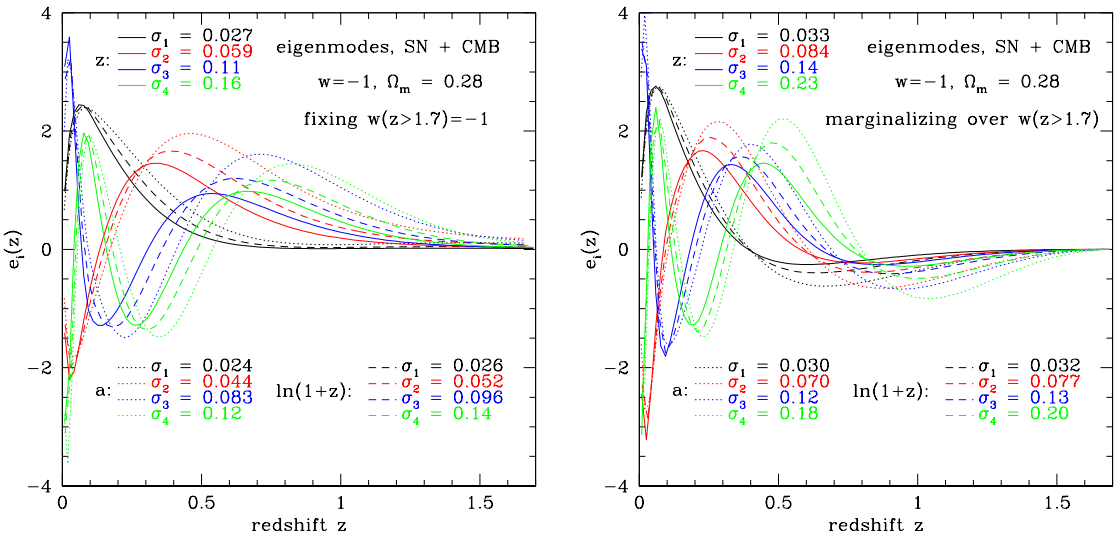

Figure 5.4: The first four eigenmodes and their uncertainties calculated using uniform binning in z, a and $\ln(1+z)$. In the first panel w_{N+1} is fixed, in the second panel it is marginalized over. For a and $\ln(1+z)$, the number of EOS bins $N = 50$, for z we use $N = 100$, enough for the modes to converge. Note the modes, and their uncertainties, depend on binning variable (even modulo normalization).

Note that, as discussed above, the modes (and their respective standard deviations) are different for the different coordinates, even modulo normalization. As the coordinate changes from z to $\ln(1+z)$ to a the modes spread out more, gaining more power at large z as expected from the relative bin widths. The difference between a binning uniform in a coordinate x and one uniform in z depends on the coordinate transformation dx/dz over the relevant redshift range. Since $da/dz = -1/(1+z)^2$, $d\ln(1+z)/dz = 1/(1+z)$, and $dz/dz = 1$, this explains the progression.

Also, comparing the modes with w_{N+1} fixed to those where it is fit from the data shows two things. The uncertainties $\sigma_i \equiv \sigma(\alpha_i)$ are smaller of course. Second, and perhaps less obvious a priori, the modes are more confined to low redshifts when w_{N+1} is made a free parameter. This becomes easier to understand when we remember that marginalizing over w_{N+1} is equivalent to not using $d_{\rm lss}$ at all. Thus only when w_{N+1} is fixed does the inclusion of CMB $d_{\rm lss}$ data count, and this spreads the eigenmodes out towards higher z.

5.3.2 Number of Eigenmodes and their Uncertainties

The eigenmode approach becomes completely general in the limit of an infinite number of bins, $N \to \infty$, as all continuous functions can be constructed from the complete basis. The downside of this is that the uncertainties approach infinity. One compromises by selecting a small set of the best determined modes, i.e. the principal components, and throwing away the others. We face two problems when we try to adopt this approach. The first is the question which set of eigenmodes to begin with (i.e. calculated using which coordinate). The second problem is that "best determined" is not well defined. We elaborate on this below.

As we have demonstrated, calculating the eigenmodes in a different coordinate yields a different set of modes so it is not clear which basis of eigenmodes to choose. Although each *full* basis spans the same space of functions, restricting oneself to the first few eigenmodes with respect to z gives an essentially different parametrization than using the first few modes with respect to a or any other coordinate that is not a linear function of z. The uncertainties will be different and there is the risk that how good one experiment is compared to another will be judged differently.

Even if we have chosen a certain basis, say the eigenmodes arising from uniform binning in the coordinate z, there is still the issue of quantifying how well determined a mode is. That is, we would like to calculate a measure for how constrained a mode $\mathbf{e}_i$ is. (Again, we suppress the primes as we will always be interested in the new basis.) An obvious choice seems to be the standard deviation of its coefficient, $\sigma_i \equiv \sigma(\alpha_i)$. However, if we rescale $\mathbf{e}_i$ by a factor A, σ_i is rescaled by A^{-1}. Thus, σ_i only has meaning if we also specify the normalization of the mode, and the normalization is arbitrary, we have no physics guidance in choosing one normalization over another. In fact, it is perfectly legitimate to rescale all modes such that their (coefficients') uncertainties σ_i are equal to one. Yes, this way it appears many modes have very large fluctuations, but without putting in any physical constraints on $w(z)$, i.e. a priori restrictions on the EOS, the word large is meaningless.

Another approach to measuring how well determined a mode is involves using not a pure uncertainty criterion but a signal to noise criterion. This was the approach advocated by [156] but is also problematic. Consider the ratio of the standard deviation σ_i over the coefficient α_i. At first sight, this seems to solve the problem of normalization as σ_i/α_i is invariant under changes of normalization. However, this approach has its own problems. From the mode expansion

$$w(z) - w_b(z) = \alpha_i \, e_i(z) \tag{5.7}$$

we see that the expectation values of the α_i's depend on which baseline function $w_b(z)$ we expand our measured EOS with respect to. For example, if we use $w_b = -1$ and the true EOS (or simulated EOS if projecting the leverage of a future survey) is also $w = -1$, then the expectation values of the α_i's are all zero. Thus the noise-to-signal σ_i/α_i blows up.

The reason why the quantities σ_i and σ_i/α_i suggested above do not work as measures for how well (or how poorly) determined a mode is, is simple. We have an estimate of the *noise* in the uncorrelated parameters α_i, but not of the typical *signal* and thus cannot define a proper signal to noise ratio to tell us which modes are well-constrained and which ones are not. It may be tempting to simply throw out modes with large uncertainties, say $\sigma_i > 1$, but then we are implicitly making the assumption that the coefficients α_i are typically of order 1 in the particular normalization – and baseline model – one has chosen for the modes. We have little knowledge on which to base such an assumption.

The method *would* be useful if in addition to knowing the observational uncertainties σ_i, we knew the typical ranges of the α_i's. For example, if we knew the expectation values $\langle\alpha_i\rangle$ and the typical deviations from their expectation values $\sqrt{\langle(\alpha_i - \langle\alpha_i\rangle)^2\rangle}$ (brackets here denote averages over realizations of the parameters, they have nothing to do with observational uncertainties, given by σ_i), we can call α_i (and the corresponding mode) well-constrained if the signal to noise ratio

$$\mathrm{SNR} \equiv \frac{\sqrt{\langle(\alpha_i - \langle\alpha_i\rangle)^2\rangle}}{\sigma_i} \tag{5.8}$$

is large.

There are two scenarios in which one has knowledge about quantities like $\langle\alpha_i\rangle$ and $\sqrt{\langle(\alpha_i - \langle\alpha_i\rangle)^2\rangle}$, both quite common in physics. One is when one can observe a (large) sample of realizations of the parameters. If for example the function of interest is a source spectrum (e.g. of quasars or supernovae [219, 59]), the sample size is equal to the number of observed sources. Unfortunately, we can only observe one universe and thus only one equation of state. The other scenario is where one knows what the underlying physics is and what natural values are for the parameters of the theory (e.g. for the ionization fraction see [168]). For example, if we knew dark energy was described by a scalar field model described by a set of n parameters and in addition we had a prior probability distribution on those parameters, we could propagate this distribution to the parameters α_i. Again unfortunately, we have a large number of possible theories for dark energy and little guidance as to the parameter values within those theories. We return to the question of placing physical constraints on the EOS and its modes in §5.7.

In conclusion, it is always possible to select a subset of modes and work with those, but it should be realized that what one is doing at that point is putting in assumptions of what the equation of state should look like – precisely what we were trying to avoid by switching to PCA from a functional form – and one cannot call the approach truly form independent anymore.

5.4 Uncorrelated Bandpowers

While using a large number of bins for the EOS increases the generality of functional forms $w(z)$, one ends up with a large number of poorly determined parameters. Instead one could use a small number of bins but perform a basis transformation to decorrelate the parameters. In large scale structure and CMB applications in cosmology this is often called uncorrelated bandpowers, e.g. where the functions are the matter power spectrum binned in wavenumber, $P(k)$, or the photon power spectrum binned in multipole, $C(\ell)$.

To increase the localization of the modes within the bins, or bands, [99] proposed letting the "square root" of the Fisher matrix define the transformation. See [120] for application specifically to the EOS. Such a transform has the advantage that, in the ideal case, the weights defining the new parameters in terms of the old ones are localized and mostly positive. This would make the new parameters easier to interpret, as true bandpowers, i.e. giving the values of the EOS in a given redshift interval, with uncertainties uncorrelated between bins. Unfortunately we will find that, as presaged in §5.2, the cosmological EOS analysis is far from the ideal case due to the broadness and skewness of the kernel, in contrast to the LSS case.

5.4.1 Modes and Weights

We briefly present the procedure for finding the square root of the Fisher matrix and the corresponding transformation. This is placed in the main text because it highlights the important distinction between the properties of the eigenvectors and the weights, which has not always been clear in the literature.

The transformation of interest is given by the symmetric matrix $\mathbf{W}$ (see Appendix B for our conventions) that transforms the Fisher matrix into the identity matrix:

$$\mathbf{W}\,\mathbf{F}\,\mathbf{W}^{\mathrm{T}} = \mathbf{1}. \tag{5.9}$$

This matrix is constructed using the matrix $\mathbf{O}$ of which the rows are the (normalized) eigenvectors of $\mathbf{F}$, i.e. the orthogonal ($\mathbf{O}^{\mathrm{T}} = \mathbf{O^{-1}}$) matrix that diagonalizes the Fisher matrix

$$\mathbf{O}\,\mathbf{F}\,\mathbf{O}^{\mathrm{T}} = \mathbf{D}. \tag{5.10}$$

$\mathbf{W}$ is now given by

$$\mathbf{W} = \mathbf{O}^{\mathrm{T}}\,\mathbf{D^{-1/2}}\,\mathbf{O}, \tag{5.11}$$

note that the square root of the Fisher matrix $\mathbf{F^{1/2}} \equiv \mathbf{W^{-1}}$ is also symmetric and it squares to the Fisher matrix (hence the name).

The new basis vectors $\mathbf{e_i'}$ are now given by the rows of $\mathbf{W}$ (see Appendix B) and their coefficients α_i' are

$$\alpha_i' = W_{ji}^{-1}\alpha_j. \tag{5.12}$$

We follow [120] and rescale the basis vectors and thus $\mathbf{W}$ such that the α'_i are weighted averages of the α_i, i.e. we rescale the rows of $\mathbf{W}$ such that

$$\sum_{j=1}^{N} W_{ji}^{-1} = 1. \tag{5.13}$$

For notational convenience we use the same name for the rescaled transformation matrix $\mathbf{W}$ as for the original one, but note that after the rescaling $\mathbf{W}$ is no longer symmetric. The α'_i are now uncorrelated and their uncertainties are given by

$$\sigma'_i = \left(\sum_{j=1}^{N} F_{ji}^{1/2} \right)^{-1}. \tag{5.14}$$

In summary, the rows of $\mathbf{W}$ contain the new basis vectors e'_i and the rows of $(\mathbf{W^{-1}})^{\mathrm{T}}$ contain the weights.

An important point is that even though the weights tell us how to construct the new parameters out of the old ones, as discussed in §5.3, to interpret the meaning of the uncertainties σ'_i for the EOS one needs to look at the basis vectors $e'_i(z) = \partial w(z)/\partial \alpha'_i$ and not at the weights. That is,

$$\sigma^2[w(z)] = \sum_i \sigma'^2_i e'^2_i(z). \tag{5.15}$$

We emphasize that plots of the weights alone cannot be directly interpreted as values of the EOS. To some extent this confusion has been exacerbated by sometimes writing the weights as $\mathcal{W}_i$ – these are *not* the EOS w_i. The distinction between vectors and weights exists because the uncorrelated bandpowers correspond to a non-orthogonal transformation (the only orthogonal transformation decorrelating the parameters is the one to a basis of eigenvectors, as already considered). This distinction will be important to the question of localization and physical interpretation of the parameters. As illustrated in the next section, one can have weights that are all positive while the corresponding basis vectors have significant negative contributions, clouding the interpretation.

5.4.2 Decorrelated Estimates of the Equation of State

Since the matrix of weights is defined as the square root of the Fisher matrix (up to a rescaling to make the weights sum to one), the positivity and localization of the weights depends on how positive and localized the Fisher matrix itself is. The idea of the square root scaling is that the square root is typically narrower, so the weights gain some localization relative to the Fisher matrix. However, we saw in §5.2 that even next generation data probing the EOS involves a very nondiagonal Fisher

matrix. This is inherent to the cosmological properties and degeneracies and does not arise from any particular binning or parametrization.

We now calculate the modes described in the previous section. To facilitate comparison to the literature, specifically [120], we choose four low redshift bins with the following ranges: $z = 0 - 0.2$, $z = 0.2 - 0.4$, $z = 0.4 - 0.6$ and $z = 0.6 - 1.7$. The bins define four EOS parameters w_1 to w_4. The other cosmological parameters, fiducial values, and data sets are as before. The Fisher matrix for the low z EOS parameters in the case where $w_5 \equiv w(z > 1.7)$ is fixed is given by

$$\mathbf{F}_{\rm fix5} = \begin{pmatrix} 205 & 84 & 17 & 5.8 \\ 84 & 65 & 27 & 19 \\ 17 & 27 & 21 & 21 \\ 5.8 & 19 & 21 & 35 \end{pmatrix} \tag{5.16}$$

and when w_5 is marginalized over,

$$\mathbf{F}_{\rm marg5} = \begin{pmatrix} 146 & 33 & -14 & -33 \\ 33 & 22 & 0.66 & -13 \\ -14 & 0.66 & 4.4 & 0.93 \\ -33 & -13 & 0.93 & 10 \end{pmatrix} \tag{5.17}$$

It is evident that the Fisher matrix is far from diagonal and furthermore that proper treatment of the high redshift EOS behavior, rather than assuming a fixed value for w_{N+1} (here w_5), has a significant effect. For one thing, marginalizing over w_5 introduces negative entries in the Fisher matrix and we will see this causes some of the weights in the decorrelated basis to be negative.

The main results of this section are illustrated in Figs. 5.5 and 5.6, giving the uncorrelated modes and the corresponding weights. First consider Fig. 5.5 where w_{N+1} is fixed. Previous results (e.g. [120, 186]) showed weights that were almost always positive and strongly localized, i.e. the weights defining the ith parameter were predominantly peaked in the ith bin. This implies that the Fisher matrix of the original parameters, including priors, must have been close to diagonal to begin with in those cases. In Fig. 5.5 the weights are indeed essentially all positive and substantially localized (slightly less than in the works referred to above but differences in the fiducial model and data could account for this.)

While the characteristics of the weights in the case where w_{N+1} is fixed look promising, recall that it is the eigenvectors that tell us how to interpret the results in terms of the EOS (see Eqs. 5.6 and 5.15). Each (uncorrelated) uncertainty $\sigma_i = \sigma(\alpha_i)$ derived from the data corresponds to a variation in the EOS behavior $w(z)$ of the form of the eigenfunction $e_i(z)$. We see that the basis functions have quite different shapes than the weights; in particular they have large negative contributions and large oscillations, far from being localized. For example, if α_1 is 1σ larger than its fiducial (and the other coefficients are exactly equal to their fiducial values), the EOS in the

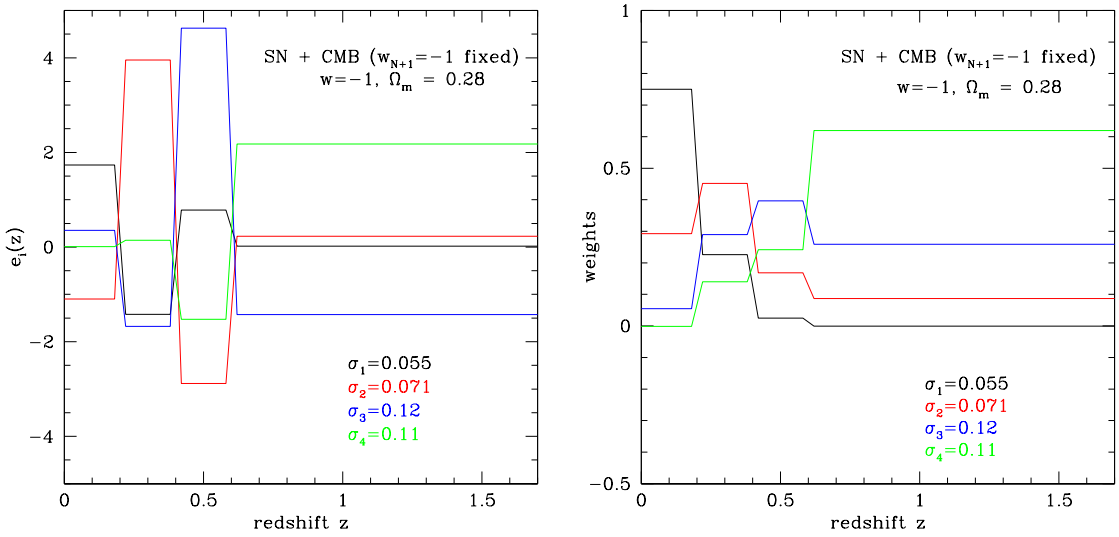

Figure 5.5: Uncorrelated basis functions, or modes, (first panel) and weights (second panel) obtained from the square root of the Fisher matrix. Here $w_5 \equiv w(z > 1.7)$ is fixed to its fiducial value ($w_5 = -1$). Note that the modes have quite different shapes than the plots of the weights; the modes are what gives the impact on EOS $w(z)$ of an uncertainty σ_i. The weights are only moderately localized (a consequence of the cosmological properties of the original Fisher matrix).

first bin, w_1, deviates by $+1.75 \times 0.055$ from its fiducial value -1, while the EOS in the second bin, w_2, deviates almost as strongly but *negatively* by -1.45×0.055 from -1.

For a deviation in the third coefficient, α_3, by 1σ, the consequences are even more dramatic: a bump in w_3 by $+4.7 \times 0.12$ and a dip in w_2 by -1.7×0.12. Note that while the α_i are decorrelated, the impact on the EOS is not localized, so the values of w_i remain correlated. Such information is hard to get from just looking at the apparently well-behaved weights (which are often the only quantities plotted).

Much of the good behavior of the weights is an artefact of fixing the high redshift behavior of the EOS, i.e. imposing a form (in a supposedly form independent approach). When we instead allow freedom in w_{N+1} and marginalize over it, the effects are dramatic as seen in Fig. 5.6. This is not surprising given the differences in the respective Fisher matrices, Eqs. (5.16) and (5.17). Some of the weights now have considerably negative values and the modes are certainly not localized in the expected bin. Instead, all of them have substantial power in the highest redshift bin shown.

To verify that it is the strength of the prior information, and not the square root of the Fisher matrix scaling per se, that causes the weights in Fig. 5.5 (and the literature examples) to look so well behaved, we imposed ever tighter priors on Ω_m. When the

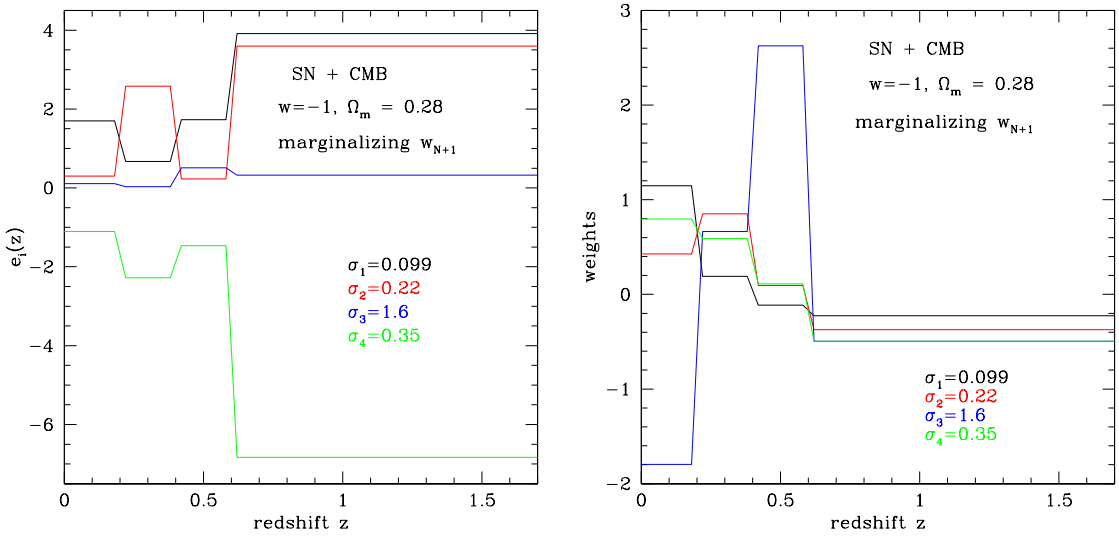

Figure 5.6: As Fig. 5.5, but with w_5 marginalized over. With w_5 as a free parameter, the weights and modes substantially lose their desired properties (being positive and localized).

prior is weak, the weights are both positive and negative. As the prior tightens, the weights become progressively more positive and localized. Figure 5.7 shows the limit as we fix Ω_m.

5.4.3 Continuum Limit

To ensure that the breakdown in positivity and locality of the weights is not an artefact of the binning, but rather is inherent to the cosmological data probing the EOS, we take the continuum limit, $N \gg 1$. Figures 5.8 and 5.9 plot the uncorrelated modes and weights corresponding to the square root of the Fisher matrix for $N = 100$. We see that even in this limit the modes fluctuate heavily and the weights are not very localized (which makes sense because they are given by the square root of the Fisher matrix depicted in Fig. 5.1) though they are more faithful, i.e. peak at the given redshift. Again, the physically appropriate act of marginalizing over w_{N+1} removes most vestiges of the desired positivity and locality.

The conclusion is that to obtain truly localized weights implies that one already started with a substantially localized (peaked, with a narrow kernel) inverse covariance matrix $\mathbf{F}$. In such a case the EOS parameters are already easy to interpret without decorrelating them. Conversely, having weights that do not become tightly localized (and we have shown they may not without a strong external prior) implies that the new basis parameters are hard to interpret – one might as well stick to the original correlated parameters. Thus, like PCA, using the square root of the Fisher

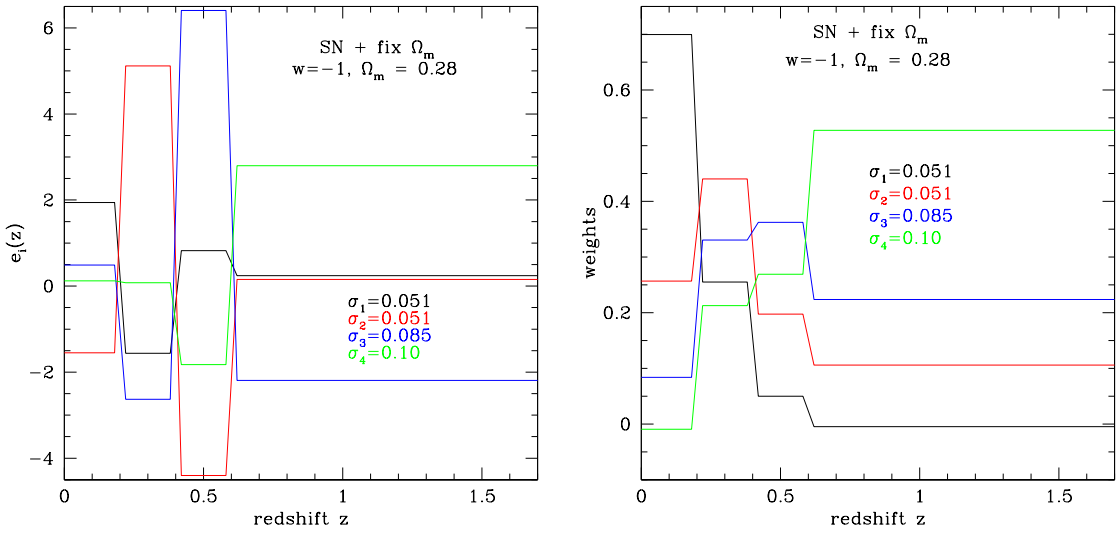

Figure 5.7: As Figs. 5.5 and 5.6, but instead of using the CMB data point (thus w_{N+1} does not enter) we fix the matter density Ω_m. This illustrates the effect of a tight prior.

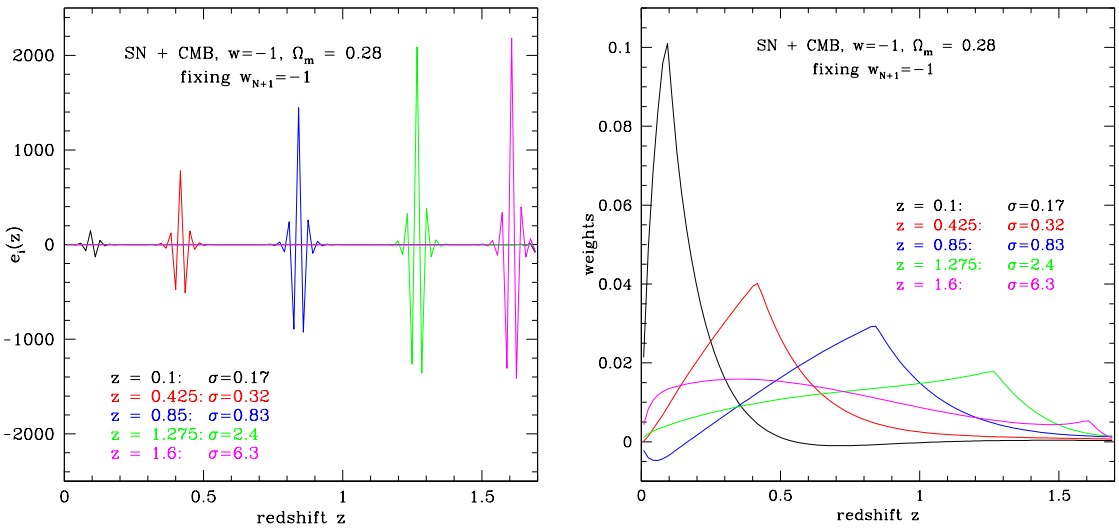

Figure 5.8: Illustration of what the modes (first panel) and weights (second panel) based on $\mathbf{F^{1/2}}$ look like in the large N case, here $N = 100$. Here we fix $w_{N+1} = -1$.

matrix in an attempt to obtain uncorrelated bandpowers is not a panacea in the quest for understanding dark energy.

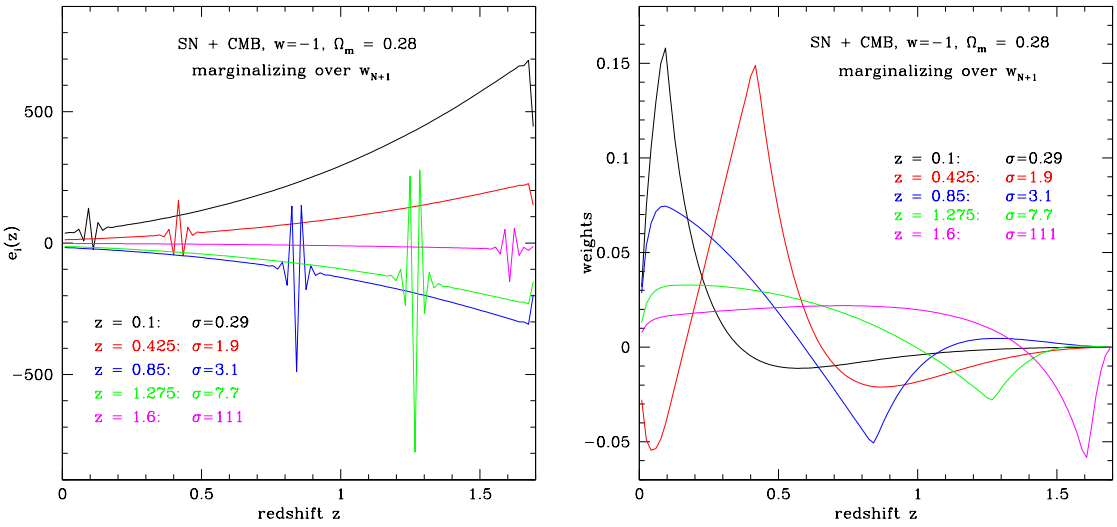

Figure 5.9: As Fig. 5.8, but marginalizing over w_{N+1}.

5.5 Binned Equation of State

The third approach to understanding the EOS is simply considering the values in a small number of redshift bins. That is, one defines piecewise constant EOS in some redshift range, e.g. $w(z) = w_i$ when $z_i < z < z_{i+1}$ (like in §5.4, but without decorrelating). This guarantees localization and straightforward physical interpretation, at the price of some correlation in the uncertainties. As we have seen, however, one cannot in practice generally have both localization and no correlation.

5.5.1 Uncertainties and Correlations

Calculation of the EOS estimation is straightforward. Here we concentrate on questions of sensitivity to changes in binning and to treatment of the high redshift bin, rather than specific numbers for the uncertainties. To see the trends most clearly, we consider only two bins below $z = 1.7$ along with the one at higher redshift.

The quantities of interest are the uncertainties σ_i on the EOS values (marginalizing over the other cosmological parameters), the correlation coefficients between EOS values,

$$r_{ij} = \frac{C_{ij}}{\sigma_i \sigma_j}\,, \tag{5.18}$$

and the global correlation coefficients [2]

$$r_i = \sqrt{1 - \frac{1}{C_{ii} F_{ii}}}\,, \tag{5.19}$$

which give the maximum correlation of w_i with a linear combination of all the other EOS bins. The covariance matrix $\mathbf{C}$ is the inverse of the Fisher matrix. The high redshift value w_3 can either be fixed to the fiducial value (see §5.6 for consequences of the true value being different than the fiducial assumed) or marginalized over.

Figures 5.10 and 5.11 illustrate several interesting points. Both the bin positions and the treatment of w_3 have a big impact on the uncertainties and correlations. Regarding the uncertainties, when w_3 is kept fixed, the effect of making the first bin larger is to decrease σ_1 (and increase σ_2). (The slight rise in σ_1 when the first bin gets very wide is due to covariance with the matter density and goes away with a tight Ω_m prior.) They are of comparable size when the boundary between the two bins lies around $z = 0.2$. Note that there is only a very narrow region where the two parameters are determined to better than 0.1, so there is virtually no possibility of determining three EOS parameters to better than 0.1 with realistic next generation SN+CMB data – and this is in the most optimistic case of fixing w_3.

The correlation between estimates of w_1 and w_2 (still fixing w_3) is not very strong, with minimum correlation at $z_{\rm div} \approx 0.5$.

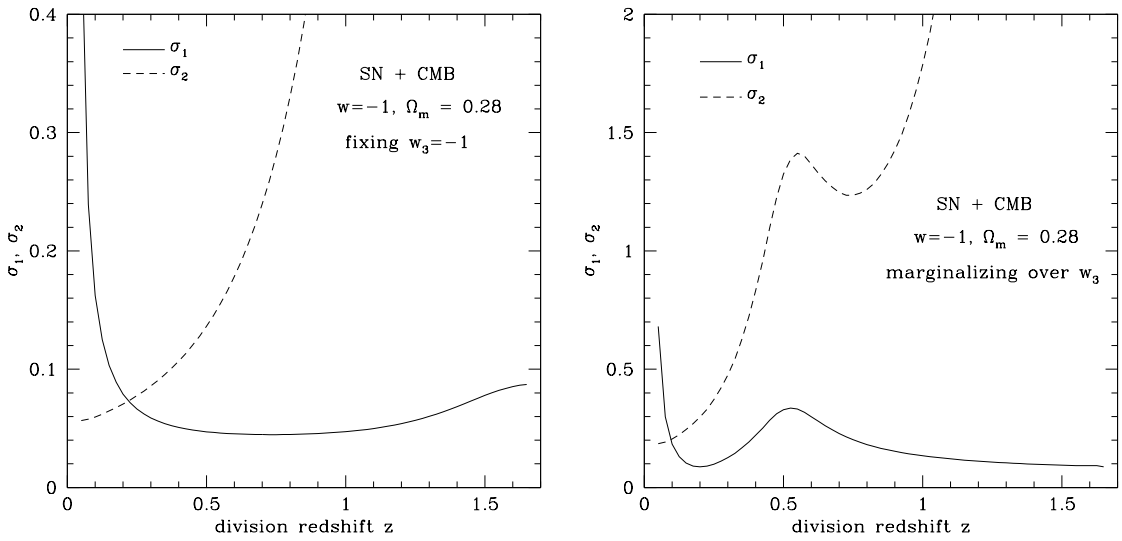

Figure 5.10: Uncertainties in the EOS values for two bins between $z = 0 - 1.7$ as a function of the redshift dividing the two bins. The first panel has fixed $w_{N+1} = -1$, the second panel has w_{N+1} marginalized over. Note the different scales.

When the high redshift behavior of the dark energy EOS, represented by w_3, is not fixed a priori (after all, we want to probe dark energy properties, not assume them), significant changes occur. Examination of the global correlation coefficient for w_3 shows this must happen: r_3 ranges between 0.97 and 1, i.e. the high redshift behavior is extremely highly correlated with the low redshift behavior. This immediately tells

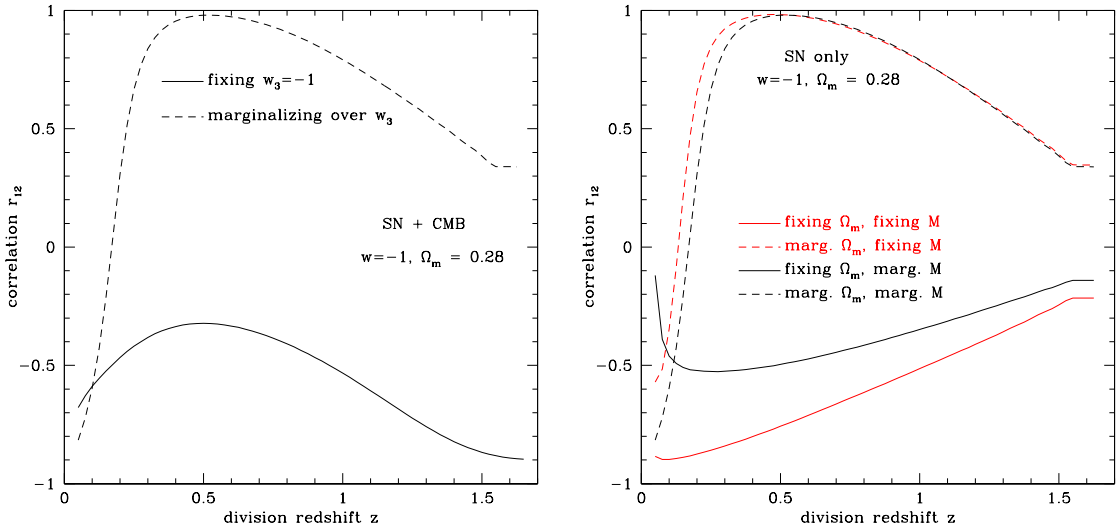

Figure 5.11: As Fig. 5.10 but showing the correlation coefficient $r_{12} = C_{12}/(\sigma_1\sigma_2)$ of the two $z < 1.7$ bins as a function of the division redshift. The first panel uses SN and CMB data and compares fixing and marginalizing over w_{N+1}. The second panel shows that a tight prior on Ω_m (without adding CMB data) has a similar effect on the correlations as adding CMB data and fixing w_{N+1}, i.e. one must be wary of priors dominating the behavior.

us it that it is dangerous to fix w_3 because if it is fixed to the wrong value, it can strongly affect the values derived for the other parameters (see §5.6).

Another consequence of the strong correlation r_3 is that including w_3 as a fit parameter makes the uncertainties in w_1 and w_2 increase, by factors up to 10. When the first bin is small ($z_{\rm div} = 0.1$), it is hardly correlated with w_3 and the change in its uncertainty is negligible, whereas σ_2 is increased by a factor of almost four. However, as the boundary redshift is moved up, the first bin grows more correlated with the third bin until at $z_{\rm div} = 0.5$ both w_1 and w_2 have quite strong correlations with each other and with w_3, e.g. $r_{13} = r_{23} = -0.99$, and both σ_1 and σ_2 degrade considerably due to w_3. The effect is so strong that the trend of σ_1 decreasing as the bin widens is broken: $\sigma_1 = 0.33$ for $z_{\rm div} = 0.5$ compared to $\sigma_1 = 0.09$ for $z_{\rm div} = 0.2$.

Interestingly, when marginalizing over w_3 there is a division redshift for which the estimations of the low redshift EOS values are uncorrelated, $z_{\rm div} \approx 0.18$. This decorrelation, or pivot, redshift arises without any need for using the square root of the Fisher matrix. But for a broad choice of $z_{\rm div}$ the correlation is near unity. The strong correlation goes away when fixing w_3, but this is an example of prior information rather than data determining our view of the dark energy properties, as we saw in §5.4.2. For example, in the second panel of Fig. 5.11, we recreate the same behavior of breaking the strong correlation r_{12} by fixing Ω_m. One must be cautious

that priors do not overwhelm the data, to see a true picture of dark energy.

5.5.2 Figures of Merit

In attempting to comprehend the nature of dark energy, some researchers advocate condensing the information down to a single figure of merit (FOM) related to the uncertainties in the parameter estimation. In §5.3 we saw some difficulties of defining this in a robust manner. Indeed, FOM's for binned EOS typically depend sensitively on both the binning adopted (which has nothing to do with the cosmology within the data) and, again, the treatment of the high redshift EOS. We now analyze some possible FOM's for binned equations of state.

Figure 5.12, first panel, plots the area (taking out a factor π) enclosed by the 1σ confidence level contour in the w_1-w_2 plane, as a function of the bin division redshift. This area is proportional to $(\det \mathbf{F})^{-1/2}$, which is invariant under any transformation $\mathbf{W}$ with $(\det \mathbf{W})^2 = 1$ (see Eq. B.4 or [123]), and in particular under any orthogonal transformation. When w_3 is fixed (first panel), the area is minimized at a division redshift of $z_{\rm div} \approx 0.25$. One might interpret this as saying that we obtain the most information (in the $N = 2$ case) with one bin from $z = 0 - 0.25$ and one from $z = 0.25 - 1.7$. When w_3 is marginalized over, the behavior changes somewhat but there is still a clear minimum, this time at slightly lower redshift $z_{\rm div} \approx 0.18$.

As more bins are added, individual bin parameters can become extremely uncertain and the volume $(\det \mathbf{F})^{-1/2}$ in the N-dimensional space of w_1-$\ldots$-w_N (see, e.g., [9]) will be dominated by these poorly determined parameters. In an attempt to "cut off" the highly uncertain parameters, a figure of merit like

$$\mathrm{FOM}_{\rm corr} \equiv \sum_i \sigma_i^{-2} \tag{5.20}$$

has been proposed (see e.g. [217]).

We first consider the σ_i in Eq. (5.20) as the uncertainties in the (correlated) bin parameters w_i. The behavior of this FOM as a function of division redshift in the two bin case is shown in Fig. 5.12, second panel (note that now a large value is good). Such a measure would advocate – for the same data – using $z_{\rm div} \approx 0.65$ when w_3 is fixed. In contrast, when w_3 is marginalized, this peak in the FOM becomes a strong dip, saying the experiment is weak. Comparing to Fig. 5.10, this FOM can give high marks to choices that lose almost all the information on the second parameter.

The FOM discussed above does not take into account correlations between parameters. As an alternative, we could use the uncertainties in the *decorrelated* weighted averages α_i' described in §5.4. It is actually this choice, or rather its inverse, that is advocated in [217]. To be consistent with our previous notation, we should now write

$$\mathrm{FOM}_{\rm decorr} \equiv \sum_i \sigma_i'^{-2} \tag{5.21}$$

(note that this is the trace of the decorrelated Fisher matrix $\mathbf{F}'$). This FOM has a very simple, but slightly disappointing interpretation:

$$\mathrm{FOM}_{\mathrm{decorr}} = \sigma(w)^{-2}, \tag{5.22}$$

i.e. the FOM is the inverse square uncertainty on a constant w, or equivalently when there is only one bin.[2]

We have confirmed numerically that, as it must be from the single bin interpretation, this trace FOM is independent of the division redshift(s) and number of bins. In conclusion, this FOM only captures the information that was already contained in the standard deviation of w when using the simplest parametrization, namely $w =$ constant.

Note that neither the area (determinant) nor trace FOM's takes particular advantage of physical foundations. We have seen that the trace FOM neglects all dark energy dynamics, reducing to a constraint on a static EOS. For the area FOM, as discussed in [150], the area of the error contour is the Snarkian, or blank map, approach where all dynamics is equal. Instead, [150] advocates that the FOM must be adapted to the physics objective, e.g. whether one wants to distinguish the EOS from the cosmological constant or thawing behavior from freezing behavior, and depends on dark energy properties. We revisit physical bases for discerning the nature of dark energy in §5.7.

5.6 High Redshift Equation of State and Bias

For each method of analysis considered the high redshift value of the EOS has been shown to be a crucial ingredient; fixing the value of $w_{N+1} = w(z > 1.7)$ has significant effects on the derived properties of the dark energy. A similar point has been made for functional forms by [153]. In addition to misestimating the uncertainties by fixing w_{N+1}, if it is fixed to the wrong value[3] (and a priori we don't know what the correct

[2]To see this, first note that in terms of the N decorrelated parameters α'_i, the constant mode

$$e_{\mathrm{const}}(z) = 1, \quad 0 < z < z_{\mathrm{max}}, \tag{5.23}$$

which is the only mode present in the mode expansion when $N = 1$, is given by the N-dimensional vector $\mathbf{e}'_{\mathrm{const}} = (1, 1, \ldots, 1)$ because the α'_i are weighted averages of the original parameters. Hence, using the transformation law Eq. (B.4) for the Fisher matrix, the diagonal element of the Fisher matrix corresponding to the coefficient of the constant mode (i.e. the Fisher information of the constant mode) is

$$\mathbf{e}'^{\mathbf{T}}_{\mathrm{const}}\,\mathbf{F}'\,\mathbf{e}'_{\mathrm{const}} = \sum_{ij} F'_{ij} = \sum_i \sigma'^{-2}_i. \tag{5.24}$$

But by definition this quantity is the inverse variance of the coefficient of the constant mode in the case of $N = 1$ bins.

[3]Treating the EOS between $z = 1.7$ and $z = 1089$ as constant may introduce a bias in itself, but here we focus on the bias introduced by using the wrong constant value.

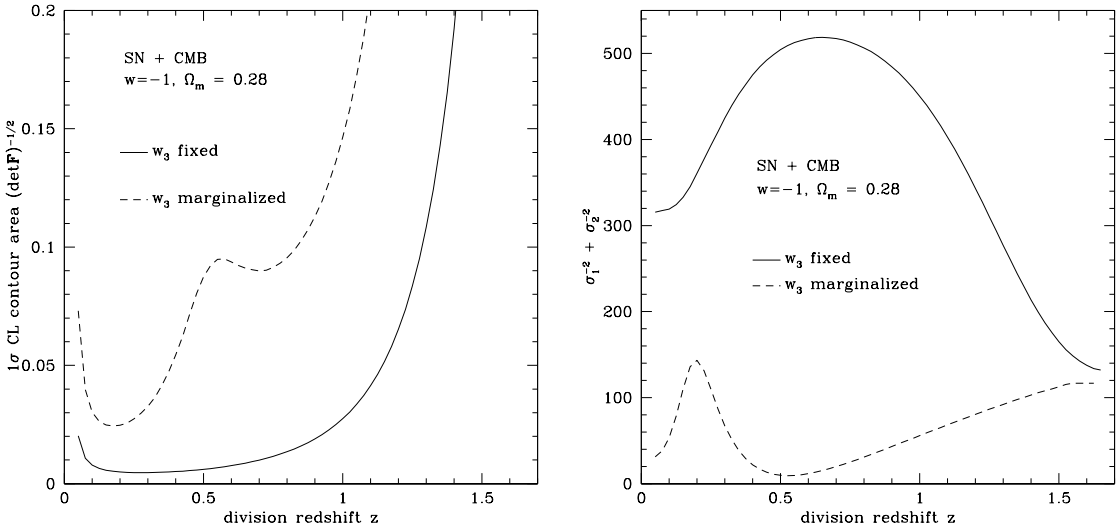

Figure 5.12: As Fig. 5.10 but showing two suggested figures of merit. The first panel shows $(\det \mathbf{F})^{-1/2} = A/\pi$ as a function of the bin division redshift z, where A is the area enclosed by the 68% confidence level contour in the $w_1 - w_2$ plane for the model with two bins between $z = 0$ and $z = 1.7$. The second panel shows $\sum_i \sigma_i^{-2} = \sigma_1^{-2} + \sigma_2^{-2}$.

value is) then the *values* themselves of all the cosmological parameters are biased – we will derive a picture of dark energy skewed from reality.

Bias in derived parameters can be calculated from offsets in observables within the Fisher matrix formalism by (see, e.g., [150])

$$\delta p_i = (F^{-1})_{ij} \sum_k \frac{\partial O_k}{\partial p_j} \frac{1}{\sigma_k^2} \Delta O_k, \tag{5.25}$$

where δp_i is the difference of the estimated parameter value from its true value, $\delta p_i \equiv p_{\mathrm{e},i} - p_{\mathrm{t},i}$, and ΔO_k is the offset in the kth observable. For bias arising from choosing the wrong value for w_{N+1} (which then propagates into the expected, i.e. simulated, observation), the expression becomes (see Appendix D)

$$\frac{dp_i}{dp_{N+1}} = -\sum_{j=1}^{N} (F^{(N)})^{-1}_{ij} \, (F^{(N+1)})_{j,N+1}, \tag{5.26}$$

where dp_{N+1} is the difference of the value w_{N+1} is fixed to from its true value, $\delta p_{N+1} = p_{\mathrm{fix},N+1} - p_{\mathrm{t},N+1}$.

To give concrete examples of the induced parameter bias, we choose two EOS models that we will fit with binned piecewise constant EOS. We use three low redshift

parameter p_i	$w_1(z<0.2)$	$w_2(z=0.2-0.5)$	$w_3(z=0.5-1.7)$	$w_4(z>1.7)$	$\mathcal{M}$	$\Omega_{\rm DE}$
PNGB true value	-0.83	-0.87	-0.93	-0.995	anything	0.72
dp_i/dw_4	-0.015	-0.019	-0.063	x	-0.00022	-0.0097
$\sigma(p_i)$ fixing w_4	0.10	0.16	0.15	x	0.016	0.012
parameter p_i	$w_1(z<0.2)$	$w_2(z=0.2-0.5)$	$w_3(z=0.5-1.7)$	$w_4(z>1.7)$	$\mathcal{M}$	$\Omega_{\rm DE}$
Bending true value	-0.84	-0.72	-0.55	-0.16	anything	0.72
dp_i/dw_4	-0.21	-0.26	-0.39	x	-0.0022	-0.14
$\sigma(p_i)$ fixing w_4	0.096	0.16	0.11	x	0.016	0.012

Table 5.1: Biases in cosmological parameter estimation due to fixing $w(z>1.7)$ to an incorrect value. The top half of the table considers a PNGB dark energy model, which has $w(z>1.7)\approx -1$, and the bottom half considers a bending dark energy model, where $w(z>1.7)$ differs substantially from -1. The amount of bias dp_i per how much w_4 is misestimated is shown in the middle row of each set.

bins $z=0-0.2$, $0.2-0.5$, $0.5-1.7$ and a high redshift bin from $z_{\rm max}=1.7$ to $z_{\rm lss}=1089$, and define a weighted average

$$w_{N+1}=\frac{1}{\Delta\ln(1+z)}\int_{z_{\rm max}}^{z_{\rm lss}}\frac{dz}{1+z}w(z). \tag{5.27}$$

(For consistency, we use an appropriately defined weighted average for each bin.)

The first model is based on a pseudo-Nambu-Goldstone boson (PNGB) model [89], which has $w_{N+1}\approx -1$,

$$w(z)=-1+(1+w_0)(1+z)^{-F} \tag{5.28}$$

with $w_0=-0.8$ and $F=1.5$. The second model is based on a so called bending model [234] motivated by dilaton fields, giving a nonnegligible contribution of early dark energy density (here $\sim 2\%$ relative to the matter density) and w_{N+1} far from -1:

$$w(z)=\frac{w_0}{\left[1+b\ln(1+z)\right]^2}\,, \tag{5.29}$$

with $w_0=-0.9$ and $b=0.415$ (this is very similar to the model $w(z)=w_0+w_a(1-a)$, with $w_0=-0.9$ and $w_a=0.7$). In both cases, $\Omega_m=0.28$.

Table 5.1 shows the EOS values in each bin for both models and also the amount of bias of the estimated parameter values per offset of w_{N+1} relative to the a priori assumption, as calculated from Eq. (5.26). For example, if one assumed that $w_{N+1}=-1$, then the bias in w_2 for the bending model would be $\delta w_2=0.22=-0.26\times(-1+0.16)$; that is, instead of measuring the true value $w_2=-0.72$ one would think $w_2=-0.50$. Assuming cosmological constant behavior at high redshift has very little effect on the PNGB model, since at high redshift it indeed is close to $w=-1$. But we don't know a priori what the true dark energy behavior will be.

To avoid bias, we must leave w_{N+1} as a fit parameter. However, this greatly increases the uncertainties, since adding a single parameter and a single data point,

PNGB	σ_1	σ_2	σ_3	σ_4	r_{12}	r_{13}	r_{14}	r_{23}	r_{24}	r_{34}
fixing w_4	0.10	0.16	0.15	x	-0.76	0.45	x	-0.72	x	x
fitting w_4 (CMB)	0.32	0.42	1.3	20	0.79	0.96	-0.95	0.89	-0.92	-0.99
fitting w_4 (CMB+d_3)	0.10	0.16	0.17	2.1	-0.73	0.48	-0.21	-0.59	-0.13	-0.53
Bending	σ_1	σ_2	σ_3	σ_4	r_{12}	r_{13}	r_{14}	r_{23}	r_{24}	r_{34}
fixing w_4	0.096	0.16	0.11	x	-0.73	0.39	x	-0.84	x	x
fitting w_4 (CMB)	0.98	1.2	1.8	4.7	0.98	1.00	-1.00	0.98	-0.99	-1.00
fitting w_4 (CMB+d_3)	0.098	0.15	0.12	0.07	-0.77	0.43	-0.20	-0.81	0.20	-0.48

Table 5.2: As Table 5.1, showing the EOS uncertainties and correlation coefficients. Fitting for $w_4 \equiv w(z > 1.7)$, which removes the bias calculated in Table 5.1, increases the uncertainties and correlations, but the addition of further high redshift data (here illustrated with $d_3 \equiv \tilde{d}(z = 3)$) can substantially restore them.

with only that data point constraining that parameter, is equivalent to adding neither the parameter nor the data as far as the uncertainties in the original parameters are concerned – essentially throwing away the high redshift bin. The solution that allows for control of both bias and uncertainty is to obtain more, useful data that depends on w_{N+1}. Such data could be higher redshift distances, such as from baryon acoustic oscillation (BAO) measurements using quasars or the Lyman alpha forest, or from matter density growth factors such as enter into weak gravitational lensing measurements. While we note that SNAP, which we took to provide the supernova sample, includes highly precise weak lensing measurements, here we continue to concentrate on distances and illustrate the effect of a 1.2% measurement of the reduced angular distance $\tilde{d}$ (transverse BAO scale) at $z = 3$ such as the BOSS experiment [197] could provide.

Table 5.2 shows the effects on the EOS uncertainties from fixing w_{N+1} (and so incurring bias), fitting for it with only a CMB $d_{\rm lss}$ measurement (and so effectively using SN alone), and fitting for it with both $d_{\rm lss}$ and $\tilde{d}(z = 3)$ measurements. We see that not only do the uncertainties greatly decrease when data give constraints on the high redshift expansion history, but the correlations between EOS parameters greatly diminish. Again we emphasize that weak lensing measurements have the same or better effect. The key point is that assuming high redshift behavior for dark energy leads to bias – to overcome this requires accurate measurements (beyond CMB data alone) of the high redshift universe, e.g. through direct $z > 1.7$ observations or through weak lensing observations involving the growth factor. Given such measurements, one recovers almost the full leverage on the EOS as when w_{N+1} was assumed, but without bias. For the two very different models we considered, the EOS parameter estimation by doing a global fit including w_{N+1} is degraded by less than 15% and the risk (the uncertainty and the bias summed in quadrature) is improved by factors up to 3. Of course if with the additional data one attempts to fit additional high redshift EOS parameters, then the constraints do not improve as much.

5.7 Physical Constraints on Equation of State

5.7.1 Eigenmode Expansion

We pointed out at the end of §5.3 that to reduce the parameter space by throwing out poorly determined modes in the eigenmode expansion, we need to make assumptions about the appropriate range of values for the parameters/coefficients α_i. One way to do this is to take constraints on $w(z)$ based on theory (if we have any such constraints) and convert these into constraints on the parameters α_i (see for example [70]). If for example we then find that $-\alpha_i^{\max} < \alpha_i < \alpha_i^{\max}$, we may want to throw out the ith mode if $\alpha_i^{\max} < \sigma_i$ (or perhaps $\alpha_i^{\max} < 2\sigma_i$) because $\alpha_i^{\max} = \sigma_i$ means that the maximum physical signal in α_i is equal to its observational uncertainty and thus we cannot get a convincing signal in this parameter. This approach is closely related to the risk minimization approach[4] of [122].

As an example, imagine we expect the equation of state to be $w = -1$ and have some reason to believe that $-2 < w(z) < 0$ is required, for all z. In other words, if we choose the baseline equation of state (see Eq. 5.2) to be $w_b = -1$, we want the magnitude of the deviation from the baseline to be smaller than one:

$$|w(z) - w_b(z)| = \left| \sum_i \alpha_i \, e_i(z) \right| < 1. \tag{5.31}$$

This constraint of course defines some complicated volume in the α_1-...-α_N space (correlating the constraints on the different α_i), but we can get simple maxima $\alpha_i^{\max}$ for the individual α_i by treating the constraint (5.31) less rigorously.

One way of doing this is to demand that the contributions of the individual modes do not exceed one, i.e. $|\alpha_i \, e_i(z)| < 1$ for all z for each i individually. This gives

$$\alpha_i^{\max} = 1/|e_i(z)|_{\max} \tag{5.32}$$

and we have checked that (using the criterion $\alpha_i^{\max} < \sigma_i$) this allows us to throw out all but the first five modes for the case depicted in Fig. 5.4 (left), independent of whether the binning is uniform in z, a or $\ln(1+z)$. One of the problems with

[4] To see this, note that

$$\text{risk} = \text{bias}^2 + \text{variance} = \sum_{i=1}^{N} \left(w(z_i) - \bar{w}(z_i)\right)^2 + \sum_{i=1}^{N} \sigma^2(w(z_i)) = \sum_{i=M+1}^{N} \alpha_i^2 + \sum_{i=1}^{M} \sigma^2(\alpha_i), \tag{5.30}$$

where we use the notation from [122] with M the number of modes kept. The coefficients α_i describe the deviation from the baseline EOS and the last equality follows from the normalization of the modes $\sum_{i=1}^{N} e_j^2(z_i) = 1$ (a different, constant normalization does not affect the risk minimization). By considering whether to keep the $M+1$ mode or not, i.e. whether to include it in the bias^2 or variance terms, we see that minimizing the risk corresponds to keeping those modes that have $\sigma_i < \alpha_i$.

this approach is that if one mode locally causes an unacceptably large deviation from $w = -1$, this deviation may be canceled by another mode with large amplitude so in those cases the constraint is stricter than Eq. (5.31). The inverse is also true, that a mode that has an acceptably small deviation might be augmented by another mode so as to exceed our desired constraint.

An alternative approach that does not suffer from the first of the two problems mentioned above is discussed in §3 of [168], where it is applied to the reionization history of the universe instead of the dark energy EOS (note the ionization fraction is bounded in [0,1]). In this approach, maxima are calculated such that if *any* coefficient violates $|\alpha_i| < \alpha_i^{\max}$, Eq. (5.31) is violated as well. The converse is not true. All modes satisfying $|\alpha_i| < \alpha_i^{\max}$ does not guarantee that the original constraint is satisfied so this approach does suffer from the second problem mentioned in the previous paragraph. The $\alpha_i^{\max}$'s calculated in this approach are greater than (or equal to, in the limiting case of a constant mode) the ones in the approach discussed above and thus give a larger range of allowed values. When applied to the case at hand, the maxima for the approach discussed in [168] are given by

$$\alpha_i^{\max} = \int dz\, |e_i(z)|. \tag{5.33}$$

We have checked, again for the case depicted in Fig. 5.4 (left), that if we require this $\alpha_i^{\max} > \sigma_i$ then this very conservative criterion means we can eliminate modes beyond the first 9 or 10 (depending on if we calculate the eigenmodes with respect to z, a or $\ln(1+z)$).

Note that even if we throw out a large number of modes using the methods described above, the remaining parameters still carry a lot of uncertainty. Also, to illustrate our ideas we have assumed an expected $w = -1$ with $-2 < w(z) < 0$, but in reality we have very little knowledge to base such assumptions on (but see the next subsection). Finally, please recall that in §5.3 we identified two main problems with the eigenmode approach. Above, we considered the problem of how to quantify which modes are well-determined and which ones are not. However, there was another problem, namely that different binnings give a different set of modes. This implies that, after throwing out poorly determined modes, essentially different models remain. For example, the first five modes with respect to a span a different set of equations of state than the first five modes with respect to z.

5.7.2 Time Variation

The EOS $w(z)$ has physical constraints not just on its value but also its time variation. The effective mass of scalar field dark energy is related to the curvature of the potential and can be written in terms of w, w', and w'', as in [40, 152], where a prime denotes a derivative with respect to $\ln a$. (Note there is a typo in the first term of Eq. 46 in [152] where $2q$ should be $q/2$.) If the mass exceeds the Hubble

parameter, $m \gg H$, then the Compton wavelength for fluctuations in the scalar field will be less than the Hubble length and dark energy will exhibit clustering [159]. If we wish to disallow such models (ideally through observational constraints, although high energy physics such as supergravity can lead to limits on mass scales [128]) then this imposes the condition

$$\frac{m}{H} \lesssim 1 \quad \Longrightarrow \quad \left|\frac{w'}{1+w}\right| \lesssim 1, \tag{5.34}$$

unless the relation between w, w', and w'' is fine tuned. For example, this imposes constraints on oscillatory behavior, saying the variation cannot be too extreme. For EOS expanded in a Fourier basis in $\ln a$, say, all terms $\cos(B \ln a)$ with $B \gg 1$ would give inhomogeneities so the physical condition of smoothness would limit which modes should be included.

In terms of binned EOS, the condition (5.34) reads

$$\left|\frac{w_{i+1}-w_i}{1+(w_{i+1}+w_i)/2}\right| \frac{1}{\ln[(1+z_{i+1})/(1+z_i)]} \lesssim 1. \tag{5.35}$$

To help satisfy this we want a large distance between bin centers. Taking the extreme case of $z_1 \approx 0$, $z_2 \approx 1.7$, then $|\Delta w| \lesssim 1 + \bar{w} \lesssim 1$. That is, bin values should not jump by of order unity. For bins closer together the jump constraint is tighter. Dark energy lying within the thawing and freezing regions defined by [44] automatically satisfies the mass constraint. For effective dark energy without a physical fluid, as in extended gravity origins, constraints on w' from inhomogeneity considerations may not apply. Other possibilities for constrained EOS behavior can arise within a particular class of models; [23] explores this for some potentials using PCA and [58] chooses a correlation function over redshift for $w(z)$.

5.7.3 Testing the Equation of State

Finally, one might want to apply several tests for physical properties to the EOS, which can be phrased simply in terms of the EOS bin values. To check consistency with the cosmological constant, $w = -1$, to a confidence level of $S\sigma$, one looks for $(1+w_i)/\sigma(w_i) > S$. To look for departures from a constant EOS, one probes whether

$$\frac{w_i - w_j}{\sigma(w_i - w_j)} = \frac{w_i - w_j}{\sqrt{\sigma_i^2 + \sigma_j^2 - 2\,C_{ij}}} > S, \tag{5.36}$$

for any i, j. This also gives a necessary but not sufficient condition for distinguishing thawing vs. freezing behavior: whether w decreases or increases with larger redshift.

Another interesting property would be nonmonotonicity in the EOS. This could be indicated by having $w_{i+p} - w_i$ of opposite sign from $w_{i+r} - w_{i+q}$, where $p < q < r$. (Note

$\sigma(w_2-w_1)$	$\sigma(w_3-w_2)$	$\sigma(w_3-w_1)$	$\sigma(w_4-w_3)$	$\sigma(w_4-w_2)$	$\sigma(w_4-w_1)$
0.47	0.94	0.57	0.88	0.36	0.35

$\sigma(w'_{12})$	$\sigma(w'_{23})$	$\sigma(w'_{34})$
2.8	6.6	2.4

Table 5.3: Uncertainties in the EOS jumps between bins and the derivatives $w' \equiv dw/d\ln a$ for the four redshift bins covering $z < 1.7$ of Eq. (5.16). Note w_{N+1} is fixed to -1.

we do not only consider consecutive bins since low σ differences between neighboring bins could add up to statistically significant deviations over a wider range.) That is, one tests whether

$$\frac{w_{i+p}-w_i}{\sigma(w_{i+p}-w_i)} < -S \quad \text{and} \quad \frac{w_{i+r}-w_{i+q}}{\sigma(w_{i+r}-w_{i+q})} > S, \tag{5.37}$$

or the opposite.

While from the above points it would appear that for testing Λ, say, the FOM should be minimizing $\sigma(w_i)$ in any one bin, this in fact does not hold. Such a criterion would drive us to create a single bin over the entire data redshift range, indeed giving a minimal $\sigma(w_i)$, but erasing any dynamics, taking a constant w. This averaged w can in fact under certain circumstances be driven to appear as $w = -1$ despite real time variation [153], so such a FOM is not useful. For checking constancy, monotonicity, and related properties, one might advocate a FOM involving $\sigma(w_{i+p} - w_i)$. This effectively takes a further derivative of the cosmological expansion and tends to yield large errors (while of course being a highly unstable procedure if applied directly to the data).

Table 5.3 demonstrates the lack of precision in determining $w_{i+p} - w_i$ or the variation $w' = dw/d\ln a$, even when fixing the high redshift behavior w_{N+1} (*not* recommended), within the binned EOS approach. Even for this optimistic case with next generation data, fitting four EOS parameters is too much: the dynamics represented by w' cannot be seen. This agrees with [156] that next generation data will only allow physical insight into two EOS parameters. For the two bin case we considered in §5.5, one can obtain $\sigma(w'_{12}) = 0.23$.

5.8 Conclusions

The dark energy equation of state properties contain clues crucial to understanding the nature of the acceleration of the cosmic expansion. Deciphering those properties from observational data involves a combination of robust analysis and clear interpretation. We considered three approaches – principal components, uncorrelated bandpowers, and binning; none of the approaches provides a panacea.

In particular, we identify issues of dependence on basis functions, binning variables, and baseline models. The three approaches are not truly nonparametric and physical interpretation (not merely the values) of the results in the two decorrelated basis techniques depends on model, priors, and data, indeed even on an implicitly assumed functional form. Nevertheless, principal components can give a useful guide to the qualitative sensitivity, the best constrained aspects, of the data.

The uncorrelated bin approach unfortunately does not truly deliver uncorrelated bandpowers for the equation of state. This approach using the square root of the Fisher matrix does not tightly localize the information (without a strong prior), making the interpretation nontrivial. This property of nonlocality is inherent in the cosmological characteristics. One might prefer to stay with the original binned equations of state used as the initial step for this technique, which are readily interpreted. Conversely, if the modes can be localized, the interpretation is easy, but in that case the original Fisher matrix is close to diagonal and thus the original bins almost uncorrelated. Hence, again, one might as well stay with the bin parameters which have a clear meaning.

Indeed the goal is understanding the physics, not obtaining particular statistical properties. Decorrelated parameters that are not readily interpretable physically are of limited use; for example one still prefers to analyze the cosmic microwave background in terms of physical quantities such as physical matter density and spectral tilt rather than the principal axes of the eigenvectors. Note that the uncertainty on the EOS behavior $\sigma(w(z))$ is the same whether calculated by PCA (if all modes are kept), uncorrelated bands, or binned EOS, since the same information is in the data. We also emphasize that the modes most clearly determine the effect on the equation of state, not the weights, which are often the only quantity displayed. Moderately localized, even all positive, weights do not guarantee a localized physical effect. A further caution is that locality and positivity of weights can owe more to prior restrictions, especially the treatment of the high redshift equation of state, than to the data itself.

Assuming a fixed value for the high redshift equation of state has major, widespread impacts on the results, ranging from strongly misestimated uncertainties to spurious localization to bias in the derived cosmology. We emphasize that it is essential to fit for the high redshift behavior in order not to be misled. Adding CMB data and marginalizing over a new, high redshift bin removes the ill effects of bias but "cancels out," providing no new constraints; multiple data points for $z > 2$ are required, such as from high redshift distances or weak lensing measurements of the mass growth behavior. Assuming that dark energy is negligible at $z > 2$ is also effectively assuming a functional form – precisely what the use of eigenmodes was supposed to avoid.

Indeed, functional forms do not have many of the basis, model, binning, etc. dependences of eigenmodes, while principal components are in turn not fully form independent. If one assumes a functional form to obtain informative constraints on the equation of state, one must indeed choose the form to represent robustly the

physical behavior (as has been shown to be widely the case for $w(a) = w_0 + w_a(1-a)$ by [149, 153]), and carefully check the range of validity of the conclusions by examining other forms. A good complementary analysis tool would be the binned equation of state approach examined here.

Regardless of the form of analysis, only a finite amount of information can be extracted from even next generation data. As has been concluded for functional equations of state and principal component analysis [156], the analysis here in terms of binned equation of state indicates that only two physically informative parameters can be fit with realistic accuracy. However, we identify several issues in the PCA and uncorrelated bin approaches that cause accuracy or signal to noise criteria to be ill defined. Similar difficulties arise in condensing the physical information on dark energy to a single figure of merit; the number is quite sensitive to cosmologically irrelevant aspects like the binning used (as well as very dependent on the treatment of the high redshift dark energy behavior).

In conclusion, physically motivated fitting of the equation of state such as the w_0-w_a parametrization in complement with a binned equation of state approach (perhaps with physical constraints such as outlined in §5.7) have the best defined, clearest to interpret, and robust insights of the approaches we considered. With any method, one must use caution regarding the influence of priors and fit the dark energy physics over the entire expansion history.

Chapter 6

Future CMB Lensing Constraints on Neutrinos and Dark Energy

A version of this chapter was previously published in *Physical Review D* [66].

6.1 Introduction

Precision studies of the cosmic microwave background have helped us formulate a standard model of cosmology and measure several global parameters that describe our universe and its contents [137, 185, 188, 184]. Six key parameters to describe the cosmology have been determined with 1-10% precision and CMB data plays a significant role in constraining other parameters, such as spatial curvature, the dark energy density, and the Hubble constant, in combination with other types of data.

However, we know in some cases and allow the possibility in other cases, that there are further fundamental parameters beyond the six. One example is the mass of neutrinos, where terrestrial experiments indicate a nonzero, though unknown, value: $m_\nu \gtrsim 0.05$ eV for at least one neutrino species [162]. Another set of parameters of great interest describes the properties of the dark energy causing acceleration of the cosmic expansion. The dark energy equation of state (EOS) may differ from the constant value $w = -1$ of the cosmological constant, and may vary with time. Indeed, this dynamics would be a key clue to the nature of the physics behind acceleration. The persistence of dark energy density to early times is another mystery that is crucial to explore. Current CMB data on the temperature and E-mode polarization spectra (and their cross-spectra) are of little use in themselves in addressing these issues, and this holds to a large extent even in combination with other cosmological information such as supernova distances and large scale structure data.

Fortunately, other types of CMB information exist, though they have not yet been measured. This includes the CMB deflection field – the action of gravitational potentials along the line of sight on the CMB – and the B-mode polarization spectra (and

cross-spectra) resulting from this. The effects carry contributions from all redshifts between the source (the last scattering surface at redshift $z \approx 1090$) and the observer, though like all lensing deflection the kernel from the geometric distance factors peaks approximately midway, $z \approx 3-4$. The growth of the gravitational potentials over this history carries within it information on the matter power spectrum. Thus the effects of neutrino masses and dark energy properties are encoded in the CMB.

While subsets of these effects have been investigated before (see, e.g., [131, 212, 143, 211, 210]), the effects have not generally been considered simultaneously (especially for dynamical dark energy), with the critical covariances between them. This is also the first investigation of the important question of early dark density using CMB lensing. We also examine for a range of cases the added leverage of lensing information extraction through use of the optimal quadratic estimator which utilizes the unique non-Gaussian structure in the map caused by lensing.

In §6.2 we lay out the methodology for obtaining precision theoretical predictions for power spectra, and their slight variations with cosmology, and summarize the observational capabilities of three benchmark CMB surveys. We explore adding neutrino mass to the standard, cosmological constant universe in §6.3, and include as well the dark energy EOS and its time variation in §6.4. Discussion includes complementarity with other cosmological probes and issues of foreground noise. In §6.5 we investigate early dark energy density, and present a simple prescription for cosmological constraints in §6.6. We summarize the key prospects for intermediate range CMB experiments in §6.7.

6.2 Power Spectra Modeling: Theory and Experiments

Primordial perturbations in the photon number density arise from Gaussian, random, adiabatic fluctuations seeded in the inflationary era. These induce a photon temperature power spectrum, and interaction with inflationary gravitational waves and scattering from electrons creates B-mode and E-mode polarization power spectra (as well as a TE cross-spectrum), respectively. Gravitational lensing shuffles the photon pattern on the sky [148, 201] and contributes to each of these spectra, as well as transforming some of the E-modes into B-modes, introducing a coupling between the two. Beyond these power spectra, lensing imprints non-Gaussianity into the CMB, and the CMB trispectrum encodes information about the deflection field power spectrum, or mapping of the photon positions, itself [109].

6.2.1 Theory

Accurate codes exist for computing each of these power spectra, at least for the standard cosmology. We utilize CMBeasy, which already implements several useful

extensions to further cosmological parameters, including neutrino masses and several classes of dark energy [72, 73]. We have crosschecked results (for constant dark energy equation of state) with another code, CAMB, to ensure accuracy. Numerical stability is crucial, because several groups of cosmological parameters are highly degenerate and the differences between the power spectra for different cosmologies can be small, so numerical noise can distort the results. We carry out parameter estimation through Fisher matrix analysis. For the precision future data we consider, this should provide accurate constraints. We check for convergence of the final results for various step sizes of the cosmological model differencing.

The set of parameters considered includes the standard ones of primordial perturbation amplitude A_s and power law index n, optical depth τ, physical baryon density $\Omega_b h^2$, cold dark matter density $\Omega_c h^2$ and dark energy density $\Omega_{\rm DE}$. The Hubble constant is a derived parameter $h^2 = (\Omega_b h^2 + \Omega_c h^2)/(1 - \Omega_{\rm DE})$ under the assumption of spatial flatness. The physical matter density is $\omega_m = \Omega_b h^2 + \Omega_c h^2$. Since neutrinos are known to have mass and this influences the lensing and other power spectra, we always include as a parameter the physical neutrino energy density $\Omega_\nu h^2$ or equivalently the sum of neutrino masses $\sum m_\nu = 94(\Omega_\nu h^2)$ eV.

Since no guarantee exists that dark energy is a cosmological constant, and generically other models have time variation of their equation of state, we consider two parameters, w_0 and w_a, to describe the dark energy equation of state, $w(a) = w_0 + w_a(1 - a)$. Consideration of the physics behind dark energy led to this form [149] and it has been shown to be accurate to 0.1% in describing observables [64]. The ΛCDM model corresponds to fixing $w_0 = -1$, $w_a = 0$. Given that the CMB has strong sensitivity to the early universe, we also consider another class of dark energy models, early dark energy, where the dark energy density is non-negligible around and before the recombination epoch. These also have two parameters, the equation of state today w_0 and the constant high redshift early dark energy density Ω_e [74]. For $z \lesssim 2$ these look identical to the w_0-w_a model where $w_a \approx 5\Omega_e$ [157], but have distinct and possibly significant effects at high redshift.

Thus we simultaneously fit either seven or nine parameters. We use the following fiducial parameter values throughout this chapter: $\{A_s,\, n,\, \tau,\, \Omega_b h^2,\, \Omega_c h^2,\, \Omega_{\rm DE},\, \sum m_\nu\}$ $=\{2.41 \times 10^{-9},\, 0.963,\, 0.084,\, 0.02255,\, 0.1176,\, 0.72,\, 0.28\,{\rm eV}\}$.

6.2.2 Deflection Field

The angular power spectrum of the CMB has been used to constrain cosmological parameters with unprecedented accuracy (see e.g. [137]), but its ability to inform us about the low redshift universe is limited by the so-called geometrical degeneracy. This arises because only angles are measured and, given some spectrum of primordial fluctuations, the power on each scale is nearly fixed for constant $\sqrt{\omega_m}\, d_{\rm lss}$ (where $d_{\rm lss}$ is the angular diameter distance to the CMB last scattering surface), which is degenerate under certain combinations of late universe parameters. (An exception to

this arises on large angular scales because the integrated Sachs-Wolfe (ISW) effect [189] leaves another signature of dark energy on large scales, however owing to cosmic variance this effect is of limited use.) Also, the primordial CMB probes the baryon distribution at last scattering, which is smoothed on scales smaller than $\sim 10'$ because of Silk damping [208] in the last scattering surface, while massive neutrinos mostly impact matter agglomerations on projected smaller scales.

The geometrical degeneracy can be broken by adding for example Type Ia supernova (SN) distance information or constraints on the expansion rate to the CMB power spectrum constraint (see, e.g., [137]). The effect of neutrinos on small scale structure can be probed through galaxy clustering or the Lyman-α forest [224, 202]. Alternatively, or in addition, deflection of CMB photons on their way to us changes the statistics of the primordial pattern in a characteristic way that can be used to infer the lensing effect. What was originally a nearly Gaussian random field becomes non-Gaussian with the coherent correlation of patterns around large scale matter fluctuations. This type of non-Gaussianity, on a typical scale of approximately 2 degrees, is different from that used to study inflationary models [19, 56], in that its three point function vanishes on most scales (except for those large scales on which the unlensed CMB is correlated with the lenses through the ISW effect).

Lensing is described by the displacement vector of CMB photons on the sky, $\alpha(\theta)$, which is given as $\alpha(\theta) = \frac{D_{\rm CMB}-D_{\rm lens}}{D_{\rm CMB}}\hat{\alpha}(\theta)$ in terms of the deflection angle

$$\hat{\alpha} = \frac{4G}{c^2}\int d^2x'\Sigma(\mathbf{x}')\frac{\mathbf{x}-\mathbf{x}'}{|\mathbf{x}-\mathbf{x}'|^2}\,, \quad \Sigma(\mathbf{x}) \equiv \int dD\,\rho(\mathbf{x},D)\,, \tag{6.1}$$

where D is the angular diameter distance. The vector $\mathbf{x}$ describes the position in the lens plane, and the surface mass density (lensing can be imagined to good approximation as progressing through multiple, infinitely thin planes) is $\sum(\mathbf{x})$, a projection of the three-dimensional density field $\rho(\mathbf{x}, D)$. In the so-called Limber approximation, the lensing power spectrum $C_L^{\alpha\alpha}$ becomes a simple integral over the matter power spectrum at all redshifts weighted by angular diameter distance ratios. In this chapter we refer to modes in the lensing power spectrum as $\mathbf{L}$ and $\mathbf{l}$, to distinguish them from the CMB multipole l.

Lensing also affects the angular power spectrum of the CMB [201]. The characteristic acoustic oscillation features are smeared out, as characteristically sized hot or cold spots are magnified or de-magnified by intervening lenses. The amount of over-smearing is scale dependent, encapsulating information about the shape of the matter power spectrum, which in turn is affected by dark energy properties and neutrino masses. Because of the distance factors (the geometric kernel) and the growth factors, the matter power spectrum is best probed over the range $z \approx 1-4$.

The effect of lensing on the CMB power spectrum is calculated within CMBeasy. In the presence of lensing, the power spectrum variance is not of the trivial Gaussian random field form. The non-Gaussian covariance is negligible in temperature and

E-mode polarization because the relative effect of lensing on these is small, however it is large for B-mode polarization, a factor of a few [211]. The effects of marginalization when constraining individual parameters generally overwhelm the effect of the excess covariance however [211, 213]. We confirmed that the effect of non-Gaussian covariance on the parameter constraints in the next sections is negligible by checking that the uncertainties change by less than 10% (typically less than 1%) if the sample variance in the B-mode is increased by a factor of five.

The power spectrum over-smearing method provides a statistical estimate of lensing that is prone to sample variance because the actual distribution of the lenses on the sky remains unknown. To reconstruct the lensing potential ψ (the line of sight projection of the gravitational potential of which the deflection vector α is the gradient) one needs to use the non-Gaussian information imprinted into the CMB. Lensing conserves surface brightness, so the probability distribution function of temperatures remains unchanged. Therefore the lowest order non-zero estimator of the lensing potential is quadratic. This has been investigated by [238, 97] and the minimum variance estimator was given by [110]. A quadratic estimator is generally of the form

$$\hat{\psi}(\mathbf{L}) = N(L) \int \frac{d^2\mathbf{l}}{2\pi^2} \theta(\mathbf{l})\theta'(\mathbf{L}-\mathbf{l}) g(\mathbf{l}, \mathbf{L}-\mathbf{l}) \,, \tag{6.2}$$

where θ and θ' stand for temperature and/or polarization modes on the sky, i.e. $\theta, \theta' = T, E, B$. The optimal weight g and normalization N can be found using the fact that the deflected position can be written as a first order expansion of the displacement around the undeflected position, $\theta^{\rm L}(\mathbf{x}) = \theta^{\rm UL}(\mathbf{x}+\alpha) = \theta^{\rm UL}(\mathbf{x}) + \nabla^i\psi(\mathbf{x})\nabla_i\theta(\mathbf{x})$. For the TT estimator, requiring an unbiased estimate and minimizing the variance leads to weighting of modes

$$g(\mathbf{l}, \mathbf{L}-\mathbf{l}) = \frac{(\mathbf{L}-\mathbf{l})\cdot\mathbf{L}C_{|\mathbf{L}-\mathbf{l}|} + \mathbf{l}\cdot\mathbf{L}C_l}{2\tilde{C}_l^{\rm tot}\tilde{C}_{|\mathbf{L}-\mathbf{l}|}^{\rm tot}} \,, \tag{6.3}$$

where C_l ($\tilde{C}_l$) is the unlensed (lensed) temperature power spectrum, following the convention of[1] [145]. Similar expressions follow for polarization. The superscript "tot" originates from the fact that the lensed CMB and noise enter in the variance calculation.

With the definition in Eq. (6.2) the noise of the lensing reconstruction equals the normalization which becomes

$$N(L) = \left[\int \frac{d^2\mathbf{l}}{2\pi^2} \left[(\mathbf{L}-\mathbf{l})\cdot\mathbf{L}C_{|\mathbf{L}-\mathbf{l}|} + \mathbf{l}\cdot\mathbf{L}C_l \right] g(\mathbf{l}, \mathbf{L}-\mathbf{l}) \right]^{-1} . \tag{6.4}$$

Physically the noise is a combination of instrumental and intrinsic shape noise (see below).

[1] Note that some papers, for example [110, 112], use the opposite notation to distinguish between lensed and unlensed spectra.

Note that this is only the best *quadratic* estimator. Maximum likelihood methods can in principle be applied [102, 103] but they have been shown to only give small improvements for temperature and polarization experiments with the sensitivity levels assumed in this work, so we do not consider them here. We also note that the approximation above leads to a bias in the quadratic estimator, however for experiments considered here, with angular resolutions larger than 3' as well as noise levels down to a micro-Kelvin, these are only a few percent and well understood (see [51, 102]).

As is the case with the lensing of background galaxies, CMB lensing obtains most information from the smallest scale resolved by any given experiment as these allow averaging over many background features. Because shapes in the CMB temperature can be intrinsically elliptical, averaging over many patterns becomes necessary to constrain relatively large lens features. Since unlensed B-type polarization patterns should be absent on scales less than a degree or so in concordance cosmology, quadratic estimators involving B, in particular the EB pair due to its higher signal-to-noise, are intrinsically more useful than temperature (as long as B can be imaged) and can be used to constrain lenses out to smaller scales. Therefore experiments beyond PLANCK, with the capability of imaging B-patterns, allow for reconstruction of lenses out to smaller angular scales [112, 103].

In the following sections we will compare the lensed power spectra method (i.e. the over-smearing of acoustic peaks) of inferring late universe parameter values to the optimal quadratic estimator (OQE) method. In the latter case we will use constraints on the unlensed power spectra in conjunction with a forecasted constraint on the lensing potential power spectrum[2] $C_L^{\psi\psi}$ using Eq. (6.4) so we do not count the lensing information twice.

6.2.3 Experiments

We consider three different experiments, two of which are scheduled to begin observations in the near future, to forecast constraints on neutrinos and dark energy. The PLANCK satellite will be launched in the second quarter of 2009 and will observe the full sky from the semi-stable Lagrange point L2. We take into account a foreground cut for galactic emission and assume a sky coverage of 0.75 to be useful for cosmological analysis. We have adopted the experimental specification values in [211].

Combining both large sky coverage and high sensitivity, we consider the futuristic CMBPOL concept of a satellite mission specialized on polarization with ultra-high sensitivity. We have used values from [237]. Our assumed specifications are summarized in Table 6.1. We postpone further discussion of POLARBEAR, an intermediate term and sensitivity experiment until Section 6.7.

[2]Using the lensing potential power spectrum is equivalent to using the deflection power spectrum. They are simply related by $C_L^{\alpha\alpha} = L^2 C_L^{\psi\psi}$ (in the flat sky approximation applied here).

Experiment	ν	$f_{\rm sky}$	$\theta_{\rm FWHM}$	Δ_T	Δ_P
Planck	100 GHz	0.75	$9.2'$	51	-
	142 GHz	0.75	$7.1'$	43	78
	217 GHz	0.75	$5.0'$	65	135
PolarBear	150 GHz	0.025	$4.0'$	3.5	5
	220 GHz	0.025	$2.7'$	8.5	12
CMBpol	all freq. comb.	0.75	$3'$	1	$\sqrt{2}$

Table 6.1: Experimental specifications assumed in the forecasts in this chapter, for the various frequency bands of PLANCK, POLARBEAR, and CMBPOL. The temperature and polarization sensitivities Δ_T, Δ_P are given in units of μK-arcmin.

From these experimental characteristics the full estimator covariance matrices for each multipole l can be constructed (e.g. [239]). The (Gaussian) covariances between the power spectrum and cross correlation estimators are given by

$$\begin{aligned}\mathbb{C}(C_l^{XY}, C_l^{ZW}) &= \frac{1}{(2l+1)f_{\rm sky}}\left[\left(C_l^{XZ}+N_l^{XZ}\right)\times\right.\\ \left(C_l^{YW}+N_l^{YW}\right) &+ \left.\left(C_l^{XW}+N_l^{XW}\right)\left(C_l^{YZ}+N_l^{YZ}\right)\right], \end{aligned} \tag{6.5}$$

where the noise power spectrum[3]

$$N_l^{XX} = \left(\frac{\Delta_X}{T_0}\right)^2 e^{l(l+1)\theta^2_{\rm FWHM}/(8\ln 2)}, \tag{6.6}$$

for $XX = TT, EE, BB$, $N_l^{\psi\psi}$ is given by Eq. (6.4) and $N_l^{XY} = 0$ when $X \neq Y$. Here Δ_T and $\Delta_E = \Delta_B = \Delta_P$ are the temperature and polarization sensitivities, $\theta_{\rm FWHM}$ is the angular resolution, and T_0 is the temperature of the CMB today.

Figure 6.1 shows that the noise of the experiments considered here is so low compared to the signal that they gather much of their information from scales beyond $l = 2000$ in the temperature power spectrum (POLARBEAR curves, not shown, would lie between PLANCK and CMBPOL curves). This is especially true for lensing, because the characteristic displacement of a CMB photon on its way from the last scattering surface to us is of order 2-3 arcminutes, and the smallest scale resolved by a given experiment contains most of the lensing information. However on scales $l \gtrsim 2000$ in the temperature power spectrum secondary anisotropies that are larger in magnitude than lensing, such as the Sunyaev-Zel'dovich (SZ) effects [218] and radio as well as infrared point sources will make extraction of lensing information challenging. This is true as well for the optimal quadratic estimator, which might get confused by

[3]When there are multiple frequency bands, the total noise power spectrum is given by $N_{l,tot}^{-1} = \sum_i N_{l,i}^{-1}$, where the sum is over the individual bands and we have suppressed the superscripts.

the extra non-Gaussianity carried by these foregrounds. In addition to the limitation due to the instrumental noise level and angular resolution, we therefore also quote our results with high-l cuts at different scales, to show how these foregrounds affect parameter constraints. We note that while point sources and the SZ are expected to be significantly dimmer in polarization than in temperature [194, 108], there the cutoff at high l does not lead to as much loss in information as the polarization signal-to-noise ratio is small on angular scales beyond $l = 2000$.

Finally, the Fisher matrix is given by the expectation value of the second derivative of the logarithm of the likelihood function $\mathcal{L}(C_l|\theta_i)$. Assuming Gaussianity of the likelihood it is of the form

$$F_{ij} = \sum_l \sum_{\alpha,\beta} \frac{\partial C_l^\alpha}{\partial \theta_i} \mathbb{C}^{-1}(C_l^\alpha, C_l^\beta) \frac{\partial C_l^\beta}{\partial \theta_j}, \tag{6.7}$$

where α and β run over the five observables: temperature, E-mode polarization, T-E cross correlation, B-mode polarization, and lensing potential power spectrum (where the OQE is used), and i, j run over the cosmological parameters. The covariance matrix between parameters is given by the inverse of the Fisher matrix.

6.3 Neutrino Mass Constraints in ΛCDM

We begin looking at cosmological constraints in the simplest model consistent with both cosmological and local observations: a cosmological constant universe with non-zero mass neutrinos. Three types of data cuts are employed – by classes of observations, experiments, and systematics.

The classes of observations are 1) unlensed TT, TE, EE power spectra, 2) adding the effect of lensing to 1), 3) adding the BB power spectrum to 2), and 4) using 1) plus information on the lensing potential through the optimal quadratic estimator discussed in §6.2.2. This allows understanding of the effects of lensing on just the temperature and E-mode spectra, the information in just the BB power spectrum caused by lensing, and methods for using the complete effects of lensing.

On the experimental side, we consider Planck, slated for launch in mid-2009, and the far future CMBpol mission. Discussion of the impact of intermediate scale ground-based missions is postponed until Section 6.7. Additionally we examine the influence of the level of systematics in terms of $l_{\rm max}$, such as induced through foregrounds external to the experiments.

Figures 6.2 and 6.3 illustrate the constraints on neutrino mass and dark energy density (cosmological constant) for the different data set types and systematics levels. All figures show 68% confidence level contours; the fiducial model is ΛCDM, with $\sum m_\nu = 0.28$ eV. Use of lensing information clearly adds substantial leverage, and measurement of B-modes or the lensing potential play an important role. The two

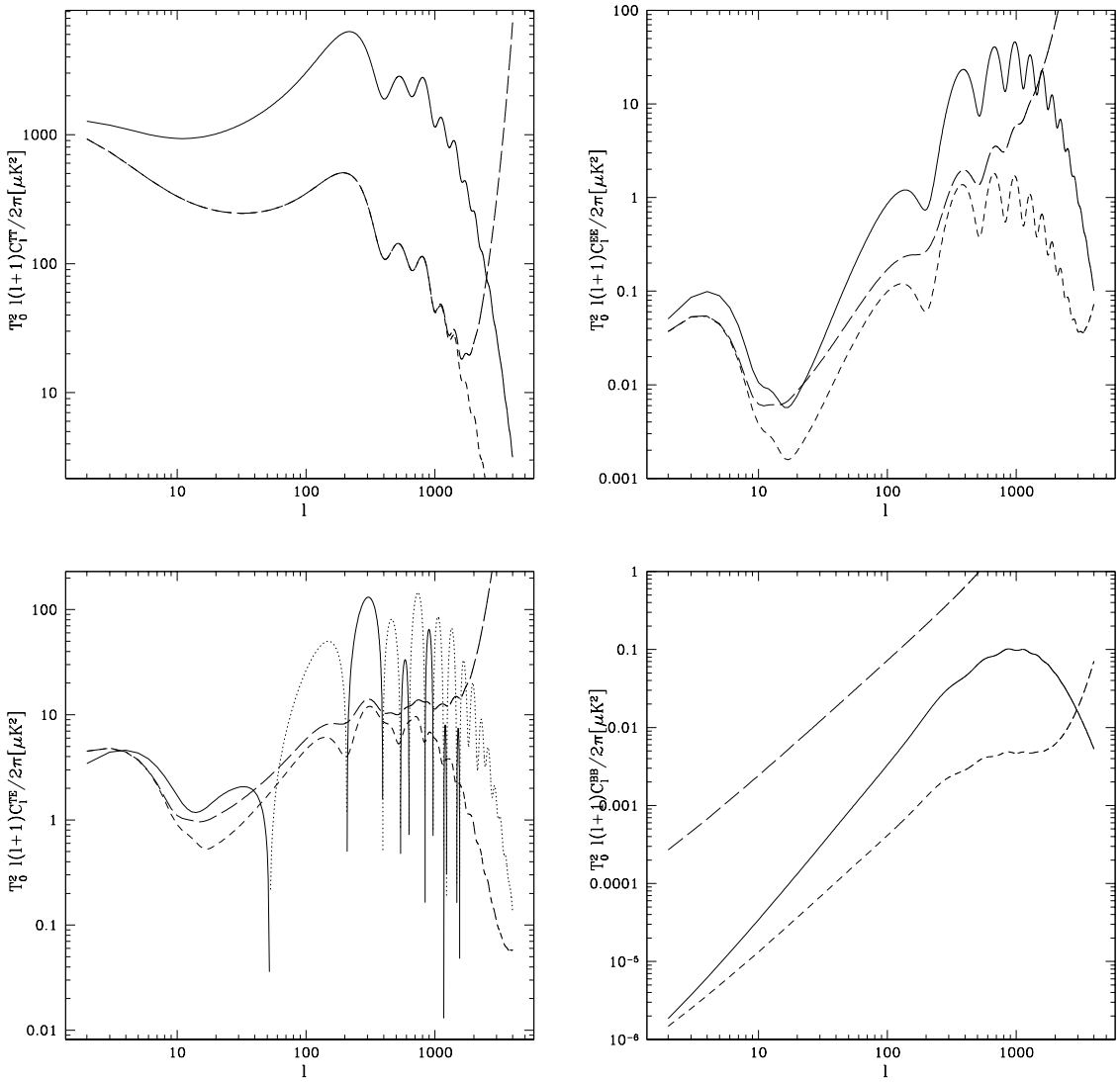

Figure 6.1: Temperature and polarization power spectra $T_0^2 l(l+1)C_l/2\pi[\mu K^2]$ vs. multipole l for the ΛCDM fiducial cosmology. TT, EE, BB, and TE spectra (solid curves, dotted where negative) run clockwise from upper left. Dashed curves show the power spectrum errors, $T_0^2 l(l+1)\Delta C_l/2\pi[\mu K^2]$, for the Planck (long dash) and CMBpol (short dash) experiments.

methods of including the full lensing information – adding B-modes or adding the lensing potential – are nearly equivalent (see §6.7 for further discussion of this).

Considering the constraints for different systematics levels, we see that much of the lensing leverage is achieved by $l_{\rm max} \approx 2000$. On smaller scales point sources and the SZ effects are expected to dominate over lensing and our limited ability to

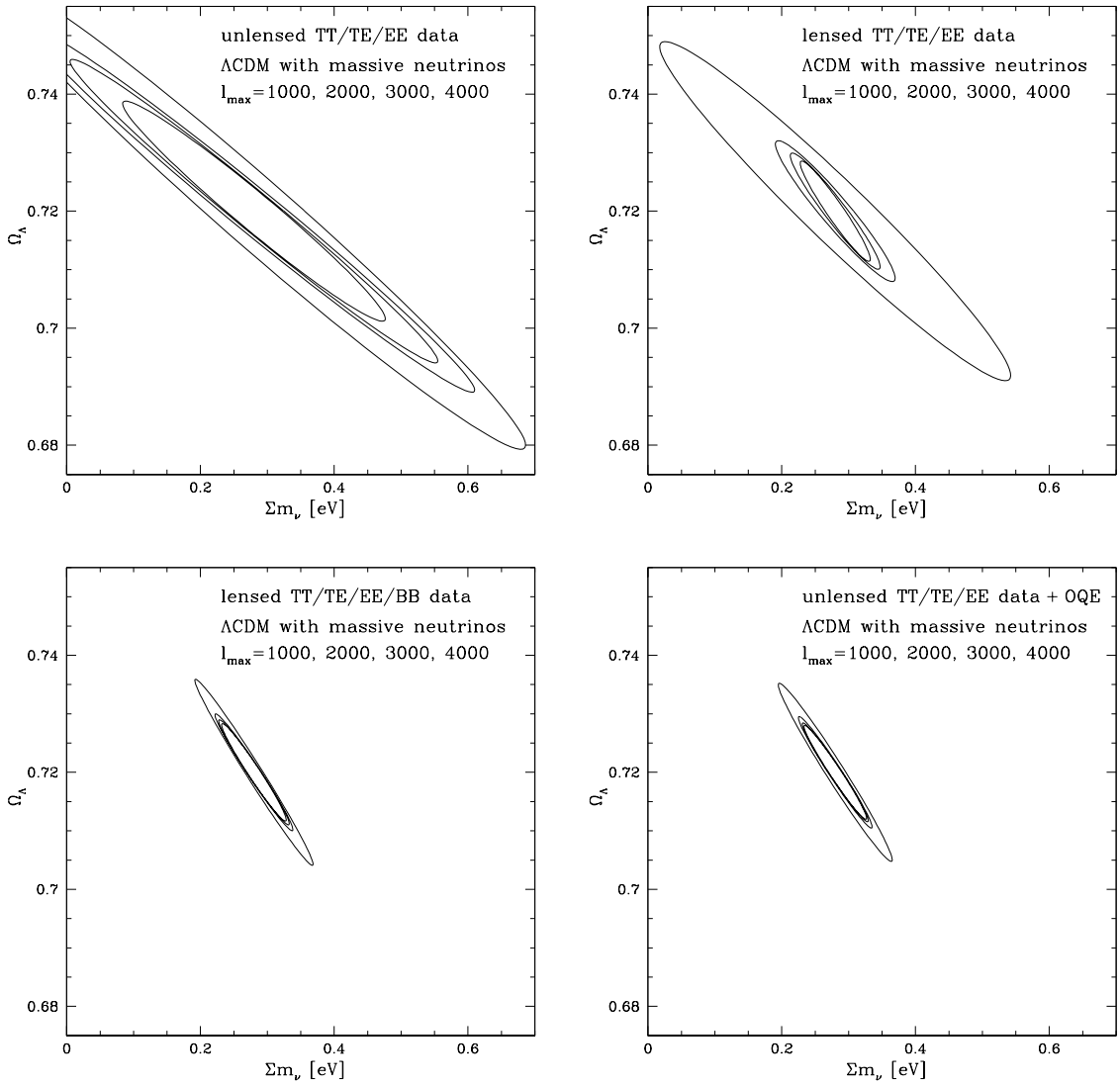

Figure 6.2: Cosmological constraints on the neutrino mass and dark energy density in the ΛCDM fiducial cosmology from CMBpol. Within each panel the contours correspond to systematic cuts at $l_{\rm max} = 1000$, 2000, 3000, 4000 from outer to inner. The panels use different data cuts: no lensing (upper left), including lensing from T- and E-modes (upper right), including lensing from T-, E- and B-modes (lower left), and including lensing through the optimal quadratic estimator of the lensing potential (lower right).

clean foregrounds through multifrequency observations will likely not allow lensing reconstruction on much smaller scales.

Finally, the dramatic improvement of CMBpol over Planck is clear in Fig. 6.4.

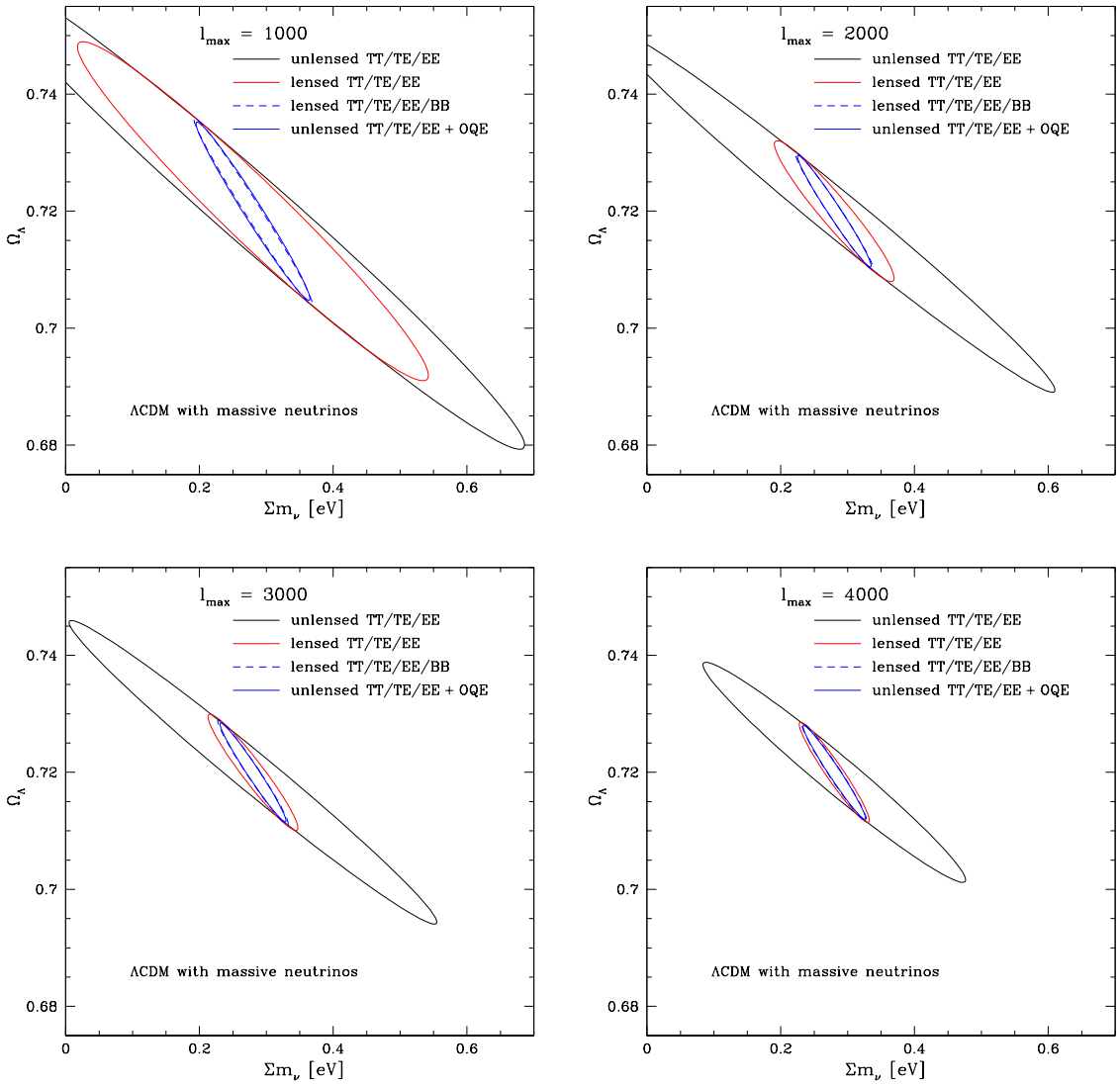

Figure 6.3: As Fig. 6.2 but here within each panel the contours correspond to data set types, and the panels use different systematics levels: $l_{\rm max} = 1000$ (upper left), 2000 (upper right), 3000 (lower left), 4000 (lower right).

Here we adopt as a standard systematics limit $l_{\rm max} = 2000$ and show the confidence contours for each data set type for both experiments. While lensing information does improve the Planck constraints, it runs into a wall due to the relatively high instrumental noise. Furthermore, Planck essentially cannot see B-mode lensing at all (see Fig. 6.1). This is one of the motivations for intermediate experiments such as PolarBear.

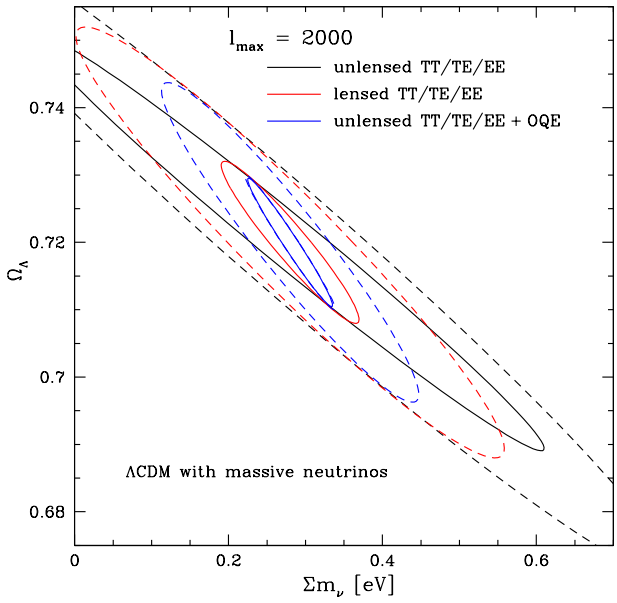

Figure 6.4: Comparing the cosmological constraints on the neutrino mass and dark energy density in the ΛCDM fiducial cosmology from Planck (dashed contours) vs. CMBpol (solid), taking $l_{\rm max} = 2000$.

6.4 Adding Dark Energy Dynamics

The cosmic microwave background plays a crucial role in breaking the degeneracies of other probes in order to constrain the properties of dark energy. However, unlensed CMB data itself has very little leverage on learning about dark energy, since the power spectra reflect mostly conditions in the high redshift universe or at best a single weighted average of dark energy influence through the distance to last scattering. With the addition of lensed CMB data we can ask if this improves the leverage on dark energy; we emphasize that it is crucial to consider at least minimally realistic models that include dynamics in the EOS: taking the value of w constant from the present to $z \approx 1100$ is highly non-generic.

It is also important to retain the inclusion of neutrino mass while making this investigation; both neutrino mass and dark energy influence the CMB in many of the same ways, e.g. suppressing structure and causing gravitational potentials to decay. Ignoring neutrino mass could lead to overoptimistic constraints on dark energy. In this section therefore we add w_0 and w_a as fit parameters to the set considered in the previous section. We explore the constraints under the same variety of data cuts as in that section.

The geometric degeneracy due to the acoustic peaks feeling dark energy mostly

through the integrated distance to last scattering remains strong, and no reasonable constraints can be placed on the dark energy EOS even with full use of the lensing information. We therefore turn to the issue of complementarity: does the CMB data substantially help other probes of dark energy? In particular we examine complementarity with luminosity distances measured by Type Ia supernovae, since the two probes are well known to strengthen each other [90, 111]. We consider luminosity distances measured to $\sim 1\%$ from $z = 0 - 1.7$, including systematics, as could be provided by a supernova sample realized by a SNAP-type Joint Dark Energy Mission [214].

Figure 6.5 shows the constraints in the w_0-w_a plane, marginalizing over the other seven parameters, for each data set type. The first thing to notice is the clear improvement in measuring the time variation w_a over the supernova sample alone due to even unlensed CMB data. Adding lensed CMB data continues to tighten the constraints, in both w_0 and w_a, except for the worst systematics level $l_{\rm max} = 1000$. Full lensing information continues the improvement modestly on the limits, and somewhat narrows the contours.

Figure 6.6 exhibits the analogous situation for different systematic limits $l_{\rm max}$. In contrast to the ΛCDM case, here the constraints continue to improve for higher $l_{\rm max}$. There are also slight differences between the two methods of fully incorporating lensing: use of B-modes or OQE of the lensing potential. This emphasizes that conclusions on systematics or analysis methods should not be based solely on examination of the vanilla ΛCDM cosmology. Finally, when systematics are low, $l_{\rm max} = 4000$, sufficient information is present in the lensed E-modes that further lensing information is unimportant.

The improvements in dark energy estimation that CMB lensing brings is illustrated in Fig. 6.7 as a function of experiment. For Planck, again no lensing information beyond E-modes is useful, though the contour area decreases by a factor 1.9 from the unlensed case to the OQE case. By contrast, CMBpol could reduce the likelihood contour area by a factor 4.2 relative to the unlensed Planck case, with the full lensing information helping by a factor 2.7 relative to unlensed CMBpol.

To test the effect of including both neutrino mass and dark energy dynamics, Fig. 6.8 shows the likelihood contours for the $l_{\rm max} = 2000$ CMBpol case, marginalizing over vs. fixing $\sum m_\nu$. The fully marginalized uncertainties are $\sigma(\sum m_\nu) = 0.041$, $\sigma(w_0) = 0.066$, $\sigma(w_a) = 0.25$. While the 1σ limits on the parameters do not change that strongly, the total area of the contour is significantly affected. For the unlensed (fully lensed) case the area increases by a factor 2.9 (1.5) when properly marginalizing over neutrino mass. (This effect would be more severe when considering CMB data alone.) Note that for the CMBpol case the correlation coefficient between w_0 and $\sum m_\nu$ is 0.23 and between w_a and $\sum m_\nu$ is -0.41; while not highly correlated, these are sufficient to give the appreciable effect.

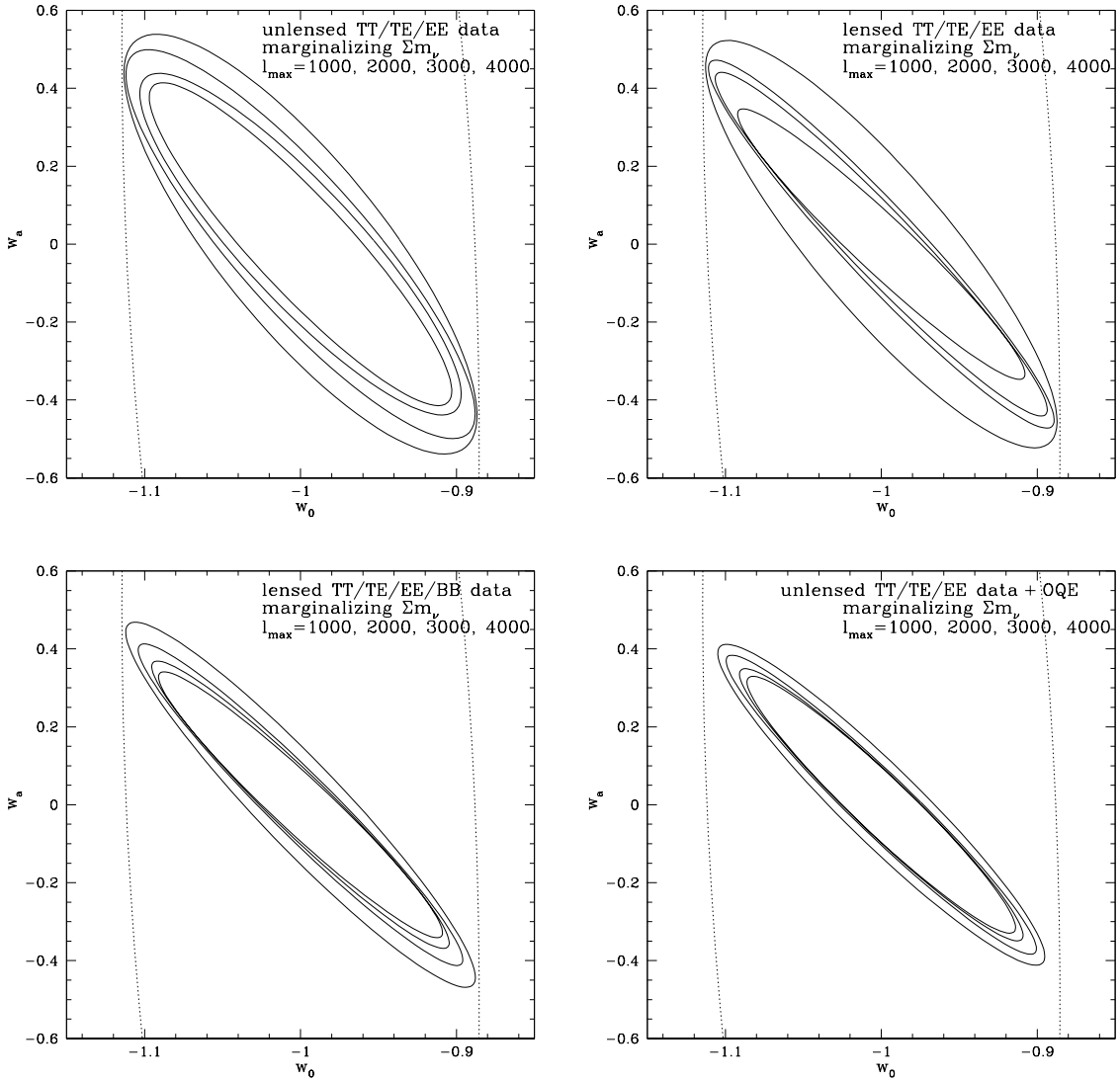

Figure 6.5: Cosmological constraints on the dark energy equation of state parameters w_0 and w_a from CMBpol in combination with SNAP-quality supernova distances. Within each panel the contours correspond to systematic cuts at $l_{\max} = 1000$, 2000, 3000, 4000 from outer to inner. The panels use different data cuts: no lensing (upper left), including lensing from T- and E-modes (upper right), including lensing from T-, E- and B-modes (lower left), and including lensing through the optimal quadratic estimator of the lensing potential (lower right). The dotted curve gives the constraints from supernovae alone.

6.5 Exploring Early Dark Energy

In ΛCDM, the fractional contribution of dark energy density is of order 10^{-9} at last scattering. However, many models exist where this can be at the percent level [75],

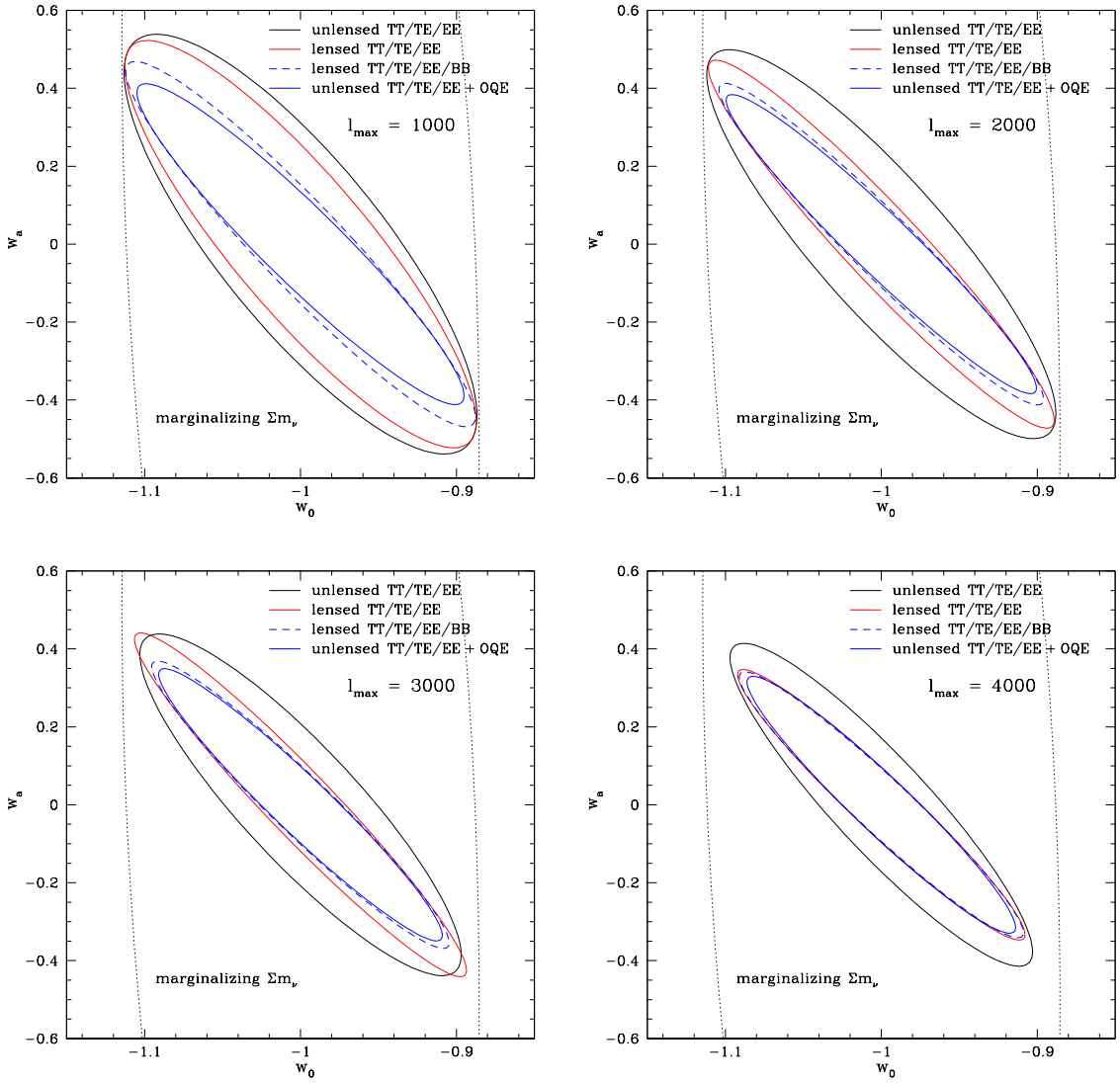

Figure 6.6: As Fig. 6.5 but here within each panel the contours correspond to data set types, and the panels use different systematics levels: $l_{\rm max} = 1000$ (upper left), 2000 (upper right), 3000 (lower left), 4000 (lower right). Since using lensed TT/EE/TE spectra is not a matter of simply adding to the Fisher matrix from unlensed spectra, it is possible for a lensed contour to lie slightly outside of the unlensed contour, as in the $l_{\rm max} = 3000$ case.

with important impacts on the sound horizon scale and baryon acoustic oscillations, structure formation, and secondary anisotropies [75, 74, 151, 190, 157, 88, 96]. Such early dark energy models follow from physics where the dark energy traces the energy density of the dominant component of the universe, as in high energy physics and

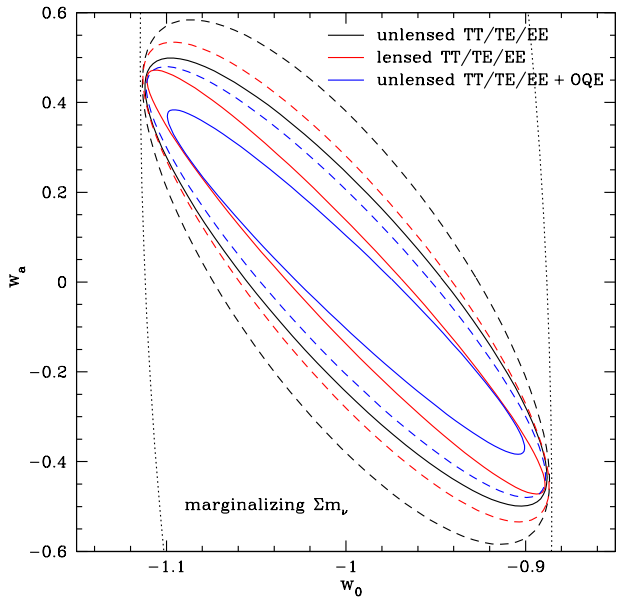

Figure 6.7: Comparing the cosmological constraints on the dark energy equation of state parameters from Planck (dashed contours) vs. CMBpol (solid), taking $l_{\rm max} = 2000$ and including SNAP-quality supernova distances. The dotted curve gives the constraints from supernovae alone.

string theory models with dilatation symmetries [233].

Although the sound horizon is altered in the presence of early dark energy by $\sim (1-\Omega_e)^{1/2}$, this shift can be hidden in the temperature power spectrum by compensating changes in the other parameters [157]. This is problematic for baryon acoustic oscillation experiments, which use the sound horizon as a standard ruler to probe cosmology through distances. More generally, definitive recognition of early dark energy is quite important to have confidence in the accurate estimation of the other parameters, ensuring that they are not biased due to incorrectly assuming no early dark energy. Furthermore, detection of early dark energy would immediately give crucial clues to understanding the nature of dark energy.

Since CMB lensing depends on the growth of structure, it is a good candidate for constraining dark energy. More generally, hints already exist in [157] that polarization information can help break degeneracies involving early dark energy. Here we carry out a more comprehensive likelihood analysis for unlensed polarization power spectra and examine for the first time CMB lensing constraints on early dark energy. To do this, we employ the parametrization for the fractional dark energy density as a

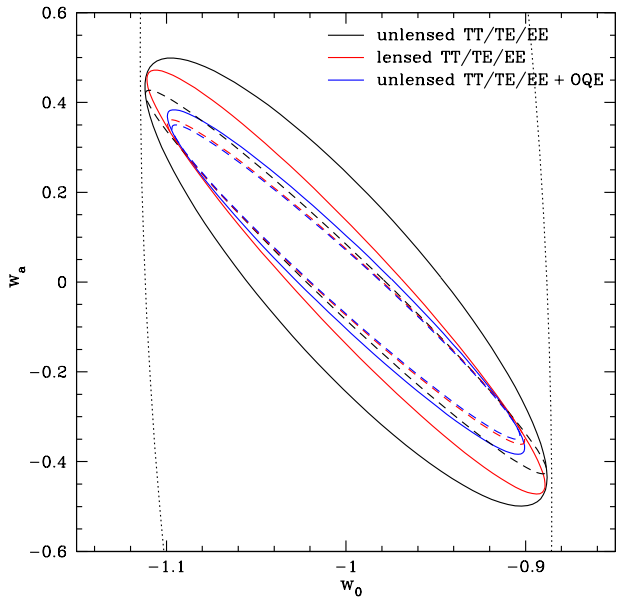

Figure 6.8: As Fig. 6.7 for CMBpol only, but here showing the effect of fixing $\sum m_\nu$ (dashed contours) rather than marginalizing over it (solid) as is standard for all parameters not shown.

function of scale factor proposed by [74],

$$\Omega_{\rm DE}(a) = \frac{\Omega_{\rm DE} - \Omega_e\left(1 - a^{-3w_0}\right)}{\Omega_{\rm DE} + \Omega_m a^{3w_0}} + \Omega_e\left(1 - a^{-3w_0}\right), \tag{6.8}$$

where $\Omega_{\rm DE}$ is the current dark energy density, Ω_e is the constant dark energy density at early times, and w_0 is the present dark energy equation of state. Hence, the two added parameters Ω_e and w_0 describe the dark energy properties.

Figure 6.9 shows the constraints in the w_0-Ω_e plane, marginalizing over the other seven parameters, for different data set types. The fiducial model has $w_0 = -0.95$, $\Omega_e = 0.03$. As in the w_0-w_a case, the CMB degeneracies are too strong to allow constraints by the CMB alone, so we have again folded in supernova distance data (which does not directly constrain Ω_e). We see that unlensed power spectra including polarization information can indeed tightly constrain early dark energy. Adding lensed CMB information in fact mostly constrains further w_0, having minimal effect on Ω_e. Recall from §6.2.1 that out to $z \approx 2$, the early dark energy model looks very much like a standard w_0-w_a model that would not give appreciable early dark energy density. Thus, early dark energy is too early for even the broad redshift kernel of CMB lensing to have significant sensitivity to it.

Figure 6.10 exhibits the analogous situation for different systematic limits $l_{\rm max}$.

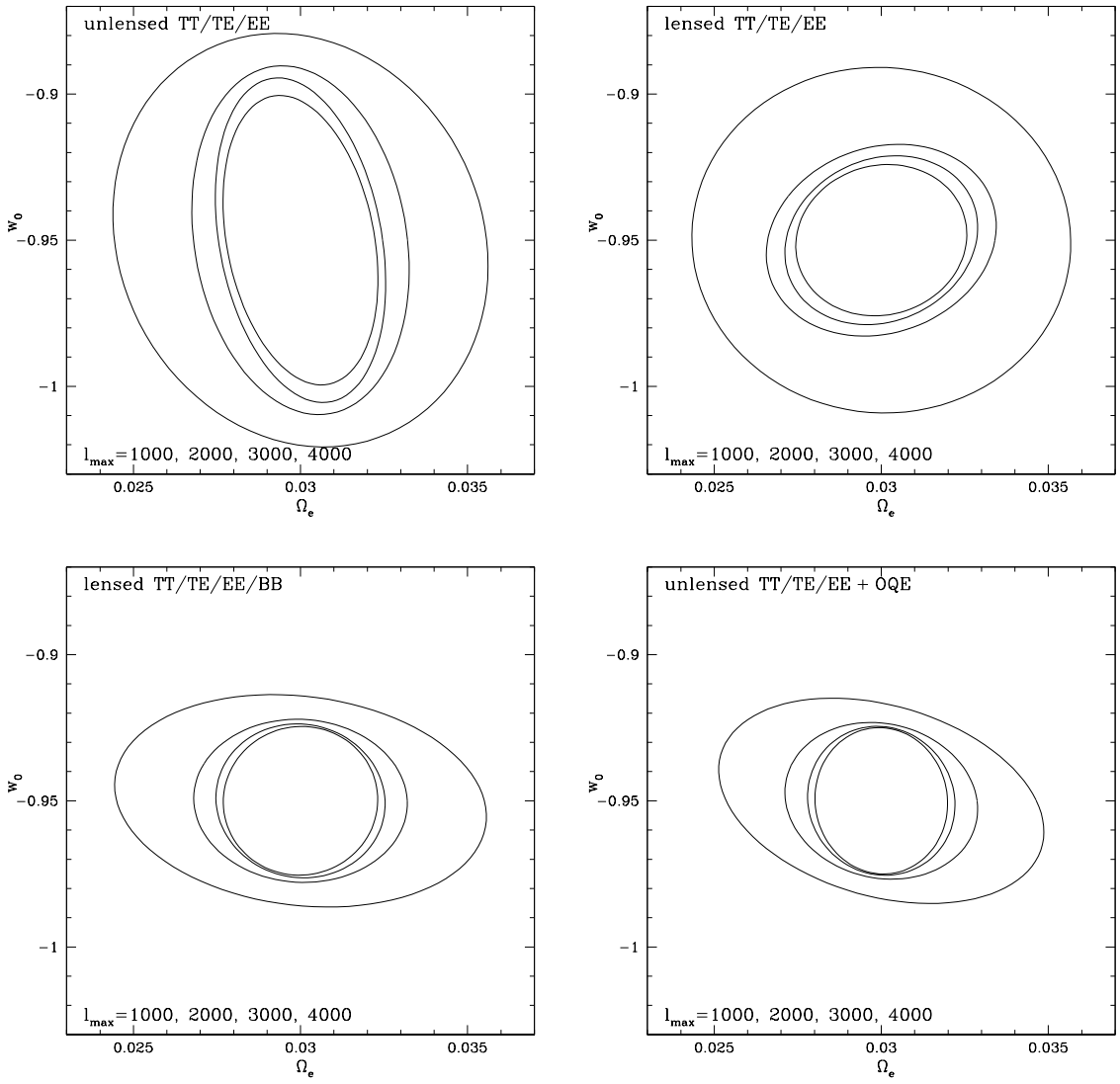

Figure 6.9: Cosmological constraints on the early dark energy fraction Ω_e and present equation of state parameter w_0 from CMBpol in combination with SNAP-quality supernova distances. Within each panel the contours correspond to systematic cuts at $l_{\rm max} = 1000$, 2000, 3000, 4000 from outer to inner. The panels use different data cuts: no lensing (upper left), including lensing from T- and E-modes (upper right), including lensing from T-, E- and B-modes (lower left), and including lensing through the optimal quadratic estimator of the lensing potential (lower right).

Again in contrast to the ΛCDM case, here the constraints continue to improve for higher $l_{\rm max}$, although less rapidly for $l_{\rm max} \gtrsim 3000$. The fully marginalized uncertainties for the $l_{\rm max} = 2000$, full lensing case are $\sigma(\sum m_\nu) = 0.047$, $\sigma(w_0) = 0.018$, $\sigma(\Omega_e) =$

0.0019. This is an impressive constraint on the early dark energy density, able to give definite guidance to the nature of dark energy, ruling out classes of models.

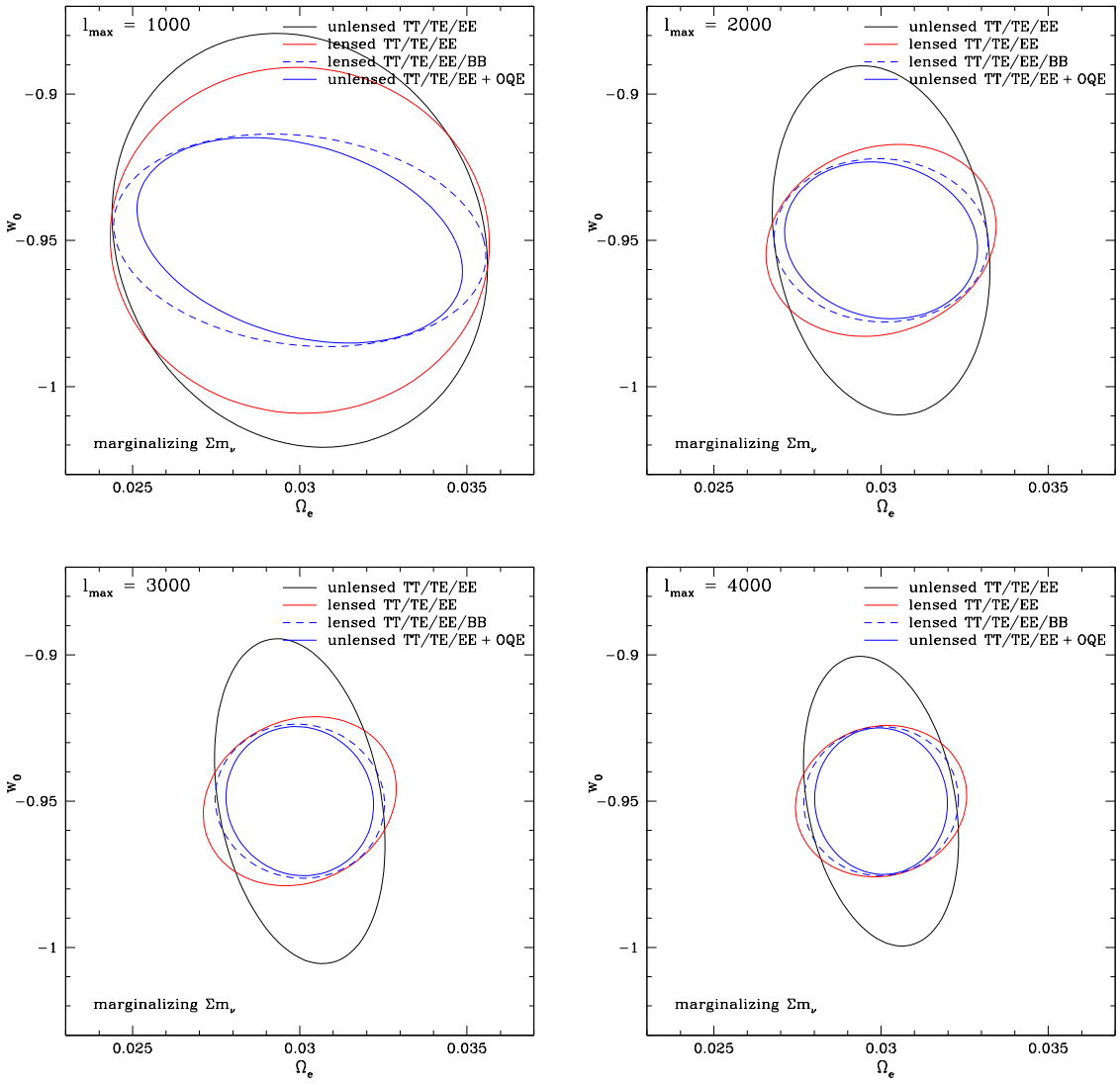

Figure 6.10: As Fig. 6.9 but here within each panel the contours correspond to data set types, and the panels use different systematics levels: $l_{\rm max} = 1000$ (upper left), 2000 (upper right), 3000 (lower left), 4000 (lower right). Since using lensed TT/EE/TE spectra is not a matter of simply adding to the Fisher matrix from unlensed spectra, it is possible for a lensed contour to lie slightly outside of the unlensed contour.

Because CMBpol would have much better polarization measurements than Planck, it will constrain Ω_e better by a factor 2.2, as shown in Fig. 6.11. The area of the dark energy properties' confidence contour improves by a factor 3.9.

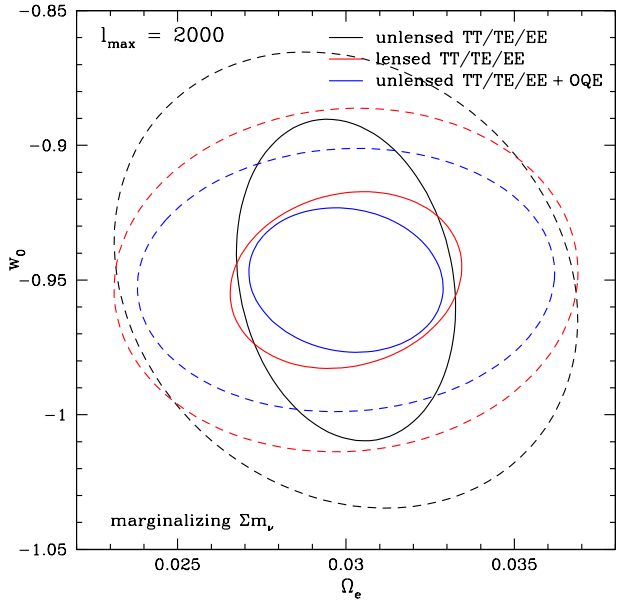

Figure 6.11: Comparing the cosmological constraints on the early dark energy fraction Ω_e and present equation of state parameter w_0 from Planck (dashed contours) vs. CMBpol (solid), taking $l_{\rm max} = 2000$ and including SNAP-quality supernova distances.

Finally, we summarize our results for the dark energy and neutrino mass uncertainties in Table 6.2 for the three cosmological models considered, assuming $l_{\rm max} = 2000$. However, one should see the figures for the full contours. Due to degeneracies in the presence of dynamical dark energy, we add supernova data in these cases to constrain the dark energy equation of state, although the uncertainties on Ω_e and $\sum m_\nu$ are not strongly affected.

6.6 Shortcut for Joint Dark Energy Constraints

As seen in Section 6.4, when CMB and supernova data are combined, we can obtain strong constraints on the nature of dark energy. While the supernova data dependence on cosmological parameters is straightforward, calculating a CMB Fisher matrix can be quite time consuming. The procedure requires computing multiple CMB spectra using a Boltzmann code (CMBeasy in our case) for different values within a set of cosmological parameters in order to obtain the derivatives of the observables with respect to the cosmological parameters.

To investigate a range of cosmological models it would therefore be quite useful to have a shortcut to calculating the constraints on the dark energy parameters

Model	Experiment	$\sigma(w_0)$	$\sigma(w_a)$	$\sigma(\Omega_e)$	$\sigma(\Sigma m_\nu)$ [eV]
ΛCDM	Planck	–	–	–	0.11
ΛCDM	CMBpol	–	–	–	0.036
w_0-w_a	Planck+SN	0.073	0.32	–	0.13
w_0-w_a	CMBpol+SN	0.066	0.25	–	0.041
w_0-Ω_e	Planck+SN	0.032	–	0.0041	0.15
w_0-Ω_e	CMBpol+SN	0.018	–	0.0019	0.047

Table 6.2: Uncertainties in parameters beyond standard ΛCDM for Planck and CMBpol. In all cases, we use unlensed temperature and polarization spectra and the optimal quadratic estimator of the lensing spectrum to extract cosmological information from the CMB data. For cases involving dynamical dark energy we fold in supernova distance information from a SNAP-like JDEM experiment, although this mostly affects only the uncertainties on w_0, w_a.

$w_0, w_a, \Omega_{\rm DE}$ from CMB data. One such shortcut is historically well known, the shift parameter [79] to encapsulate the information in the temperature power spectrum acoustic peaks. However, as polarization data gets added, other parameters have been suggested as additions, e.g. the acoustic peak scale l_A [137], although [154] showed that the shift parameter is still quite accurate. Here we investigate the cosmological constraints from combining CMB temperature, polarization, and possibly deflection, spectra and supernova data, and we show that a simple use of the shift parameter has excellent accuracy.

Specifically, for constraints on the dark energy parameters a strong prior on the shift parameter, or reduced distance to last scattering, $\tilde{d} = \sqrt{\omega_m}\, d_{\rm lss}$, is nearly equivalent to the full CMB data, even including polarization and lensing data. That is, the CMB Fisher matrix for $\Omega_{\rm DE}, w_0, w_a$ after marginalizing over the other parameters is almost identical to the Fisher matrix calculated from a single constraint on $\tilde{d}$[4]. The prior on the quantity $\tilde{d}$ required to match the CMB data depends on the CMB experiment and on whether or not we fix the neutrino mass. We emphasize that the level of the prior does not correspond to the actual determination of $\tilde{d}$ from the experiment, because the prior also encodes the other spectra information. For the CMB experiments we consider, the equivalent prior on $\tilde{d}$ is $0.2\% - 1.2\%$.

Note that because early dark energy does not merely affect the projection of the last scattering surface onto our sky, but also affects the shape of the anisotropy spectrum at last scattering directly, we do not expect the $\tilde{d}$ prior to be a complete description there and indeed we found the prior is not effective in this case.

We compare the shift parameter prescription to the use of the actual CMB Fisher matrix in Fig. 6.12 by considering 1σ joint contours in the $w_0 - w_a$ plane for CMB +

[4]Note this holds for the CMB Fisher matrix itself, without any supernova information.

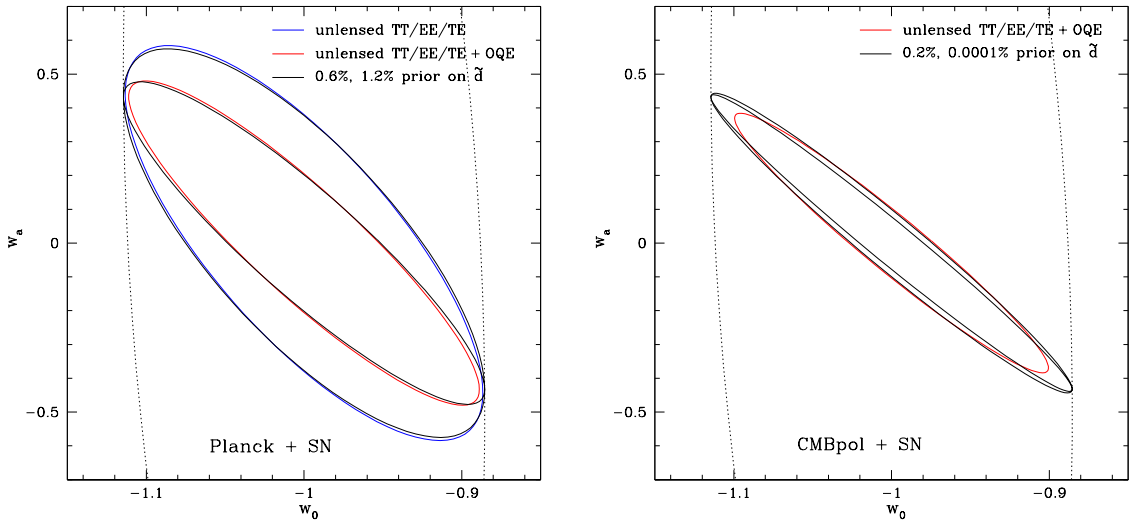

Figure 6.12: Joint constraints from CMB and supernovae can be well approximated by simply replacing the CMB data by an appropriately sized prior on the shift parameter $\tilde{d} = \sqrt{\omega_m}\, d_{\rm lss}$. [Left panel] Combining Planck data with supernovae, the dark blue (light red) curves represent not using (using) lensing information. These two cases are well approximated by replacing CMB data by $\tilde{d}$ priors of 1.2% and 0.6% respectively. [Right panel] Combining CMBpol data with supernovae, the light red curve represents using lensing information. This is fairly well approximated by a $\tilde{d}$ prior of 0.2% (outer black curve). Tighter priors have little effect (see inner black curve). Both panels take $l_{\rm max} = 2000$, and the dotted line in both panels is the contour from just supernova data.

SN. For Planck (top panel), if we marginalize over $\sum m_\nu$ and if we do not include the information from CMB lensing, the constraints from the CMB+SN are almost exactly the same as those with a 1.2% prior on $\tilde{d}$. The constraints are improved quite a bit if the lensing information is added. In this case, the constraints are about the same as the constraints one gets with a 0.6% prior on $\tilde{d}$. In the case of fixing $\sum m_\nu$ instead of marginalizing over it, the shift parameter prior applies as well, at 0.2% matching the CMB+SN contours whether lensing information is used or not. Interestingly, in the case of fixed $\sum m_\nu$, adding lensing information does not appreciably improve the constraints on w_0 and w_a any more.

Note that the Planck experiment can be approximated extremely well by the shift parameter prior in all these cases. The extent $\sigma(w_0)$, $\sigma(w_a)$, width $\sigma(w_p)$, area $1/\sqrt{\det \mathbf{F}}$, and orientation of the dark energy EOS contours match, as seen in Fig. 6.12 and quantified in Table 6.3.

For CMBpol (bottom panel of Fig. 6.12), the constraints on dark energy can be very well approximated by a 0.2% prior on the shift parameter. This is true

Data	$\sigma(w_0)$	$\sigma(w_a)$	$\sigma(w_p)$	$\sqrt{\det \mathbf{F}}$
SN+Planck	0.073	0.32	0.031	101
SN+0.6% $\tilde{d}$	0.076	0.31	0.032	99
SN+CMBpol	0.066	0.25	0.018	223
SN+0.2% $\tilde{d}$	0.076	0.29	0.017	202

Table 6.3: Dark energy constraints from supernovae and CMB compared to constraints from supernovae and a prior on the shift parameter $\tilde{d}$. We assume $l_{\rm max} = 2000$ and use the optimal quadratic estimator to extract lensing information for both Planck and CMBpol. We marginalize over the sum of the neutrino masses and over the other parameters of the model. Note $\sigma(w_p)$ is the width of the w_0-w_a contour at $w_a = 0$ (i.e. the uncertainty in constant w) and $\sqrt{\det \mathbf{F}}$ is the inverse area of the contour (sometimes used as a figure of merit).

independent of whether one fixes m_ν or marginalizes over it because for CMBpol with lensing, fixing m_ν only improves the constraints on w_0 and w_a a little bit compared to marginalizing over m_ν (see Fig. 6.8). Note that making the prior on $\tilde{d}$ even smaller than 0.2% does not change the contour significantly. To illustrate this, Fig. 6.12 shows the contour for a prior of 0.0001%, essentially fixing $\tilde{d}$. It is almost the same as the contour for 0.2%.

The combination of supernova data with a prior on $\tilde{d}$ always gives an ellipse with ends touching the contour from supernovae alone. This means that while both the area enclosed by the contour and the uncertainty in w_a may be improved, the uncertainty in w_0 is the same as the uncertainty from supernova data only. Since Planck constraints are described almost perfectly by the shift parameter, this is also true for Planck. However, once we include precision measurements of polarization by considering CMBpol, the ends of the error ellipse can move away from the "SN only" contour and thus (slightly) improve the constraint on w_0. This effect cannot be reproduced by the prior on the shift parameter. Hence, for CMBpol, the shift parameter prescription works less well than for Planck, although it is still quite adequate. Again, Table 6.3 quantifies the accuracy of substituting the prior in place of the full CMB spectra.

6.7 Progress in Near-term Experiments: PolarBear

In this section we explore the merit of near term ground-based polarization sensitive CMB missions to constrain dark energy and neutrino properties. A number of such experiments are currently being built or have been funded including BI-

CEP/BICEP2 [222], BRAIN [46], CℓOVER [171], EBEX [173], QUIET [191], Spider [57], SPTpol. Here we focus on one of them, PolarBear, as it represents a good combination of the high angular resolution and sensitivity some of these experiments will be capable of.

PolarBear is a ground based telescope with scheduled beginning of operations in 2009, and deployment to Northern Chile in 2010. It plans to observe 2.5% of the sky. The low noise of its detectors will enable this experiment to go beyond Planck in imaging the B-type polarization pattern, which on small scales is a clear signature of gravitational lensing as it cannot be produced by scalar fluctuations. However, the smaller sky coverage does not allow the lensing potential power spectrum to be constrained with as high a signal-to-noise on most scales, making forecasted constraints generally somewhat less good. To describe this experiment's capabilities, we have adopted specifications from [50], and the resulting likelihood contours are shown in Fig. 6.13.

The cosmological constraints from PolarBear lensing reconstruction are less good than those from Planck, despite the significantly lower noise level. The reason is simply that the limited sky coverage does not allow most modes in the temperature, polarization, and lensing potential power spectra to be constrained with as high overall signal-to-noise. However the constraints are still interesting relative to current limits. Moreover, we particularly note that our parameter space has been limited to not include tensor fluctuations, which are a natural consequence of inflationary models. With its low noise level PolarBear will attempt to measure these gravitational waves from inflation and will help break degeneracies between the tensor-to-scalar ratio and other parameters that are present in the Planck data. Furthermore, we have not included running of the scalar spectral index; again, PolarBear's high resolution and low noise will provide an advantage in breaking degeneracies once running is included.

We have found that with Planck the use of the quadratic estimator vs. lensed power spectra leads to a significant improvement of the constraints on parameters to which lensing is sensitive. To be specific, we find a 39% improvement on the neutrino mass scale and a 26% improvement on Ω_Λ. The improvement in the case of PolarBear and CMBpol is however only marginal. To illuminate this trend, in Figure 6.14 we plot the power spectra of the lensing potential and lensing reconstruction noises as well as the total errors. The dotted lines show the lensing reconstruction noises for each experiment. PolarBear has better capability to map the lensing potential in the observed patches on the sky than Planck (although it reconstructs far fewer of these patches and therefore the total error is larger than for Planck). The lower lensing noise feeds into the estimation with the optimal quadratic estimator for reconstruction.

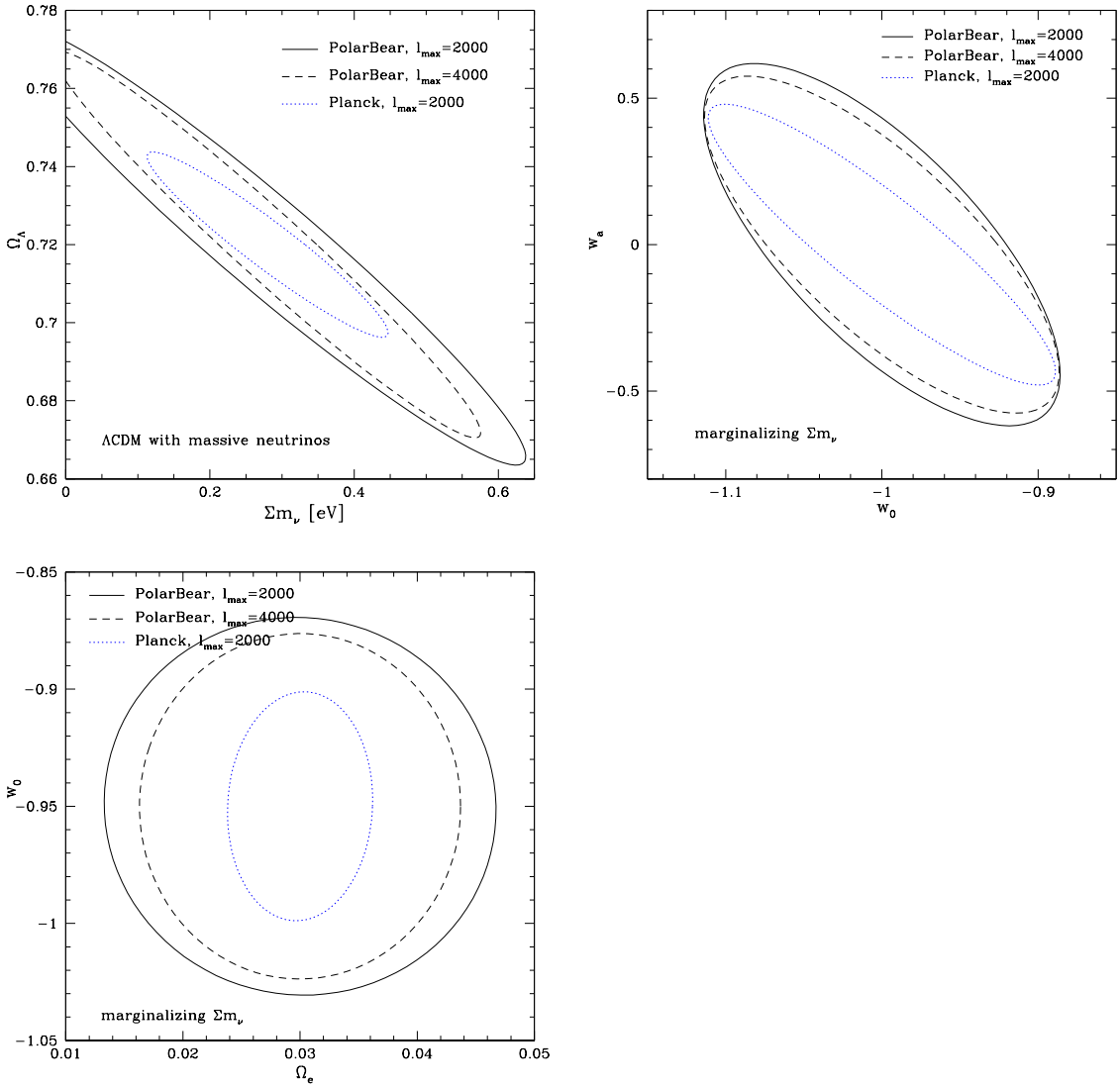

Figure 6.13: Constraints from the intermediate experiment PolarBear are not as strong as Planck within the restricted inflationary scenario assumed here. Contours are constructed using unlensed TT/TE/EE data plus the optimal quadratic estimator for the lensing spectrum. Blue dotted contours repeat the results for Planck from Figs. 6.4, 6.7, 6.11.

6.8 Conclusions

Continued advances are expected in measuring the cosmic microwave background radiation including lower noise and better systematics control, smaller beams and wider surveys, and extension to polarization, cross spectra, and CMB lensing in-

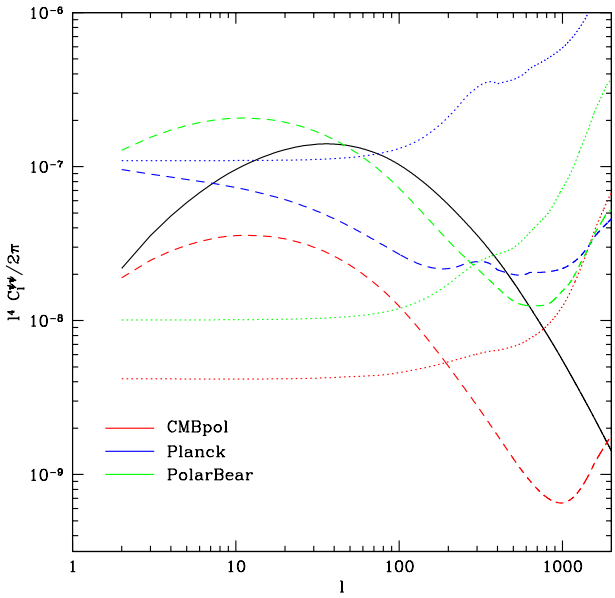

Figure 6.14: The lensing potential power spectrum (solid line) is shown together with the lensing reconstruction noises for the three experiments considered in this work (dotted lines) and the total error on individual multipoles in the lensing potential, a combination of sample variance and noise (dashed lines).

formation. These will greatly improve our knowledge of a variety of cosmological parameters related to primordial perturbations. Here we have explored their impact on physics where the CMB has not had as much direct leverage – extensions to the standard model of cosmology such as the necessary neutrino mass and the suspected dynamics of dark energy.

We find the following general points to guide the design and analysis of CMB experiments, both ground based and the CMBpol satellite concept:

- Systematics, such as point sources and other foreground contamination, will affect the lensing potential and other power spectra, and should be removed at the level of at least $l_{\rm max} = 2000$. Constraints improve only slowly for higher $l_{\rm max}$ when using the full information in the CMB.

- Analysis of gravitational lensing of the CMB can proceed either through consideration of induced B-mode polarization or through an optimal quadratic estimator directly of the deflection field; the optimum is not steep so the two approaches are nearly equivalent for these purposes with data beyond Planck.

- For exploration of suites of cosmological models, we establish the accuracy of

a shortcut in terms of an effective prior on the CMB shift parameter. This is remarkably efficient in summarizing the information from the CMB spectra.

Determination of the sum of neutrino masses can be accomplished by CMBpol with an uncertainty of 0.05 eV, marginalizing over all other parameters including dark energy properties. This corresponds to greater than a 5σ detection for the fiducial value adopted, and represents a factor 3 improvement over Planck expectations. Restricted to a ΛCDM cosmology, the constraints tighten by a factor ~ 1.3.

Determination of the dynamical properties of dark energy is less powerful. Complementary information, such as from distance measurements, is required with the leverage of the two data sets together allowing significant constraints. The present dark energy equation of state w_0 could be estimated to 0.07 and the time variation w_a to 0.25, including marginalization over other cosmological parameters including neutrino mass. This would improve further as other probes are added. While the marginalized constraints do not improve greatly in going from Planck to CMBpol, the area of the uncertainty contour shrinks by a factor 2.

The most significant impact from the CMB comes within early dark energy models. Here the improvement from Planck to CMBpol is a factor 2 in estimation of both w_0 (to 0.02 for CMBpol plus distances) and early dark energy density Ω_e (to 0.002 for CMBpol plus distances), while the uncertainty area shrinks by a factor 4. This provides the possibility of a $\sim 10\sigma$ detection of early dark energy, which would immediately revolutionize our physics thinking.

CMB lensing offers an intriguing new window on the universe, especially because of its sensitivity to the properties of expansion and growth in the poorly probed epoch $z \approx 1-4$. Experiments nearly in the process of data collection will teach us not only about the primordial conditions but also about the interesting period when dark energy first becomes significant, as well as establishing a link to terrestrial experiments to measure the neutrino masses.

Bibliography

[1] http://jdem.gsfc.nasa.gov/.

[2] http://rkb.home.cern.ch/rkb/an16pp/node40.html.

[3] http://sci.esa.int/euclid/.

[4] http://www.lsst.org/.

[5] http://www.sciops.esa.int/planck/.

[6] L. R. Abramo and N. Pinto-Neto. Stability of phantom k-essence theories. *Phys.Rev.D*, 73(6):063522, March 2006, arXiv:astro-ph/0511562.

[7] N. Afshordi. Integrated Sachs-Wolfe effect in cross-correlation: The observer's manual. *Phys.Rev.D*, 70(8):083536, October 2004, arXiv:astro-ph/0401166.

[8] N. Afshordi, Y.-S. Loh, and M. A. Strauss. Cross-correlation of the cosmic microwave background with the 2MASS galaxy survey: Signatures of dark energy, hot gas, and point sources. *Phys.Rev.D*, 69(8):083524, April 2004, arXiv:astro-ph/0308260.

[9] A. Albrecht and G. Bernstein. Evaluating dark energy probes using multidimensional dark energy parameters. *Phys.Rev.D*, 75(10):103003, May 2007, arXiv:astro-ph/0608269.

[10] A. Albrecht, G. Bernstein, R. Cahn, W. L. Freedman, J. Hewitt, W. Hu, J. Huth, M. Kamionkowski, E. W. Kolb, L. Knox, J. C. Mather, S. Staggs, and N. B. Suntzeff. Report of the Dark Energy Task Force. *ArXiv Astrophysics e-prints*, September 2006, arXiv:astro-ph/0609591.

[11] A. Albrecht and C. Skordis. Phenomenology of a Realistic Accelerating Universe Using Only Planck-Scale Physics. *Phys.Rev.Lett.*, 84:2076–2079, March 2000, arXiv:astro-ph/9908085.

[12] D. Alighieri. *Inferno, Canto I, 2.*

[13] S. W. Allen, D. A. Rapetti, R. W. Schmidt, H. Ebeling, R. G. Morris, and A. C. Fabian. Improved constraints on dark energy from Chandra X-ray observations of the largest relaxed galaxy clusters. *MNRAS*, 383:879–896, January 2008, arXiv:0706.0033.

[14] R. Amanullah *et al.* Spectra and Light Curves of Six Type Ia Supernovae at $0.511 < z < 1.12$ and the Union2 Compilation. *Astrophys.J. accepted*, April 2010, arXiv:1004.1711.

[15] L. Amendola, I. Waga, and F. Finelli. Observational constraints on silent quartessence. *JCAP*, 11:9, November 2005, arXiv:astro-ph/0509099.

[16] C. Armendáriz-Picón, T. Damour, and V. Mukhanov. k-Inflation. *Phys.Lett.B*, 458:209–218, July 1999, arXiv:hep-th/9904075.

[17] C. Armendariz-Picon, V. Mukhanov, and P. J. Steinhardt. Dynamical Solution to the Problem of a Small Cosmological Constant and Late-Time Cosmic Acceleration. *Phys.Rev.Lett.*, 85:4438–4441, November 2000, arXiv:astro-ph/0004134.

[18] C. Armendariz-Picon, V. Mukhanov, and P. J. Steinhardt. Essentials of k-essence. *Phys.Rev.D*, 63(10):103510, May 2001, arXiv:astro-ph/0006373.

[19] D. Babich. Optimal estimation of non-Gaussianity. *Phys.Rev.D*, 72(4):043003, August 2005, arXiv:astro-ph/0503375.

[20] J. S. Bagla, H. K. Jassal, and T. Padmanabhan. Cosmology with tachyon field as dark energy. *Phys.Rev.D*, 67(6):063504, March 2003, arXiv:astro-ph/0212198.

[21] Guillermo Ballesteros and Antonio Riotto. Parameterizing the Effect of Dark Energy Perturbations on the Growth of Structures. *Phys. Lett.*, B668:171–176, 2008, arXiv:0807.3343.

[22] J. M. Bardeen. Gauge-invariant cosmological perturbations. *Phys.Rev.D*, 22:1882–1905, October 1980.

[23] M. Barnard, A. Abrahamse, A. Albrecht, B. Bozek, and M. Yashar. Measure of the impact of future dark energy experiments based on discriminating power among quintessence models. *Phys.Rev.D*, 78(4):043528, August 2008, arXiv:0804.0413.

[24] M. Bartelmann and P. Schneider. Weak gravitational lensing. *Physics Reports*, 340:291–472, January 2001, arXiv:astro-ph/9912508.

[25] S. Bashinsky. Mapping Cosmological Observables to the Dark Kinetics. *ArXiv e-prints*, July 2007, arXiv:0707.0692.

[26] R. Bean, S. H. Hansen, and A. Melchiorri. Early-universe constraints on dark energy. *Phys.Rev.D*, 64(10):103508, November 2001, arXiv:astro-ph/0104162.

[27] Rachel Bean and Olivier Dore. Probing dark energy perturbations: the dark energy equation of state and speed of sound as measured by WMAP. *Phys. Rev.*, D69:083503, 2004, arXiv:astro-ph/0307100.

[28] M. C. Bento, O. Bertolami, and A. A. Sen. Generalized Chaplygin gas, accelerated expansion, and dark-energy-matter unification. *Phys.Rev.D*, 66(4):043507, August 2002, arXiv:gr-qc/0202064.

[29] G. Bernstein and B. Jain. Dark Energy Constraints from Weak-Lensing Cross-Correlation Cosmography. *Astrophys.J.*, 600:17–25, January 2004, arXiv:astro-ph/0309332.

[30] E. Bertschinger. On the Growth of Perturbations as a Test of Dark Energy and Gravity. *Astrophys.J.*, 648:797–806, September 2006, arXiv:astro-ph/0604485.

[31] N. Bilić, G. B. Tupper, and R. D. Viollier. Unification of dark matter and dark energy: the inhomogeneous Chaplygin gas. *Phys.Lett.B*, 535:17–21, May 2002, arXiv:astro-ph/0111325.

[32] S. Boughn and R. Crittenden. A correlation between the cosmic microwave background and large-scale structure in the Universe. *Nature*, 427:45–47, January 2004, arXiv:astro-ph/0305001.

[33] R. Bousso. The cosmological constant. *General Relativity and Gravitation*, 40:607–637, February 2008, arXiv:0708.4231.

[34] L. A. Boyle, R. R. Caldwell, and M. Kamionkowski. Spintessence! New models for dark matter and dark energy. *Phys.Lett.B*, 545:17–22, October 2002, arXiv:astro-ph/0105318.

[35] B. Bozek, A. Abrahamse, A. Albrecht, and M. Barnard. Exploring parameter constraints on quintessential dark energy: The exponential model. *Phys.Rev.D*, 77(10):103504, May 2008, arXiv:0712.2884.

[36] P. H. Brax and J. Martin. Quintessence and supergravity. *Physics Letters B*, 468:40–45, November 1999, arXiv:astro-ph/9905040.

[37] J.-P. Bruneton. Causality and superluminal behavior in classical field theories: Applications to k-essence theories and modified-Newtonian-dynamics-like theories of gravity. *Phys.Rev.D*, 75(8):085013, April 2007, arXiv:gr-qc/0607055.

[38] A. Cabre, Enrique Gaztanaga, M. Manera, P. Fosalba, and F. Castander. Cross-correlation of WMAP 3rd year and the SDSS DR4 galaxy survey: new evidence for Dark Energy. *Mon. Not. Roy. Astron. Soc.*, 372:L23–L27, 2006, arXiv:astro-ph/0603690.

[39] R. N. Cahn, R. de Putter, and E. V. Linder. Field flows of dark energy. *Journal of Cosmology and Astro-Particle Physics*, 11:15, November 2008, arXiv:0807.1346.

[40] R. Caldwell. in sources and detection of dark matter in the universe (dm2000), ed. d. cline, p. 74 (springer: 2001); http://www.dartmouth.edu/∼caldwell/index_files/dm2000.ps.

[41] R. R. Caldwell. A phantom menace? Cosmological consequences of a dark energy component with super-negative equation of state. *Phys.Lett.B*, 545:23–29, October 2002, arXiv:astro-ph/9908168.

[42] R. R. Caldwell and M. Doran. Dark-energy evolution across the cosmological-constant boundary. *Phys.Rev.D*, 72(4):043527, August 2005, arXiv:astro-ph/0501104.

[43] R. R. Caldwell and M. Kamionkowski. The Physics of Cosmic Acceleration. *Ann.Rev.Nucl.& Part.Sci*, 59:397–429, November 2009, arXiv:0903.0866.

[44] R. R. Caldwell and E. V. Linder. Limits of Quintessence. *Phys.Rev.Lett.*, 95(14):141301, September 2005, arXiv:astro-ph/0505494.

[45] S. Chaplygin. *Sci. Mem. Moscow Univ. Math. Phys.*, 21:1, 1904.

[46] R. Charlassier and for the BRAIN Collaboration. The BRAIN experiment, a bolometric interferometer dedicated to the CMB B-mode measurement. *ArXiv e-prints*, May 2008, arXiv:0805.4527.

[47] T. Chiba, T. Okabe, and M. Yamaguchi. Kinetically driven quintessence. *Phys.Rev.D*, 62(2):023511, July 2000, arXiv:astro-ph/9912463.

[48] L. P. Chimento and A. Feinstein. Power-Low Expansion in k-ESSENCE Cosmology. *Mod.Phys.Lett.A*, 19:761–768, 2004, arXiv:astro-ph/0305007.

[49] M. Chu, H. K. Eriksen, L. Knox, K. M. Górski, J. B. Jewell, D. L. Larson, I. J. O'Dwyer, and B. D. Wandelt. Cosmological parameter constraints as derived from the Wilkinson Microwave Anisotropy Probe data via Gibbs sampling and the Blackwell-Rao estimator. *Phys.Rev.D*, 71(10):103002, May 2005, arXiv:astro-ph/0411737.

[50] The PolarBear Collaboration. http://bolo.berkeley.edu/polarbear .

[51] A. Cooray and M. Kesden. Weak lensing of the CMB: extraction of lensing information from the trispectrum. *New Astronomy*, 8:231–253, March 2003, arXiv:astro-ph/0204068.

[52] E. J. Copeland, A. R. Liddle, and D. Wands. Exponential potentials and cosmological scaling solutions. *Phys.Rev.D*, 57:4686–4690, April 1998, arXiv:gr-qc/9711068.

[53] E. J. Copeland, M. Sami, and S. Tsujikawa. Dynamics of Dark Energy. *Int.Jour.Mod.Phys.D*, 15:1753–1935, 2006, arXiv:hep-th/0603057.

[54] Pier-Stefano Corasaniti, Tommaso Giannantonio, and Alessandro Melchiorri. Constraining dark energy with cross-correlated CMB and Large Scale Structure data. *Phys. Rev.*, D71:123521, 2005, arXiv:astro-ph/0504115.

[55] D. Cormier and R. Holman. Spinodal Instabilities and the Dark Energy Problem. *Phys.Rev.Lett.*, 84:5936–5939, June 2000, arXiv:hep-ph/0001168.

[56] P. Creminelli, L. Senatore, and M. Zaldarriaga. Estimators for local non-Gaussianities. *JCAP*, 3:19, March 2007, arXiv:astro-ph/0606001.

[57] B. P. Crill, P. A. R. Ade, E. S. Battistelli, S. Benton, R. Bihary, J. J. Bock, J. R. Bond, J. Brevik, S. Bryan, C. R. Contaldi, O. Doré, M. Farhang, L. Fissel, S. R. Golwala, M. Halpern, G. Hilton, W. Holmes, V. V. Hristov, K. Irwin, W. C. Jones, C. L. Kuo, A. E. Lange, C. Lawrie, C. J. MacTavish, T. G. Martin, P. Mason, T. E. Montroy, C. B. Netterfield, E. Pascale, D. Riley, J. E. Ruhl, M. C. Runyan, A. Trangsrud, C. Tucker, A. Turner, M. Viero, and D. Wiebe. SPIDER: a balloon-borne large-scale CMB polarimeter. In *Society of Photo-Optical Instrumentation Engineers (SPIE) Conference Series*, volume 7010 of *Presented at the Society of Photo-Optical Instrumentation Engineers (SPIE) Conference*, August 2008.

[58] R. G. Crittenden and L. Pogosian. Investigating dark energy experiments with principal components. *ArXiv Astrophysics e-prints*, October 2005, arXiv:astro-ph/0510293.

[59] T. M. Davis, J. B. James, B. P. Schmidt, and A. G. Kim. Type Ia supernova diversity: Standardizing the candles. *AIP Conf. Ser.*, 924:330, August 2007, arXiv:astro-ph/0701904.

[60] P. de Bernardis, P. A. R. Ade, J. J. Bock, J. R. Bond, J. Borrill, A. Boscaleri, K. Coble, B. P. Crill, G. De Gasperis, P. C. Farese, P. G. Ferreira, K. Ganga, M. Giacometti, E. Hivon, V. V. Hristov, A. Iacoangeli, A. H. Jaffe, A. E. Lange, L. Martinis, S. Masi, P. V. Mason, P. D. Mauskopf, A. Melchiorri, L. Miglio, T. Montroy, C. B. Netterfield, E. Pascale, F. Piacentini, D. Pogosyan, S. Prunet,

S. Rao, G. Romeo, J. E. Ruhl, F. Scaramuzzi, D. Sforna, and N. Vittorio. A flat Universe from high-resolution maps of the cosmic microwave background radiation. *Nature*, 404:955–959, April 2000, arXiv:astro-ph/0004404.

[61] A. De Felice and S. Tsujikawa. f(R) theories. *ArXiv e-prints*, February 2010, arXiv:1002.4928.

[62] R. de Putter, D. Huterer, and E. V. Linder. Measuring the speed of dark: Detecting dark energy perturbations. *Phys.Rev.D*, 81(10):103513, May 2010, arXiv:1002.1311.

[63] R. de Putter and E. V. Linder. Kinetic k-essence and quintessence. *Astropart.Phys.*, 28:263–272, November 2007, arXiv:0705.0400.

[64] R. de Putter and E. V. Linder. Calibrating dark energy. *JCAP*, 10:42, October 2008, arXiv:0808.0189.

[65] R. de Putter and E. V. Linder. To bin or not to bin: Decorrelating the cosmic equation of state. *Astropart.Phys.*, 29:424–441, July 2008, arXiv:0710.0373.

[66] R. de Putter, O. Zahn, and E. V. Linder. CMB lensing constraints on neutrinos and dark energy. *Phys.Rev.D*, 79(6):065033, March 2009, arXiv:0901.0916.

[67] Simon DeDeo, R. R. Caldwell, and Paul J. Steinhardt. Effects of the sound speed of quintessence on the microwave background and large scale structure. *Phys. Rev.*, D67:103509, 2003, arXiv:astro-ph/0301284.

[68] C. Deffayet, G. Dvali, and G. Gabadadze. Accelerated universe from gravity leaking to extra dimensions. *Phys.Rev.D*, 65(4):044023, February 2002, arXiv:astro-ph/0105068.

[69] James B. Dent, Sourish Dutta, and Thomas J. Weiler. A new perspective on the relation between dark energy perturbations and the late-time ISW effect. *Phys. Rev.*, D79:023502, 2009, arXiv:0806.3760.

[70] J. Dick, L. Knox, and M. Chu. Reduction of cosmological data for the detection of time-varying dark energy density. *JCAP*, 7:1, July 2006, arXiv:astro-ph/0603247.

[71] S. Dodelson. *Modern cosmology*. 2003.

[72] M. Doran. CMBEASY: an object oriented code for the cosmic microwave background. *JCAP*, 10:11, October 2005, arXiv:astro-ph/0302138.

[73] M. Doran and C. M. Müller. Analyse this! A cosmological constraint package for CMBEASY. *JCAP*, 9:3, September 2004, arXiv:astro-ph/0311311.

[74] M. Doran and G. Robbers. Early dark energy cosmologies. *JCAP*, 6:26, June 2006, arXiv:astro-ph/0601544.

[75] M. Doran, G. Robbers, and C. Wetterich. Impact of three years of data from the Wilkinson Microwave Anisotropy Probe on cosmological models with dynamical dark energy. *Phys.Rev.D*, 75(2):023003, January 2007, arXiv:astro-ph/0609814.

[76] R. Durrer. The theory of CMB anisotropies. *Journal of Physical Studies*, 5:177–215, 2001, arXiv:astro-ph/0109522.

[77] G. Dvali, G. Gabadadze, and M. Porrati. 4D gravity on a brane in 5D Minkowski space. *Phys.Lett.B*, 485:208–214, July 2000, arXiv:hep-th/0005016.

[78] G. Dvali and M. S. Turner. Dark Energy as a Modification of the Friedmann Equation. *ArXiv Astrophysics e-prints*, January 2003, arXiv:astro-ph/0301510.

[79] G. Efstathiou and J. R. Bond. Cosmic confusion: degeneracies among cosmological parameters derived from measurements of microwave background anisotropies. *MNRAS*, 304:75–97, March 1999, arXiv:astro-ph/9807103.

[80] A. Einstein. Kosmologische Betrachtungen zur allgemeinen Relativitätstheorie. *Sitzungsberichte der Königlich Preußischen Akademie der Wissenschaften (Berlin), Seite 142-152.*, pages 142–152, 1917.

[81] Joel K. Erickson, R. R. Caldwell, Paul J. Steinhardt, C. Armendariz-Picon, and Viatcheslav F. Mukhanov. Measuring the speed of sound of quintessence. *Phys. Rev. Lett.*, 88:121301, 2002, arXiv:astro-ph/0112438.

[82] H. K. Eriksen, G. Huey, R. Saha, F. K. Hansen, J. Dick, A. J. Banday, K. M. Górski, P. Jain, J. B. Jewell, L. Knox, D. L. Larson, I. J. O'Dwyer, T. Souradeep, and B. D. Wandelt. A Reanalysis of the 3 Year Wilkinson Microwave Anisotropy Probe Temperature Power Spectrum and Likelihood. *Astrophys.J.*, 656:641–652, February 2007, arXiv:astro-ph/0606088.

[83] G. Esposito-Farèse and D. Polarski. Scalar-tensor gravity in an accelerating universe. *Phys.Rev.D*, 63(6):063504, March 2001, arXiv:gr-qc/0009034.

[84] R. Fardon, A. E. Nelson, and N. Weiner. Dark energy from mass varying neutrinos. *JCAP*, 10:5, October 2004, arXiv:astro-ph/0309800.

[85] P. G. Ferreira and M. Joyce. Cosmology with a primordial scaling field. *Phys.Rev.D*, 58(2):023503, July 1998, arXiv:astro-ph/9711102.

[86] P. Fosalba and E. Gaztañaga. Measurement of the gravitational potential evolution from the cross-correlation between WMAP and the APM Galaxy Survey. *MNRAS*, 350:L37–L41, May 2004, arXiv:astro-ph/0305468.

[87] P. Fosalba, E. Gaztañaga, and F. J. Castander. Detection of the Integrated Sachs-Wolfe and Sunyaev-Zeldovich Effects from the Cosmic Microwave Background-Galaxy Correlation. *Astrophys.J.Lett.*, 597:L89–L92, November 2003, arXiv:astro-ph/0307249.

[88] M. J. Francis, G. F. Lewis, and E. V. Linder. Can early dark energy be detected in non-linear structure? *MNRAS*, 394:605–614, April 2009, arXiv:0808.2840.

[89] J. A. Frieman, C. T. Hill, A. Stebbins, and I. Waga. Cosmology with Ultralight Pseudo Nambu-Goldstone Bosons. *Phys.Rev.Lett.*, 75:2077–2080, September 1995, arXiv:astro-ph/9505060.

[90] J. A. Frieman, D. Huterer, E. V. Linder, and M. S. Turner. Probing dark energy with supernovae: Exploiting complementarity with the cosmic microwave background. *Phys.Rev.D*, 67(8):083505, April 2003, arXiv:astro-ph/0208100.

[91] J. A. Frieman, M. S. Turner, and D. Huterer. Dark Energy and the Accelerating Universe. *Ann.Rev.Astron.&Astrophys.*, 46:385–432, September 2008, arXiv:0803.0982.

[92] L. Fu, E. Semboloni, H. Hoekstra, M. Kilbinger, L. van Waerbeke, I. Tereno, Y. Mellier, C. Heymans, J. Coupon, K. Benabed, J. Benjamin, E. Bertin, O. Doré, M. J. Hudson, O. Ilbert, R. Maoli, C. Marmo, H. J. McCracken, and B. Ménard. Very weak lensing in the CFHTLS wide: cosmology from cosmic shear in the linear regime. *Astronomy & Astrophysics*, 479:9–25, February 2008, arXiv:0712.0884.

[93] Tommaso Giannantonio *et al.* Combined analysis of the integrated Sachs-Wolfe effect and cosmological implications. *Phys. Rev.*, D77:123520, 2008, arXiv:0801.4380.

[94] P. Gondolo and K. Freese. Fluid interpretation of Cardassian expansion. *Phys.Rev.D*, 68(6):063509, September 2003, arXiv:hep-ph/0209322.

[95] V. Gorini, A. Kamenshchik, U. Moschella, and V. Pasquier. The Chaplygin Gas as a Model for Dark Energy. In M. Novello, S. Perez Bergliaffa, & R. Ruffini, editor, *The Tenth Marcel Grossmann Meeting. On recent developments in theoretical and experimental general relativity, gravitation and relativistic field theories*, page 840, January 2005.

[96] M. Grossi and V. Springel. The impact of early dark energy on non-linear structure formation. *MNRAS*, 394:1559–1574, April 2009, arXiv:0809.3404.

[97] J. Guzik, U. Seljak, and M. Zaldarriaga. Lensing effect on polarization in the microwave background: Extracting the convergence power spectrum. *Phys.Rev.D*, 62(4):043517, August 2000, arXiv:astro-ph/9912505.

[98] L. J. Hall, Y. Nomura, and S. J. Oliver. Evolving Dark Energy with $w \neq -1$. *Phys.Rev.Lett.*, 95(14):141302, September 2005, arXiv:astro-ph/0503706.

[99] A. J. S. Hamilton and M. Tegmark. Decorrelating the power spectrum of galaxies. *MNRAS*, 312:285–294, February 2000, arXiv:astro-ph/9905192.

[100] Steen Hannestad. Constraints on the sound speed of dark energy. *Phys. Rev.*, D71:103519, 2005, arXiv:astro-ph/0504017.

[101] C. Heymans, M. White, A. Heavens, C. Vale, and L. van Waerbeke. Potential sources of contamination to weak lensing measurements: constraints from N-body simulations. *MNRAS*, 371:750–760, September 2006, arXiv:astro-ph/0604001.

[102] C. M. Hirata and U. Seljak. Analyzing weak lensing of the cosmic microwave background using the likelihood function. *Phys.Rev.D*, 67(4):043001, February 2003, arXiv:astro-ph/0209489.

[103] C. M. Hirata and U. Seljak. Reconstruction of lensing from the cosmic microwave background polarization. *Phys.Rev.D*, 68(8):083002, October 2003, arXiv:astro-ph/0306354.

[104] C. M. Hirata and U. Seljak. Intrinsic alignment-lensing interference as a contaminant of cosmic shear. *Phys.Rev.D*, 70(6):063526, September 2004, arXiv:astro-ph/0406275.

[105] Shirley Ho, Christopher Hirata, Nikhil Padmanabhan, Uros Seljak, and Neta Bahcall. Correlation of CMB with large-scale structure: I. ISW Tomography and Cosmological Implications. *Phys. Rev.*, D78:043519, 2008, arXiv:0801.0642.

[106] H. Hoekstra, Y. Mellier, L. van Waerbeke, E. Semboloni, L. Fu, M. J. Hudson, L. C. Parker, I. Tereno, and K. Benabed. First Cosmic Shear Results from the Canada-France-Hawaii Telescope Wide Synoptic Legacy Survey. *Astrophys.J.*, 647:116–127, August 2006, arXiv:astro-ph/0511089.

[107] R. Holman and S. Naidu. Dark Energy from Wet Dark Fluid. *ArXiv Astrophysics e-prints*, August 2004, arXiv:astro-ph/0408102.

[108] W. Hu. Reionization Revisited: Secondary Cosmic Microwave Background Anisotropies and Polarization. *Astrophys.J.*, 529:12–25, January 2000, arXiv:astro-ph/9907103.

[109] W. Hu. Angular trispectrum of the cosmic microwave background. *Phys.Rev.D*, 64(8):083005, October 2001, arXiv:astro-ph/0105117.

[110] W. Hu. Mapping the Dark Matter through the Cosmic Microwave Background Damping Tail. *Astrophys.J.Lett.*, 557:L79–L83, August 2001, arXiv:astro-ph/0105424.

[111] W. Hu, D. Huterer, and K. M. Smith. Supernovae, the Lensed Cosmic Microwave Background, and Dark Energy. *Astrophys.J.Lett.*, 650:L13–L16, October 2006, arXiv:astro-ph/0607316.

[112] W. Hu and T. Okamoto. Mass Reconstruction with Cosmic Microwave Background Polarization. *Astrophys.J.*, 574:566–574, August 2002, arXiv:astro-ph/0111606.

[113] W. Hu and T. Okamoto. Principal power of the CMB. *Phys.Rev.D*, 69(4):043004, February 2004, arXiv:astro-ph/0308049.

[114] W. Hu and R. Scranton. Measuring dark energy clustering with CMB-galaxy correlations. *Phys.Rev.D*, 70(12):123002, December 2004, arXiv:astro-ph/0408456.

[115] Wayne Hu. Structure Formation with Generalized Dark Matter. *Astrophys. J.*, 506:485–494, 1998, arXiv:astro-ph/9801234.

[116] Wayne Hu. Dark Synergy: Gravitational Lensing and the CMB. *Phys. Rev.*, D65:023003, 2001, arXiv:astro-ph/0108090.

[117] Wayne Hu, Daniel J. Eisenstein, Max Tegmark, and Martin J. White. Observationally Determining the Properties of Dark Matter. *Phys. Rev.*, D59:023512, 1998, arXiv:astro-ph/9806362.

[118] E. Hubble. A Relation between Distance and Radial Velocity among Extra-Galactic Nebulae. *Proceedings of the National Academy of Science*, 15:168–173, March 1929.

[119] D. Huterer. Weak lensing, dark matter and dark energy. *ArXiv e-prints*, January 2010, arXiv:1001.1758.

[120] D. Huterer and A. Cooray. Uncorrelated estimates of dark energy evolution. *Phys.Rev.D*, 71(2):023506, January 2005, arXiv:astro-ph/0404062.

[121] D. Huterer and H. V. Peiris. Dynamical behavior of generic quintessence potentials: Constraints on key dark energy observables. *Phys.Rev.D*, 75(8):083503, April 2007, arXiv:astro-ph/0610427.

[122] D. Huterer and G. Starkman. Parametrization of Dark-Energy Properties: A Principal-Component Approach. *Phys.Rev.Lett.*, 90(3):031301, January 2003, arXiv:astro-ph/0207517.

[123] D. Huterer and M. S. Turner. Probing dark energy: Methods and strategies. *Phys.Rev.D*, 64(12):123527, December 2001, arXiv:astro-ph/0012510.

[124] Kiyotomo Ichiki and Tomo Takahashi. Constraints on Generalized Dark Energy from Recent Observations. *Phys. Rev.*, D75:123002, 2007, arXiv:astro-ph/0703549.

[125] A. H. Jaffe, P. A. Ade, A. Balbi, J. J. Bock, J. R. Bond, J. Borrill, A. Boscaleri, K. Coble, B. P. Crill, P. de Bernardis, P. Farese, P. G. Ferreira, K. Ganga, M. Giacometti, S. Hanany, E. Hivon, V. V. Hristov, A. Iacoangeli, A. E. Lange, A. T. Lee, L. Martinis, S. Masi, P. D. Mauskopf, A. Melchiorri, T. Montroy, C. B. Netterfield, S. Oh, E. Pascale, F. Piacentini, D. Pogosyan, S. Prunet, B. Rabii, S. Rao, P. L. Richards, G. Romeo, J. E. Ruhl, F. Scaramuzzi, D. Sforna, G. F. Smoot, R. Stompor, C. D. Winant, and J. H. Wu. Cosmology from MAXIMA-1, BOOMERANG, and COBE DMR Cosmic Microwave Background Observations. *Phys.Rev.Lett.*, 86:3475–3479, April 2001, arXiv:astro-ph/0007333.

[126] M. Jarvis, B. Jain, G. Bernstein, and D. Dolney. Dark Energy Constraints from the CTIO Lensing Survey. *Astrophys.J.*, 644:71–79, June 2006, arXiv:astro-ph/0502243.

[127] K. Kadota, S. Dodelson, W. Hu, and E. D. Stewart. Precision of inflaton potential reconstruction from CMB using the general slow-roll approximation. *Phys.Rev.D*, 72(2):023510, July 2005, arXiv:astro-ph/0505158.

[128] R. Kallosh, A. Linde, S. Prokushkin, and M. Shmakova. Supergravity, dark energy, and the fate of the universe. *Phys.Rev.D*, 66(12):123503, December 2002, arXiv:hep-th/0208156.

[129] N. Kaloper and L. Sorbo. Of pNGB quiScript Ntessence. *JCAP*, 4:7, April 2006, arXiv:astro-ph/0511543.

[130] A. Kamenshchik, U. Moschella, and V. Pasquier. An alternative to quintessence. *Phys.Lett.B*, 511:265–268, July 2001, arXiv:gr-qc/0103004.

[131] M. Kaplinghat, L. Knox, and Y.-S. Song. Determining Neutrino Mass from the Cosmic Microwave Background Alone. *Phys.Rev.Lett.*, 91(24):241301, December 2003, arXiv:astro-ph/0303344.

[132] E. A. Kazin, M. R. Blanton, R. Scoccimarro, C. K. McBride, A. A. Berlind, N. A. Bahcall, J. Brinkmann, P. Czarapata, J. A. Frieman, S. M. Kent, D. P. Schneider, and A. S. Szalay. The Baryonic Acoustic Feature and Large-Scale Clustering in the Sloan Digital Sky Survey Luminous Red Galaxy Sample. *Astrophys.J.*, 710:1444–1461, February 2010, arXiv:0908.2598.

[133] A. G. Kim, E. V. Linder, R. Miquel, and N. Mostek. Effects of systematic uncertainties on the supernova determination of cosmological parameters. *MNRAS*, 347:909–920, January 2004, arXiv:astro-ph/0304509.

[134] H. Kodama and M. Sasaki. Cosmological Perturbation Theory. *Progress of Theoretical Physics Supplement*, 78:1, 1984.

[135] Tomi Koivisto and David F. Mota. Dark Energy Anisotropic Stress and Large Scale Structure Formation. *Phys. Rev.*, D73:083502, 2006, arXiv:astro-ph/0512135.

[136] E. W. Kolb and M. S. Turner. *The early universe*. 1990.

[137] E. Komatsu, J. Dunkley, M. R. Nolta, C. L. Bennett, B. Gold, G. Hinshaw, N. Jarosik, D. Larson, M. Limon, L. Page, D. N. Spergel, M. Halpern, R. S. Hill, A. Kogut, S. S. Meyer, G. S. Tucker, J. L. Weiland, E. Wollack, and E. L. Wright. Five-Year Wilkinson Microwave Anisotropy Probe Observations: Cosmological Interpretation. *Astropys.J.Suppl.*, 180:330–376, February 2009, arXiv:0803.0547.

[138] E. Komatsu, K. M. Smith, J. Dunkley, C. L. Bennett, B. Gold, G. Hinshaw, N. Jarosik, D. Larson, M. R. Nolta, L. Page, D. N. Spergel, M. Halpern, R. S. Hill, A. Kogut, M. Limon, S. S. Meyer, N. Odegard, G. S. Tucker, J. L. Weiland, E. Wollack, and E. L. Wright. Seven-Year Wilkinson Microwave Anisotropy Probe (WMAP) Observations: Cosmological Interpretation. *ArXiv e-prints*, January 2010, arXiv:1001.4538.

[139] L. M. Krauss and B. Chaboyer. Age Estimates of Globular Clusters in the Milky Way: Constraints on Cosmology. *Science*, 299:65–70, January 2003.

[140] L. M. Krauss and M. S. Turner. The cosmological constant is back. *General Relativity and Gravitation*, 27:1137–1144, November 1995, arXiv:astro-ph/9504003.

[141] D. Larson, J. Dunkley, G. Hinshaw, E. Komatsu, M. R. Nolta, C. L. Bennett, B. Gold, M. Halpern, R. S. Hill, N. Jarosik, A. Kogut, M. Limon, S. S. Meyer, N. Odegard, L. Page, K. M. Smith, D. N. Spergel, G. S. Tucker, J. L. Weiland, E. Wollack, and E. L. Wright. Seven-Year Wilkinson Microwave Anisotropy Probe (WMAP) Observations: Power Spectra and WMAP-Derived Parameters. *ArXiv e-prints*, January 2010, arXiv:1001.4635.

[142] S. Leach. Measuring the primordial power spectrum: principal component analysis of the cosmic microwave background. *MNRAS*, 372:646–654, October 2006, arXiv:astro-ph/0506390.

[143] J. Lesgourgues, L. Perotto, S. Pastor, and M. Piat. Probing neutrino masses with CMB lensing extraction. *Phys.Rev.D*, 73(4):045021, February 2006, arXiv:astro-ph/0511735.

[144] A. Lewis and S. Bridle. Cosmological parameters from CMB and other data: A Monte Carlo approach. *Phys.Rev.D*, 66(10):103511, November 2002, arXiv:astro-ph/0205436.

[145] A. Lewis and A. Challinor. Weak gravitational lensing of the CMB. *Physics Reports*, 429:1–65, June 2006, arXiv:astro-ph/0601594.

[146] A. Lewis, A. Challinor, and A. Lasenby. Efficient Computation of Cosmic Microwave Background Anisotropies in Closed Friedmann-Robertson-Walker Models. *Astrophys.J.*, 538:473–476, August 2000, arXiv:astro-ph/9911177.

[147] A. Linde. *Inflation and quantum cosmology*, pages 604–630. 1987.

[148] E. V. Linder. Analysis of gravitationally lensed microwave background anisotropies. *MNRAS*, 243:353–361, April 1990.

[149] E. V. Linder. Exploring the Expansion History of the Universe. *Phys.Rev.Lett.*, 90(9):091301, March 2003, arXiv:astro-ph/0208512.

[150] E. V. Linder. Biased cosmology: Pivots, parameters, and figures of merit. *Astropart.Phys.*, 26:102–110, September 2006, arXiv:astro-ph/0604280.

[151] E. V. Linder. Dark energy in the dark ages. *Astropart.Phys.*, 26:16–21, August 2006, arXiv:astro-ph/0603584.

[152] E. V. Linder. Paths of quintessence. *Phys.Rev.D*, 73(6):063010, March 2006, arXiv:astro-ph/0601052.

[153] E. V. Linder. The Mirage of w=-1. *ArXiv e-prints*, 708, August 2007, arXiv:0708.0024.

[154] E. V. Linder. Mapping the cosmological expansion. *Reports on Progress in Physics*, 71(5):056901, May 2008, arXiv:0801.2968.

[155] E. V. Linder. The dynamics of quintessence, the quintessence of dynamics. *General Relativity and Gravitation*, 40:329–356, February 2008, arXiv:0704.2064.

[156] E. V. Linder and D. Huterer. How many dark energy parameters? *Phys.Rev.D*, 72(4):043509, August 2005, arXiv:astro-ph/0505330.

[157] E. V. Linder and G. Robbers. Shifting the Universe: early dark energy and standard rulers. *JCAP*, 6:4, June 2008, arXiv:0803.2877.

[158] Eric V. Linder and Robert J. Scherrer. Aetherizing Lambda: Barotropic Fluids as Dark Energy. *Phys. Rev.*, D80:023008, 2009, arXiv:0811.2797.

[159] C.-P. Ma, R. R. Caldwell, P. Bode, and L. Wang. The Mass Power Spectrum in Quintessence Cosmological Models. *Astrophys.J.Lett.*, 521:L1–L4, August 1999, arXiv:astro-ph/9906174.

[160] Chung-Pei Ma and Edmund Bertschinger. Cosmological perturbation theory in the synchronous and conformal Newtonian gauges. *Astrophys. J.*, 455:7–25, 1995, arXiv:astro-ph/9506072.

[161] M. Malquarti, E. J. Copeland, A. R. Liddle, and M. Trodden. A new view of k-essence. *Phys.Rev.D*, 67(12):123503, June 2003, arXiv:astro-ph/0302279.

[162] M. Maltoni and T. Schwetz-Mangold. Three-flavour neutrino oscillation update and comments on possible hints for a non-zero θ_{13}. In *Identification of Dark Matter 2008*, page 72, 2008.

[163] R. Mandelbaum, C. Blake, S. Bridle, F. B. Abdalla, S. Brough, M. Colless, W. Couch, S. Croom, T. Davis, M. J. Drinkwater, K. Forster, K. Glazebrook, B. Jelliffe, R. J. Jurek, I. Li, B. Madore, C. Martin, K. Pimbblet, G. B. Poole, M. Pracy, R. Sharp, E. Wisnioski, D. Woods, and T. Wyder. The WiggleZ Dark Energy Survey: Direct constraints on blue galaxy intrinsic alignments at intermediate redshifts. *ArXiv e-prints*, November 2009, arXiv:0911.5347.

[164] R. Massey, J. Rhodes, R. Ellis, N. Scoville, A. Leauthaud, A. Finoguenov, P. Capak, D. Bacon, H. Aussel, J.-P. Kneib, A. Koekemoer, H. McCracken, B. Mobasher, S. Pires, A. Refregier, S. Sasaki, J.-L. Starck, Y. Taniguchi, A. Taylor, and J. Taylor. Dark matter maps reveal cosmic scaffolding. *Nature*, 445:286–290, January 2007, arXiv:astro-ph/0701594.

[165] R. Massey, J. Rhodes, A. Leauthaud, P. Capak, R. Ellis, A. Koekemoer, A. Réfrégier, N. Scoville, J. E. Taylor, J. Albert, J. Bergé, C. Heymans, D. Johnston, J.-P. Kneib, Y. Mellier, B. Mobasher, E. Semboloni, P. Shopbell, L. Tasca, and L. Van Waerbeke. COSMOS: Three-dimensional Weak Lensing and the Growth of Structure. *Astrophys.J.Supp.*, 172:239–253, September 2007, arXiv:astro-ph/0701480.

[166] A. Melchiorri, L. Mersini, C. J. Ödman, and M. Trodden. The state of the dark energy equation of state. *Phys.Rev.D*, 68(4):043509, August 2003, arXiv:astro-ph/0211522.

[167] J. J. Mohr, B. O'Shea, A. E. Evrard, J. Bialek, and Z. Haiman. Studying dark energy with galaxy cluster surveys. *Nucl.Phys.B Proc.Supp.*, 124:63–67, July 2003, arXiv:astro-ph/0208102.

[168] M. J. Mortonson and W. Hu. Model-independent constraints on reionization from large-scale CMB polarization. *ArXiv e-prints*, 705, May 2007, arXiv:0705.1132.

[169] D. F. Mota, J. R. Kristiansen, T. Koivisto, and N. E. Groeneboom. Constraining Dark Energy Anisotropic Stress. *Mon. Not. Roy. Astron. Soc.*, 382:793–800, 2007, arXiv:0708.0830.

[170] M. Nolta *et al.* First Year Wilkinson Microwave Anisotropy Probe Observations: Dark Energy Induced Correlation with Radio Sources. *Astrophys.J.*, 608:10–15, June 2004, arXiv:astro-ph/0305097.

[171] C. E. North, B. R. Johnson, P. A. R. Ade, M. D. Audley, C. Baines, R. A. Battye, M. L. Brown, P. Cabella, P. G. Calisse, A. D. Challinor, W. D. Duncan, P. G. Ferreira, W. K. Gear, D. Glowacka, D. J. Goldie, P. K. Grimes, M. Halpern, V. Haynes, G. C. Hilton, K. D. Irwin, M. E. Jones, A. N. Lasenby, P. J. Leahy, J. Leech, B. Maffei, P. Mauskopf, S. J. Melhuish, D. O'Dea, S. M. Parsley, L. Piccirillo, G. Pisano, C. D. Reintsema, G. Savini, R. Sudiwala, D. Sutton, A. C. Taylor, G. Teleberg, D. Titterington, V. Tsaneva, C. Tucker, R. Watson, S. Withington, G. Yassin, and J. Zhang. Detecting the B-mode Polarisation of the CMB with Clover. *ArXiv e-prints*, May 2008, arXiv:0805.3690.

[172] J. P. Ostriker and P. J. Steinhardt. The observational case for a low-density Universe with a non-zero cosmological constant. *Nature*, 377:600–602, October 1995.

[173] P. Oxley, P. A. Ade, C. Baccigalupi, P. deBernardis, H.-M. Cho, M. J. Devlin, S. Hanany, B. R. Johnson, T. Jones, A. T. Lee, T. Matsumura, A. D. Miller, M. Milligan, T. Renbarger, H. G. Spieler, R. Stompor, G. S. Tucker, and M. Zaldarriaga. The EBEX experiment. In M. Strojnik, editor, *Society of Photo-Optical Instrumentation Engineers (SPIE) Conference Series*, volume 5543 of *Presented at the Society of Photo-Optical Instrumentation Engineers (SPIE) Conference*, pages 320–331, November 2004.

[174] Nikhil Padmanabhan *et al.* Correlating the cmb with luminous red galaxies : The integrated sachs-wolfe effect. *Phys. Rev.*, D72:043525, 2005, arXiv:astro-ph/0410360.

[175] J. A. Peacock. *Cosmological Physics*. January 1999.

[176] R. D. Peccei. Neutrino models of dark energy. *Phys.Rev.D*, 71(2):023527, January 2005, arXiv:hep-ph/0411137.

[177] P. J. E. Peebles. *Principles of physical cosmology*. 1993.

[178] W. J. Percival, B. A. Reid, D. J. Eisenstein, N. A. Bahcall, T. Budavari, J. A. Frieman, M. Fukugita, J. E. Gunn, Ž. Ivezić, G. R. Knapp, R. G. Kron, J. Loveday, R. H. Lupton, T. A. McKay, A. Meiksin, R. C. Nichol, A. C. Pope, D. J. Schlegel, D. P. Schneider, D. N. Spergel, C. Stoughton, M. A. Strauss, A. S. Szalay, M. Tegmark, M. S. Vogeley, D. H. Weinberg, D. G. York, and I. Zehavi. Baryon acoustic oscillations in the Sloan Digital Sky Survey Data Release 7 galaxy sample. *MNRAS*, 401:2148–2168, February 2010, arXiv:0907.1660.

[179] S. Perlmutter and B. P. Schmidt. Measuring Cosmology with Supernovae. In K. Weiler, editor, *Supernovae and Gamma-Ray Bursters*, volume 598 of *Lecture Notes in Physics, Berlin Springer Verlag*, pages 195–217, 2003.

[180] S. Perlmutter *et al.* Measurements of Omega and Lambda from 42 High-Redshift Supernovae. *Astrophys.J.*, 517:565–586, June 1999, arXiv:astro-ph/9812133.

[181] J. Polchinski. The Cosmological Constant and the String Landscape. *ArXiv High Energy Physics - Theory e-prints*, March 2006, arXiv:hep-th/0603249.

[182] C. Pryke, N. W. Halverson, E. M. Leitch, J. Kovac, J. E. Carlstrom, W. L. Holzapfel, and M. Dragovan. Cosmological Parameter Extraction from the First Season of Observations with the Degree Angular Scale Interferometer. *Astrophys.J.*, 568:46–51, March 2002, arXiv:astro-ph/0104490.

[183] B. Ratra and P. J. E. Peebles. Cosmological consequences of a rolling homogeneous scalar field. *Phys.Rev.D*, 37:3406–3427, June 1988.

[184] A. C. S. Readhead, B. S. Mason, C. R. Contaldi, T. J. Pearson, J. R. Bond, S. T. Myers, S. Padin, J. L. Sievers, J. K. Cartwright, M. C. Shepherd, D. Pogosyan, S. Prunet, P. Altamirano, R. Bustos, L. Bronfman, S. Casassus, W. L. Holzapfel, J. May, U.-L. Pen, S. Torres, and P. S. Udomprasert. Extended Mosaic Observations with the Cosmic Background Imager. *Astrophys.J.*, 609:498–512, July 2004, arXiv:astro-ph/0402359.

[185] C. L. Reichardt, P. A. R. Ade, J. J. Bock, J. R. Bond, J. A. Brevik, C. R. Contaldi, M. D. Daub, J. T. Dempsey, J. H. Goldstein, W. L. Holzapfel, C. L. Kuo, A. E. Lange, M. Lueker, M. Newcomb, J. B. Peterson, J. Ruhl, M. C. Runyan, and Z. Staniszewski. High-Resolution CMB Power Spectrum from the Complete ACBAR Data Set. *Astrophys.J.*, 694:1200–1219, April 2009, arXiv:0801.1491.

[186] Riess, A. G. *et al.* New Hubble Space Telescope Discoveries of Type Ia Supernovae at z $>$ 1: Narrowing Constraints on the Early Behavior of Dark Energy. *Astrophys.J.*, 659:98–121, April 2007, arXiv:astro-ph/0611572.

[187] A. Riess *et al.* Observational Evidence from Supernovae for an Accelerating Universe and a Cosmological Constant. *Astron.J.*, 116:1009–1038, September 1998, arXiv:astro-ph/9805201.

[188] J. E. Ruhl, P. A. R. Ade, J. J. Bock, J. R. Bond, J. Borrill, A. Boscaleri, C. R. Contaldi, B. P. Crill, P. de Bernardis, G. De Troia, K. Ganga, M. Giacometti, E. Hivon, V. V. Hristov, A. Iacoangeli, A. H. Jaffe, W. C. Jones, A. E. Lange, S. Masi, P. Mason, P. D. Mauskopf, A. Melchiorri, T. Montroy, C. B. Netterfield, E. Pascale, F. Piacentini, D. Pogosyan, G. Polenta, S. Prunet, and G. Romeo. Improved Measurement of the Angular Power Spectrum of Temperature Anisotropy in the Cosmic Microwave Background from Two New Analyses of BOOMERANG Observations. *Astrophys.J.*, 599:786–805, December 2003, arXiv:astro-ph/0212229.

[189] R. K. Sachs and A. M. Wolfe. Perturbations of a cosmological model and angular variations of the microwave background. *Astrophys. J.*, 147:73–90, 1967.

[190] S. Sadeh, Y. Rephaeli, and J. Silk. Cluster abundances and Sunyaev-Zel'dovich power spectra: effects of non-Gaussianity and early dark energy. *MNRAS*, 380:637–645, September 2007, arXiv:0706.1340.

[191] D. Samtleben and for the QUIET collaboration. QUIET - Measuring the CMB polarization with coherent detector arrays. *ArXiv e-prints*, June 2008, arXiv:0806.4334.

[192] H. B. Sandvik, M. Tegmark, M. Zaldarriaga, and I. Waga. The end of unified dark matter? *Phys.Rev.D*, 69(12):123524, June 2004, arXiv:astro-ph/0212114.

[193] D. Sapone and M. Kunz. Fingerprinting dark energy. *Phys.Rev.D*, 80(8):083519, October 2009, arXiv:0909.0007.

[194] S. Y. Sazonov and R. A. Sunyaev. Microwave polarization in the direction of galaxy clusters induced by the CMB quadrupole anisotropy. *MNRAS*, 310:765–772, December 1999, arXiv:astro-ph/9903287.

[195] R. J. Scherrer. Purely Kinetic k Essence as Unified Dark Matter. *Phys.Rev.Lett.*, 93(1):011301, June 2004, arXiv:astro-ph/0402316.

[196] R. J. Scherrer. Dark energy models in the $w - w^{'}$ plane. *Phys.Rev.D*, 73(4):043502, February 2006, arXiv:astro-ph/0509890.

[197] D. Schlegel, M. White, and D. Eisenstein. The Baryon Oscillation Spectroscopic Survey: Precision measurement of the absolute cosmic distance scale. In *astro2010: The Astronomy and Astrophysics Decadal Survey*, volume 2010 of *Astronomy*, page 314, 2009.

[198] D. J. Schlegel, C. Bebek, H. Heetderks, S. Ho, M. Lampton, M. Levi, N. Mostek, N. Padmanabhan, S. Perlmutter, N. Roe, M. Sholl, G. Smoot, M. White, A. Dey, T. Abraham, B. Jannuzi, D. Joyce, M. Liang, M. Merrill, K. Olsen,

and S. Salim. BigBOSS: The Ground-Based Stage IV Dark Energy Experiment. *ArXiv e-prints*, April 2009, arXiv:0904.0468.

[199] T. Schrabback, J. Hartlap, B. Joachimi, M. Kilbinger, P. Simon, K. Benabed, M. Bradač, T. Eifler, T. Erben, C. D. Fassnacht, F. W. High, S. Hilbert, H. Hildebrandt, H. Hoekstra, K. Kuijken, P. Marshall, Y. Mellier, E. Morganson, P. Schneider, E. Semboloni, L. Van Waerbeke, and M. Velander. Evidence for the accelerated expansion of the Universe from weak lensing tomography with COSMOS. *ArXiv e-prints*, November 2009, arXiv:0911.0053.

[200] Ryan Scranton *et al.* Physical Evidence for Dark Energy. July 2003, arXiv:astro-ph/0307335.

[201] U. Seljak. Gravitational Lensing Effect on Cosmic Microwave Background Anisotropies: A Power Spectrum Approach. *Astrophys.J.*, 463:1, May 1996, arXiv:astro-ph/9505109.

[202] U. Seljak, A. Slosar, and P. McDonald. Cosmological parameters from combining the Lyman-α forest with CMB, galaxy clustering and SN constraints. *JCAP*, 10:14, October 2006, arXiv:astro-ph/0604335.

[203] Uros Seljak and Matias Zaldarriaga. A Line of Sight Approach to Cosmic Microwave Background Anisotropies. *Astrophys. J.*, 469:437–444, 1996, arXiv:astro-ph/9603033.

[204] A. Sen. Field Theory of Tachyon Matter. *Mod.Phys.Lett.A*, 17:1797–1804, 2002, arXiv:hep-th/0204143.

[205] A. Sen. Tachyon Dynamics in Open String Theory. *International Journal of Modern Physics A*, 20:5513–5656, 2005, arXiv:hep-th/0410103.

[206] A. A. Sen. Reconstructing k-essence. *JCAP*, 3:10, March 2006, arXiv:astro-ph/0512406.

[207] C. Shapiro and M. S. Turner. What Do We Really Know about Cosmic Acceleration? *Astrophys.J.*, 649:563–569, October 2006, arXiv:astro-ph/0512586.

[208] J. Silk. Cosmic Black-Body Radiation and Galaxy Formation. *Astrophys.J.*, 151:459, February 1968.

[209] F. Simpson and S. Bridle. Redshift sensitivities of dark energy surveys. *Phys.Rev.D*, 73(8):083001, April 2006, arXiv:astro-ph/0602213.

[210] K. M. Smith, A. Cooray, S. Das, O. Doré, D. Hanson, C. Hirata, M. Kaplinghat, B. Keating, M. LoVerde, N. Miller, G. Rocha, M. Shimon, and O. Zahn. CMBPol Mission Concept Study: Gravitational Lensing. *ArXiv e-prints*, November 2008, arXiv:0811.3916.

[211] K. M. Smith, W. Hu, and M. Kaplinghat. Cosmological information from lensed CMB power spectra. *Phys.Rev.D*, 74(12):123002, December 2006, arXiv:astro-ph/0607315.

[212] S. Smith, A. Challinor, and G. Rocha. What can be learned from the lensed cosmic microwave background B-mode polarization power spectrum? *Phys.Rev.D*, 73(2):023517, January 2006, arXiv:astro-ph/0511703.

[213] T. Smith. Private Communication.

[214] SNAP Collaboration: G. Aldering, W. Althouse, R. Amanullah, J. Annis, P. Astier, C. Baltay, E. Barrelet, S. Basa, C. Bebek, L. Bergstrom, G. Bernstein, M. Bester, B. Bigelow, R. Blandford, R. Bohlin, A. Bonissent, C. Bower, M. Brown, M. Campbell, W. Carithers, E. Commins, W. Craig, C. Day, F. DeJongh, S. Deustua, T. Diehl, S. Dodelson, A. Ealet, R. Ellis, W. Emmet, D. Fouchez, J. Frieman, A. Fruchter, D. Gerdes, L. Gladney, G. Goldhaber, A. Goobar, D. Groom, H. Heetderks, M. Hoff, S. Holland, M. Huffer, L. Hui, D. Huterer, B. Jain, P. Jelinsky, A. Karcher, S. Kent, S. Kahn, A. Kim, W. Kolbe, B. Krieger, G. Kushner, N. Kuznetsova, R. Lafever, J. Lamoureux, M. Lampton, O. Le Fevre, M. Levi, P. Limon, H. Lin, E. Linder, S. Loken, W. Lorenzon, R. Malina, J. Marriner, P. Marshall, R. Massey, A. Mazure, T. McKay, S. McKee, R. Miquel, N. Morgan, E. Mortsell, N. Mostek, S. Mufson, J. Musser, P. Nugent, H. Oluseyi, R. Pain, N. Palaio, D. Pankow, J. Peoples, S. Perlmutter, E. Prieto, D. Rabinowitz, A. Refregier, J. Rhodes, N. Roe, D. Rusin, V. Scarpine, M. Schubnell, M. Sholl, G. Smadja, R. M. Smith, G. Smoot, J. Snyder, A. Spadafora, A. Stebbins, C. Stoughton, A. Szymkowiak, G. Tarle, K. Taylor, A. Tilquin, A. Tomasch, D. Tucker, D. Vincent, H. von der Lippe, J. Walder, G. Wang, and W. Wester. Supernova / Acceleration Probe: A Satellite Experiment to Study the Nature of the Dark Energy. *ArXiv Astrophysics e-prints*, May 2004, arXiv:astro-ph/0405232.

[215] T. P. Sotiriou and V. Faraoni. f(R) Theories Of Gravity. *ArXiv e-prints*, May 2008, arXiv:0805.1726.

[216] C. Stephan-Otto. Optimized supernova constraints on dark energy evolution. *Phys.Rev.D*, 74(2):023507, July 2006, arXiv:astro-ph/0605403.

[217] S. Sullivan, A. Cooray, and D. E. Holz. Narrowing constraints with type Ia supernovae: converging on a cosmological constant. *JCAP*, 9:4, September 2007, arXiv:0706.3730.

[218] R. A. Sunyaev and I. B. Zeldovich. The velocity of clusters of galaxies relative to the microwave background - The possibility of its measurement. *MNRAS*, 190:413–420, February 1980.

[219] N. Suzuki. Quasar Spectrum Classification with Principal Component Analysis (PCA): Emission Lines in the Lyα Forest. *Astrophys.J.Supp.*, 163:110–121, March 2006.

[220] M. Takada and B. Jain. Cosmological parameters from lensing power spectrum and bispectrum tomography. *MNRAS*, 348:897–915, March 2004, arXiv:astro-ph/0310125.

[221] Masahiro Takada. Can A Galaxy Redshift Survey Measure Dark Energy Clustering? *Phys. Rev.*, D74:043505, 2006, arXiv:astro-ph/0606533.

[222] Y. D. Takahashi, D. Barkats, J. O. Battle, E. M. Bierman, J. J. Bock, H. C. Chiang, C. D. Dowell, E. F. Hivon, W. L. Holzapfel, V. V. Hristov, W. C. Jones, J. P. Kaufman, B. G. Keating, J. M. Kovac, C.-L. Kuo, A. E. Lange, E. M. Leitch, P. V. Mason, T. Matsumura, H. T. Nguyen, N. Ponthieu, G. M. Rocha, K. W. Yoon, P. Ade, and L. Duband. CMB polarimetry with BICEP: instrument characterization, calibration, and performance. In *Society of Photo-Optical Instrumentation Engineers (SPIE) Conference Series*, volume 7020 of *Presented at the Society of Photo-Optical Instrumentation Engineers (SPIE) Conference*, August 2008.

[223] M. Tegmark, A. Aguirre, M. J. Rees, and F. Wilczek. Dimensionless constants, cosmology, and other dark matters. *Phys.Rev.D*, 73(2):023505, January 2006, arXiv:astro-ph/0511774.

[224] M. Tegmark, D. J. Eisenstein, M. A. Strauss, D. H. Weinberg, M. R. Blanton, J. A. Frieman, M. Fukugita, J. E. Gunn, A. J. S. Hamilton, G. R. Knapp, R. C. Nichol, J. P. Ostriker, N. Padmanabhan, W. J. Percival, D. J. Schlegel, D. P. Schneider, R. Scoccimarro, U. Seljak, H.-J. Seo, M. Swanson, A. S. Szalay, M. S. Vogeley, J. Yoo, I. Zehavi, K. Abazajian, S. F. Anderson, J. Annis, N. A. Bahcall, B. Bassett, A. Berlind, J. Brinkmann, T. Budavari, F. Castander, A. Connolly, I. Csabai, M. Doi, D. P. Finkbeiner, B. Gillespie, K. Glazebrook, G. S. Hennessy, D. W. Hogg, Ž. Ivezić, B. Jain, D. Johnston, S. Kent, D. Q. Lamb, B. C. Lee, H. Lin, J. Loveday, R. H. Lupton, J. A. Munn, K. Pan, C. Park, J. Peoples, J. R. Pier, A. Pope, M. Richmond, C. Rockosi, R. Scranton, R. K. Sheth, A. Stebbins, C. Stoughton, I. Szapudi, D. L. Tucker, D. E. vanden Berk, B. Yanny, and D. G. York. Cosmological constraints from the SDSS luminous red galaxies. *Phys.Rev.D*, 74(12):123507, December 2006, arXiv:astro-ph/0608632.

[225] A. Torres-Rodríguez, C. M. Cress, and K. Moodley. Covariance of dark energy parameters and sound speed constraints from large HI surveys. *MNRAS*, 388:669–676, August 2008, arXiv:0804.2344.

[226] S. Tsujikawa and T. Torii. Spinodal effect in the natural inflation model. *Phys.Rev.D*, 62(4):043505, August 2000, arXiv:hep-ph/9912499.

[227] M. S. Turner. Coherent scalar-field oscillations in an expanding universe. *Phys.Rev.D*, 28:1243–1247, September 1983.

[228] A. Vikman. Can dark energy evolve to the phantom? *Phys.Rev.D*, 71(2):023515, January 2005, arXiv:astro-ph/0407107.

[229] S. Weinberg. Anthropic bound on the cosmological constant. *Phys.Rev.Lett.*, 59:2607–2610, November 1987.

[230] S. Weinberg. The cosmological constant problem. *Reviews of Modern Physics*, 61:1–23, January 1989.

[231] S. Weinberg. *Cosmology*. Oxford University Press, 2008.

[232] Jochen Weller and A. M. Lewis. Large Scale Cosmic Microwave Background Anisotropies and Dark Energy. *Mon. Not. Roy. Astron. Soc.*, 346:987–993, 2003, arXiv:astro-ph/0307104.

[233] C. Wetterich. Cosmology and the fate of dilatation symmetry. *Nucl.Phys.B*, 302:668–696, June 1988.

[234] C. Wetterich. Phenomenological parameterization of quintessence. *Phys.Lett.B*, 594:17–22, July 2004, arXiv:astro-ph/0403289.

[235] C. Wetterich and V. Pettorino. Growing neutrino cosmology. *ArXiv e-prints*, May 2009, arXiv:0905.0715.

[236] Jun-Qing Xia, Yi-Fu Cai, Tao-Tao Qiu, Gong-Bo Zhao, and Xinmin Zhang. Constraints on the Sound Speed of Dynamical Dark Energy. *Int. J. Mod. Phys.*, D17:1229–1243, 2008, arXiv:astro-ph/0703202.

[237] M. Zaldarriaga, L. Colombo, E. Komatsu, A. Lidz, M. Mortonson, S. P. Oh, E. Pierpaoli, L. Verde, and O. Zahn. CMBPol Mission Concept Study: Reionization Science with the Cosmic Microwave Background. *ArXiv e-prints*, November 2008, arXiv:0811.3918.

[238] M. Zaldarriaga and U. Seljak. Reconstructing projected matter density power spectrum from cosmic microwave background. *Phys.Rev.D*, 59(12):123507, June 1999, arXiv:astro-ph/9810257.

[239] M. Zaldarriaga, D. N. Spergel, and U. Seljak. Microwave Background Constraints on Cosmological Parameters. *Astrophys.J.*, 488:1, October 1997, arXiv:astro-ph/9702157.

[240] Y. B. Zel'dovich. Special Issue: the Cosmological Constant and the Theory of Elementary Particles. *Soviet Physics Uspekhi*, 11:381–393, March 1968.

[241] I. Zlatev, L. Wang, and P. J. Steinhardt. Quintessence, Cosmic Coincidence, and the Cosmological Constant. *Phys.Rev.Lett.*, 82:896–899, February 1999, arXiv:astro-ph/9807002.

Appendix A

Angular Power Spectra: Definitions

Here we review how the observable power spectra of various quantities on the sky are related to the three-dimensional primordial power spectrum and the transfer functions. This is relevant to the work presented in chapters 2 and 6. We consider the CMB temperature anisotropies and galaxy overdensities in redshift slices, or populations, labeled with the subscript j, and write the observables in direction $\hat{n}$ as line of sight projections along comoving radial coordinate χ,

$$X(\hat{n}) = \int d\chi \, S^X(\hat{n}\chi, \tau_0 - \chi), \tag{A.1}$$

with $S^X(\vec{x}, \tau)$ the "source term" as a function of comoving position and conformal time (τ_0 is the age of the universe in conformal time). Here X represents the observable, which could be a galaxy overdensity g_j in the jth redshift bin or a CMB temperature anisotropy T. For the galaxy overdensity g_j, the source is

$$S^{g_j}(\vec{x}, \tau) = H(z(\tau)) \frac{n_j(z(\tau))}{n_j^A} b_j \delta_m(\vec{x}, \tau), \tag{A.2}$$

where $n_j(z)dz$ is the average angular galaxy density of galaxy population j in the redshift interval $(z, z + dz)$, $n_j^A = \int dz \, n_j(z)$ is the total average angular galaxy density of population j, and b_j is the galaxy bias relative to the matter overdensity of bin j. The Hubble factor $H(z)$ arises because the source was defined in terms of an integral over χ while $n_j(z)/n_j^A$ is normalized to unity in terms of an integral over z.

For CMB temperature anisotropies, the (Fourier transform of the) source is given in Eq. (12) of [203]. The Integrated Sachs-Wolfe contribution to the CMB anisotropy is nonzero when the universe is *not* matter dominated, and thus the gravitational potentials ϕ and ψ are not constant. The ISW source is given by

$$S^{\rm ISW}(\vec{x}, \tau) = \dot{\phi}(\vec{x}, \tau) + \dot{\psi}(\vec{x}, \tau), \tag{A.3}$$

where dots denote derivatives with respect to conformal time.

If we expand the anisotropy field in spherical harmonics, $X(\hat{n}) = \sum_{\ell m} a^X_{\ell m} Y_{\ell m}(\hat{n})$, the expansion coefficients are given by

$$\begin{aligned} a^X_{\ell m} &= \int d\Omega\, Y^*_{\ell m}(\hat{n}) X(\hat{n}) \\ &= (2\pi)^{-3/2} \int d\Omega\, Y^*_{\ell m}(\hat{n}) \int d^3\vec{k} \int d\chi\, e^{i\vec{k}\hat{n}\chi} S^X(\vec{k}, \tau_0 - \chi) \\ &= \sqrt{\frac{2}{\pi}}\, i^\ell \int d^3\vec{k}\, Y^*_{\ell m}(\hat{k}) \int d\chi\, j_\ell(k\chi) S^X(\vec{k}, \tau_0 - \chi), \end{aligned} \tag{A.4}$$

where we have Fourier expanded

$$S^X(\vec{x}, \tau) = \int \frac{d^3\vec{k}}{(2\pi)^{3/2}}\, e^{i\vec{k}\vec{x}} S^X(\vec{k}, \tau)\,, \tag{A.5}$$

and we have used the Rayleigh plane-wave expansion

$$e^{i\vec{k}\cdot\hat{n}\chi} = 4\pi \sum_{\ell,m} i^\ell j_\ell(k\chi) Y^*_{\ell m}(\hat{k}) Y_{\ell m}(\hat{n})\,, \tag{A.6}$$

where the j_ℓ is the spherical Bessel function. We now write $S^X(\vec{k}, \tau) = \psi_i(\vec{k})\, S^X(k, \tau)$ where $\psi_i(\vec{k})$ is the initial potential perturbation and $S^X(k, \tau)$ is the source for $\psi_i = 1$, i.e. it is a transfer function. Due to the assumption of homogeneity, the transfer function does not depend on the direction of the wavenumber, but only on its magnitude $k \equiv |\vec{k}|$. The statistics of the initial perturbations are given by

$$\left\langle \psi_i(\vec{k}) \psi_i(\vec{k}') \right\rangle = P^\psi_i(k)\, \delta^{(3)}(\vec{k} + \vec{k}'), \tag{A.7}$$

where $P^\psi_i(k)$ is the primordial potential power spectrum. Assuming statistical isotropy, the angular correlations between two quantities on the sky X and Y (where they may or may not be the same) is given by the angular power spectrum

$$\left\langle a^X_{\ell m} a^{Y*}_{\ell' m'} \right\rangle = C^{XY}_\ell\, \delta_{\ell\ell'} \delta_{mm'} \tag{A.8}$$

where, using Eq. (A.4),

$$\begin{aligned} C^{XY}_\ell &= \frac{2}{(2\pi)^2} \int d^3\vec{k}\, P^\psi_i(k) \int d\chi\, j_\ell(k\chi) S^X(k, \tau_0 - \chi) \times \\ &\quad \int d\chi'\, j_\ell(k\chi') S^Y(k, \tau_0 - \chi')\,. \end{aligned} \tag{A.9}$$

In this work, we are specifically interested in the combinations $\{XY\} = \{TT, Tg_i, g_i g_j\}$, but Eq. (A.9) is the general expression for angular power or crosscorrelation spectra.

When the sources S^X and S^Y vary slowly compared to the spherical Bessel functions in Eq. (A.9), the triple integral can to a good approximation be reduced to a single integral. Setting $P(k) = P(k = (\ell + 1/2)/\chi(z))$ and using the asymptotic (for $\ell \gg 1$) formula that $(2/\pi) \int k^2 dk j_\ell(k\chi) j_\ell(k\chi') = (1/\chi^2)\, \delta(\chi - \chi')$, we find

$$\begin{aligned} C_\ell^{XY} &= \frac{2\pi^2}{(\ell+1/2)^3} \int d\chi\, \chi\, \Delta_i^\psi \left(\frac{\ell+1/2}{\chi}\right) \times \\ &\quad S^X\left(\frac{\ell+1/2}{\chi}, \tau_0 - \chi\right)\, S^Y\left(\frac{\ell+1/2}{\chi}, \tau_0 - \chi\right) \end{aligned} \tag{A.10}$$

where $\Delta(k) \equiv k^3 P(k)/(2\pi^2)$. We use the power spectra to calculate the χ^2 (signal-to-noise) in Eq. (2.15).

Finally, we need to specify formulae for noise in the observed spectra C_ℓ^{XY}. The covariances between the spectra are given by

$$\mathbf{Cov}(C_\ell^{XY}, C_{\ell'}^{ZW}) = \delta_{\ell\ell'} \frac{1}{(2\ell+1) f_{\rm sky}} \left(\tilde{C}_\ell^{XZ} \tilde{C}_\ell^{YW} + \tilde{C}_\ell^{XW} \tilde{C}_\ell^{YZ}\right), \tag{A.11}$$

where

$$\tilde{C}_\ell^{XY} = C_\ell^{XY} + N_\ell^{XY}\,. \tag{A.12}$$

Here $f_{\rm sky}$ is the sky coverage, C_ℓ^{XY} are the fiducial spectra and N_ℓ^{XY} are the noise power spectra. For the galaxy density fields, the white noise power spectra are given by

$$N_\ell^{g_j g_j} = \frac{1}{n_j^A}\,, \tag{A.13}$$

and for the CMB it is given by

$$N_\ell^{TT} = \Delta_T^2\, e^{\ell(\ell+1)\theta^2_{\rm FWHM}/(8\ln 2)}\,, \tag{A.14}$$

where Δ_T is the sensitivity and $\theta_{\rm FWHM}$ is the full width half max angle of the Gaussian beam. The noise cross power spectra can be assumed to vanish.

The treatment of the covariances for actual data is typically more complicated than the above. We use the covariances and treatment of the observables as given by the data packages in COSMOMC, [105, 224, 137, 49, 82] for the angular spectra, and the Union2 supernovae covariance matrix including systematics (see chapter 2).

Appendix B

Properties of Decorrelated Modes

In this Appendix, which provides the theory behind some of th work presented in chapter5, we first introduce some definitions and discuss some useful general properties of decorrelated modes (§B.1). We then show that eigenvectors are formally ill-defined for a Fisher matrix (§B.2) and that the eigenmodes (eigenvectors in the limit of a large number of bins) depend on the coordinate (redshift z, scale factor a, etc.) one uses to write the EOS w as a function of (§B.3). We consider the latter to be the main result of this Appendix.

B.1 Basis Expansion

The matrix $\mathbf{W}$ defines a basis transformation by

$$\mathbf{e_i'} = W_{ij}\mathbf{e_j}, \tag{B.1}$$

so that the rows of $\mathbf{W}$ contain the new basis vectors as expressed with respect to the old basis[1]. The coefficients, or components, $\alpha = (\alpha_1, ..., \alpha_N)$ then transform according to

$$\alpha' = (\mathbf{W^{-1}})^{\mathrm{T}}\alpha. \tag{B.2}$$

If the transformation is orthogonal, $\mathbf{W}^{\mathrm{T}} = \mathbf{W^{-1}}$, the basis vectors and the coefficients transform in the same way. However, this is not the case in general.

Since the Fisher matrix is a Hessian matrix, i.e. it is defined in terms of second order partial derivatives,

$$F_{ij} = \left\langle -\frac{\partial^2 \ln L}{\partial\alpha_i \partial\alpha_j} \right\rangle, \tag{B.3}$$

it transforms according to

$$\mathbf{F'} = \mathbf{W}\,\mathbf{F}\,\mathbf{W}^{\mathrm{T}}. \tag{B.4}$$

[1]Note that in some literature (e.g. [120, 186]) the transformation matrix is defined as the matrix transforming the coordinates: our $\mathbf{W}$ is the inverse transpose of that matrix.

It will become clear below that one of the main points of §5.3, namely that eigenmodes depend on the binning used to calculate them in, is essentially a consequence of this transformation behavior.

Diagonalizing $\mathbf{F}$ comes down to finding a matrix $\mathbf{W}$ such that

$$\mathbf{W}\,\mathbf{F}\,\mathbf{W}^{\mathrm{T}} = \mathbf{D} \tag{B.5}$$

is diagonal. In such a basis the uncertainties in the coefficients α_i' are uncorrelated. It is straightforward to show that there is an infinite number of bases that achieve this. The remainder of this Appendix focuses on the particular choice of eigenvectors as basis (see also §5.3).

B.2 Basis Dependence of Eigenmodes

If a set of eigenvectors is orthonormal (which can always be arranged), the eigenvalues are equal to the diagonal elements of the diagonal Fisher matrix, i.e. the inverse variances. Eigenvectors are defined by

$$\mathbf{F}\mathbf{v} = \lambda\mathbf{v}, \tag{B.6}$$

and their components transform according to Eq. (B.2). However, since the Fisher matrix transforms according to Eq. (B.4), this is not a covariant statement:

$$\mathbf{F}'\mathbf{v}' = \mathbf{W}\,\mathbf{F}\,\mathbf{W}^{\mathrm{T}}\left(\mathbf{W}^{-\mathbf{1}}\right)^{\mathrm{T}}\mathbf{v} = \lambda\mathbf{W}\mathbf{v}. \tag{B.7}$$

This is only equal to

$$\lambda\mathbf{v}' = \lambda(\mathbf{W}^{-\mathbf{1}})^{\mathrm{T}}\mathbf{v} \tag{B.8}$$

if the coordinate transformation is orthogonal, i.e. $\mathbf{W}^{\mathrm{T}} = \mathbf{W}^{-\mathbf{1}}$, but not in general! This means that, formally, eigenvectors of a Fisher matrix are not well-defined.

Of course, we can take a pragmatic approach and just compute the eigenvectors (for lack of a better word, we will still call them eigenvectors) in a particular basis and work with those. This is what we will do, but it is important to remember that the set of eigenvectors found in this way depends on the particular basis we chose to compute them in.

B.3 Coordinate Dependence of Eigenmodes

We now turn our attention to the eigenmodes in the $N \to \infty$ limit, where N is the number of EOS bins. We start with the basis of modes $e_i(z)$ discussed in §5.2 that are equal to one inside the ith bin and zero everywhere else. In the limit $N \to \infty$ (keeping the *relative* bin widths the same) the eigenvectors approach a set

of continuous functions (eigenmodes) and these eigenmodes and the corresponding standard deviations converge (see for example [122]).

In this section, we address the question of whether the eigenmodes are independent of which coordinate we use to write w as a function of. For example, we may choose a binning that is uniform in terms of the scale factor $a = 1/(1+z)$, i.e. Δa constant instead of uniform in z, i.e. Δz constant. Note that this is equivalent to a non-uniform binning in z,

$$\Delta z_i \approx \frac{dz}{da}(z_i)\,\Delta a, \tag{B.9}$$

where z_i is a redshift inside the ith bin. Since we saw before that eigenvectors of the Fisher matrix are basis dependent, it should not be too surprising if the eigenmodes turn out to depend on the relative bin sizes. Indeed, we find this is the case. We will explain this in the remainder of this section (specific examples are shown in §5.3).

Assume a binning that is uniform in a variable $x = x(z)$, which is either monotonically increasing or decreasing as a function of z in the relevant redshift range. For example, x could be the scale factor a or perhaps its logarithm. To see if the eigenmodes calculated using x are the same as the ones calculated using z, we will need to make use of the following results.

Let $\mathbf{F}$ be the Fisher matrix for a set of N bins with widths Δz_i and $\mathbf{F'}$ be the one for a set of N' bins with widths $\Delta z'_i$. Then for large enough N and N',

$$F'(z,z') \approx \frac{\Delta z'}{\Delta z}(z)\,\frac{\Delta z'}{\Delta z}(z')F(z,z'), \tag{B.10}$$

where we have replaced discrete indices by the redshifts of the corresponding bins. For example, $F(z,z') \equiv F_{ij}$ where the ith bin contains z and the jth bin contains z'. Eq. (B.10) follows from the fact that derivatives with respect to EOS bin parameters should scale with the bin width for small enough bins. If we apply the above result to the cases of a binning with Δz constant and one with Δx constant, we get

$$F^{(x)}(z,z') \approx \left(\frac{\Delta x}{\Delta z}\right)^2 \frac{dz}{dx}(z)\frac{dz}{dx}(z')F^{(z)}(z,z'), \tag{B.11}$$

where the superscript on F denotes in which binning the Fisher matrix is calculated.

We can now apply the results from the previous paragraph to the eigenmodes discussion. Let us assume that $v(z)$ is an eigenmode calculated using z, i.e.

$$\sum_{z'(\Delta z)} F^{(z)}(z,z')\,v(z') = \lambda\,v(z), \tag{B.12}$$

where the (Δz) below the summation symbol indicates that the sum is supposed to

be carried out over the bins (labeled by z') uniformly spaced in z. Then,

$$\begin{aligned}
\sum_{z'(\Delta x)} F^{(x)}(z,z')\,v(z') &= \left(\frac{\Delta x}{\Delta z}\right)^2 \sum_{z'(\Delta x)} \frac{dz}{dx}(z)\frac{dz}{dx}(z')F^{(z)}(z,z')\,v(z') \\
&= \left(\frac{\Delta x}{\Delta z}\right)^2 \sum_{z'(\Delta z)} \frac{\Delta z}{\Delta x}\frac{dx}{dz}(z')\,\frac{dz}{dx}(z)\frac{dz}{dx}(z')F^{(z)}(z,z')\,v(z') \\
&= \frac{\Delta x}{\Delta z}\frac{dz}{dx}(z) \sum_{z'(\Delta z)} F^{(z)}(z,z')\,v(z') \\
&= \lambda\,\frac{\Delta x}{\Delta z}\,\frac{dz}{dx}(z)\,v(z), \qquad \text{(B.13)}
\end{aligned}$$

where in the first equality we have used Eq. (B.11), in the second equality we went from the binning uniform in x to the binning uniform in z, which forced us to put in a factor $\frac{\Delta z}{\Delta x}\frac{dx}{dz}(z')$, and in the fourth equality we use the fact that $v(z)$ is an eigenmode in the binning uniform in z, i.e. Eq. (B.12). What the above shows is that $v(z)$ is an eigenmode in the x-binning only if $\frac{dz}{dx} = \text{const}$ (recall that Δx and Δz are just constants by construction). Hence, using the scale factor a or any other coordinate that is not a linear function of z will result in a different set of eigenmodes. (We illustrate this with numerical results in Fig. 5.4 of §5.3.1). The above has strong implications when we try to decide how many modes/parameters are well determined, an issue that is explored further in §5.7.1.

Appendix C

Model Dependence of Decorrelated Equation of State Modes

This appendix is closely related ot the work presented in chapter 5. In addition to the modes and weights depending on basis, binning variable, and specific binning choice (see Appendix B), we now consider dependence on the fiducial model. We analyze how the uncorrelated bandpowers that were discussed in §5.4 change as the fiducial EOS is changed from the $w = -1$ ΛCDM cosmology to the (discretized) PNGB and bending models discussed in §5.6.

Figures C.1 and C.2 show how the first and third modes, the corresponding weights, and the uncertainties change between these models. We again show results both for the case where we fix the EOS at $z > 1.7$ to the respective fiducials (Fig. C.1) and for the case where we treat it as a free parameter (Fig. C.2). While the PNGB results lie rather close to the ΛCDM ones, the bending model results in significantly different bandpowers and uncertainties. Fiducial models deviating appreciably from each other will induce appreciable model dependence in the mode analysis. Note that changing the fiducial does not make the weights look "better". i.e. they do not get significantly more localized or positive.

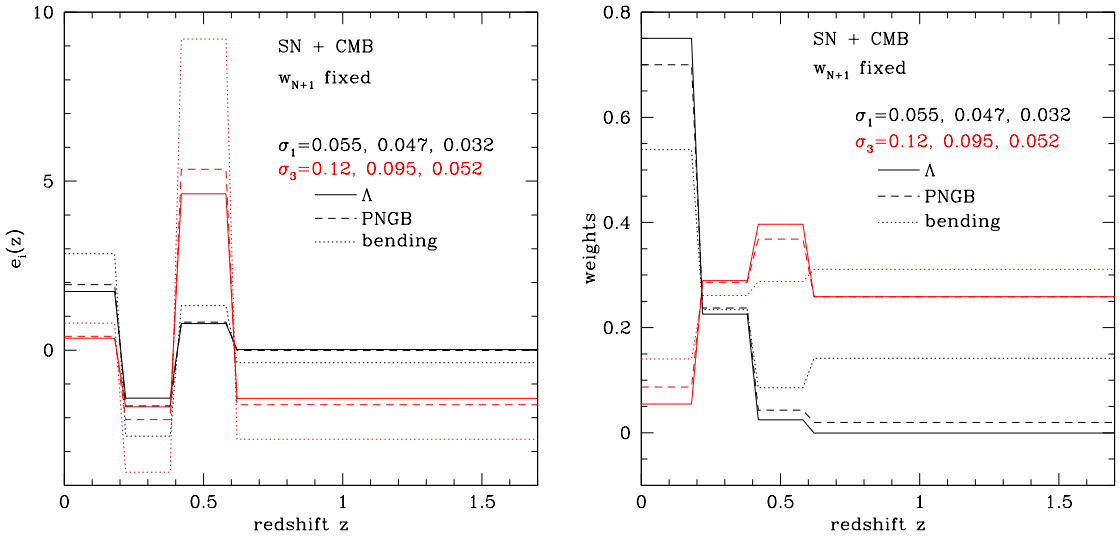

Figure C.1: As Fig. 5.5, but comparing the first and third modes (left panel) and associated weights (right panel) for three dark energy fiducial models: cosmological constant Λ, PNGB, and bending (see §5.6). Here we fix w_{N+1} to its appropriate fiducial value for each model.

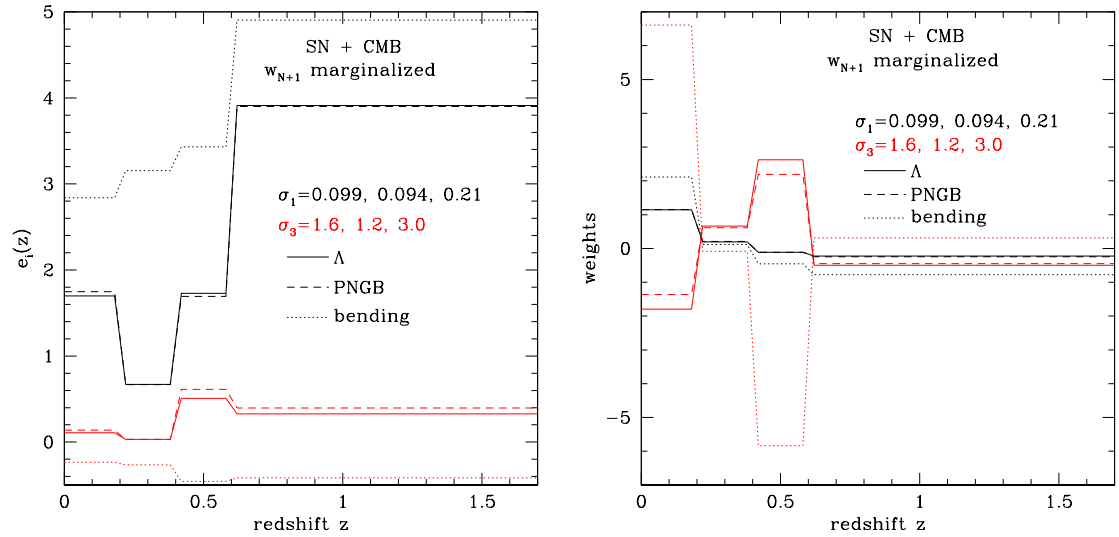

Figure C.2: As Fig. C.1, but marginalizing over w_{N+1}.

Appendix D

Fisher Parameter Bias Formula

In this section we derive Eq. (5.26) from chapter 5, which tells us how much we misestimate the other parameters when we fix one of the parameters to the wrong value. Consider the general case where the observables $O_k = O_k(\{p_i\}_{i=1}^{n+1})$ depend on $n+1$ parameters p_i. We call the true values of the parameters $p_{\mathrm{t},i}$. Now imagine that, instead of fitting all $n+1$ parameters to the data, we first fix p_{n+1} to $p_{\mathrm{fix},n+1}$ and then fit the resulting n parameters to the data. To get the correct values for these parameters, the observables would have to be given by $O_k(\{p_{\mathrm{t},i}\}_{i=1}^{n}, p_{\mathrm{fix},n+1})$. In reality, ignoring observational uncertainties (we do not want to write "the expectation values of" over and over), the data are given by $O_k = O_k(\{p_{\mathrm{t},i}\}_{i=1}^{n+1})$. Hence, if $p_{\mathrm{fix},n+1} \neq p_{\mathrm{t},n+1}$, the n parameter values $p_{\mathrm{e},i}$ derived from the data will be different from the actual values.

If we define

$$\Delta O_k \equiv O_k(\{p_{\mathrm{t},i}\}_{i=1}^{n+1}) - O_k(\{p_{\mathrm{t},i}\}_{i=1}^{n}, p_{\mathrm{fix},n+1}) = -\frac{\partial O_k}{\partial p_{n+1}}\,\delta p_{n+1}, \tag{D.1}$$

where $\delta p_{n+1} = p_{\mathrm{fix},n+1} - p_{\mathrm{t},n+1}$, we can use Eq. (5.25),

$$\delta p_i \equiv p_{\mathrm{e},i} - p_{\mathrm{t},i} = (F^{(n)})^{-1}_{ij} \sum_k \frac{\partial O_k}{\partial p_j}\,\frac{1}{\sigma_k^2}\,\Delta O_k, \tag{D.2}$$

where the superscript (n) means that we need the $n \times n$ Fisher matrix calculated using the first n parameters (the ones that we have not fixed). Inserting Eq. (D.1) into Eq. (D.2) gives

$$\delta p_i = -\delta p_{n+1} \times \sum_{j=1}^{n} (F^{(n)})^{-1}_{ij}\,(F^{(n+1)})_{j,n+1} \tag{D.3}$$

$(i = 1, ..., n)$, where we have used Eq. (5.1) to substitute the $(n+1) \times (n+1)$ Fisher matrix. We then obtain Eq. (5.26),

$$\frac{dp_i}{dp_{n+1}} = -\sum_{j=1}^{n} (F^{(n)})^{-1}_{ij}\,(F^{(n+1)})_{j,n+1}. \tag{D.4}$$

Note that since Eq. (5.25) is only valid to first order, we can calculate the Fisher matrix using the true parameter values.